Spin Dynamics in Ferromagnetic Nanostructures

Thesis submitted for the degree of

Doctor of Philosophy (Science)

in

Physics (Experimental)

by

Kartik Adhikari

Department of Physics
Jadavpur University
2021

CERTIFICATE FROM THE SUPERVISOR

This is to certify that the thesis entitled "**Spin Dynamics in Ferromagnetic Nanostructures**" submitted by **Shri Kartik Adhikari** who got his name registered on 26th April, 2016 for the award of Ph.D. (Science) degree of Jadavpur University, is absolutely based upon his own work under the supervision of **Prof. Anjan Barman** and that neither this thesis nor any part of it has been submitted for either any degree / diploma or any other academic award anywhere before.

Anjan Barman 30/11/2021

(Signature of the supervisor with date and official seal)

Dr. Anjan Barman, Ph.D.
Senior Professor & [redacted] Dean (Faculty)
Dept. of Condensed Matter Physics and Material Sciences
S. N. Bose National Centre for Basic Sciences
Block-JD, Sector-III, Salt Lake, Kolkata-700106, India

Dedicated to my loving family. . . . .

Abstract

The continuous improvement of electronic devices demand more power efficient and miniaturized circuit elements. However, the silicon-based electronics are approaching its limits regarding performance, miniaturization and power consumption. On the other hand, spin based devices offer some exciting advantages, for instance, substantially reduced resistive (Joule) heating energy loss unlike electronics and spin waves (SWs) with GHz frequencies, which enable fabrication of compact integrated circuits. In magnonic crystals (MCs), the periodic modulation of the magnetic properties in space allows manipulation of the magnons (quanta of SWs) in controlled manner with the aid of external magnetic field. These features make MCs suitable candidates for the applications in nanoscale on-chip data processing and communications devices.

This thesis is based on the investigation of magnetic configuration and spin dynamics in $Ni_{80}Fe_{20}$ (Permalloy; Py) patterned nanostructures by varying different physical and geometrical parameters, for instance, size and shape of the nanostructures as well as various external parameters such as strength and orientation of the bias magnetic field and microwave power of the input signal. We have utilized a broadband ferromagnetic resonance spectrometer to probe the magnetization dynamics in frequency domain. Whereas the ultrafast precessional magnetization dynamics is detected by a time-resolved magneto-optical Kerr effect (TR-MOKE) microscope. The experimental observations are interpreted with the assistance of micromagnetic simulations (OOMMF and LLG Micromagnetics simulator) to underpin the explanations. A rich anisotropic SW dynamics is explored in cross-shaped nanodot (nanocross) arrays by using ferromagnetic resonance technique. The static magnetic configuration at different bias field values are studied. Various interesting phenomena such as mode crossover, mode softening, mode merging and mode splitting are detected in magnetization dynamics. These prime features are substantially modulated with the variation of sizes of the nanocrosses. Further, the in-plane bias field orientation is varied and the critical angles are tabulated where different prime features are detected for varying dimensions of the nanocrosses. The direction of propagation of the SW can manipulated by varying the in-

plane orientation of the bias field. Consequently, a bias field strength and in-plane orientation dependent tunable static magnetic configuration and magnetization dynamics are observed in Py nanocross arrays of varying sizes. In addition, the microwave power of the input signal is varied using vector network analyzer. A microwave power dependent ferromagnetic resonance shift is detected in FMR frequency where sign of the shift depends on the strength of the bias field and static magnetic configuration. In addition, strong magnon-magnon coupling induced two anticrossing features are detected in dipolar coupled nanocross array. This dynamics in ferromagnetic nanocross array can be transformed from linear to nonlinear by enhancing the microwave power of the input signal. We have further investigated the spin dynamics in $Ni_{80}Fe_{20}$ cross-shaped nanoring (CNR) array with the help of a TR-MOKE microscope and micromagnetic simulations. A magnon-magnon coupling induced anticrossing feature is detected between the two lowest frequency spin wave modes. The magnon-magnon coupled modes can propagate longer distance as opposed to the other spin wave modes present in the ferromagnetic CNR array.

All the aforementioned experimental observations are important in the field of magnonics in terms of their applicability in microwave-assisted fast data storage, logic, and various communication devices.

List of Publications

[1] "Bias Field Tunable Magnetic Configuration and Magnetization Dynamics in $Ni_{80}Fe_{20}$ Nano-cross Structures with Varying Arm Length"

K. Adhikari, S. Choudhury, R. Mandal, S. Barman, Y. Otani, and A. Barman, J. Appl. Phys. **121**, 043909 (2017).

[2] "Tunable Angle-Dependent Magnetization Dynamics in $Ni_{80}Fe_{20}$ Nanocross Structures of Varying Size"

K. Adhikari, S. Barman, R. Mandal, Y. Otani, and A. Barman, Phys. Rev. Appl. **10**, 044010 (2018).

[3] "Large Nonlinear Ferromagnetic Resonance Shift and Strong Magnon-Magnon Coupling in $Ni_{80}Fe_{20}$ Nanocross Array"

K. Adhikari, S. Sahoo, A. K. Mondal, Y. Otani, and A. Barman, Phys. Rev. B **101**, 054406 (2020).

[4] "Observation of Magnon-Magnon Coupling with High Cooperativity in $Ni_{80}Fe_{20}$ Cross-shaped Nanoring Array"

K. Adhikari, S. Choudhury, S. Barman, Y. Otani, and A. Barman, Nanotechnology **32**, 395706 (2021).

Acknowledgements

I joined in the department of condensed matter physics and material sciences (CMPMS) of S. N. Bose National Centre for Basic Sciences (SNBNCBS), Kolkata in 2015 as a junior research fellow. Now on the verge of my PhD journey, it is a great pleasure for me to express my sincere gratitude to all the individuals who were integrated part of this journey.

At first, I would like express my profound gratitude and deepest respect to my PhD supervisor Prof. Anjan Barman for giving me a wonderful opportunity to doing research work under his guidance. I am sincerely thankful to him for his tireless efforts and constant support throughout my PhD work. It was really a privilege and an honour to work under his outstanding guidance. His dedication, commitment and the enthusiasm towards research always motivated me a lot. I am forever indebted to him for his encouragement and valuable inputs to accomplish my research problems. I am extremely grateful for his efforts to improve my writing and presentation skills. Above all, he has always been kind and caring in all situations.

I am extremely thankful to Dr. Samiran Choudhury who first introduced me broadband ferromagnetic resonance (FMR) spectrometer and taught me how to handle and perform FMR measurement. He trained me to calibrate the vector network analyzer based FMR set up and data processing.

I am also grateful to Dr. Saswati Barman for her support in LLG micromagnetics simulator. She gave me valuable advice regarding research works. I am thankful to Dr. Jaivardhan Sinha for his guidance and useful suggestions. He helped me in sample characterization process.

I express sincere gratitude to Prof. Yoshichika Otani and his group (from Riken, Japan) for helping us to fabricate such high quality samples for the measurements. I would like to acknowledge Dr. Ruma Mandal for assistance in sample fabrication and Dr. Dheeraj Kumar for developing DotMag code and assistance in some numerical calculations.

I am also thankful to all my senior group members Dr. Semanti Pal, Dr. Susmita Saha, Dr. Arnab Ganguly, Dr. Chandrima Banerjee, Dr. Kallol Mukherjee, Dr. Debanjan Polley, Dr.

Sumona Sinha, Dr. Rakhi Acharyya, and Dr. Arpan Bhattacharyya for their help and support. I express heartiest thanks to my senior colleagues Dr. Sucheta Mondal, Dr. Samiran Choudhury, Dr. Santanu Pan, and Anulekha De for their help in experimental and simulation works and sharing their in-depth knowledge with me. I would like to thank my lab batchmate Avinash Kumar Chaurasiya for the fruitful discussions and sharing nice memories during various conferences. My special thanks to my junior colleagues Sourav Sahoo, Amrit Kumar Mondal, Sudip Majumdar, Koustuv Dutta, Suryanarayan Panda, Arundhati Adhikari, Pratap Kumar Pal, Sreya Pal, and Soma Dutta for their direct and indirect help in my research works. I have enjoyed the presence of Subham, Anuj, Daisy and Gaurav during their projects. I will always cherish the colourful memories that I have shared with my lab members of the Spintronics and Spin Dynamics group.

I would like to express my gratitude to all my friends in this campus. Specially, I had some nice memories with Avishek Maity, Alik Panja, chandan Samanta, and Rahul Bandyopadhyay. I am thankful to my seniors and juniors in this campus for many indoor-outdoor activities. I am also thankful to SNB mess and institute canteen.

I convey my deepest gratitude to my parents for their love, support and encouragement. They always trust me on my decisions. I am indebted forever to my father for all his sacrifices. I am also thankful to my wife Nabanita (Payel) for her support and motivation.

Finally, I thank the S. N. Bose National Centre for Basic Sciences for giving me the opportunity to work. I also thank the Jadavpur University for the registration of my PhD. I gratefully acknowledge University Grant Commission, India for providing me research fellowship. I also acknowledge various funding agencies including Department of Science and Technology, Government of India for their key role in the development of research facilities.

Kartik Adhikari

S. N. Bose National Centre for Basic Sciences,

Salt Lake, Kolkata, India

List of Abbreviations

(A)FM	: (Anti) Ferromagnetic
AFM	: Atomic force microscope
BBO	: Barium beta-borate
cm	: Centimeter
CW	: Continuous wave
CPW	: Coplanar waveguide
CVD	: Chemical vapour deposition
DC (dc)	: Direct current
DE	: Damon-Eshbach
DW	: Domain Wall
DMI	: Dzyaloshinskii-Moriya interaction
DUT	: Device under test
DOF	: Depth of field
DPSS	: Diode pumped solid state laser
EBL	: Electron beam lithography
EBE	: Electron beam evaporation
EM	: Electromagnetic
(FE)SEM	: (Field emission) scanning electron microscopy
EDXS	: Energy dispersive x-ray spectroscopy
EPD	: End point detection
EPMA	: Electron probe micro-analyzer
fs	: Femtosecond
FDM	: Finite difference method
FEM	: Finite element method
FMR	: Ferromagnetic resonance
FWHM	: Full width at half maximum
GMR	: Giant magnetoresistance
GSG	: Ground-signal-ground
GVD	: Group velocity dispersion
GHz	: Gigahertz
Hz	: Hertz

HWHM : Half width at half maximum
IPA : Iso-propyl alcohol
IR : Infrared
LLG : Landau-Lifshitz-Gilbert
LBO : Lithium triborate
LED : Light emitting diode
ms : Millisecond
mm : Millimeter
mW : Milliwatt
MFM : Magnetic force microscope
MTJ : Magnetic tunnel junction
MO : Microscope objective
MRAM : Magneto-resistive random-access memory
MFVM : Magnetostatic forward volume mode
MBVM : Magnetostatic backward volume mode
MSSW : Magnetostatic surface spin wave
MHz : Megahertz
ns : Nanosecond
nm : Nanometer
NA (N.A.) : Numerical aperture
OBD : Optical bridge detector
OOMMF : Object oriented micromagnetic framework
ps : Picosecond
(I)PMA : (Interfacial) perpendicular magnetic anisotropy
(P)BS : (Polarized) beam splitter
PCB : Printed circuit board
PSSW : Perpendicular standing spin wave
PVD : Physical vapour deposition
PWM : Plane wave method
Py : Permalloy
(P)MMA : (Poly) methyl methacrylate
Rpm : Revolution per minute

RF (rf) : Radio frequency

SOT : Spin-orbit torque

SHG : Second harmonic generator

SW : Spin wave

SOC : Spin-orbit coupling

SOI : Spin-orbit interaction

SSE : Spin Seebeck effect

SL : Stripline

SNA : Scalar network analyzer

TR-MOKE : Time resolved magneto-optical Kerr effect

TEM : Transmission electron microscopy

THz : Terahertz

TMR : Tunnelling magnetoresistance

UV : Ultraviolet

VSM : Vibrating sample magnetometry

VNA : Vector network analyzer

μs : Microsecond

μm : Micrometer or micron

Å : Angstrom

i.e. : That is

e.g. : For example

vs. : versus

List of Tables

List of Figures

Table of Contents

Chapter 1

1. Introduction

From the beginning of human civilization, mankind is constantly improving their quality of lifestyle through relentless scientific investigation and invention of improved technology. Currently, various electronic gadgets and digital communication systems play an important role in our day-to-day life. The present advancement of electronics technology and communication systems have been made possible by some extraordinary inventions such as transistors [1], optical fibres [2], internet [3] etc. In the last century, we have observed an immense improvement in electronics technology that deals with the efficient controlling of flow of electronic charges.

In addition to charge degree of freedom, an electron has a spin degree of freedom, which is nothing but the intrinsic angular momentum. Although spin was discovered in the early of twentieth century, significant amount of spin-dependent fascinating phenomena has been explored in the course of last few decades only. It has opened up plenty of new fields for the spin related research. Notably, the spin related research fields are growing very fast. Therefore, it has brought a radical change in materials science in terms of fundamental science and technological revolution.

So far, the semiconductor based electronics technology has always been fulfilling our growing demand with its continuous improvement in terms of data storage capacity, data processing capability and processing speed. However, scientists are concerned that the further development of semiconductor-based technology will soon be hampered in terms of power efficiency and data integration density because according to the report in the next few years, the semiconductor-based devices will touch their supreme limits [4] regarding miniaturization and operating speed. Another basic and unavoidable shortcoming of semiconductor-based devices is waste of energy in the form of heat due to motion of electron (charge) through the resistive medium. Therefore, the target is to innovate better alternative of charge-based technology, which can address all these shortcomings. Initially, this effort started with the invention of artificial crystals such as photonic and phononic crystals. Photonic crystals [5-9] are patterned dielectric

structures that are artificially designed to create frequency band for photons by making periodic modulation of refractive index and by tuning geometrical parameters. This artificially created frequency band allows or forbids specific frequency range of electromagnetic waves in the photonic crystals. Consequently, photonic crystals act to control the propagation of photons analogous to electrons in crystal lattices. This striking property makes them suitable for application in various nanometre scale optical devices, for instance, photonic waveguides [10-17] and integrated circuits [18-22]. In case of phononic crystals [23-25], the propagation of acoustic waves is controlled by making periodic modulation of elastic constants.

Meanwhile, a sharp rise of attention towards the study of magnetization switching and dynamics at nanoscale have been observed among the researchers worldwide. A plenty of novel and fascinating phenomena have been reported in magnetic materials of micro to nanometre length scale. Consequently, a new term spintronics [26] was introduced in the 1990s into the field of magnetism analogous to electronics. Spintronics or spin electronics research describes the significant role of electron-spin rather than its charge in solid state physics and other potential devices that utilize spin properties. The discovery of giant magnetoresistance (GMR) effect ignited an explosion of intensive investigation on thin film magnetism. In 1988, Albert Fert and Peter Grünberg independently discovered the GMR in magnetic (Fe/Cr) multilayered system and both were awarded the Nobel Prize in physics in 2007 for this ground breaking discovery. GMR is the significant change of electrical resistance due to the impact of externally applied magnetic field to a magnetic multilayer composed of two ferromagnetic (FM) layers separated by a thin layer of nonmagnetic metal [27-30]. The electrical resistance of such multilayer systems is determined by the relative orientation of magnetization of two FM layers. GMR effect has revolutionized the data storage industry [31]. Magnetism based diverse research areas are categorized into various sub-branches such as magnonics [32-36], spintronics [37-39], magnon-spintronics [40], magneto-photonics [41,42], topological magnonics [43,44], magneto-electronics [45,46], magneto-phononics [47-49] etc.

Magnonics is a sharply growing research field, which studies generation, propagation, and control or manipulation of magnons (quanta of spin wave) in periodically modulated magnetic systems. Felix Bloch [50-53] first predicted the existence of spin

waves (SWs) in magnetic medium in 1930. SW is the propagation of perturbation in magnetic medium in the form of phase of coherently precessing microscopic magnetization vectors. Interestingly, SW offers GHz range working frequency that makes it suitable candidate for data carrier in nanoscale on-chip communication systems. In addition, spin-based devices are generally more energy efficient than charge-based devices because there is no waste of heat energy due to the propagation of spin current alike joule heating energy loss during propagation of charge current. SWs manifest various fascinating properties and novel phenomena while propagate through patterned magnetic nanostructures. S. A. Nikitov et al. [54] coined the term "magnon crystal". Magnonic crystals (MCs) are one type of artificial crystal composed of periodically patterned magnetic media. The magnetization dynamics of these MCs can be efficiently controlled via broad range of internal parameters such as size, shape, lattice arrangement of the nanomagnets, and selection of the magnetic material and various external parameters such as strength and orientation of bias magnetic field and microwave power of the excitation signal. By playing with these parameters, different new types of MCs have been introduced such as artificial spin ice [55-61], skyrmions [62-65], and quasicrystals [66]. Interestingly, SWs display variety of dispersion relations depending upon the relative orientation of the wave vector and magnetization due to anisotropic nature of the dipolar interactions. Those dipolar interaction dominated SW modes in ferromagnetic thin film are classified as magnetostatic surface spin wave (MSSW) mode or Damon-Eshbach (DE) mode [67], magnetostatic backward volume mode (MBVM) [68,69] and magnetostatic forward volume mode (MFVM) [70]. In addition, SW can propagate along the perpendicular direction of the ferromagnetic thin film surface with different quantization numbers and forms perpendicular standing SW (PSSW) mode. A complete control over SW dynamics by manipulating the key properties of SWs such as group velocity [71], frequency dispersion [72], non-reciprocity [73], band structure [74], phase [75], amplitude [76] and anisotropy [77] is required for the development of spin-based energy efficient magnetic storage, logic, memory, and communication devices. Furthermore, magnon-based hybrid systems [78-82] have become promising systems for the application in quantum information processing.

In the subsequent sections, an outline of promising systems included in the magnonic crystals will be presented with the aim of to spark motivation for the thesis. At the end, the framework of this thesis will be briefly stated.

1.1. Magnonic Crystals (MCs)

The intention to explore the rich fundamental physics as well as control the static and dynamic magnetic properties of a system with periodically modulated magnetic parameters have started long back for the development of modern magnon based devices [83-86]. The efficient tunability of magnonic band structure and magnon frequency by varying structural patterning, external stimuli, and intrinsic magnetic anisotropy of the MCs [87,88] make them attractive. The current advancement of nanofabrication techniques and experimental systems facilitate to fabricate the new MCs and probe their complex spin dynamics. As a result, during the last two decades a rapidly growing interest has been observed in magnonics research. Various magnetic materials have been exploited to fulfil the different aspects of the field of magnonics. For example, yttrium iron garnet (YIG) [89] has been widely investigated for the study of SW propagation because it offers very low magnetic damping value and hence long propagation length. However, this insulating YIG shows low magnetic moment value and suffers difficulty during fabrication of high quality nanopatterning. On the other hand, other metallic ferromagnetic materials and their alloys such as Fe [90], Ni [91], and $Ni_{80}Fe_{20}$ (permalloy, soft ferromagnet with negligible magnetocrystalline anisotropy) [92] have manifested their efficacy for nanopatterning. Furthermore, Co and Co based alloys such as CoFe, CoFeB have been applied in magnetic tunnel junctions, and spin valves to acquire higher TMR or GMR values [93] because these magnetic materials offer comparatively higher magnetic moment value. Magnetic multilayer systems with high perpendicular magnetic anisotropy value are potential candidates for the fabrication of new MCs. Basically, modulation of the magnetic properties due to the perturbation by various external stimuli such as magnetic field [94], electric field [95], charge current [96], stress [97] etc. induce changes in coercive field, switching field, effective anisotropy [98], and collective magnetization dynamics in MCs.

The MCs can be categorized depending upon their structures and dimensions. Array of magnetic stripes or wires are categorized as 1D MCs while two-dimensional array of

magnetic dots [99,100], antidots [101,102] or rings [103] can be categorized as 2D MCs. Recently, researchers have paid attention on 3D MCs (array of magnetic spheres or three dimensional magnetic patterned structures) [104,105] due to their novel physical phenomena. Typically, experimental study of spin dynamics of 1D or 2D MCs have been performed with the assistance of ferromagnetic resonance (FMR) [106,107] technique, time-resolved magneto-optical Kerr effect (TR-MOKE) [108,109] microscopy, and Brillouin light scattering (BLS) [110,111] spectroscopy. Plenty of fascinating physical phenomena have been detected in MCs such as SW mode splitting, mode crossover, mode hopping, mode softening, mode hybridization etc. Recent studies on 3D MCs have proved their ability to control the SW propagation and have shown the possibility to apply in next generation data storage and memory devices.

1.1.1. One-Dimensional (1D) Magnonic Crystals

Extensive research has been performed on one-dimensional magnonic crystals to test their ability to control the propagation of SWs. They offer various unique properties such as confinement of SWs, filtering and guiding of SWs, and phase shifting (slowing) of SWs. Array of 1D nanomagnets (i.e. nanowires or nanostripes) exhibit magnonic band structure where the artificial periodicity of ordered nanomagnets determine the corresponding Brillouin Zone boundaries. On the other hand, uniformly magnetized 1D nanowires can behave as a waveguide for SW by controlling the propagation of SW beams. The effect of dipolar coupling by varying the separation between 1D nanomagnets and exchange interaction by changing the magnetic materials (such as Co, Ni, NiFe etc.) on the SW dynamics has been widely studied [112-114]. Furthermore, many experimental and theoretical reports have clearly demonstrated [115,116] the magnonic band structure and propagation of SW in 1D nanostructures.

1.1.2. Two-Dimensional (2D) Magnonic Crystals

Two-dimensional MCs can be classified into various groups depending on the shape of the elements and the distinct physical properties. Some of them are briefly described in the following.

1.1.2.1. Ferromagnetic Dot Array

The arrangement of periodically placed array of micro or nanoscale ferromagnetic elements on top of a substrate is known as ferromagnetic dot array. The wavelength and nature of SWs can be manipulated by playing with the exchange and dipolar interactions in ferromagnetic dot array. Various novel and tunable magnetization properties present in these systems are highly significant for the construction of next generation communication, logic and storage devices.

Interestingly, a significant divergent of the static and dynamic magnetization properties are observed in dot structure due to spatial confinements unlike their bulk counterparts. In case of ferromagnetic dot array, the inter-dot dipolar interactions, various intrinsic and extrinsic anisotropies, shape and lattice arrangement of the magnetic element [117-120] play a pivotal role to determine the domain formation and magnetization dynamics. In addition, the spin dynamics of these systems can be efficiently manipulated by external bias magnetic field strength and orientation as well as microwave power of the input signal. The periodic modulation of the magnetic parameters in the array and the complex magnetic configuration inside dot structure induce multiple SW modes with distinct properties. Hence, profound understanding and control of spin dynamics in ferromagnetic dot array of new shape and lattice arrangement are required for the development of future magnonic devices.

1.1.2.2. Ferromagnetic Antidot Array

Ferromagnetic antidot array, which comprises of periodically created holes in a continuous ferromagnetic thin film. These ordered nonmagnetic holes promote novel domain configurations, which strongly affect spin dynamics of the system. Various static and dynamic magnetic properties such as coercive field, effective anisotropy, and the magnetization reversal can be modulated in antidot systems with the variation of antidot shape, size as well as the geometry and order parameter of array. Such variations in the antidot systems strongly affect their magnonic band structure and anisotropic nature of the spin waves. Hence, ferromagnetic antidot system offers tunable magnetic properties, which make them suitable candidate for the construction of high-density storage media, magnetic sensors, and microwave devices. SW can propagate longer distance with higher speed in ferromagnetic antidot system due to the

strong dipole-exchange coupling in comparison with ferromagnetic dot system with only dipolar coupling. These systems are potential candidates for the investigation of coupling between photon and plasmon as magneto-photonic crystals. Therefore, a significant amount of research has been carried out to investigate the static and dynamic magnetization properties in 1D and 2D ferromagnetic antidot arrays with the assistance of various experimental and theoretical techniques [121,122]. Interestingly, splitting of SW modes in antidot systems due to nonmagnetic holes induced modulation of demagnetizing field and interlayer coupling have been reported. In addition, external bias magnetic field strength and orientation-controlled SW filter can be made using antidot systems.

1.1.2.3. Ferromagnetic Nanorings

Nanorings can be considered as the amalgamation of both dot and antidot structures. The desired antidot shape is fabricated inside each component of the dot array. Previous studies show that circular and square shaped ferromagnetic nanoring structures can be used for the construction of memory devices because it has two specific magnetic states: onion state and vortex state. So far, substantial research has been performed on magnetic ring structures to explore the static and dynamic magnetization properties in micrometre to nanometre length scale [123-125]. The inhomogeneous internal field inside magnetic nanoring plays crucial role for the SW confinements and both radial and azimuthal modes with varying mode quantization numbers are observed.

1.1.2.4. Three Dimensional (3D) Magnetic Nanostructures

The scientific investigation on 3D magnetic nanostructures is an emerging field of research. These systems show various novel physical phenomena evolving from the complex magnetic configurations, frustration, and topology [126-128] in 3D systems that are important both fundamental and technological points of view. However, the major challenging tasks for the researchers to explore this field are fabrication and characterization of the desired 3D samples and subsequently probing the high-frequency dynamics.

The investigation of SW properties in various potential 3D magnetic nanostructures has opened a new door toward the construction of plenty of spin-based devices for instance ultra-dense data storage devices [126,129], logic [130,131], interferometers [132], conduit [133], neuromorphic computing [134,135], actuators [136], sensors [137], reconfigurable magnonics [138], and spintronic devices [139]. Interestingly, the interaction between neighbouring elements in 2D artificial spin ice systems can be balanced by incorporating frustration into the added third dimension. In addition, such structures have the potential for the development of 3D racetrack memory and other promising systems that could bring revolution in the future computing technology.

1.2. Objectives of the Thesis

The central focus of this thesis is to explore the static and dynamic magnetization in ferromagnetic nanostructures with the assistance of broadband ferromagnetic resonance, time-resolved magneto-optical Kerr effect microscopy and micromagnetic simulations. The principal objectives are to investigate the tunability of the magnetization dynamics and SW properties in ferromagnetic patterned nanostructures with the variation of external bias magnetic field strength and orientation and microwave power of the input excitation signal. A brief description of the investigated systems are as follows:

(A) Magnonic crystals made of array of Py nanocross structure: The effect of bias field strength and orientation and microwave power of the input excitation signal on the static magnetic configuration, magnetization dynamics and SW properties in presence of nonuniform demagnetizing field and anisotropic dipolar interactions have been investigated by using ferromagnetic resonance technique. The tunability of the various fascinating phenomena and their applicability for the construction of new potential magnonic devices are demonstrated.

(B) Magnonic crystals made of array of Py cross-shaped nanorings (CNRs): The influence of modulated demagnetizing field and dynamic dipolar coupling on magnetization dynamics, magnon-magnon coupling and nature of the spin waves is investigated.

References

[1] J. Bardeen, W. H. Brattain, Phys. Rev. **74**, 230 (1948).

[2] F. Van Laere, G. Roelkens, M. Ayre, J. Schrauwen, D. Taillaert, D. Van Thourhout, T. F. Krauss, R. Baets, J. Light. Technol. **25**, 151 (2007).

[3] B. M. Leiner, V. G. Cerf, D. D. Clark, R. E. Kahn, L. Kleinrock, D. C. Lynch, J. Postel, L. G. Roberts, S. Wolff, SIGCOMM Comput. Commun. Rev. **39**, 22 (2009).

[4] Semiconductor Industry and Association, "International Technology Roadmap for Semiconductors" http://www.itrs.ne/Links/2011ITRS/2011Chapters/2011ERD.pdf, (2011).

[5] S. S. Oh, C. S. Kee, J.-E. Kim, *et al.*, Appl. Phys. Lett. **76**, 2301 (2000).

[6] A. D'Orazio, M. D. Sario, V. Petruzzelli, *et al.*, Opt. Express **11**, 230 (2003).

[7] M. Loncar, T. Doll, J. Vuckovic, *et al.*, J. Lightwave Technol. **18**, 10 (2000).

[8] M. Loncar, T. Doll, J. Vuckovic, *et al.*, J. Lightwave Technol. **18**, 1402 (2000).

[9] E. Yablonovitch, J. Mod. Opt. **41**, 173 (1994).

[10] J. Li, K. S. Chiang, J. Opt. Soc. Am. B **24**, 1942 (2007).

[11] A. Yu. Petrov, M. Eich, IEEE J. Sel. Areas Commun. **23**, 1396 (2005).

[12] J. Li, T. P. White, L. O'Faolin, A. Gomez-Iglesias, T. F. Krauss, Opt. Express **16**, 6227 (2008).

[13] J. C. Knight, Nature **424**, 847 (2003).

[14] J. Li, K. S. Chiang, Opt. Commun. **281**, 5797 (2008).

[15] N. T. Otterstrom, R. O. Behunin, E. A. Kittlaus, Z. Wang, P. T. Rakich, Science **360**, 1113 (2018).

[16] A. Khelif, B. Djafari-Rouhani, J. O. Vasseur, P. A. Deymier, Phys. Rev. B **68**, 024302 (2003).

[17] M. Kurosu, D. Hatanaka, K. Onomitsu, H. Yamaguchi, Nat. Commun. **9**, 1331 (2018).

[18] S. J. McNab, N. Moll, Y. A. Vlasov, Opt. Express **11**, 2927 (2003).

[19] F. V. Laere, T. Stomeo, C. Cambournac, *et al.*, J. Lightwave Technol. **27**, 417 (2009).

[20] F. V. Laere, G. Roelkens, M. Ayre, *et al.*, J. Lightwave Technol. **25**, 151 (2007).

[21] Y.-F. Wang, T.-T. Wang, Y.-S. Wang, V. Laude, Phys. Rev. Appl. **8**, 014006 (2017).

[22] S.-Y. Yu, C. He, Z. Wang, *et al.*, Nat. Commun. **9**, 3072 (2018).

[23] M.-H. Lu, L. Feng, Y.-F. Chen, Mater. Today **12**, 34 (2009).

[24] M. S. Kushwaha, P. Halevi, L. Dobrzynski, B. D. Rouhani, Phys. Rev. Lett. **71**, 2022 (1993).

[25] M. Jacoby, Chem. Eng. News **76**, 38 (1998).

[26] S. A. Wolf, D. D. Awschalom, R. A. Buhrman, *et al.*, Science **294**, 1488 (2001).

[27] P. Grünberg, R. Schreiber, Y. Pang, M. B. Brodsky, H. Sowers, Phys. Rev. Lett. **57**, 2442 (1986).

[28] M. N. Baibich, J. M. Broto, A. Fert, *et al.*, Phys. Rev. Lett. **61**, 2472 (1988).

[29] G. Binasch, P. Griinberg, F. Saurenbach, *et al.*, Phys. Rev. B **39**, 4828 (1989).

[30] S. S. P. Parkin, Z. G. Li, D. J. Smith, Appl. Phys. Lett. **58**, 2710 (1991).

[31] S. Tehrani, E. Chen, M. Durlam, *et al.*, J. Appl. Phys. **85**, 5822 (1999).

[32] V. V. Kruglyak, R. J. Hicken, J. Magn. Magn. Mater. **306**, 191 (2006).

[33] S. Neusser, D. Grundler, Adv. Mater. **21**, 2927 (2009).

[34] V. V. Kruglyak, S. O. Demokritov, D. Grundler, J. Phys. D: Appl. Phys. **43**, 264001 (2010).

[35] B. Lenk, H. Ulrichs, F. Garbs, M. Münzenberg, Phys. Rep. **507**, 107 (2011).

[36] A. A. Serga, A. V. Chumak, B. Hillebrands, J. Phys. D: Appl. Phys. **43**, 264002 (2010).

[37] S. A. Wolf, D. D. Awschalom, R. A. Buhrman, *et al.*, **294**, 1488 (2001).

[38] A. Fert, Rev. Mod. Phys. **80**, 1517 (2008).

[39] G. Beach, Nat. Mater. **9**, 959 (2010).

[40] A. V. Chumak, V. I. Vasyuchka, A. A. Serga, B. Hillebrands, Nat. Phys. **11**, 453 (2015).

[41] J. Wang, C. Zhang, H. Liu, *et al.*, Nat. Commun. **10**, 129 (2019).

[42] G. Ctistis, E. Papaioannou, P. Patoka, et al., Nano Lett. **9**, 1 (2009).

[43] X. S. Wang, H. W. Zhang, X. R. Wang, Phys. Rev. Appl. **9**, 024029 (2018).

[44] X. S. Wang, X. R. Wang, J. Phys. D: Appl. Phys. **51**, 194001 (2018).

[45] G. A. Prinz, Science **282**, 1660 (1998).

[46] C. Chappert, A. Fert, F. N. Van Dau, Nat. Mater. **6**, 813 (2007).

[47] V. L. Zhang, F. S. Ma, H. H. Pan, *et al.*, Appl. Phys. Lett. **100**, 163118 (2012).

[48] H. H. Pan, V. L. Zhang, K. Di, *et al.*, Nanoscale Res. Lett. **8**, 115 (2013).

[49] P. Graczyk, M. Krawczyk, Phys. Rev. B **96**, 024407 (2017).

[50] F. Bloch, Z. Phys. **61**, 206 (1930).

[51] T. Holstein, H. Primakoff, Phys. Rev. **58**, 1098 (1940).

[52] C. Herring, C. Kittel, Phys. Rev. **81**, 869 (1951).

[53] F. J. Dyson, Phys. Rev. **102**, 1217 (1956).

[54] S. A. Nikitov, P. Tailhadesa, C. S. Tsai, J. Magn. Magn. Mater. **236**, 320 (2001).

[55] Y. Qi, T. Brintlinger, J. Cumings, Phys. Rev. B **77**, 094418 (2008).

[56] W. R. Branford, S. Ladak, D. E. Read, K. Zeissler, L. F. Cohen, Science **335**, 1597 (2012).

[57] A. P. Ramirez, A. Hayashi, R. J. Cava, R. Siddharthan, B. S. Shastry, Nature **399**, 333 (1999).

[58] Y.-L. Wang, Z.-L. Xiao, A. Snezhko, *et al.*, Science **352**, 962 (2016).

[59] R. F. Wang, C. Nisoli, R. S. Freitas, *et al.*, Nature **439**, 303 (2006).

[60] C. Castelnovo, R. Moessner, S. L. Sondhi, Nature **451**, 42 (2008).

[61] Z. Budrikis, P. Politi, R. L. Stamps, New J. Phys. **14**, 045008 (2012).

[62] L. Sun, R. X. Cao, B. F. Miao, *et al.*, Phys. Rev. Lett. **110**, 167201 (2013).

[63] F. S. Ma, Y. Zhou, H. B. Braun, W. S. Lew, Nano Lett. **15**, 4029 (2015).

[64] A. Fert, N. Reyren, V. Cros, Nat. Rev. Mater. **2**, 17031 (2017).

[65] Y. Fujishiro, N. Kanazawa, T. Nakajima, *et al.*, Nat. Commun. **10**, 1059 (2019).

[66] D. Levine, P. J. Steinhardt, Phys. Rev. Lett. **53**, 26 (1984).

[67] R. W. Damon, J. R. Eshbach, J. Phys. Chem. Solids **19**, 308 (1961).

[68] A. N. Slavin, S. O. Demokritov, B. Hillebrands, *Spin Dynamics in Confined Magnetic Structures I*, edited by B. Hillebrands and K. Ounadjela (Springer Berlin Heidelberg, Berlin, Heidelberg, 2002), p. 35.

[69] M. Chen, M. A. Tsankov, J. M. Nash, C. E. Patton, Phys. Rev. B **49**, 12773 (1994).

[70] R. Carter, C. Smith, J. Owens, IEEE Trans. Magn. **16**, 1159 (1980).

[71] T. Schwarze, D. Grundler, Appl. Phys. Lett. **102**, 222412 (2013).

[72] V. L. Zhang, H. S. Lim, C. S. Lin, et al., Appl. Phys. Lett. **99**, 143118 (2011).

[73] M. Mruczkiewicz, M. Krawczyk, G. Gubbiotti, S. Tacchi, A. F. Yu, D. V. Kalyabin, *et al.*, New J. Phys. **15**, 113023 (2013).

[74] J. O. Vasseur, L. Dobrzynski, B. Djafari-Rouhani, H. Puszkarski, Phys. Rev. B **54**, 1043 (1996).

[75] V. E. Demidov, S. Urazhdin, S. O. Demokritov, Appl. Phys. Lett. **95**, 262509 (2009).

[76] P. S. Keatley, P. Gangmei, M. Dvornik, *et al.*, Appl. Phys. Lett. **98**, 082506 (2011).

[77] B. Rana, D. Kumar, S. Barman, *et al.*, J. Appl. Phys. **111**, 07D503 (2012).

[78] D. Zhang, X.-Q. Luo, Y.-P. Wang, *et al.*, Nat. Commun. **8**, 1368 (2017).

[79] Y. Li, T. Polakovic, Y.-L. Wang, J. Xu, S. Lendinez, *et al.*, Phys. Rev. Lett. **123**, 107701 (2019).

[80] N. Zhu, X. Han, C.-L Zou, *et al.*, Phys. Rev. A **101**, 043842 (2020).

[81] L. V. Abdurakhimov, S. Khan, N. A. Panjwani, J. D. Breeze, M. Mochizuki, *et al.*, Phys. Rev. B **99**, 140401(R) (2019).

[82] J. Bourhill, N. Kostylev, M. Goryachev, *et al.*, Phys. Rev. B **93**, 144420 (2016).

[83] C. G. Sykes, J. D. Adam, J. H. Collins, Appl. Phys. Lett. **29**, 388 (1976).

[84] J. P. Parekh, H. S. Tuan, Appl. Phys. Lett. **30**, 667 (1977).

[85] J. O. Vasseur, L. Dobrzynski, B. Djafari-Rouhani, H. Puszkarski, Phys. Rev. B **54**, 1043 (1996).

[86] Yu. V. Gulyaev, A. A. Nikitov, Dokl. Phys. **46**, 687 (2001).

[87] A. V. Chumak, A. A. Serga, B. Hillebrands, J. Phys. D: Appl. Phys. **50**, 244001 (2017).

[88] J. Rychly, P. Gruszecki, M. Mruczkiewicz, *et al.*, Low Temp. Phys. **41**, 745 (2015).

[89] A. A. Serga, A. V. Chumak, B. Hillebrands, J. Phys. D: Appl. Phys. **43**, 264002 (2010).

[90] E. T. Papaioannou, V. Kapaklis, P. Patoka, *et al.*, Phys. Rev. B **81**, 054424 (2010).

[91] M. Rollinger, P. Thielen, E. Melander, *et al.*, Nano Lett. **16**, 2432 (2016).

[92] B. Rana, D. Kumar, S. Barman, *et al.*, ACS Nano **5**, 9559 (2011).

[93] H. Ulrichs, B. Lenk, M. Münzenberg, Appl. Phys. Lett. **97**, 092506 (2010).

[94] L. Bai, M. Kohda, J. Nitta, Appl. Phys. Lett. **98**, 172508 (2011).

[95] Q. Wang, A. V. Chumak, L. Jin, *et al.*, Phys. Rev. B **95**, 134433 (2017).

[96] A. V. Chumak, T. Neumann, A. A. Serga, B. Hillebrands, *et al.*, J. Phys. D: Appl. Phys. **42**, 205005 (2009).

[97] K. Roy, S. Bandyopadhyay, J. Atulasimha, Phys. Rev. B **83**, 224412 (2011).

[98] N. I. Polushkin, S. A. Michalski, L. Yue, *et al.*, Phys. Rev. Lett. **97**, 256401 (2006).

[99] S. Jung, B. Watkins, L. DeLong, *et al.*, Phys. Rev. B **66**, 132401 (2002).

[100] K. Adhikari, S. Choudhury, R. Mandal, et al., J. Appl. Phys. **121**, 043909 (2017).

[101] S. Neusser, B. Botters, D. Grundler, Phys. Rev. B **78**, 054406 (2008).

[102] S. Neusser, B. Botters, M. Becherer, *et al.*, Appl. Phys. Lett. **93**, 122501 (2008).

[103] C. Banerjee, S. Saha, S. Barman, *et al.*, J. Appl. Phys. **116**, 163912 (2014).

[104] M. Hänze, C. F. Adolff, B. Schulte, *et al.*, Sci. Rep. **6**, 22402 (2016).

[105] S. Mamica, J. Appl. Phys. **114**, 043912 (2013).

[106] K. Adhikari, S. Barman, R. Mandal, *et al.*, Phys. Rev. Appl. **10**, 044010 (2018).

[107] K. Adhikari, S. Sahoo, A. K. Mondal, *et al.*, Phys. Rev. B **101**, 054406 (2020).

[108] B. Rana, D. Kumar, S. Barman, *et al.*, ACS Nano **5**, 9559 (2011).

[109] B. K. Mahato, B. Rana, R. Mandal, *et al.*, Appl. Phys. Lett. **102**, 192402 (2013).

[110] A. De, S. Mondal, C. Banerjee, *et al.*, J. Phys. D: Appl. Phys. **50**, 385002 (2017).

[111] A. K. Mondal, C. Banerjee, A. Adhikari, *et al.*, Physical Review B **101**, 224426 (2020).

[112] G. Gubbiotti, S. Tacchi, G. Carlotti, *et al.*, Phys. Rev. B **72**, 224413 (2005).

[113] S. Goolaup, A. O. Adeyeye, N. Singh, *et al.*, Phys. Rev. B **75**, 144430 (2007).

[114] S. Tacchi, M. Madami, G. Gubbiotti, *et al.*, Phys. Rev. B **82**, 184408 (2010).

[115] V. E. Demidov, J. Jersch, K. Rott, *et al.*, Phys. Rev. Lett. **102**, 177207 (2009).

[116] A. V. Chumak, P. Pirro, A. A. Serga, *et al.*, Appl. Phys. Lett. **95**, 262508 (2009).

[117] S. Jung, B. Watkins, L. DeLong, J. B. Ketterson, *et al.*, Phys. Rev. B **66**, 132401 (2002).

[118] G. N. Kakazei, P. E. Wigen, K. Y. Guslienko, *et al.*, Appl. Phys. Lett. **85**, 443 (2004).

[119] S. M. Weekes, F. Y. Orgin, P. S. Keatley, *et al.*, J. Appl. Phys. **99**, 08B102 (2006).

[120] V. V. Kruglyak, A. Barman, R. J. Hicken, *et al.*, J. Appl. Phys. **97**, 10A706 (2005).

[121] C. T. Yu, H. Jiang, L. Shen, P. J. Flanders, *et al.*, J. Appl. Phys. **87**, 6322 (2000).

[122] S. McPhail, C. M. Gürtler, J. M. Shilton, *et al.*, Phys. Rev. B **72**, 094414 (2005).

[123] V. Metlushko, et al., *In Proceedings of the 2nd IEEE Conference on Nanotechnology* 2002, pp. 63.

[124] L. Tripp S., E. Dunin-B. R., A. Wei, Angew. Chem. **42**, 5591 (2003).

[125] P. Vavassori, M. Grimsditch, V. Novosad, *et al.*, J. Appl. Phys. **93**, 7900 (2003).

[126] S. S. P. Parkin, M. Hayashi, L. Thomas, Science **320**, 190 (2008).

[127] H. Forster, T. Schrefl, D. Suess, *et al.*, J. Appl. Phys. **91**, 6914 (2002).

[128] M. Yan, C. Andreas, A. Kákay, *et al.*, Appl. Phys. Lett. **99**, 122505 (2011).

[129] C. Bran, E. Berganza, J. A. Fernandez-Roldan, *et al*., ACS Nano **12**, 5932 (2018).

[130] I. Eichwald, S. Breitkreutz, G. Ziemys, *et al*., Nanotechnology **25**, 335202 (2014).

[131] M. Gavagnin, H. D. Wanzenboeck, S. Wachter, *et al*., ACS Appl. Mater. Interfaces **6**, 20254 (2014).

[132] M. Balynsky, D. Gutierrez, H. Chiang, *et al*., Sci. Rep. **7**, 11539 (2017).

[133] D. Sanz-Hernandez, R. F. Hamans, J-W Liao, *et al*., ACS Nano **11**, 11066 (2017).

[134] J. Torrejon, M. Riou, F. A. Araujo, *et al*., Nature **428**, 547 (2017).

[135] E. C. Burks, D. A. Gilbert, P. D. Murray, et al., Nano Lett. **1**, 716 (2021).

[136] P. Vavassori, M. Pancaldi, M. J. Perez-Roldan, *et al*., Small **12**, 1013 (2016).

[137] C. Xu, X. Wu, G. Huang, Y. Mei, Adv. Mater. Technol. **4**, 1800486 (2019).

[138] M. Krawczyk, D. Grundler, J. Phys.: Condens. Matter **26**, 123202 (2014).

[139] A. Fernandez-Pacheco, R. Streubel, O. Fruchart, *et al*., Nat. Commun. **8**, 15756 (2017).

Chapter 2

2. Theoretical Background

2.1. Introduction

The origin of intrinsic magnetic properties of a substance lies in its molecular structuring and electronic configuration. The magnetic response (microscopic and macroscopic) of a substance depends on the number of unpaired electrons and the interaction between spin and orbital momenta. Depending on the magnetic response, all materials can be classified as ferromagnet [1-5], paramagnet [6], diamagnet [7-10], ferrimagnet [11,12], and antiferromagnet [13,14]. Among them, the ferromagnet and ferrimagnet show spontaneous magnetization [15]. This thesis will stress on the magnetic properties of ferromagnetic (FM) systems. In 1926, Werner Heisenberg and Paul Dirac introduced the concept of exchange interaction in magnetic system. This short-range exchange interaction is responsible for the alignment of spins in a magnetic system. The interplay between different internal energy terms leads the formation of domain structure in a ferromagnet in order to achieve the minimum free energy of the system.

Initially, few simpler models on spin system were macroscopically depicted to explain the various magnetic phenomena, e.g. domain formation, magnetic reversal etc. However, the current scenario becomes different with the introduction of nanomagnetism. For instance, the confined nanomagnetic systems show many new and interesting phenomena. Some properties in confined nanostructures differ substantially from their bulk counterparts.

Below, we will discuss about different energies hold by a magnetic system and the brief concept of magnetization dynamics followed by the generation of SW and its classification. Subsequently, different probing techniques of magnetization dynamics will be discussed.

2.2. Magnetic Energies

Both the static and dynamic properties of a magnetic system depend on the relative contribution of various energy terms such as Zeeman energy, exchange energy, magnetic anisotropy energy and magnetostatic energy or demagnetizing energy [3,4,16-18]. In equilibrium condition, every magnetic system tries to stay always at the state of minimum of total free energy following the interplay between these different energy terms.

2.2.1. Zeeman Energy

Zeeman energy [19,20] explains the interaction energy between the magnetization ($\boldsymbol{M}$) and the external static magnetic field ($\boldsymbol{H}$). For example, in a magnetic system having volume V, the expression for the Zeeman energy is given by:

$$E_z = -\mu_0 \int_V \boldsymbol{M}.\boldsymbol{H}\, dV \tag{2.1}$$

Where, dV is the volume element and the above equation suggests $\boldsymbol{M}$ tends to align along the $\boldsymbol{H}$ to achieve minimum Zeeman energy in presence of $\boldsymbol{H}$.

2.2.2. Exchange Energy

Exchange interaction [21,22] is a quantum-mechanical phenomenon, where individual magnetic moment attempts to align all nearby magnetic moments within the spin system itself. When the intrinsic magnetic moments align themselves in a parallel fashion, the material is called ferromagnet. On the other hand, if they align in antiparallel fashion the material is called antiferromagnet. If we consider only nearest neighbor interaction, the expression for the Heisenberg Hamiltonian for exchange energy can be expressed as:

$$H_{ex} = -2 \sum_{i \neq j} J_{ij}\, \boldsymbol{S}_i.\boldsymbol{S}_j \tag{2.2}$$

Here $\boldsymbol{S}$ is the spin operator and J_{ij} is the exchange integral. In continuum model, the exchange energy can be expressed as:

$$E_{ex} = A \int_V (\nabla m)^2 \, dV \tag{2.3}$$

Here m is the magnetic moment and A is called exchange stiffness constant defined as:

$$A_{ex} = \frac{2JS^2}{a} \tag{2.4}$$

Here a is the lattice constant and J is the isotropic exchange integral. Notably, the above-mentioned exchange interaction is completely direct interaction where two nearest neighbor electrons of magnetic atoms interact directly. Apart from this direct exchange, there are few indirect exchange interactions also. For example, (1) super-exchange where exchange is intermediated via various non-magnetic ions [23], (2) Ruderman-Kittel-Kasuya-Yosida (RKKY) interaction [24,25], where metallic ions are coupled via of itinerant electrons, (3) anisotropic exchange interaction, (well-known as Dzyaloshinskii-Moriya interaction: DMI) [26], where spin-orbit interaction acts crucial role.

2.2.3. Magnetic Dipolar Interaction

It refers to the direct interaction between two magnetic dipoles and this is also known as dipolar coupling. The corresponding energy can be expressed as:

$$E_{\mathrm{d}} = \frac{\mu_0}{4\pi r^3}\left[\boldsymbol{m_1}.\boldsymbol{m_2} - \frac{3}{r^2}(\boldsymbol{m_1}.\boldsymbol{r})(\boldsymbol{m_2}.\boldsymbol{r})\right] \tag{2.5}$$

Here μ_0 is the free space permeability, $\boldsymbol{m_1}$ and $\boldsymbol{m_2}$ are the magnetic moment of the corresponding dipoles and $\boldsymbol{r}$ is the vector joining of these two dipoles. Magnetic dipolar energy [27] plays a key role in various important phenomena such as domain formation, demagnetizing field profile and the stabilization of various nonuniform spin textures, including chiral spin textures.

2.3. Magnetic Anisotropy

It is the property of a magnetic system that confers some preferential directions along which the magnetization tends to align itself. These preferential directions are called easy axes and this property of a magnetic system is known as magnetic anisotropy [28,29]. The spin-orbit interaction and magnetic dipolar interaction are two primary sources of magnetic anisotropy. The various anisotropy contributions are discussed briefly in the following.

2.3.1. Magneto-crystalline Anisotropy

This is an intrinsic property of a magnetic material and solely originates from the spin-orbit interaction (SOI). The crystallographic structure decides the spatial arrangement of electrons in the orbitals in a crystalline material. The SOI plays a key role in determining certain crystallographic directions along which the material manifest magneto-crystalline anisotropy [30,31]. In a cubic structure, the magneto-crystalline anisotropy energy can be expressed as:

$$E_{Crystal} = K_0 + K_1(\alpha_1^2\alpha_2^2 + \alpha_2^2\alpha_3^2 + \alpha_3^2\alpha_1^2) + K_1\alpha_1^2\alpha_2^2\alpha_3^2 + \cdots \quad (2.6)$$

Here α_1, α_2 and α_3 are the three direction cosines of magnetization in Cartesian coordinate system. In addition, K_0 and K_1 are magneto-crystalline anisotropy constants in increasing order, respectively. The energy density of a crystal having uniaxial anisotropy is given by:

$$E_{Crystal} = K_U\alpha_x^2 \quad (2.7)$$

Here K_U is the uniaxial anisotropy constant.

2.3.2. Shape Anisotropy

The anisotropic shape of the confined magnetic element can generate some preferential directions for the alignment of magnetization. It appears entirely from the dipolar interaction between uncompensated magnetic moments at the boundaries of the magnetic element. The shape anisotropy becomes more prominent when size of the magnetic element goes down to micro- or nanoscale. The uncompensated magnetic moments at the boundaries usher stray field distribution outside the element and demagnetizing field inside it. The demagnetizing field energy [32-35] is given by:

$$E_{demag} = -\frac{1}{2}\int_0^V \mu_0 \boldsymbol{M}.\boldsymbol{H}_{demag}\, dV \quad (2.8)$$

For a homogenously magnetized ellipsoid the demagnetizing field ($\boldsymbol{H}_{demag}$) is given by:

$$\boldsymbol{H}_{demag} = -N\boldsymbol{M} \quad (2.9)$$

Here N is the demagnetizing tensor. The value of N strongly depends on the shape and geometry of the corresponding magnetic element.

2.3.3. Configurational Anisotropy

The configurational anisotropy arises due to shape of the magnetic element as well as their spatial arrangement. The competition between magnetostatic energy and exchange energy becomes crucial when the dimensions of the magnetic element goes down to micro- or nanoscale. For instance, in case of a non-ellipsoidal magnetic element the uniform magnetization state transforms to non-uniform magnetization state due to this configurational anisotropy [36,37].

2.3.3.1. Intrinsic Configurational Anisotropy

The intrinsic configurational anisotropy [38] depends on shape and size of the single magnetic element as well as on inter-element separation. This anisotropy creates different types of non-uniform magnetization states e.g., S-state, C-state, leaf state or flower state.

2.3.3.2. Extrinsic Configurational Anisotropy

The magnetostatic stray field distribution impacts on the formation of spin texture inside the magnetic element. This field distribution varies drastically depending on the strength and orientation of the external bias magnetic field. In addition, the stray field distribution substantially influences on the configurational magnetic anisotropy [39] via inter-element interaction depending upon the geometrical arrangement of the magnetic element.

2.3.4. Perpendicular Magnetic Anisotropy

Sometime the direction of the equilibrium magnetization becomes perpendicular to the sample plane. This effect is called perpendicular magnetic anisotropy (PMA) [40]. The PMA is observed typically in ultrathin magnetic films and multilayers magnetic system. The major reasons for the origin of PMA include reduced coordination symmetry, localized epitaxial strain at the interface, altered electronic structure and spin-orbit interactions. The PMA enhances thermal stability of the magnetization, which is useful for the application in next generation magnetic storage, magnetoresistive random access memory (MRAM) and logic devices.

2.4. Magnetization Dynamics

When a magnetic material is placed in presence of a bias magnetic field the magnetic moments inside the material experience a torque. Therefore, all the magnetic moments start precessing about the bias magnetic field direction due to this torque. On the other hand, all the magnetic moments try to align themselves along the magnetic field direction to minimize the Zeeman energy [41,42] of the system. Consequently, they follow a damped spiral motion about the magnetic field direction. This phenomenon is known as precessional magnetization dynamics [43,44]. The trajectory of the dynamic magnetization is illustrated by Landau-Lifshitz-Gilbert (LLG) equation of motion.

The torque ($\boldsymbol{\tau}$) experiences by a magnetic moment ($\boldsymbol{m}$) in presence of an effective magnetic field ($\boldsymbol{H}_{eff}$) given by:

$$\boldsymbol{\tau} = \boldsymbol{m} \times \boldsymbol{H}_{eff} \tag{2.10}$$

The magnetic moment ($\boldsymbol{m}$) and the angular momentum ($\boldsymbol{l}$) of an electron can be related in semiclassical approach as follows:

$$\boldsymbol{m} = -\gamma \boldsymbol{l} \tag{2.11}$$

Here γ is the gyromagnetic ratio. We know that the first order time derivative of angular momentum is torque. Therefore, the Eqn. (2.10) can be written as:

$$\frac{d\boldsymbol{l}}{dt} = \boldsymbol{m} \times \boldsymbol{H}_{eff} \tag{2.12}$$

Using Eqn. (2.11) the above equation can be rewritten as:

$$\frac{d\boldsymbol{m}}{dt} = -\gamma \boldsymbol{m} \times \boldsymbol{H}_{eff} \tag{2.13}$$

In case of continuum limit, the individual atomic magnetic moment ($\boldsymbol{m}$) can be replaced by the macroscopic magnetization ($\boldsymbol{M}$) to consider the whole system, which produces Landau-Lifshitz (LL) equation of motion:

$$\frac{d\boldsymbol{M}}{dt} = -\gamma \boldsymbol{M} \times \boldsymbol{H}_{eff} \tag{2.14}$$

Since there is no dissipative term in the above equation, the precessional motion of the magnetization continues for infinitely long time and which is impractical. To fix this issue, a relaxation or damping term ($\boldsymbol{D}$) must be incorporated with the LL equation. Therefore,

$$\frac{d\boldsymbol{M}}{dt} = -\gamma \boldsymbol{M} \times \boldsymbol{H}_{eff} + \boldsymbol{D}\,(\boldsymbol{M}, \boldsymbol{H}_{eff}) \tag{2.15}$$

Landau-Lifshitz suggested damping term was $-\frac{\lambda}{M_s^2}\boldsymbol{M} \times (\boldsymbol{M} \times \boldsymbol{H}_{eff})$. Finally, Gilbert introduced a damping torque term, which is incorporated in the Eqn. (2.14). The proposed damping term [45] is $\frac{\alpha}{M_S}(\boldsymbol{M} \times \frac{d\boldsymbol{M}}{dt})$. Consequently, we get the famous Landau-Lifshitz-Gilbert (LLG) equation after incorporating this Gilbert damping term in LL equation.

$$\frac{d\boldsymbol{M}}{dt} = -\gamma \boldsymbol{M} \times \boldsymbol{H}_{eff} + \frac{\alpha}{M_S}(\boldsymbol{M} \times \frac{d\boldsymbol{M}}{dt}) \tag{2.16}$$

Here α is the Gilbert damping parameter and M_S is the saturation magnetization of the magnetic system.

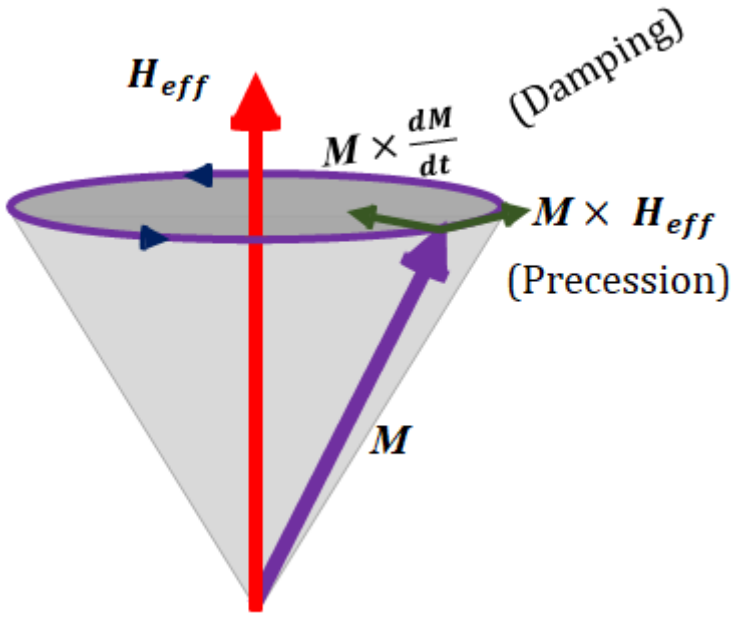

Figure 2.1: The precessional motion of the magnetization ($\boldsymbol{M}$) around the effective magnetic field ($\boldsymbol{H}_{eff}$).

The Fig. (2.1) shows the interplay between two torque terms acting on the magnetization vector ($\boldsymbol{M}$). The first torque term (precessional torque) on the right hand side of Eqn. (2.16) forces tip of the magnetization vector to precess about the effective magnetic field, while the second torque term (damping torque) acts to align magnetization vector along the effective magnetic field direction. Consequently, the tip of the magnetization vector follows a damped spiral motion. The Gilbert damping parameter (α) is a dimensionless constant and determines how fast the magnetization vector comes back to its equilibrium position. Since this damping originates primarily from the spin orbit interaction thus α [46] is a material property of a magnetic system. Apart from this intrinsic damping part, there exists other extrinsic damping parts also such as magnon-magnon scattering, spin pumping, eddy current [47-49] etc. All these damping parts determine the effective damping of the system and contribute for relaxation of the precessional motion of the magnetization.

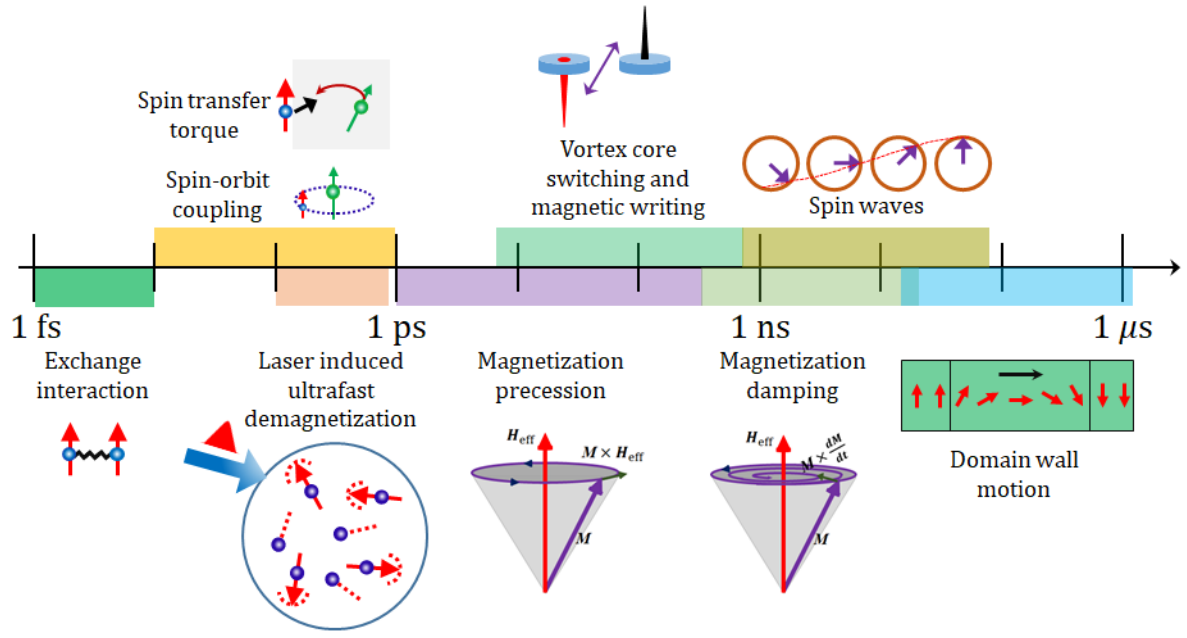

Figure 2.2: Magnetization dynamics at various time-scales.

2.4.1. Time Scales of the Magnetization Dynamics

Magnetization dynamics cover a wide range of events, which occur at different time scales [50] starting from microseconds (μs) to few femtoseconds (fs). The events with their characteristic timescale are schematically illustrated in Fig. (2.2). Among these events, the domain wall motion is the slowest phenomenon that typically occurs in the

timescale of few nanoseconds (ns) to few μs. The precessional motion of the magnetization is comparatively faster process that occurs within 10 - 100 picoseconds (ps) and this precessional motion can produce SW propagation in a ferromagnetic system before the precession is damped in sub-ns to tens of ns. The characteristic timescale of vortex core switching phenomenon is few tens of ps to several ns. Whereas the magnetization reversal dynamics occurs in the time scale of few ps to few hundreds of ps. In addition, dynamics in fs time range include fundamental exchange interaction (~10 fs), spin-transfer-torque/spin-orbit torque (~10 fs – 1 ps), and the laser induced ultrafast demagnetization (~hundreds of fs).

2.4.2. Laser-Induced Ultrafast Magnetization Dynamics

When a highly energized ultrashort (order of fs) laser pulse interacts with a magnetized ferromagnetic material, very shortly it leads to the ultrafast demagnetization or decay magnetism of the ferromagnet. Interestingly, the underlying mechanism of this ultrafast demagnetization is still highly controversial. In 1996, Beaurepaire *et al*. first reported the experimental observation of ultrafast demagnetization in a Ni thin film. The explanation of the experimental results were modelled by the phenomenological three temperature model where it is considered that magnetic system comprises of three thermalized reservoirs, which are spin, electron and lattice with corresponding temperatures T_S, T_e, and T_l, respectively. Till date, a huge amount of investigations have been carried out on various ferromagnetic systems to explore the underlying mechanism of this phenomenon. Consequently, various theories have been proposed to describe the mechanism of ultrafast demagnetization such as Elliott-Yafet (EY) scattering, Coulomb scattering, relativistic quantum electrodynamic process, laser induced spin flip process, superdiffusive spin transport [51,52], optically induced spin transfer (OISTR) effect [53,54] etc. The increase of spin temperature through various mechanisms after incidence of a highly energized laser pulse causes ultrafast demagnetization within hundreds of fs timescale. After laser perturbation, the magnetic system tries to come back to its equilibrium condition via relaxation process. At first, the energy transfer from spin and electron systems to lattice system [55] leads to the fast relaxation. Subsequently, a slower relaxation is started when energy is dissipated from electron and lattice systems to the surroundings. During this slow relaxation process, the magnetization vector undergoes a continuous damped precessional motion.

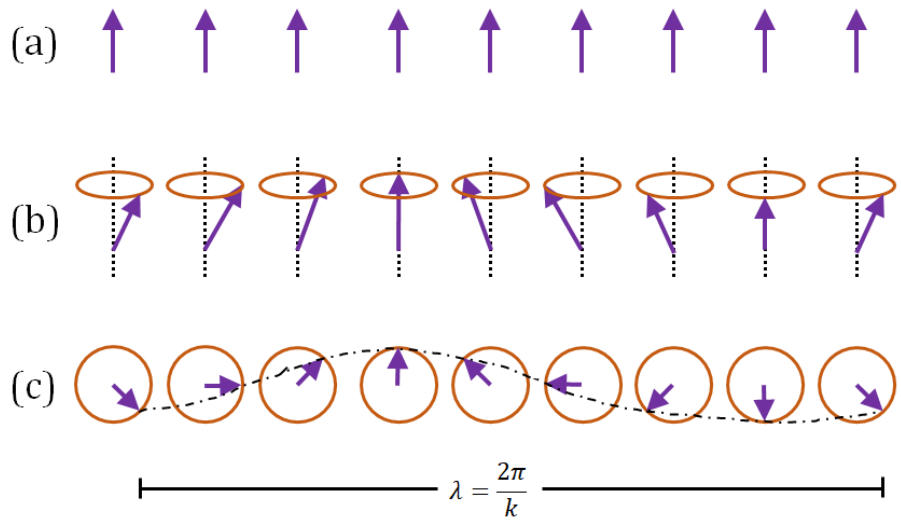

Figure 2.3: Semiclassical representation of spin wave in a ferromagnet: (a) the ground state configuration of the magnetic moments, (b) precessing magnetic moments and (c) the spin wave (top view) showing a full wavelength.

2.5. Spin Waves

Bloch introduced the concept of SWs in 1930. According to the semi-classical approach, the magnetic ground state of a ferromagnetic system means all the atomic magnetic moments are aligned along the same direction at absolute zero temperature as shown in Fig. (2.3). This magnetic ground state can be disturbed by applying various kinds of external perturbation, e.g. temperature, magnetic field or pressure. SW [56] is the propagating phase of the disturbance through an ordered magnetic system as depicted in Fig. (2.3). The uniform precession means in presence of an external magnetic field all spins precess in phase about the direction of the magnetic field. The frequency of this uniform precession (well known as ferromagnetic resonance or FMR frequency) can be obtained by solving the LLG equation (Eqn. (2.16)) with condition of $\frac{d\boldsymbol{M}}{dt} = 0$. In case of an ellipsoid, the calculated FMR frequency is given by the following equation (Kittel equation):

$$f_{\mathrm{FMR}} = \frac{\gamma}{2\pi}\left[\{H + (N_{\mathrm{y}} - N_z)\, M_{\mathrm{s}}\}\{H + (N_{\mathrm{x}} - N_{\mathrm{z}})\, M_{\mathrm{s}}\}\right]^{\frac{1}{2}} \qquad (2.17)$$

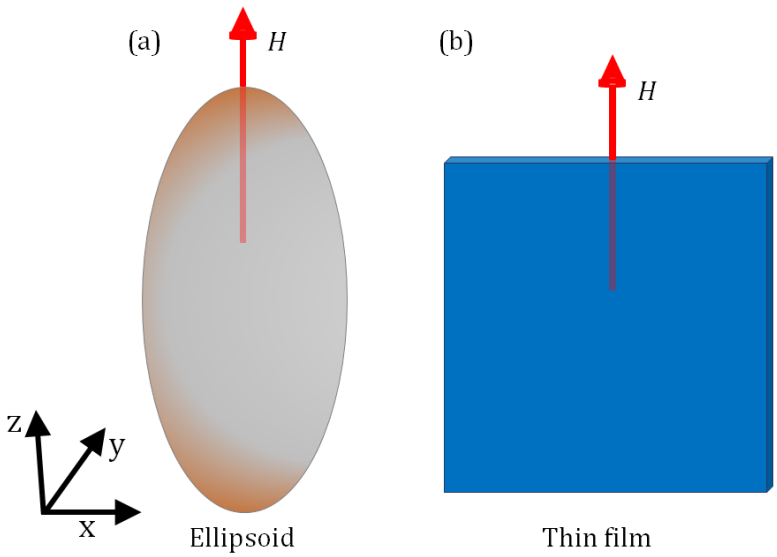

Figure 2.4: Schematic of the geometry considered for ferromagnetic material in the forms of (a) an ellipsoid and (b) thin film.

Here N_x, N_y and N_z are the demagnetizing factors along x, y, z directions, respectively, and H is the bias magnetic field, which is applied along the z-axis as shown in Fig. (2.4). However, for a ferromagnetic thin film, $N_x = N_z = 0$ and $N_y = 4\pi$. Thus, by putting these values in Eqn. (2.17) we get:

$$f_{FMR} = \frac{\gamma}{2\pi}\left[H\,(H + 4\pi M_s)\right]^{\frac{1}{2}} \tag{2.18}$$

On the other hand, in case of non-uniform precession, the mutual interactions between the magnetic moments decide the nature of the SW and those SWs can be categorized with respect to their wavelength. In long wavelength regime, the dipolar energy dominates and corresponding SWs are referred as dipolar-dominated or magnetostatic SWs. On the other hand, SWs with short wavelength are primarily controlled by the exchange interaction and hence, they are called as exchange SWs. The intermediate region is known as dipole-exchange SW. The prime features of these SWs are discussed in the following.

2.5.1. Magnetostatic Spin Waves

The anisotropic nature of dipolar interaction makes magnetostatic SWs direction dependent. Therefore, the magnetostatic SWs can be classified depending upon the

relative orientation of the wave vector (***k***) with magnetization (***M***) and the sample plane. If both ***k*** and ***M*** lie in the sample plane and perpendicular to each other then it is called magnetostatic surface SW (MSSW) mode or Damon-Eshbach (DE) mode [57].

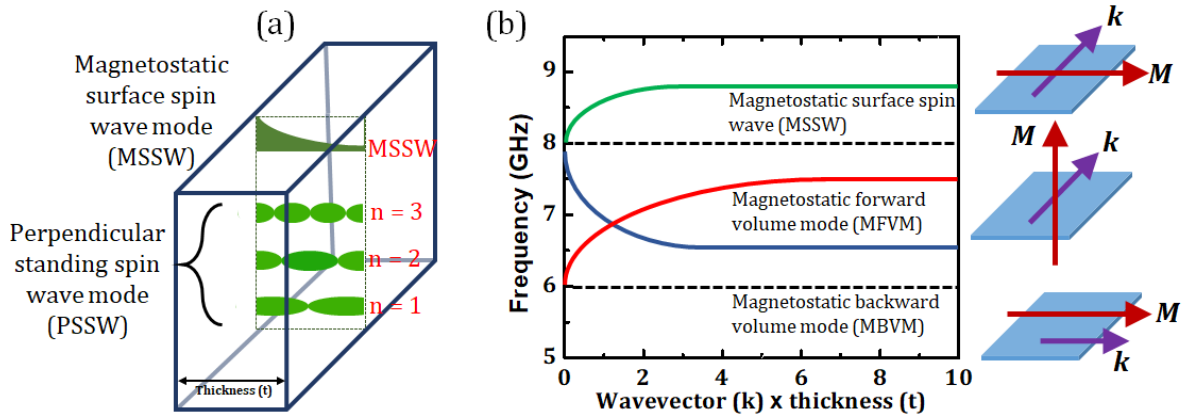

Figure 2.5: Schematic diagram of (a) magnetostatic surface spin wave (MSSW) mode and perpendicular standing spin wave (PSSW) mode for a ferromagnetic thin film with thickness t. (b) Typical dispersion relations for different types of magnetostatic spin wave modes.

Whereas if both ***k*** and ***M*** lie in the sample plane but parallel to each other then it is called magnetostatic backward volume (BV) mode. On the contrary, if the bias magnetic field (***H***) is applied out of the sample plane (out-of-plane magnetization) and ***k*** lies in the sample plane then it is called as magnetostatic forward volume mode (MFVM). The dispersion characteristics (frequency versus wave vector relation) of these SW modes are presented in Fig. (2.5). By neglecting the magnetic anisotropy and exchange interaction, the MSSW or DE mode shows positive dispersion relation, which is given by:

$$f_{\mathrm{DE}} = \frac{\gamma}{2\pi}\left[H\,(H + M_{\mathrm{s}}) + (2\pi M_{\mathrm{s}})^2\left(1 - e^{-2k_{\parallel}t}\right)\right]^{\frac{1}{2}} \qquad (2.19)$$

Here $k_{\parallel}$ is the in-plane component of wave vector and t is the thickness of the sample.

In case of MBVM, the dispersion relation gives negative slope and the corresponding mathematical expression [58] is given by:

$$f_{\mathrm{MBVM}} = \frac{\gamma}{2\pi}\left[H\left(H + 4\pi M_{\mathrm{s}}\frac{1-e^{-2k_{\parallel}t}}{k_{\parallel}t}\right)\right]^{\frac{1}{2}} \tag{2.20}$$

This MBVM becomes FMR mode or Kittel mode for $k = 0$. The dispersion relation of the MFVM [59] is given by:

$$f_{\mathrm{MFVM}} = \frac{\gamma}{2\pi}\left[(H - 4\pi M_{\mathrm{s}})\left(H - 4\pi M_{\mathrm{s}}\frac{1-e^{-k_{\parallel}t}}{k_{\parallel}t}\right)\right]^{\frac{1}{2}} \tag{2.21}$$

2.5.2. Exchange Spin Waves

The exchange interaction becomes significant when wavelength of a SW is comparable to the exchange length of that ferromagnetic material. The exchange length (l_{ex}) of a ferromagnet is given by:

$$l_{\mathrm{ex}} = \sqrt{\frac{2A_{ex}}{\mu_0 M_s^2}} \tag{2.22}$$

Here A_{ex} is the exchange stiffness constant. By considering both dipolar and exchange interactions [60], the SW dispersion relation is given by:

$$f = \frac{\gamma}{2\pi}\left[\left(H + 2\pi M_{\mathrm{s}}k_{\parallel}t\sin^2\theta_{k_{\parallel}} + \frac{2A}{M_{\mathrm{s}}}{k_{\parallel}}^2\right)\left(H + 4\pi M_{\mathrm{s}} - 2\pi M_{\mathrm{s}}k_{\parallel}t + \frac{2A}{M_{\mathrm{s}}}{k_{\parallel}}^2\right)\right]^{\frac{1}{2}} \tag{2.23}$$

Here $\theta_{k_{\parallel}}$ is the angle between $k_{\parallel}$ and H. In case of a thin film, sometimes it is observed that SW propagates along the perpendicular direction of the film surface and forms PSSW mode, which is shown in Fig. (2.5). The perpendicular quantized wave vector ($k_{\perp}$) of PSSW [61] mode is given by:

$$k_{\perp} = \frac{n\pi}{t} \tag{2.24}$$

Here t is the thickness of the film and n is the quantization number. By neglecting the contribution from in-plane wave vector, the dispersion relation for PSSW mode is given by:

$$f_{\mathrm{PSSW}} = \frac{\gamma}{2\pi}\left[\left(H_{\mathrm{eff}} + \frac{2A}{M_s}{k_\perp}^2\right)\left(H_{\mathrm{eff}} + 4\pi M_{\mathrm{eff}} + \frac{2A}{M_s}{k_\perp}^2\right)\right]^{\frac{1}{2}} \tag{2.25}$$

Here H_{eff} is the effective magnetic field and M_{eff} is the effective magnetization.

2.5.3. Confined Spin Wave Modes in Magnetic Nanostructures

We have discussed various types of SW by considering of infinitely long thin film system. However, the SW properties can be substantially modulated by additional boundary conditions arising from the finite lateral dimensions of the sample. The distribution of potential barriers imposed by structuring [62] of the thin film guides the propagation of SW. Consequently, the SW forms standing wave or propagates through the confined channel. When the sample dimension becomes comparable to the wavelength of the SW, the standing wave produces quantized SW mode with BV and DE like character. The characteristics of the SW strongly depends on the strength and orientation of the bias magnetic field. Alike photonic crystals, the periodic patterning of a magnetic system in nanoscale produces MCs. The MC [63] produces artificial band structure for SW consisting of allowed and forbidden frequency gaps. Hence, the full control of the dynamics of the propagation of SW is achieved. In this thesis, we have characterized this kind of SW modes by simulating the spatial distribution of power and phase maps using a home-built code [64].

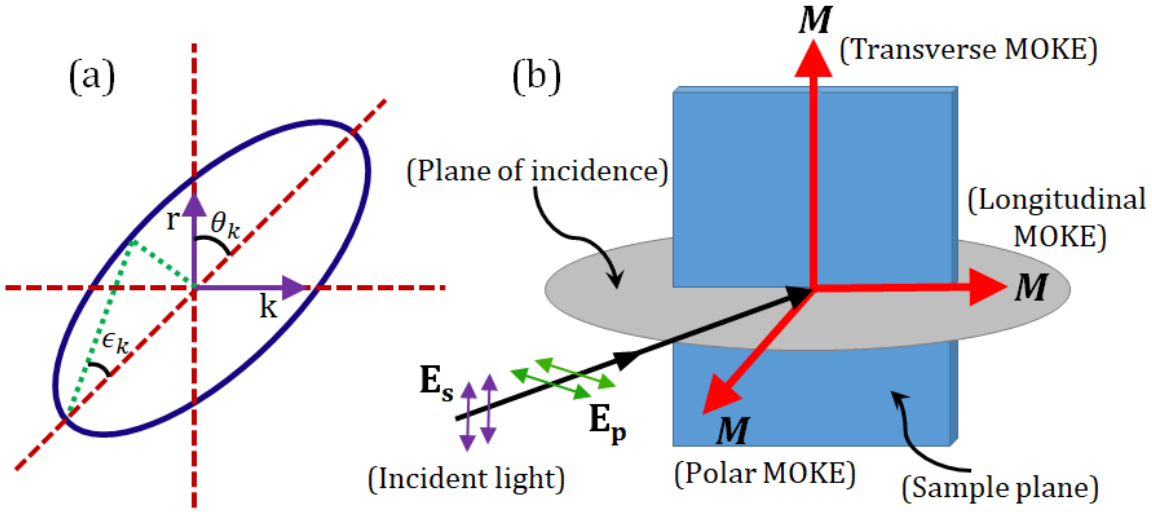

Figure 2.6: (a) Geometry of the Kerr ellipticity (ε_k) and Kerr rotation (θ_k). (b) Schematics of transverse, longitudinal and polar MOKE geometries are shown.

2.6. Magneto-Optical Kerr Effect (MOKE)

The magneto-optical Kerr effect [65] is one of the magneto-optic phenomena that was discovered by Michael Faraday in 1845. It describes the modification of light reflected from a surface of magnetized material. The polarization of a light can change when it is reflected from a magnetized sample. For instance, a plane polarized light is transformed into an elliptically polarized light after reflecting from a magnetized surface. This phenomenon is known as Kerr effect and the amount of rotation of the plane of polarization of light is called the Kerr rotation. This is widely used in materials science research such as investigation of domain structure of a magnetic material by using Kerr microscope. The Kerr rotation (θ_k) and Kerr ellipticity (ε_k) are shown schematically in Fig. (2.6). If r and k respectively represent the parallel and perpendicular electric field components of the reflected light *w.r.t.* the incident light then they satisfy the following relation [64] as:

$$\theta_k + i\varepsilon_k = \frac{k}{r}, \text{ where } k \ll r. \tag{2.26}$$

2.6.1. Origin of Magneto-Optical Kerr Effect

The origin of magneto-optic Kerr effect is generally described with the help of macroscopic dielectric theory and microscopic quantum theory [66,67]. In macroscopic case, the dielectric property of a medium shows anisotropic nature in presence of an external magnetic field, which leads magneto-optic effects. A linearly polarized light can be considered as a superposition of right circularly polarized (RCP) and left circularly polarized (LCP) light. During the propagation of light, all nearby electrons of the medium feel perturbation due to the electric field component of light. Consequently, the LCP light guides the electrons to left circular motion whereas the RCP light guides the electrons to right circular motion. However, in absence of magnetic field both of these circular motions are identical except direction of rotation. Since the magnitude of the electric dipole moment is proportional to the radius of the circular orbit, hence net Faraday rotation will be zero. On the other hand, in presence of a magnetic field there will be a finite difference between the radius of left and right circularly polarized light due to the action of additional Lorentz force. Consequently, this finite difference in radii

produces a finite difference in dielectric constants, which is responsible for the magneto-optical Kerr effect.

In microscopic quantum theory, it is considered that spin-orbit interaction couples the electrons with their motion responsible for the Kerr effect. The dynamics of electrons due to the impact of electric field of light modifies the corresponding spin-orbit interaction. This spin-orbit interaction is considered as an effective field vector potential (A), which acts on the electrons. The relation between A and the electric field of light is given by:

$$A = S \times \Delta V \tag{2.27}$$

Here S is the electron spin and ΔV is the electric field. This effect becomes significant for a system contains unbalanced population of spin up and spin down state such as ferromagnetic system.

2.6.2. MOKE Geometries

MOKE can be further classified depending upon the relative orientation of magnetization ($\boldsymbol{M}$) with respect to the reflection surface and the plane of incidence as depicted in Fig. (2.6). There are three MOKE configurations, namely, polar, longitudinal and transverse MOKE [68-70].

In case of polar MOKE, the magnetization is parallel to the plane of incidence and perpendicular to the reflection surface. The plane of polarization of light and the direction of magnetization makes right angle between them. Consequently, an effective Lorentz force is always there irrespective of the incident angle of light that ensures Kerr rotation.

In longitudinal MOKE, the magnetization is parallel to the plane of incidence and lies parallel to the reflection surface. Hence, longitudinal Kerr effect strongly depends upon the angle of incidence. For example, there is no longitudinal Kerr effect in normal incidence because the Lorentz force either acts along the direction of light (for s-polarized light) or becomes zero (for p-polarized light).

In transverse MOKE geometry, the magnetization is perpendicular to the plane of incidence and lies parallel to the reflection surface. The transverse Kerr effect associates with the change of reflectivity of a p-polarized light when orientation of the

magnetization is changed. The change in reflectivity depends on the component of magnetization perpendicular to the plane of incidence and parallel to the reflection surface.

2.7. Ferromagnetic Resonance

When an external magnetic field is applied to a ferromagnetic (FM) material, its magnetization starts to precess around the effective magnetic field ($\boldsymbol{H}_{eff}$) experienced by the FM. The angular frequency (ω_L) of precession is governed by the Larmor condition for the electron spin:

$$\omega_L = \gamma \boldsymbol{H}_{eff} \tag{2.28}$$

Here γ is the gyromagnetic ratio. The resonance will occur when an alternating magnetic field (h_{rf}) having angular frequency (ω) is applied along the transverse direction of the static magnetic field under the following condition:

$$\omega = \gamma \sqrt{B H_{eff}} \tag{2.29}$$

Here B is the magnetic induction. Consequently, the magnetization will start to precess with resonant frequency by absorbing power from the alternating magnetic field. This phenomenon is called ferromagnetic resonance (FMR).

2.7.1. Microwave Excitation and Detection

FMR spectroscopy is a spectroscopic method to probe the magnetization dynamics of a magnetic system. It is one of the standard techniques for investing the SWs and spin dynamics. Currently, various methods are available to perform FMR experiment such as stripline-based FMR (SL-FMR) [71], pulsed inductive microwave magnetometry-based FMR (PIMM-FMR) [72] and vector network analyzer-based FMR (VNA-FMR). The SL-FMR technique is comparatively simpler but its sensitivity is poor. The PIMM-FMR technique uses a dc magnetic field instead of a microwave excitation field. The main advantage of a VNA-FMR setup is it can extract both amplitude and phase information of the signal. However, the VNA-FMR setup needs complicated calibration and data analysis procedure.

In the following, the VNA-FMR technique is discussed comprehensively.

2.7.1.1. Vector Network Analyzer Incorporated FMR

The information about the magnetization dynamics of a sample is obtained directly in the frequency domain. The microwave input signal with broad frequency window is launched into the sample by a VNA and the output scattering (S) parameters [73] are recorded as absorption spectra at a fixed static magnetic field. The excitation power of the input signal can be varied by the VNA, which is useful for the study of nonlinear spin dynamics.

2.7.2. Vector Network Analyzer

A network analyzer [74] is typically used for the impedance measurement of a device. At lower frequency regime, one can measure the impedance of a device by using simpler tools. Whereas for higher frequencies like radio and microwave frequencies, this measurement becomes complex and therefore, the VNA-FMR spectrometer is used. The VNA measures both amplitude and phase of the incident signal as well as transmitted and/or reflected signal from the device under test. A complicated calibration process is required before starting the experiment to eliminate systematic errors. Finally, the S parameters are calculated by computing of appropriate ratios of the signals, which are similar to our familiar results. The prime characteristics of a broadband FMR (or VNA-FMR) spectrometer, which makes it superior than the conventional FMR spectrometer, are in the following:

a) In conventional FMR spectrometer, a resonance cavity is used that works at a specific resonance frequency with a high quality factor [75]. Whereas in broadband FMR spectrometer, a non-resonant cavity is used that works for broad frequency range and offers flat quality factor. It makes broadband FMR spectrometer more convenient for the study of magnonic crystals, which support broadband multi-mode SW frequencies.
b) Sometimes, the low frequency regime (< 1 GHz) becomes more important in some systems like magnetic vortex core dynamics. In such cases, the broadband FMR spectrometer is more suitable than the conventional technique.
The description about a VNA system is briefly discussed in the following.

2.7.2.1. Compositions

The very basic building blocks of a vector network analyzer include a signal generator, signal separation blocks (test set), receivers, processor and display. Two test ports are typically employed for the measurement of *S* parameters of a device under test.

2.7.2.1.A. Signal Generator

The VNA contains a signal generator (source), which is used to generate an oscillating known stimulus signal in the form of radio frequency (RF) current to excite the spin system.

2.7.2.1.B. Signal Separation Blocks (Test Set)

The test set makes connection between the signal generator and the receivers to conduct the measurement of the device under test (DUT). The current and voltage probes are sufficient for the low frequency measurements whereas to execute a measurement in microwave frequency regime it requires power splitters, couplers, slotted lines and directional bridges. The test set collects signal generator output and route it towards the DUT. Subsequently, the outcome signal from the DUT enters into the receivers through the test set. It often channelizes incident/primary signal as a reference signal for the computation of phase calculation.

2.7.2.1.C. Signal Receiver

Receivers are employed to conduct the final measurements. Receivers measure both the applied stimulus signal and response signals that are generated from the DUT. They can measure magnitude as well as phase of the signal simultaneously. It requires a dedicated reference channel for the phase determination. Therefore, a VNA requires at least two receivers, which are connected to its test ports.

2.7.2.1.D. Processor and Display

The processor with display section is one of the crucial blocks of hardware in a VNA. In this section, the reflected and transmitted signal are formatted and displayed. It makes

interpretation of the experimental results simple. Nowadays, the available high-performance processor makes data processing and interpretation procedure simpler.

2.7.2.2. Transmission Line

The efficient transfer of microwave (RF) power is one of the principal goals behind the use of transmission lines [76] in a VNA-FMR setup. The wavelength of a signal with frequency of 60 Hz is 5000 km, while it is 30 cm for a signal with frequency of 1 GHz. At low frequencies where the length of the circuit conductors is much smaller compare to the wavelengths of the signals, a simple conductor is enough efficient for carrying electric power. The measured current and voltage values show invariance along different positions of the conductor. However, at high frequencies where the length of the circuit conductors is comparable to or much higher than the wavelengths of the signals then signals can be considered as travelling waves for the better realization of power transfer phenomenon. Currently, various transmission media, e.g. coplanar, coaxial, stripline, waveguide, microstrip etc. are developed to make efficient RF transmission lines. The characteristic impedance (Z_0) is one of the fundamental parameters of a transmission line, which defines the voltage-current relationship. The value of Z_0 varies from 50 ohms to 75 ohms for most of the RF systems. Z_0 depends on the dielectric constant of the non-conducting material used in the transmission line and the dimensions of the transmission line. According to maximum power transfer theorem when a transmission line is terminated with a characteristic impedance, then maximum power will transfer to the load and the reflected signal will be zero. However, in case of arbitrary load with impedance other than Z_0 a portion of the incident signal will reflect back depending on the value of load impedance. For instance, when transmission line is terminated in short circuit fashion a reflection of the incident signal is occurred from the load because purely reactive materials cannot dissipate power. On the other hand, when transmission line is terminated in open condition the current propagation at the open will be zero. Consequently, in both the above-mentioned cases, a formation of standing wave pattern is occurred due to superposition of incident signal and reflected back signal.

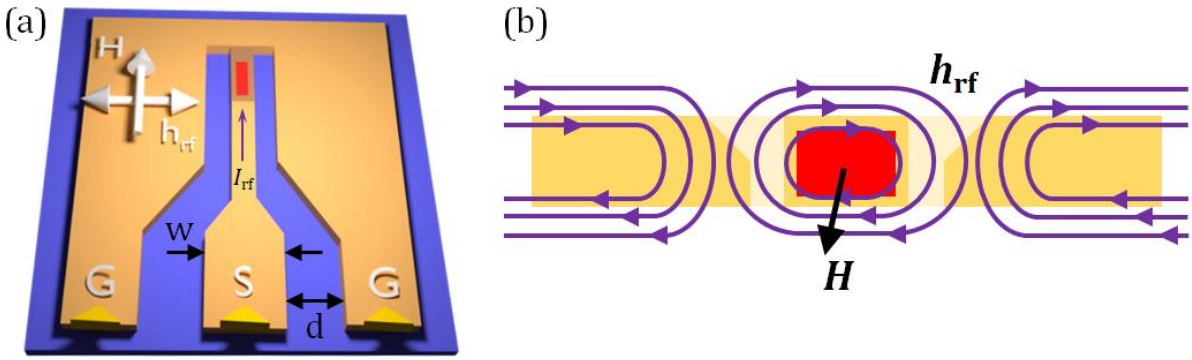

Figure 2.7: (a) Schematic diagram of a coplanar waveguide (CPW) with sample and the measurement geometry. (b) Cross-sectional view of the CPW showing the distribution of magnetic field lines of RF field (h_{rf}) generated by the RF current (I_{rf}).

2.7.2.2.A. Coplanar Waveguide

Cheng P. Wen invented coplanar waveguide (CPW) in 1969. A CPW can be fabricated by using optical lithography technique and it is generally used for the propagation of microwave signals [75]. The CPW is generally designed with a single conductor (signal line) in between a pair of return conductors (ground lines). All these lines are typically fabricated on the same plane of a dielectric medium hence, it is called coplanar waveguide. However, in case of a grounded CPW (GCPW) the ground lines are fabricated on the opposite plane (from the signal line plane) of the dielectric medium. The width (w) of the signal line and the separation gap (d) between signal line to ground line play crucial roles for the determination of impedance of the whole system. In reflection geometry, these three transmission lines are shorted at one end, while in transmission geometry, they are always separated by a small gap. All the FMR measurements presented in this thesis have been accomplished in reflection geometry as shown in Fig. (2.7). An insulating layer separates the FM samples and the signal line to avoid damaging/shorting of the samples from direct RF current. The magnetic field lines generating from RF current (I_{rf}) get flattened close to the surface of signal line due to its rectangular shape. This in-plane RF magnetic field (h_{rf}) perturbs the spin system from its equilibrium state as illustrated in Fig. (2.7).

2.7.2.3. High Frequency Device Characterization

In a common network analyzer, the incident signal is measured with a reference receiver. Whereas the reflected and transmitted signals are measured with two other different receivers. We can extract the transmission and reflection characteristics of a DUT by using the magnitude and phase information of all three measured signals. Both scalar and vector terms can be extracted as results. For instance, the return loss is a scalar term and the impedance is a vector term.

2.7.2.3.A. Reflection Parameters

The most general reflection parameter is reflection coefficient (Γ). Γ is a complex number and its magnitude is called rho (ρ). Γ is defined by the ratio of voltage level of the reflected signal (V_{refl}) and the incident signal (V_{inc}). Thus, it is expressed as $\Gamma = \frac{V_{refl}}{V_{inc}}$. When the load impedance (Z_L) is equal to the characteristic impedance (Z_0) then according to the maximum power transfer theorem, V_{refl} becomes zero and thus $\rho = 0$. However, if $Z_L \neq Z_0$, then V_{refl} becomes nonzero and $\rho > 0$. For both short and open circuit cases, $|V_{refl}| = |V_{inc}|$, which gives $\rho = 1$. Consequently, the value of ρ ranges from $0 \leq \rho \leq 1$. Return loss is the logarithmic (decibel) expression of reflection coefficient. Mathematically it is expressed as Return Loss $= -20\log(\rho)$. It signifies how much the reflected signal is lower than the incident signal in decibel unit. The value of return loss ranges from 0 dBm to infinity. The return loss becomes infinity when $Z_L = Z_0$ and 0 dBm for open or short condition. The voltage standing wave ratio (VSWR) is another very common parameter used to quantify the reflection. The relation between VSWR and ρ is, VSWR $= \frac{(1-\rho)}{(1+\rho)}$. The value of VSWR ranges from 1 to infinity. The VSWR becomes infinity for full reflection and 1 for no reflection.

2.7.2.3.B. Transmission Parameters

Transmission coefficient (T) is expressed as the ratio of the transmitted signal voltage (V_{trans}) to the incident signal voltage (V_{inc}). If $|V_{trans}| < |V_{inc}|$, this is called insertion loss. It is typically expressed in dBm unit. The phase part of T is called the insertion phase.

2.7.2.3.C. Group Delay

Group delay is the actual transit time of a propagating signal through a DUT as a function of frequency. It is the derivative of insertion phase response of a DUT *w.r.t.* frequency. Hence, group delay can be considered as the measure of transmission line response.

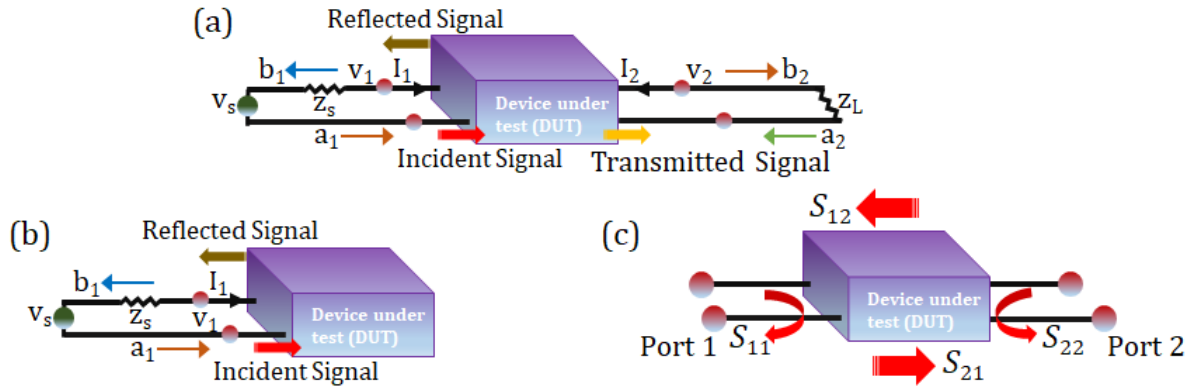

Figure 2.8: Schematic representation of (a) two- and (b) one-port microwave excitation and detection systems. (c) A graphical representation of the scattering (*S*) parameters.

2.7.2.4. Scattering (*S*-) Parameters

S-parameters are the components of scattering (*S*-) matrix to describe the electrical behaviour of a circuit in frequency domain. They are useful to study the electrical behaviour of a circuit working at RF or microwave (MW) frequencies. These parameters depend on the measurement frequency and port impedance. An electrical circuit is usually treated as a black box and it can interact with surrounding circuits through connecting ports. The network (interconnection of different electrical elements) is characterized with the help of *S*-matrix. To characterize a network having *N* number of ports an *N*-dimensional *S*-matrix is required, which has N^2 complex components. At very high frequencies, direct measurement of impedance (*Z*) or admittance (*Y*) or hybrid (*h*) parameters of a network become hard due to the underneath reasons:

1. It is difficult to measure total current and voltage of a network in that high frequency regime.
2. It is challenging to achieve perfect open/short condition.

3. The DUT may not stay stable under such high frequency regime or in open/short condition.

However, to avoid the above-mentioned difficulties, *S*-parameters offer the following advantages:

1. It is easier to measure *S*-parameters in such high frequency regime.
2. *S*-parameters can relate with various familiar measurements, such as return loss, insertion loss, and VSWR of a network.
3. These parameters can also be used to calculate *Y*, *Z*, or *h*- parameters.

2.7.2.4.A. Calculations for the Scattering (*S*-) Parameters

According to the numbering convention of *S*-parameters, the first number signifies the port associated with output signal and second number signifies the port associated with input signal. If S_{21} represents a measurement then the output signal connecting with port 2 and incident signal entering to port 1. Whereas if both the numbers are same (e.g., S_{11}), this corresponds to reflection measurement geometry. Figure (2.8) shows schematically the measurement conditions for (a) two-port and (b) one-port measurement geometries, respectively. Here Z_S and Z_L respectively correspond to the source and load impedances and both are terminated at Z_0. V_S represents input signal voltage level. On the other hand, V_1, V_2 and I_1, I_2 represent corresponding potential differences and currents across the respective loads. If the incident signals (a_1, a_2) and acquired signals (b_1, b_2) represent corresponding voltage traveling waves from the two-port device then both the b_1 and b_2 wave can be described as a linear combination of a_1 wave and a_2 wave. These relationships can be expressed as follows:

$$b_1 = S_{11}a_1 + S_{12}a_2 \tag{2.30}$$

$$b_2 = S_{21}a_1 + S_{22}a_2 \tag{2.31}$$

The above two equations can be written in the matrix notation as,

$$\begin{bmatrix} b_1 \\ b_2 \end{bmatrix} = \begin{bmatrix} S_{11} & S_{12} \\ S_{21} & S_{22} \end{bmatrix} \begin{bmatrix} a_1 \\ a_2 \end{bmatrix} \tag{2.32}$$

Now, the four *S*-parameters can be expressed as:

1. Forward reflection coefficient,

$$S_{11} = \left.\frac{b_1}{a_1}\right|_{a_2 = 0} \tag{2.33}$$

2. Reverse reflection coefficient,

$$S_{22} = \left.\frac{b_2}{a_2}\right|_{a_1 = 0} \tag{2.34}$$

3. Forward transmission coefficient,

$$S_{21} = \left.\frac{b_2}{a_1}\right|_{a_2 = 0} \tag{2.35}$$

4. Reverse transmission coefficient,

$$S_{12} = \left.\frac{b_1}{a_2}\right|_{a_1 = 0} \tag{2.36}$$

These parameters are also shown in Fig. (2.8). The FMR works presented in this thesis, only S_{11} parameter is extracted by one-port measurement in reflection geometry to collect the SW spectra from ferromagnetic nanostructure samples.

References

[1] R. M. Bozorth, *Ferromagnetism*, (1978).

[2] B. D. Cullity, C. D. Graham, in *Introduction to Magnetic Materials*, IEEE, 1 (2009).

[3] A. Aharoni, *Introduction to the theory of Ferromagnetism*, (2000).

[4] S. Chikazumi, *Physics of Ferromagnetism*, (OUP Oxford, (2009).

[5] R. P. Feynman, R. B. Leighton, M. Sands, *The Feynman Lectures on Physics*, *Vol. **I***: *The New Millennium Edition*: *Mainly Mechanics*, *Radiation*, *and Heat* (Basic Books, 2011).

[6] A. Abragam, B. Bleaney, *Electron Paramagnetic Resonance of Transition Ions*, (OUP Oxford, 2012).

[7] L. Landau, Z. Phys. **64**, 629 (1930).

[8] E. H. Sondheimer, A. H. Wilson, Philos. Trans. Royal Soc. A **210**, 173 (1951).

[9] C. Kittel, *Introduction to Solid State Physics*, (2005).

[10] P. Langevin, J. Phys. Theor. Appl. **4** (1905).

[11] M. L. Néel, Ann. Phys. **12**, 137 (1948).

[12] N. A. Spaldin, *Magnetic Materials*: *Fundamentals and Applications*, (Cambridge University Press, 2010).

[13] P. W. Anderson, Phys. Rev. **79**, 350 (1950).

[14] T. Kasuya, Prog. Theor. Exp. Phys. **16**, 45 (1956).

[15] C. N. Yang, Phys. Rev. **85**, 808 (1952).

[16] A. H. Morrish, *The Physical Principles of Magnetism*, (R. E. Krieger Publishing Company, 1980).

[17] K. H. J. Buschow, *Handbook of Magnetic Materials*, **18**, 168 (2009).

[18] J. M. D. Coey, *Magnetism and Magnetic Materials*, (Cambridge University Press, 2010).

[19] D. J. Griffiths, *Introduction to Quantum Mechanics*, (Pearson Prentice Hall, 2005).

[20] M. Pioro-Ladrière, T. Obata, Y. Tokura, Y. S. Shin, T. Kubo, K. Yoshida, T. Taniyama, S. Tarucha, Nat. Phys. **4**, 776 (2008).

[21] W. Heisenberg, Z. Physik **38**, 411 (1926).

[22] P. A. M. Dirac, Philos. Trans. Royal Soc. **112**, 661 (1926).

[23] K.-I. Gondaira, Y. Tanabe, J. Phys. Soc. Jpn. **21**, 1527 (1966).

[24] M. A. Ruderman, C. Kittel, Phys. Rev. **96**, 99 (1954).

[25] J. H. Van Vleck, Rev. Mod. Phys. **34**, 681 (1962).

[26] T. Moriya, Phys. Rev. **120**, 91 (1960).

[27] P. A. Abragam, A. Abragam, *The Principles of Nuclear Magnetism*, (Clarendon Press, 1961).

[28] P. Bruno, J. P. Renard, Appl. Phys. A. **49**, 499 (1989).

[29] M. McCaig, *Permanent Magnets in Theory and Practice*, (Pentech Press, 1977).

[30] P. Bruno, Phys. Rev. B **39**, 865 (1989).

[31] H. B. Callen, E. Callen, J. Phys. Chem. Solids **27**, 1271 (1966).

[32] J. A. Osborn, Phys. Rev. **67**, 351 (1945).

[33] D.-X. Chen, J. A. Brug, R. B. Goldfard, IEEE Trans. Magn. **27**, 3601 (1991).

[34] B. Krüger, G. Selke, A. Drews, D. Pfannkuche, IEEE Trans. Magn. **49**, 4749 (2013).

[35] D.-X. Chen, E. Pardo, A. Sanchez, IEEE Trans. Magn. **37**, 3877 (2001).

[36] M. E. Schabes, H. N. Bertram, J. Appl. Phys. **64**, 1347 (1988).

[37] V. V. Kruglyak, P. S. Keatley, R. J. Hicken, J. R. Childress, J. A. Katine, Phys. Rev. B **75**, 024407 (2007).

[38] B. K. Mahato, S. Choudhury, R. Mandal, S. Barman, Y. Otani, A. Barman, J. Appl. Phys. **117**, 213909 (2015).

[39] S. Jain, Y. Ren, A. O. Adeyeye, N. Singh, Phys. Rev. B **80**, 132401 (2009).

[40] L. Zhong, M. Kim, X. Wang, A. J. Freeman, Phys. Rev. B **53**, 9770 (1996).

[41] J. Miltat, G. Albuquerque, A. Thiaville, in *Spin Dynamics in Confined Magnetic Structures I*, edited by B. Hillebrands, and K. Ounadjela (Springer Berlin Heidelberg, Berlin Heidelberg, 2002).

[42] M. Getzlaff, *Fundamentals of Magnetism*, (Springer Berlin Heidelberg, 2007).

[43] J. Stöhr, H. C. Siegmann, *Magnetism: From Fundamentals to Nanoscale Dynamics*, (Springer Berlin Heidelberg, 2007).

[44] B. Koopmans, J. J. M. Ruigrok, F. D. Longa, W. J. M. de Jonge, Phys. Rev. Lett. **95**, 267207 (2005).

[45] T. L. Gilbert, IEEE Trans. Magn. **40**, 3443 (2004).

[46] H. Suhl, IEEE Trans. Magn. **34**, 1834 (1998).

[47] V. Kambersky, C. E. Patton, Phys. Rev. B **11**, 2668 (1975).

[48] K. Gilmore, Y. U. Idzerda, M. D. Stiles, J. Appl. Phys. **103**, 07D303 (2008).

[49] Y. Tserkovnyak, A. Brataas, G. E. W. Bauer, Phys. Rev. B **66**, 224403 (2002).

[50] S.-K. Kim, J. Phys. D: Appl. Phys. **43**, 264004 (2010).

[51] B. Koopmans, G. Malinowski, F. Dalla Longa, D. Steiauf, M. Fähnle, T. Roth, M. Cinchetti, M. Aeschlimann, Nat. Mater. **9**, 259 (2009).

[52] J.-Y. Bigot, M. Vomir, E. Beaurepaire, Nat. Phys. **5**, 515 (2009).

[53] D. Steil, J. Walowski, F. Gerhard, *et al*., Phys. Rev. Research **2**, 023199 (2020).

[54] M. Hofherr, S. Häuser, J. K. Dewhurst, *et al*., Sci. Adv. **6**, 8717 (2020).

[55] E. Beaurepaire, J. C. Merle, A. Daunois, J. Y. Bigot, Phys. Rev. Lett. **76**, 4250 (1996).

[56] D. D. Stanil, A. Prabhakar, *Spin Waves: Theory and Applications*, (Springer US, 2009).

[57] R. W. Damon, J. R. Eshbach, J. Phys. Chem. Solids **19**, 308 (1961).

[58] B. A. Kalinikos, A. N. Slavin, J. Phys. C: Solid State Phys. **19**, 7013 (1986).

[59] B. A. Kalinikos, in *IEE Proceedings H*, (*Microwaves, Optics and Antennas*, 1980).

[60] B. Lenk, H. Ulrichs, F. Garbs, M. Münzenberg, Phys. Rep. **507**, 107 (2011).

[61] M. G. Cottam, D. J. Lockwood, *Light Scattering in Magnetic Solids*, (Wiley, 1986).

[62] B. Hillebrands, A. Thiaville, *Spin Dynamics in Confined Magnetic Structures III*, (Springer, 2006).

[63] S. Neusser, D. Grundler, Adv. Mater. **21**, 2927 (2009).

[64] D. Kumar, O. Dmytriiev, S. Ponraj, A. Barman, J. Phys. D: Appl. Phys. **45**, 015001 (2012).

[65] M. Faraday, T. Martin, R. I. o. G. Britain, *Faraday's diary* (Bell, 1932).

[66] T. W. McDaniel, R. Victoria, *Handbook of Magneto-Optical Data Recording: Materials, Subsystems, Techniques*, (Elsevier Science, 1995).

[67] P. Bruno, Y. Suzuki, C. Chappert, Phys. Rev. B **53**, 9214 (1996).

[68] Z. Q. Qiu, S. D. Bader, Rev. Sci. Instrum. **71**, 1243 (2000).

[69] C.-Y. You, S.-C. Shin, J. Appl. Phys. **84**, 541 (1998).

[70] A. Barman, A. Haldar, in *Solid State Physics*, edited by R. E. Camley, and R. L. Stamps (Academic Press, 2014).

[71] C. E. Patton, J. Appl. Phys. **39**, 3060 (1968).

[72] T. J. Silva, C. S. Lee, T. M. Crawford, C. T. Rogers, J. Appl. Phys. **85**, 7849 (1999).

[73] J. Ding, M. Kostylev, A. O. Adeyeye, Appl. Phys. Lett. **100**, 062401 (2012).

[74] K. Hoffmann, Z. Skvor, IEEE Trans. Microw. Theory Tech. **46**, 2520 (1998).

[75] R. S. Kwok, L. Ji-Fuh, IEEE Trans. Microw. Theory Tech. **47**, 111 (1999).

[76] C. Caloz, T. Itoh, *Electromagnetic Metamaterials: Transmission Line Theory and Microwave Applications*, (Wiley, 2005).

[77] R. N. Simons, *Coplanar Waveguide Circuits, Components, and Systems*, (Wiley, 2004).

Chapter 3

3. Fabrication and Characterization Techniques

3.1. Introduction

The major challenges to investigate the magnetization dynamics of ferromagnetic thin films and nanostructures are fabrication [1,2] of the desired samples and their proper characterization. The ongoing trend of miniaturization in the magnetism based research demands fabrication of gradually smaller magnets with minimal structural and compositional defects. Depending upon the requirements, various cost-effective fabrication techniques are used to obtain the desired sample. Subsequently, the obtained samples are characterized by using suitable techniques.

To accomplish the experimental works presented in this thesis, thin films were deposited by using magnetron sputtering and electron beam evaporation techniques whereas nano-patterning was done with the help of electron beam lithography [3,4] and photolithography methods [5]. The surface morphology of these samples was investigated by using scanning electron microscope (SEM) [6,7] and atomic force microscope (AFM) [8]. The static and quasi-static magnetic characteristics of these samples were studied with the help of magnetic force microscopy (MFM) [9-12] and magneto-optical Kerr effect (MOKE) magnetometry [13-15]. In the following, we will briefly discuss about the aforementioned fabrication and characterization techniques.

3.2. Lithography Techniques

Lithography [16] is a widely used fabrication technique that enables to create precise and complicated patterned structures at extremely small length scale. There are several types of lithographic techniques available in the market depending upon the radiation applied for exposure, namely, optical (photo-) lithography [17], x-ray lithography [18], electron beam lithography [19] and ion beam lithography [20]. Out of these, we will briefly discuss about optical (photo-) lithography and electron beam lithography.

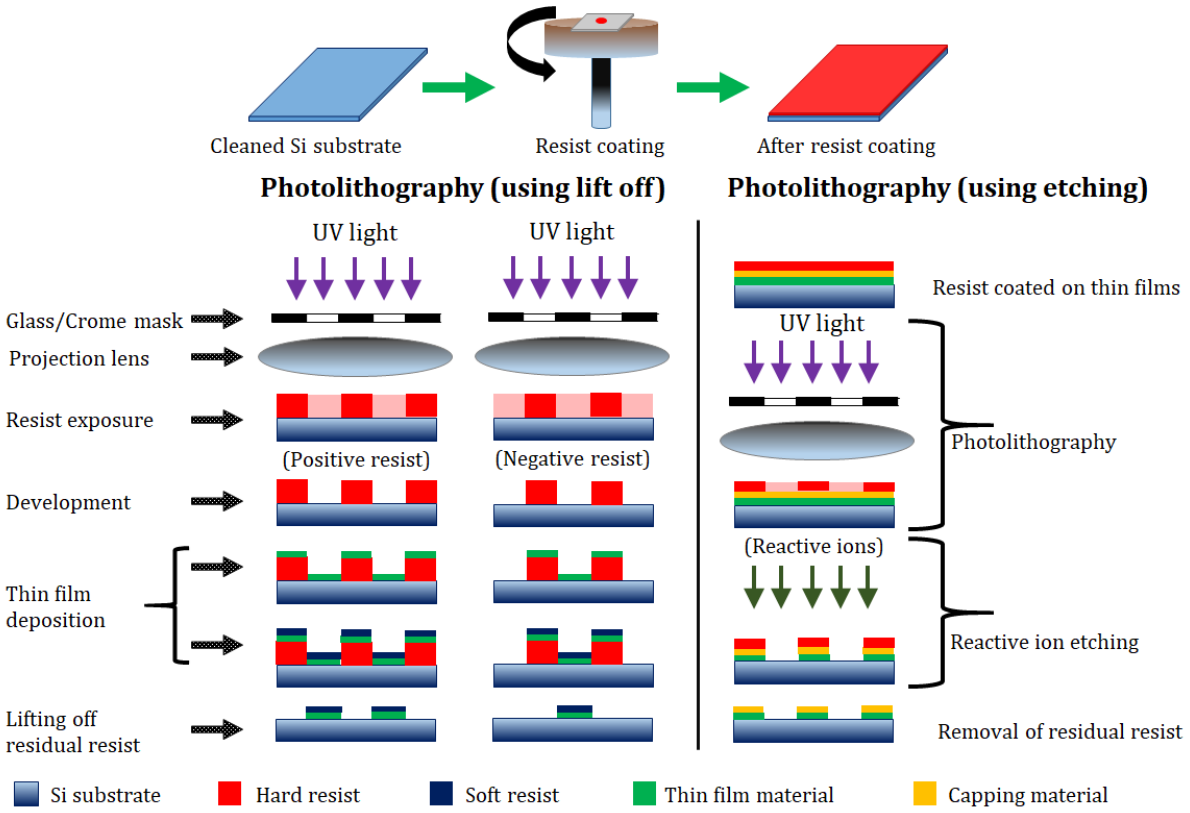

Figure 3.1: Schematic illustration of the photolithography process using lift off and ion etching techniques.

3.2.1. Optical (Photo-) Lithography

This is a popular technique used to fabricate various patterned microstructures. In this technique, a light (illumination) is used to create a geometric pattern using optical mask (also called photo mask) on the substrate, which is coated with a light-sensitive chemical photoresist. This light-sensitive resist enables region-selective removing (either the illuminated or the non-illuminated region) of the resist by immersing it into the developer as depicted in Fig. (3.1). The whole fabrication setup is composed of four fundamental components:

I. Illumination setup with power supply
II. Photo mask with desired pattern
III. Exposure system
IV. Photoresist

The photolithography is faster than the other lithography processes. However, the fabrication of a sub-micrometer (< 1 μm) feature using this system is limited by the diffraction limit of the light. In the following, we will discuss about four major steps to fabricate a sample using photolithography technique.

3.2.1.1. Substrate Cleaning

The self-oxidized Si (001) is selected as a substrate material. A diamond scriber is used to prepare the substrate by cutting several square shaped pieces from a single Si wafer. These substrates are cleaned by using ultrasonication method in acetone (propanone). Subsequently, they are rinsed thoroughly by isopropyl alcohol (IPA). The two above-mentioned processes remove organic and inorganic contaminants from the substrates. All these cleaned substrates are blow-dried by using high pure N_2 gas.

3.2.1.2. Resist Coating

At first, the omnicoat or hexamethyldisilazane (HMDS) [21] primer is coated on the substrate as a release layer by using a spin coater system [22,23]. This uniform thin layer of primer provides better adhesion between the substrate and the photoresist. Thereafter, the primer-coated substrate is baked at a predefined temperature for a fixed time duration. Subsequently, a thin layer of either positive photoresist [24] (AZ-1500) or negative photoresist [25] (SU8) is coated on top of the primer by utilizing same spin coater system. It is baked again to remove solvent from the photoresist that increases the adhesion capability. The thickness of the resist layer can be achieved in the range from ~0.5 - 2 μm by applying the aforementioned procedure. Two types of photoresist is mentioned here, namely, positive and negative. In case of positive photoresist (AZ-1500), the light changes the solubility of photoresist in such a way that the developer will dissolve away only exposed regions. Whereas for negative photoresist (SU8), the developer will dissolve away only unexposed regions.

3.2.1.3. UV light Exposure and Developing

The photomask is placed above the resist-coated substrate. This photomask contains the desired patterns, which is to be fabricated on the substrate. Subsequently, the photoresist is exposed to ultraviolet light with typical intensity range of 70 - 90

mJ/mm^2 through the photomask. A convex lens is placed in between the light source and photomask to illuminate the photomask uniformly. Therefore, the exposed regions of the photoresist become soluble or insoluble into the developer depending upon the type of photoresist (positive or negative) employed. Thereafter, the exposed substrate is immersed into the developer solution AZ/SU8 for ~40 - 80 seconds. Subsequently, it is rinsed for ~1 – 2 min by either de-ionized water suitable for AZ-1500 or IPA suitable for SU8. In the next step, it is blow-dried by applying high pure N_2 gas. The above-mentioned process provides the resist pattern on the substrate. Thereafter, a thin film of desired material (such as permalloy) is deposited on top of the resist pattern by using electron beam evaporation technique.

3.2.1.4. Lift-off and Etch-back Processes

The residual photoresist is removed from the top surface of the substrate through lift-off process by using either acetone (for AZ-1500) or remover PG (for SU8). Subsequently, the processed substrate is cleaned by using ultrasonic agitation in IPA for few minutes. Afterwards, it is blow-dried by applying high pure N_2 gas and the patterned microstructures of desired material is obtained. The aforementioned steps are familiar with the bottom-up approach of lithography technique. Whereas in top-down approach, initially a thin film of desired material is deposited and then the photoresist is patterned on top of this thin film by photolithography technique. In this case, ion milling instrument is employed to conduct region-selective etch back of the thin film by using reactive ions. Lastly, the residual photoresist is removed from the substrate and the desired patterned microstructures is obtained as shown in Fig. (3.1).

All the coplanar waveguides (CPWs) are patterned by using maskless photolithography technique to perform the broadband vector network analyzer (VNA) based ferromagnetic resonance (FMR) measurements. In the following, we will briefly discussed about the maskless UV photolithography technique.

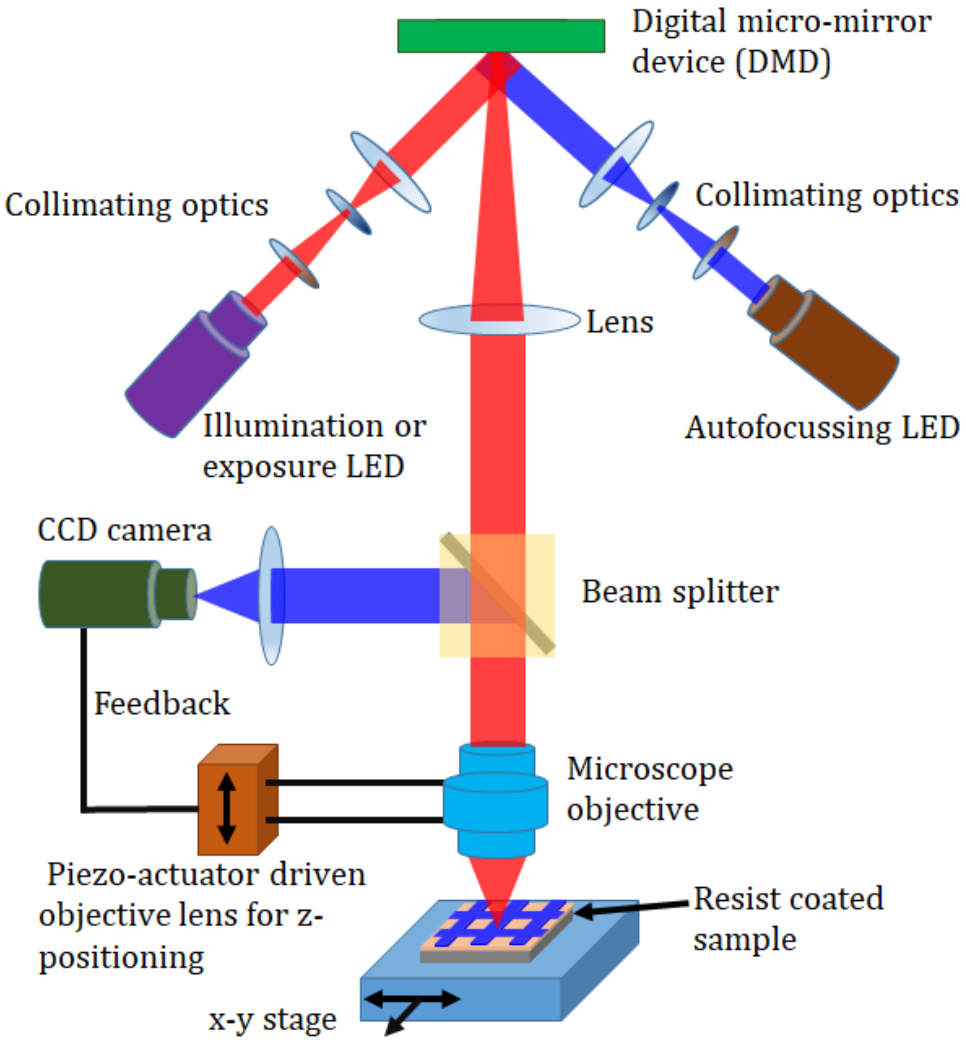

Figure 3.2: Schematic diagram of maskless photolithography system.

3.2.2. Maskless Optical Photolithography

In case of conventional photolithography, the blueprint of the desired geometric pattern is transferred from physical photomask to the light-sensitive resist applying illumination via photomask. A physical photomask is used in that system, which is typically comprised of chrome or glass substrate. Whereas no physical photomask is required for maskless lithography [26,27] technique that makes it cheaper and faster. A schematic diagram of the maskless photolithography system is presented in Fig. (3.2). The current advancement of microelectronic mechanical systems (MEMS) has opened new door toward the light manipulation that enables manufacturing of new lithographic tools like spatial light modulators (SLMs). For instance, liquid crystal (LC) light modulators and digital micromirror devices (DMDs) [28] are useful lithographic tools,

which are used to create intensity pattern of light to illuminate the photoresist. A projection system is required in SLM based lithography system to fabricate the desired structures particularly in submicron regime. Several focusing lenses with large numerical aperture (NA) are employed in the projection system to achieve few hundreds of nm depth of field. In addition, a highly precise projection of illumination is required for the fabrication of high quality microstructures using the SLM based technique. The autofocus based projection system is typically used because manual focussing is less precise than autofocussing. In addition, autofocus is faster process than the manual focus. The autofocus systems can be categorized into active and passive approaches.

3.2.2.1. Active Autofocus System

The autofocus systems achieve the required focus by maintaining the autofocusing (AF) parameter at a desired value by adjusting the distance between the lens and the surface of an object. This is a repetitive process and it continues until the focusing is obtained according the specified AF parameter. The optical triangulation sensing or time-of-flight (TOF) sensing based techniques are typically used to measure distance and displacement of the surface. Reflected waves are studied in optical triangulation sensor to locate position on the surface. Whereas in TOF sensing, the time of light is measured to travel from source to the surface and back. To accomplish this process various type of light sources are used such as light emitting diode (LED), laser, or infrared light. However, the poor contrast of the sample, shallow depths of field and low illumination on the surface are some factors, which can result low-quality autofocusing.

3.2.2.2. Passive Autofocus System

The correct focus of the image is determined by the passive analysis of the captured image. The passive autofocusing can be obtained by contrast measurement or phase detection technique. The contrast-measurement autofocus is obtained by measuring the contrast of the image within a sensor field. When the image is correctly focused, the adjacent pixels of sensor show higher intensity difference. Hence, the adjustment of the imaging system continues until the highest contrast of the image is achieved. However, the contrast-measurement autofocus systems are cost-effective and robust. In case of

phase detection measurement, pairs of images of the surface are created with the help of a beam splitter, set of lenses, mirrors and autofocus sensors. Subsequently, the phase detection is achieved by analysing these two images for identical light intensity pattern. Therefore, the phase-detection autofocus systems demand additional sensors and more complex imaging system that makes it expensive.

We have used two maskless photolithography systems to fabricate our samples, which are D-light-DL1000RS and DL1000SG/RWC from NanoSystem Solutions. Some salient features of these lithography systems are in the following.

1. Long durability illumination source (such as semiconductor laser or/and LED).
2. The exposure system employs DMD and a telecentric optics based illumination system to ensure immediate exposure of predefined pattern on the photoresist. The AutoCAD [29] software is used to create the desired pattern. It makes alignment procedure more precise and simple.
3. The combination of the laser light source and DMD system enables high pattering speed with the help of high-resolution pattern generator including ultrafast mirror switching speed.
4. The dimension of patterned structures can be tuned in the range from few mm to few tens of cm.
5. The real-time autofocus system enables to pattern microstructures even on transparent or warped substrates.
6. Both surface pattern and exposure pattern can be observed simultaneously with the aid of coaxial observation system.
7. The CCD camera enables viewing of the substrate along optical path of exposure, which facilitates to achieve better alignment.

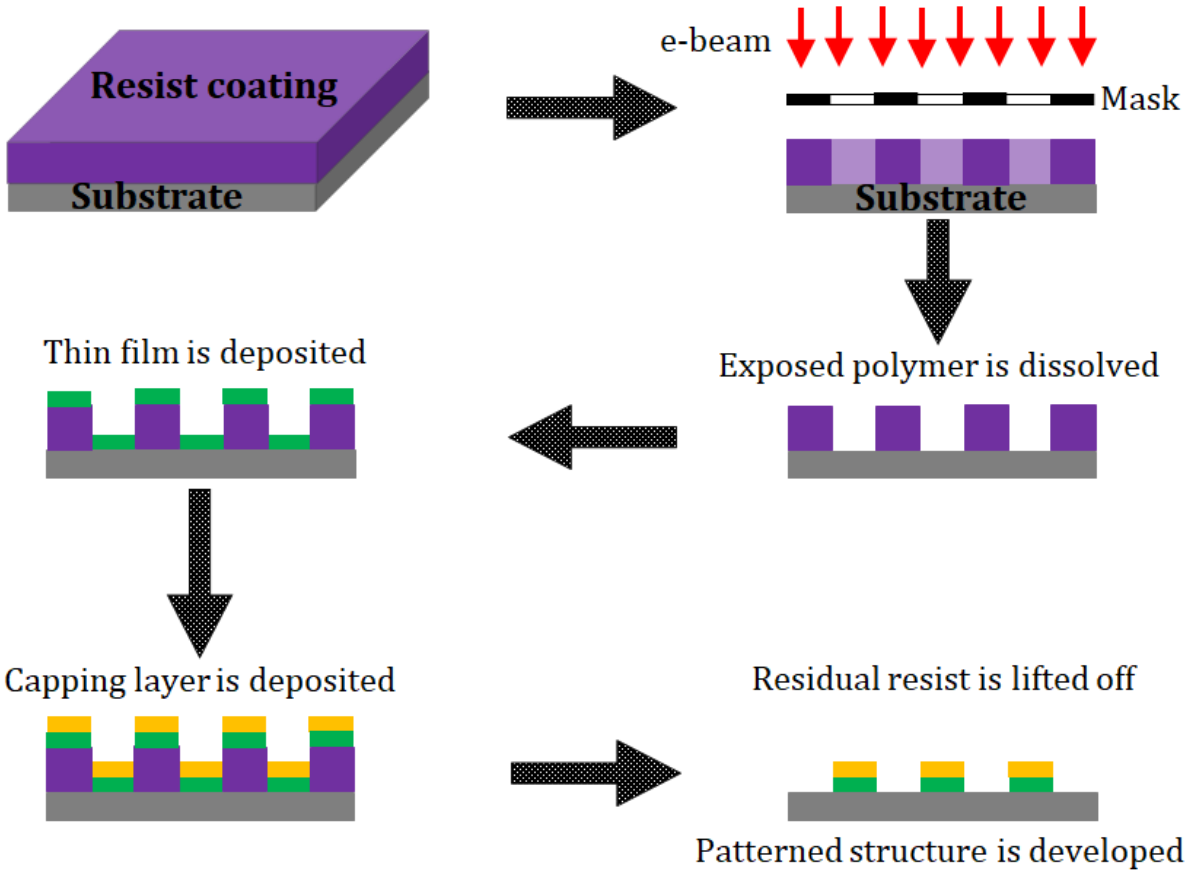

Figure 3.3: Schematic diagram of the electron-beam lithography process.

3.2.3. Electron Beam Lithography (EBL)

The electron-beam lithography (e-beam lithography or EBL) technique is widely used to draw custom shapes onto a substrate by scanning with a focused electron beam. At first, the substrate is coated with an electron-sensitive layer called resist as shown in Fig. (3.3). The solubility of the resist changes when the electron beam is incident on it, which enables region-selective removal (either the exposed or the non-exposed areas) of the resist by immersing the processed resist into a solvent. Very tiny structures are fabricated onto the resist using this technique. Subsequently, it is transferred to the substrate by etching process. This technique offers very high resolution. It can fabricate structures with sub-10 nm resolution, which is much better than the optical lithography in terms of resolution. However, the basic principles are same for both the techniques. In case of EBL, the substrate is cleaned in a similar process as mentioned in 3.2.2.1. Subsequently, the bottom layer of polymethyl methacrylate (PMMA) [30,31] is spin coated on the substrate at some specific conditions to achieve predefined thickness of

this positive resist. Similarly, the upper layer of copolymer resist, namely, methyl methacrylate (MMA) [32] is prepared on top of the PMMA layer at some specific conditions. Hence, the bilayer (PMMA/MMA) resist coated substrate is obtained. This bilayer resist enables more uniform patterns and the lesser missing features as compare to the single layer resist. However, sometimes people use single layer resist PMMA in EBL technique. In our measurement, a scanning electron microscope (Elionix Inc.: ELS-7700H) was employed to produce focused electron beam for writing on the resist. On the other hand, the Auto CAD system is used to design the custom shapes. Subsequently, the system scans the resist according to the design by using the focused electron beam with predefined parameters e.g., resolution, electron beam current, dose, and energy. This processed resist is then immersed in MIBK [33,34] (methyl isobutyl ketone) developer to obtain the desired 3-D patterns onto the substrate. Finally, the substrate is rinsed with IPA to remove the residual developer and the desired sample is obtained. The maskless e-beam lithography technique provides better control in fabrication but it takes longer time to prepare the sample compare to other lithographic techniques.

3.3. Thin Film Deposition Techniques

The e-beam lithography technique was employed to fabricate the ferromagnetic nanostructures on top of the Si substrate, which we have discussed in the previous section. However, to grow a high quality thin film on top of the substrate or coat the nanostructures as protective layer, the sputtering [35,36] and electron beam evaporation [37] techniques were used. In the following, we will briefly discuss about these two thin film deposition techniques.

3.3.1. Sputtering

Sputtering is a kind of high-vacuum based physical vapor deposition (PVD) [38] technique to grow thin films. This technique facilitates to the growth of very high quality single or multilayer thin films in a well-controlled manner. The basic principles of this technique involve producing positively charged ions of a controlled gas (usually chemically inert gas) in a vacuum chamber, which are then accelerated toward source (target) material to dislodge atoms or molecules. Subsequently, this sputtered material

traverses the vacuum chamber as a vapor stream and hits the substrate to form desired thin film.

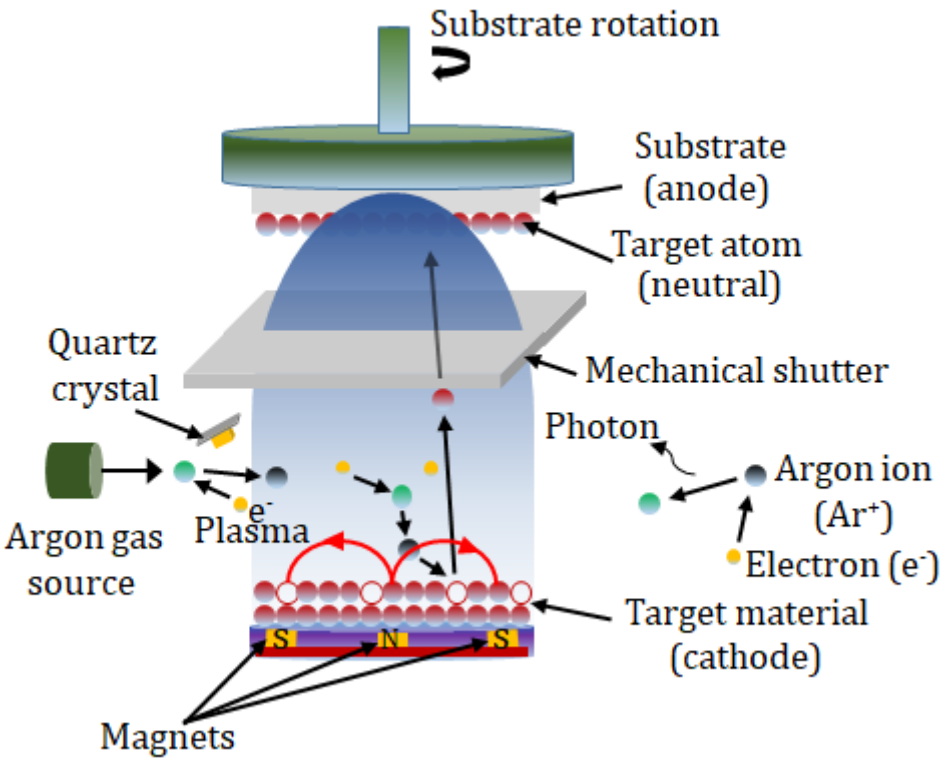

Figure 3.4: Schematic illustration of the sputtering technique.

At first, an inert gas (typically Ar) is inserted into the vacuum chamber as shown in Fig. (3.4). Subsequently, a negative potential is applied to the target (source) material and positive potential is applied to the substrate. Therefore, the target and substrate act like cathode and anode, respectively. The inert gas, which is placed in between the target and the substrate, creates sustainable plasma when a very high voltage is applied. In case of non-conductive material [39] (such as SiO_2, Al_2O_3) deposition, the AC power supply (RF) is used to avoid accumulation of positive ions on the surface of the target. However, a conductive material can be deposited (such as Ni, Co, NiFe) with either of RF or DC power supply. The sputtering process starts when the free electrons from the negatively charged target material accelerate toward the substrate through plasma environment. During this motion, the collision between a free electron and neutral Ar atom produces a positively charged Ar^+ ion with secondary electron. Now, these positively charged Ar^+ ions attract toward negatively charged target material and hence they strike the target surface with very high momentum. These collisions lead to

'sputter off' of neutral atoms from the target surface due to sufficient momentum transfer. Finally, the sputter yield travels and deposit on the substrate to form a thin film. The optimized rotation of the substrate makes uniform deposition.

However, the conventional sputtering technique shows two major drawbacks, which are slow rate of deposition and overheating of the target material due to exhaustive bombardment of electrons. These issues can be removed by employing magnetron sputtering. The additional magnets are placed at the backside of the cathode to trap the free electrons. This technique controls the target's temperature by managing the speed of electrons before bombardment, and hence, it enhances the ionization probability of the Ar atoms. Consequently, the deposition rate is automatically increased.

The traditional DC sputtering technique provides cost effective way to deposit thin films of conductive material (such as gold). Whereas the RF sputtering technique is used for the deposition of dielectric material, as previously mentioned, although it is comparatively cost expensive technique. However, the RF sputtering has several advantages over the traditional DC sputtering. When a non-conductive material is used as target, it can generate polarized charges during sputtering. This polarized charges cause non-uniform deposition, which can be eliminated by employing RF system where sign of the potential changes in alternative cycle. In addition, the RF sputtering system reduces development of racetrack erosion [40] on the target during sputtering. In case of magnetron sputtering, specially for DC magnetron sputtering system, the target is sputtered in circular fashion due to presence of circular magnetic field profile. However, the RF sputtering system provides less confined magnetic field, which leads racetrack erosion profile with much less depth and width. Consequently, the RF sputtering system makes more uniform thin films of non-conductive material and utilizes a target efficiently. However, the RF sputtering system provides slower deposition rate due to the absence of secondary electron generation, and it requires higher power than the DC sputtering system.

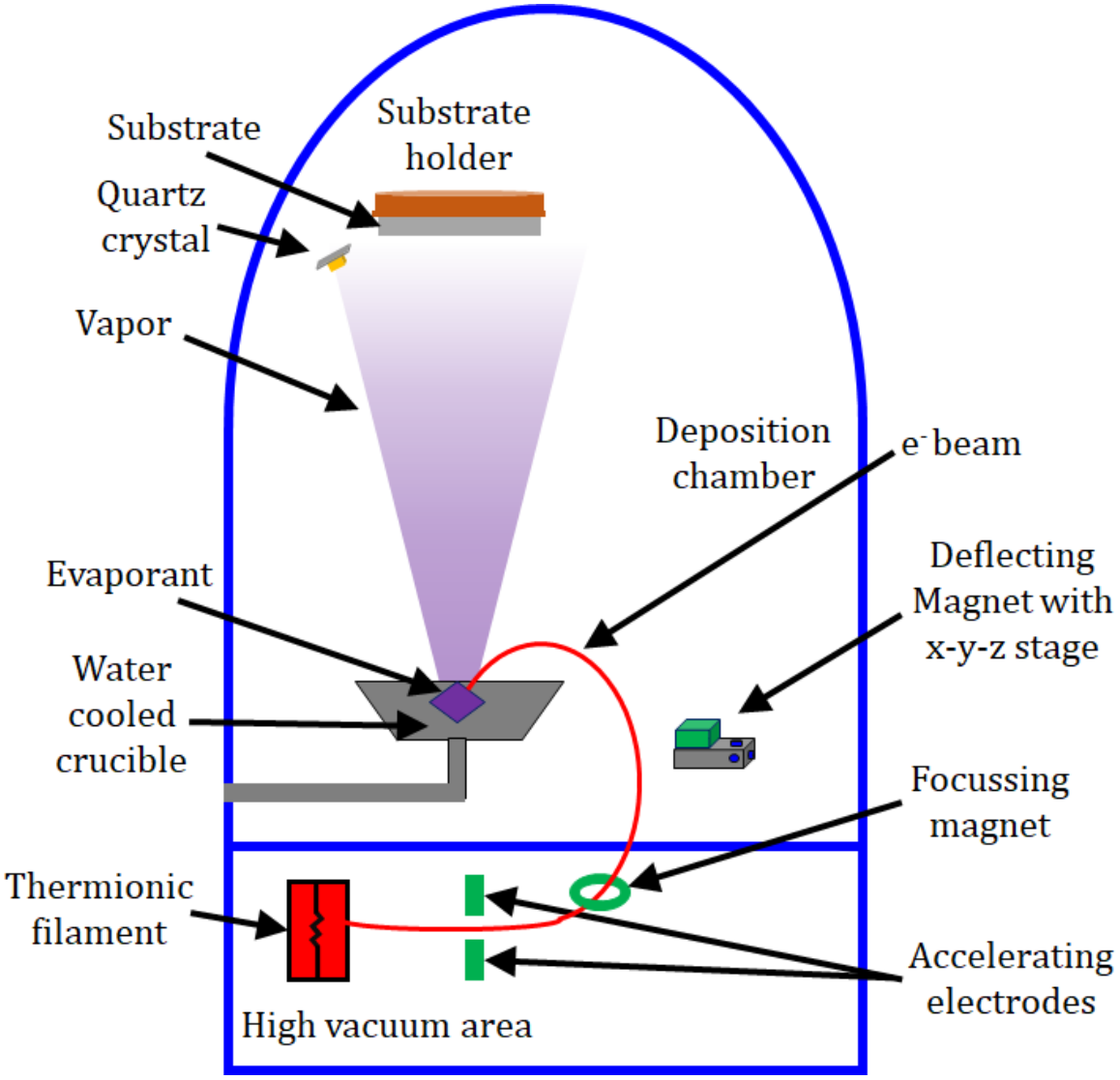

Figure 3.5: Schematic illustration of electron beam evaporation (EBE) system.

3.3.2. Electron Beam Evaporation (EBE)

Electron beam (e-beam) evaporation is also a variant of PVD. This technique facilitates to deposit thin films, which are harder to deposit by thermal evaporation technique (such as Au and Ti). In this technique, the target material is placed in a graphite crucible, which is then kept inside a vacuum chamber. The e-beam is produced from a hot tungsten filament by using thermionic emission process [41]. The deflecting magnet is used to guide the e-beam and subsequently the beam is focused on the target by the focusing magnet. The target material is bombarded with this focused electron beam. As a result, thermal energy is generated, which heats up the surface of the target material very rapidly. Once temperature reaches sufficiently high, the target material is

evaporated (or sublimate) within a vacuum environment. Finally, the vapor is condensed onto the substrate and deposition of the thin film is occurred. The sample holder attached with the substrate is continuously rotated during the deposition with the aid of a rotation motor to ensure uniform deposition. If perpendicular deposition is required the distance between substrate to target material is kept long enough ($\sim 15 - 20$ cm) in a highly evacuated deposition chamber. The focused e-beam enables confined bombardment i.e., only the area occupied by target material, which eliminates any unwanted contamination from the crucible. Additional advantages of this technique include rapid deposition rate, high thermal efficiency, high reliability and high productivity.

3.4. Sample Characterization Techniques

In materials science, sample characterization is an essential step before performing any experiment on that sample. Specially, precise sample characterization is required for the patterned nanostructures fabricated using lithographic techniques. Although a set of delicate equipment are used to perform these lithography techniques, the fabricated nanostructures frequently show deviation from the desired dimensions, physical shape and chemical composition due to various factors including fabrication conditions, complicated fabrication process, mishandling of the samples, etc. The electron beam evaporation or the sputtering technique are used to prepare the high quality magnetic thin films. In this case, sample characterization is required to check chemical composition, thickness, roughness and different magnetic properties. All the techniques used for sample characterization in this thesis are briefly discussed in the following.

3.4.1. Scanning Electron Microscope

The scanning electron microscope (SEM) is a very popular and widely used research equipment for the imaging of samples in the size range from nanometer (nm) to millimeter (mm). It is used to study the surface topography and morphology by scanning with a focused beam of electrons. The interaction between the focused beam of electrons and sample surface produces various signals, which are investigated to get information about the texture and composition of the sample surface. This technique provides far better spatial resolution (~ 1 nm) compare to the conventional optical

microscopy because electron has much shorter de Broglie wavelength. A cathode is used here to generate a stream of electrons either by employing thermionic emission technique or by applying a high electric field. In case of thermionic emission technique, an electron gun with tungsten filament cathode is typically used as the electron source, whereas in second case a field emission cathode is employed to generate electrons. The field emission technique [42] provides higher spatial resolution than the thermionic emission technique because field emission technique generates comparatively narrower electron beam profile. To accelerate these emitted free electrons a gradient of electric field is applied. The energy of these electrons can be tuned in range from few hundreds of eV to few tens of kV.

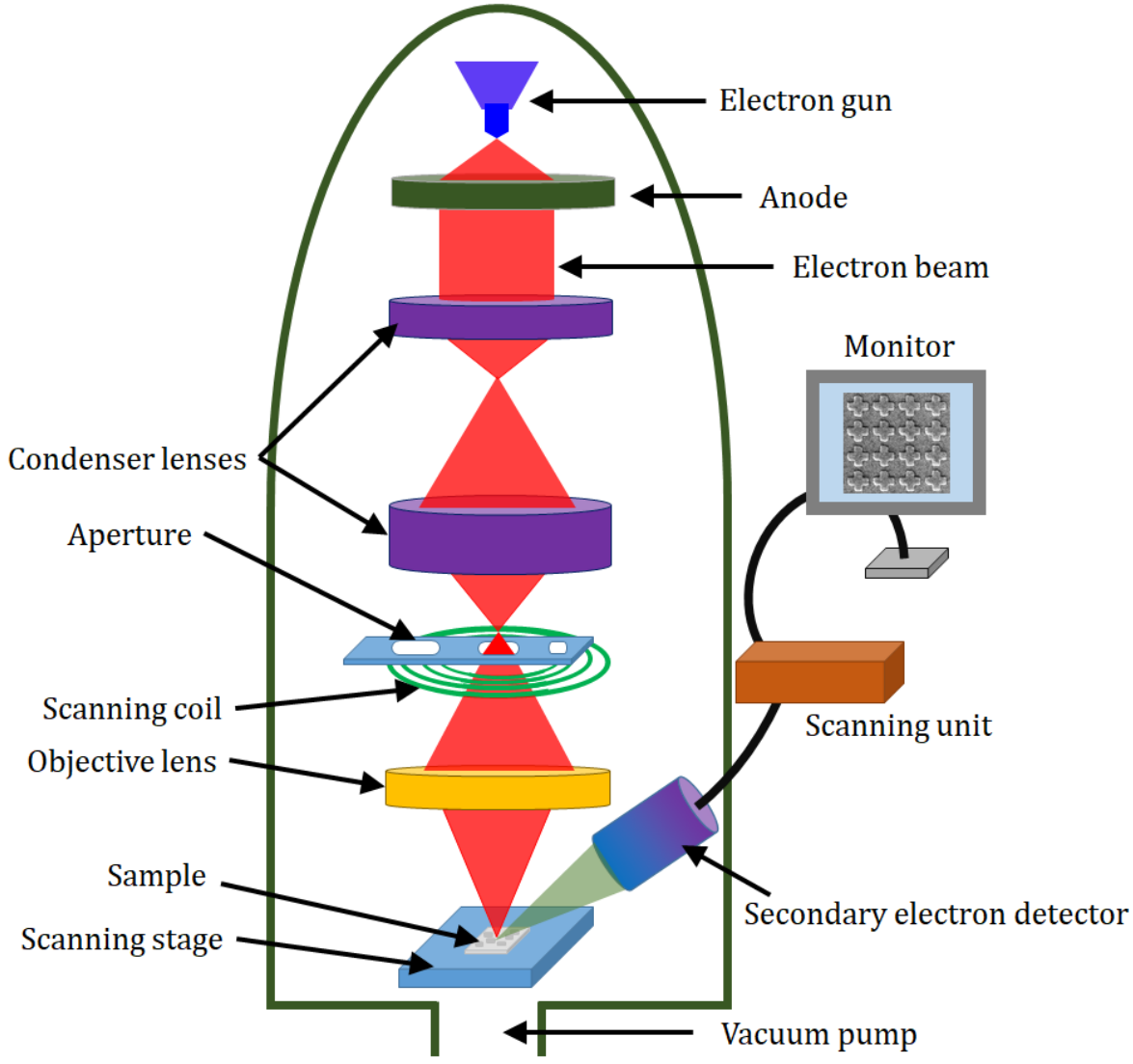

Figure 3.6: Schematic illustration of the scanning electron microscope (SEM).

The accelerated electron beam is focused by placing one or two electromagnetic condenser lenses as shown in Fig. (3.6). Subsequently, the beam is traversed through a pair of deflector plates or scanning coils. As a result, the beam is deflected in the *x* and *y* directions (i.e., in the sample plane), which enables the beam to raster scan the two dimensional rectangular area of the sample surface. On the other hand, when the high-energy electron beam falls on the sample surface, electrons lose their energy due to scattering and absorption phenomena. Consequently, the formation of variety of signals is occurred, which include secondary electrons, backscattered electrons, transmitted electrons, auger electrons, visible light, and photons. Out of them, only secondary electrons are used to produce a SEM micrograph. The secondary electrons are generated because of the inelastic scattering between the incident electrons and atoms of sample. Finally, the two-dimensional SEM micrograph for the selected sample area is formed by plotting the spatial intensity variations of these secondary electrons with respect to that of incident primary electrons.

In addition, the SEM micrograph shows large depth of field because a very narrow electron beam is utilized here. Therefore, SEM can also generate three-dimensional (3-D) image, which is very important to investigate the surface structure of the samples. However, the sample surface should be electrically conductive and electrically grounded to prevent any defects in the micrograph because a nonconductive sample surface accumulates electrostatic charge when it is scanned by a beam of electrons. This issue can be fixed by coating the sample surface with a thin layer of conducting material.

3.4.2. Atomic Force Microscope and Magnetic Force Microscope

Atomic force microscope (AFM) [43] is one type of very high-resolution scanning probe microscope. This equipment is specially designed to image the topography of a specimen with resolution of sub-nanometer length scale. The reaction of the probe due to the forces applied by the sample is used to generate a three-dimensional image of the topography of a sample. Piezoelectric elements are incorporated to balance the interaction force. It enables precise scanning of the sample surface by measuring very small but accurate and precise movements of the sample. The AFM probe typically consists of a sharp tip attached at the free-swinging end of a cantilever. In general, the radius of the AFM tip varies in the range of a few nm to few tens of nm whereas the

dimension of the cantilever is in μm length scale. When the tip approaches the sample surface, the close-range, it experiences deflection due to the effects of various long and short-range forces such as magnetic force, Van der Walls force, electrostatic force, chemical bonding and capillary force. The different features present on the sample surface influence the deflection of the cantilever. A laser beam is employed to detect the deflection of the cantilever by reflecting it from top flat surface of the cantilever. This reflected laser beam is incident on a position-sensitive photo-detector (PSPD) that is used to map the deflection changes. The PSPD consists of four segments and their differences indicate the laser spot position on the detector, which indirectly helps to estimate angular deflection of the cantilever. A 3-D topography of the sample surface is achieved by raster scanning over surface as schematically shown in Fig. (3.7).

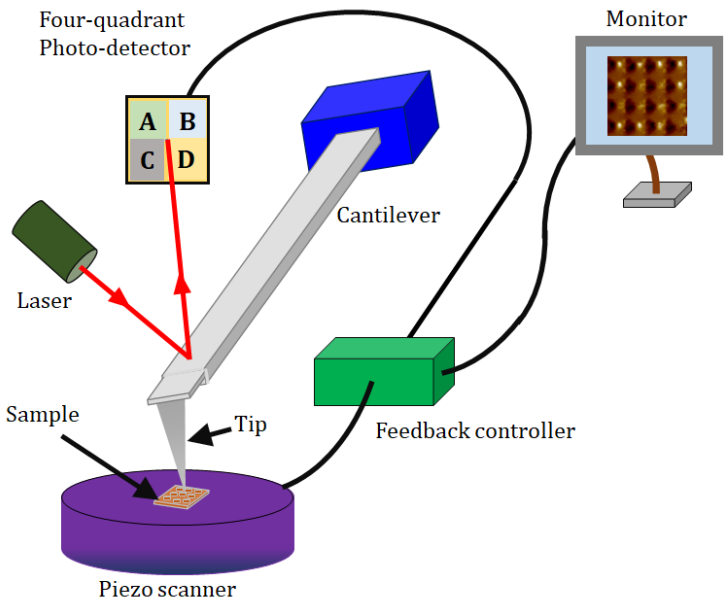

Figure 3.7: Schematic illustration of atomic force microscope (AFM) technique.

Depending on the tip-to-sample distances, the AFM offers three different working modes, namely, the contact mode, the non-contact mode, and the tapping mode. Below, these three working modes are discussed in briefly:

1. Contact Mode: In this mode, the tip raster scans [44] the sample in continuous physical contact with the surface. This technique is typically employed to image hard surfaces where the presence of lateral forces due to the tip can be neglected for modification of the morphological features. This mode provides

very high-resolution images in atomic and molecular length scale for crystalline surfaces. In this case, a constant repulsive force is maintained between the tip and the sample surface, and thus, this mode also called the static mode AFM. To sustain this constant repulsive force, a feedback loop is used to supply feedback voltage to the piezo. These feedback responses are mapped to generate a topographic image of the surface. A cantilever with low stiffness constant is used to avoid substantial damaging of the sample surface by achieving large enough deflection for a feedback response of small interaction force.

2. Non-Contact Mode: To avoid modification of a soft sample surface due to physical contact of the tip, the non-contact AFM mode [45,46] is used. In this mode, the tip remains very close (few tens of Å) to the sample surface and the longer-range attractive interactions such as Van der Walls force is traced to generate the topographic image of a surface. In this case, the deflection of the tip is very low in magnitude due to the variation of much weaker attractive forces compare to the forces act in contact mode. Therefore, the cantilever is given a small vibration externally and the weak force between the surface and tip is measured by recording the modulation in amplitude, frequency or phase of the vibrating cantilever as encounter the sample features during scanning process.
3. Tapping Mode: This mode [47] is commonly applied to conduct AFM measurement in ambient conditions or in liquids. In ambient conditions, a liquid meniscus layer is developed on the surface of most samples. The contact mode AFM is not applicable in this case due to surface damaging issue. In tapping mode, the cantilever is typically excited to oscillate by using a small piezoelectric crystal connected with the cantilever holder. The oscillation frequency of the cantilever is set near to its resonance frequency. Subsequently, the tip is brought close proximity of the sample surface and then the tip starts to tap the surface during oscillation. During scanning, the amplitude of the cantilever's oscillation changes according to the varying forces act on the tip due to surface topography. Finally, the micrograph for surface topography is obtained by monitoring these amplitude changes.

The magnetic force microscope or MFM is a special variant of an AFM. This technique is employed for studying the sample surfaces with magnetic properties. The probe

(scanning tip) is coated with a magnetic material to sense the variation of the magnetic field. A magnetic material with high coercivity (like Co-Cr) is used as the coating material so that the magnetization state of the tip remains unaffected during surface scanning. The MFM tip experiences various forces including magnetic force, atomic force and electrostatic force when it is placed very close to the magnetic surface. However, a good quality AFM image is captured before starting the MFM measurement. Subsequently, the tip height is adjusted to suppress the other forces in comparison of magnetic force. Finally, the tip is placed at the optimum height and scans the surface again to acquire the MFM image with best possible magnetic contrast.

3.4.3. Static Magneto-Optical Kerr Effect (SMOKE) Microscope

The static magneto-optic Kerr effect (SMOKE) microscopy is a useful optical technique [48-50] to study static magnetic properties of diverse ferromagnetic systems including thin films, patterned nanostructures or nanoparticles. The vibrating sample magnetometer (VSM) is used to measure the bulk magnetic properties of a whole sample whereas static MOKE provides localized and surface sensitive detection. This measurement technique functions on the principle of magneto-optic Kerr effect. In our laboratory, static MOKE setup is used to measure Kerr rotation as a function of the applied bias magnetic field i.e., hysteresis loop of a ferromagnetic sample in longitudinal MOKE geometry. The schematic diagram of the static MOKE setup in our laboratory is shown in Fig. (3.8).

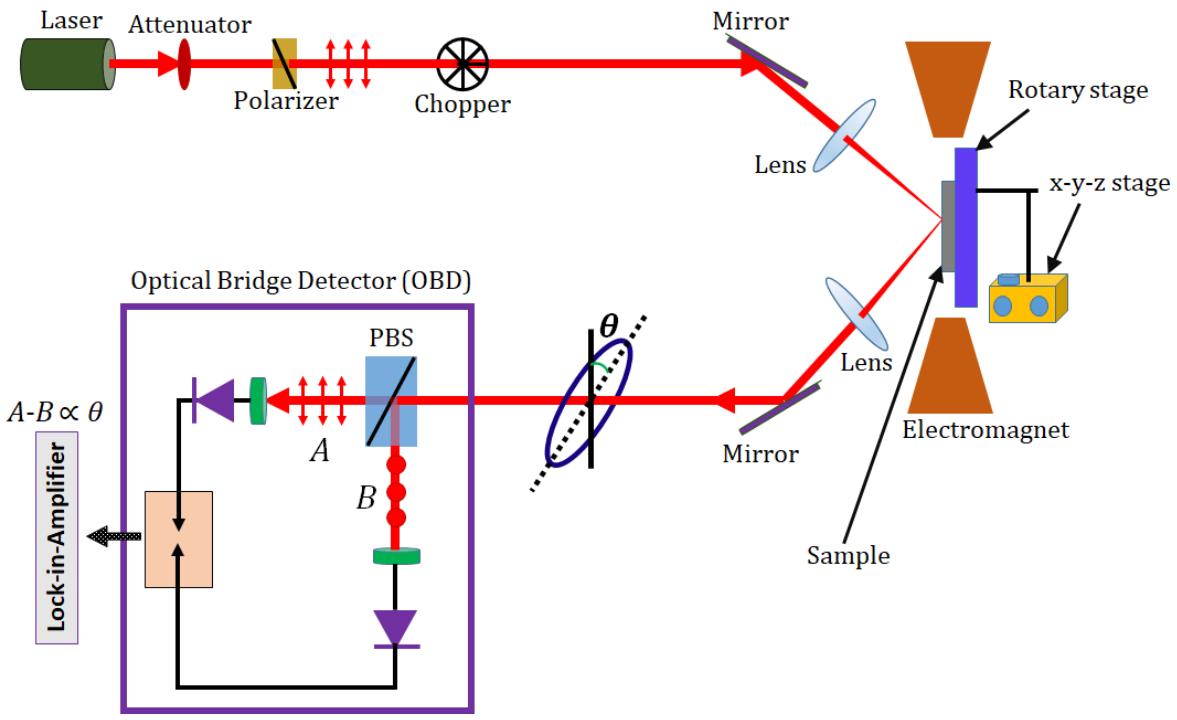

Figure 3.8: Schematic diagram of static magneto-optical Kerr effect (static MOKE) microscope in longitudinal geometry.

A continuous laser output from the helium-neon (He-Ne) laser is employed as a light source. This He-Ne laser produces output beam of wavelength 632.8 nm with power ~15 mW. At first, the laser beam is passed through a variable attenuator for intensity optimization. Subsequently, this beam is traversed through a Glan-Thompson Polarizer. After that, the plane polarized (*s*-polarization) beam is chopped with the help of a mechanical chopper at ~2 kHz frequency. The chopper is controlled by operating a controller unit. The frequency of the chopper is saved as the reference frequency in the lock-in amplifier to execute a phase-sensitive measurement. The beam is then steered by the highly reflecting mirror to a lens and subsequently the laser is incident on the sample. This lens is used to focus the chopped beam onto the sample under test. The external magnetic field is applied with the aid of an electromagnet. The sample is mounted in between two cylindrical pole pieces of the electromagnet using a suitable sample holder that is attached with an *x*-*y*-*z* stage. The strength of the magnetic field is varied by sending variable current through the coils of the electromagnet by using a variable voltage source. The plane of polarization of the plane-polarized beam is rotated after reflecting from the magnetic sample surface because of the magneto-optical Kerr

effect. The reflected beam is then guided through another lens and finally this elliptically polarised laser is entered into the optical bridge detector (OBD).

The polarized beam splitter (PBS) is one of the important components of OBD. This PBS splits incident laser beam into two orthogonally polarized components A and B. Subsequently, two photodiodes are used to convert these split optical signals into electrical signals with the help of electronic circuitry including a lock-in amplifier (Model: SR830 DSP, Stanford Research System). In absence of the bias magnetic field, the 'balanced' condition (i.e., $A = B$) of OBD is achieved by manually tuning the axis of orientation of the PBS. Whereas in presence of the bias magnetic field, the magnetization of the sample is manipulated and hence the plane of polarization of the reflected light is changed due to the magneto-optical Kerr effect. Consequently, the reflected beam is now divided into two unequal components i.e., $A \neq B$ by the PBS. The difference signal $(A-B)$ is directly proportional to the magnetization present in the sample. The hysteresis loop is obtained by measuring the value of $(A-B)$ as a function of strength of the bias magnetic field. The calibration factor is calculated by rotating the axis of the PBS by 1° (or suitable amount) away from the balanced position on both sides and the corresponding dc outputs in the detector are recorded. This calibration factor is used to convert the lock-in voltage or $(A-B)$ into Kerr rotation or magnetization. We can extract various information of the magnetic sample from the obtained hysteresis loop for instance, coercivity, switching field, remanence, anisotropy, saturation magnetization, which are used for the sample characterization.

References

[1] B. Ziaie, A. Baldi, M. Z. Atashbar, in *Springer Handbook of Nanotechnology*, edited by B. Bhushan (Springer Berlin Heidelberg, Berlin, Heidelberg, p. 147, 2004).

[2] A. Sarangan, in *Fundamentals and Applications of Nanophotonics*, edited by J. W. Haus (Woodhead Publishing, p. 149, 2016).

[3] T. R. Groves, in *Nanolithography*, edited by M. Feldman (Woodhead Publishing, p. 80, 2014).

[4] A. A. Tseng, C. Kuan, C. D. Chen, K. J. Ma, IEEE Trans. Adv. Packag. **26**, 141 (2003).

[5] R. C. Jaeger, *Introduction to Microelectronic Fabrication*, (Prentice Hall, 2002).

[6] D. McMullan, Scanning **17**, 175 (1995).

[7] K. C. A. Smith, C. W. Oatley, Br. J. Appl. Phys. **6**, 391 (1955).

[8] G. Binnig, C. F. Quate, C. Gerber, Phys. Rev. Lett. **56**, 930 (1986).

[9] H. Hopster, H. P. Oepen, *Magnetic Microscopy of Nanostructures*, (Springer, 2005).

[10] L. Abelmann et *al*., J. Magn. Magn. Mater. **190**, 135 (1998).

[11] U. Hartmann, Annu. Rev. Mater. Sci. **29**, 53 (1999).

[12] Y. Martin, H. K. Wickramasinghe, Appl. Phys. Lett. **50**, 1455 (1987).

[13] J. Kerr, Philos. Mag. **3**, 321 (1877).

[14] P. Weinberger, Philos. Mag. Lett. **88**, 897 (2008).

[15] Z. Q. Qiu, S. D. Bader, Rev. Sci. Instrum. **71**, 1243 (2000).

[16] P. Weaver, *The Technique of Lithography*, (Batsford, 1964).

[17] C. G. Willson, R. R. Dammel, A. Reiser, *Photoresist materials: a historical perspective*, (SPIE, 1997), Vol. **3049**, P. AL Microlithography' 97.

[18] F. Cerrina, G. Grenci, in *Reference Module in Materials Science and Materials Engineering*, (Elsevier, 2016).

[19] N. W. Parker, A. D. Brodie, J. H. McCoy, *High-throughput NGL electron- beam direct write lithography system*, (SPIE, 2000), Vol. **3997**, P. AL Microlithography 2000.

[20] H. Morimoto, Y. Sasaki, K. Saitoh, Y. Watakabe, T. Kato, Microelectron. Eng. **4**, 163 (1986).

[21] A. Kawai, J. Kawakami, J. Photopolym. Sci. Technol. **20**, 815 (2007).

[22] S. K. Wilson, R. Hunt, B. R. Duffy, J. Fluid Mech. **413**, 65 (2000).

[23] L. E. Scriven, Mater. Res. Soc. Symp. Proc. **121**, 717717 (2011).

[24] A. Fauthan, M. N. Hamidon, B. Y. Majlis, Ieee, *Lithography Method for Selective Area of CNTs Growth*, (Ieee, New York, 2013), 2013 Ieee Regional Symposium on Micro and Nanoelectronics.

[25] S. M. P. Kalaiselvi, T. L. Tan, A. Talebitaher, P. Lee, S. P. Heussler, M. B. H. Breese, R. S. Rawat, Phys. Lett. A **379**, 560, (2015).

[26] M. J. Yin, Q. Zhao, J. S. Wu, K. Seefeldt, J. Y. Yuan, Acs Nano **12**, 12551 (2018).

[27] K. E. Paul, T. L. Breen, J. Aizenberg, G. M. Whitesides, Appl. Phys. Lett. **73**, 2893 (1998).

[28] M. Rahlves, C. Kelb, M. Rezem, S. Schlangen, K. Boroz, D. Gödeke, M. Ihme, B. Roth, *Digital mirror devices and liquid crystal displays in maskless lithography for fabrication of polymer-based holographic structures*, (SPIE, Vol. **14**, 4, 2015).

[29] M. K. Lubow, Adv. Mater. Process. **132**, 18 (1987).

[30] V. A. Kudryashov, P. D. Prewett, A. G. Michette, Microelectron. Eng. **53**, 333 (2000).

[31] A. Uhl, J. Bendig, U. Jagdhold, J. Bauer, in *Microlithography 1999: Advances in Resist Technology and Processing Xvi, Pts 1 and 2*, edited by W. Conley (Spie-Int Soc Optical Engineering, Bellingham, p. 1381, 1999).

[32] P. Mansky, Y. Liu, E. Huang, T. P. Russell, C. Hawker, Science **275**, 1458 (1997).

[33] S. Yasin, D. G. Hasko, H. Ahmed, Microelectron. Eng. 61-2 (2002) 745 Pii s0167-9317(02)00468-9.

[34] P. R. Deshmukh, W. S. Khokle, Microelectron. Reliab. **31**, 1091 (1991).

[35] R. Behrisch, Sputtering by particle bombardment (Springer- Verlag, Vol. **1**, 1981).

[36] T. Schenkel, M. A. Briere, H. Schmidt-Böcking, K. Bethge, D. H. Schneider, Phys. Rev. Lett. **78**, 2481 (1997).

[37] K. Wasa, M. Kitabatake, H. Adachi, *in Thin Film Materials Technology*, edited by K. Wasa, M. Kitabatake, and H. Adachi (William Andrew Publishing, Norwich, NY, p. 191, 2004).

[38] J. E. Mahan, *Physical Vapor Deposition of Thin Films*, (Wiley, 2000).

[39] K. Wasa, M. Kitabatake, H. Adachi, *in Thin Film Materials Technology*, edited by K. Wasa, M. Kitabatake, and H. Adachi (William Andrew Publishing, Norwich, NY, p. 465, 2004).

[40] Y. Ohtsu, S. Tsuruta, T. Tabaru, M. Akiyama, Surf. Coat. Technol. **307**, 1134 (2016).

[41] K. Masood, M. Iqbal, M. Zakaullah, Nucl. Instrum. Methods Phys. Res. A **584**, 9 (2008).

[42] S. Fan, M. G. Chapline, N. R. Franklin, T. W. Tombler, A. M. Cassell, H. Dai, Science **283**, 512 (1999).

[43] E. Meyer, Prog. Surf. Sci. **41**, 3 (1992).

[44] C. Le Grimellec, E. Lesniewska, M.-C. Giocondi, E. Finot, V. Vié, J.-P. Goudonnet, Biophys. J. **75**, 695 (1998).

[45] T. Uchihashi, Y. Sugawara, T. Tsukamoto, M. Ohta, S. Morita, M. Suzuki, Phys. Rev. B **56**, 9834 (1997).

[46] Y. Sugawara, M. Ohta, H. Ueyama, S. Morita, Science **270**, 1646 (1995).

[47] J. P. Cleveland, B. Anczykowski, A. E. Schmid, V. B. Elings, Appl. Phys. Lett. **72**, 2613 (1998).

[48] R. Lavrijsen, J.-H. Lee, A. Fernández-Pacheco, D. C. M. C. Petit, R. Mansell, R. P. Cowburn, Nature **493**, 647 (2013).

[49] R. P. Cowburn, A. Ercole, S. J. Gray, J. A. C. Bland, J. Appl. Phys. **81**, 6879 (1997).

[50] W. Zhou, T. Seki, K. Takanashi, J. Appl. Phys. **122**, 5093902 (2017).

Chapter 4

4. Experimental Measurement Techniques to Study Magnetization Dynamics

4.1. Introduction

Several experimental measurement techniques have been developed to study the magnetization dynamics at ultrashort time scales and lengths over last few decades. In this thesis, two very involved measurement techniques have been used, namely, vector network analyzer based FMR (VNA-FMR) [1] and time-resolved magneto-optic Kerr effect (TR-MOKE) microscopy [2,3]. The VNA-FMR operates in frequency domain and provides very high resolution and sensitivity over a broad frequency regime. Whereas the TR-MOKE microscope offers ultra-high temporal resolution (~ sub-100 fs) as well as spatial resolution of sub-μm regime. Freeman *et al*. first performed the time-resolved MOKE measurement in 1991 [4]. The TR-MOKE microscope works in time domain and its temporal resolution depends on the pulse width of the laser. These two above-mentioned methods have been used to acquire experimental data for the study of magnetization dynamics in FM thin films and nanostructures. In the following, we will briefly describe about the principles, components and advantages of the above-mentioned measurement techniques.

4.2. Broadband Ferromagnetic Resonance (FMR) Spectrometer

The magnetic system is excited by an RF current launched from the VNA. The dynamics of the magnetization can be studied as a function of the bias magnetic field and power of the microwave input signal. A coplanar waveguide (CPW) is employed to measure the real part of forward reflection coefficient (S_{11}) in reflection geometry. This technique provides a straightforward measurement of FMR over a broad frequency window. The complete broadband VNA-FMR setup is shown in Fig. (4.1).

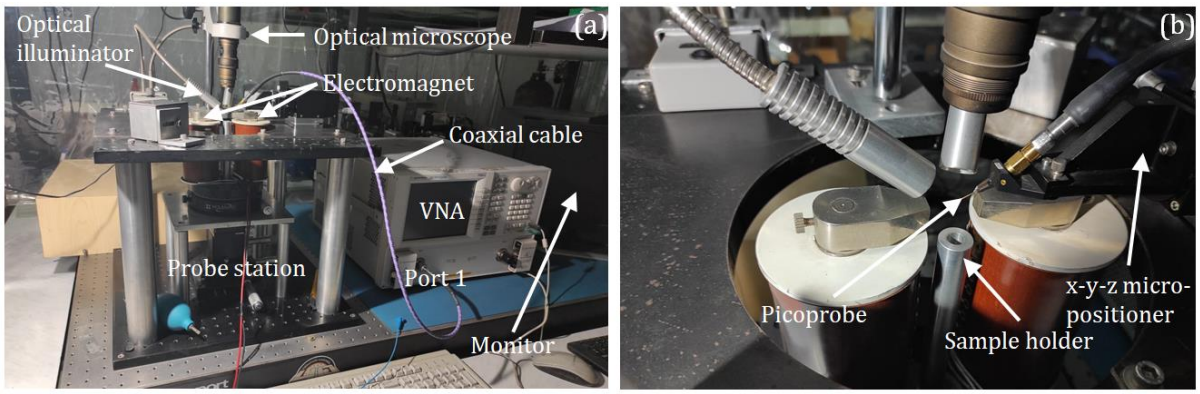

Figure 4.1: A photograph of the ferromagnetic resonance spectrometer equipped with broadband vector network analyzer and probe station, installed in the laboratory of Prof. Anjan Barman at the S. N. Bose National Centre for Basic Sciences, Kolkata, India. (b) A pictorial illustration of the sample holder and the GHz-frequency picoprobe mounted on a custom-built probe station.

4.2.1. Experimental Setup

The broadband FMR experiments in FM samples are performed using a VNA (Agilent, PNA-L N5230C) along with a home-built probe station as schematically illustrated in Fig. (4.1). This high-frequency probe station has an electromagnet to apply in-plane bias magnetic field to the samples. The electromagnet is powered by a high voltage bipolar power supply (KEPCO, BOP 36-6D). It can deliver DC current up to 6A and DC voltage ranges from 0 to $\pm$ 36V. The probe station is equipped in such a way that the azimuthal angle of the in-plane bias magnetic field can rotate by up to 360 degrees. Two pole-pieces of the electromagnet are mounted on a rotation base having 1-degree angular resolution. A CCD camera-based microscope (Shodensha Inc.) supported with illumination setup is used as a sample viewing system. A multi-axis micro positioner (NPS, 800MRF-L) is used to make contact between microscale picoprobes and the CPW. The stimulus input signal is swept in a wide frequency range (10 MHz to 50 GHz) in the form of a microwave current (I_{rf}) and fed into the CPW microstructure using a nonmagnetic ground-signal-ground (G-S-G) type probe (GGB industries, Bandwidth of 40 GHz, Model No. 40A-GSG-150-EDP) via a RF coaxial cable (Model No. N1501A-203). This microwave current generates a microwave magnetic field (h_{rf}) perpendicular to the I_{rf}. The microwave power (P) of the input signal can be varied by the VNA in the range of -15 dBm to $+20$ dBm. As discussed in section (2.7.2.2.A.) of chapter 2, all the

experiments using VNA have been performed in reflection measurement geometry. In reflection measurement, the short-circuited CPW is used to measure forward reflection coefficient (S_{11}) using a single picoprobe. The microwave power is absorbed from both incident and reflected signals by the sample because of ferromagnetic resonance. Consequently, it generates the characteristic FMR spectrum of that ferromagnetic sample in reflection measurement. The characteristic FMR spectrum is subtracted from a reference signal measured at a highest bias magnetic field to minimize the nonlinear backgrounds present in the spectrum. However, sometimes nonmagnetic humps still appear in the FMR spectrum that do not show any bias magnetic field dependence. Finally, the real part of S_{11} parameters as a function of microwave power, bias field strength or orientation are extracted to study the FMR resonance spectra of ferromagnetic samples.

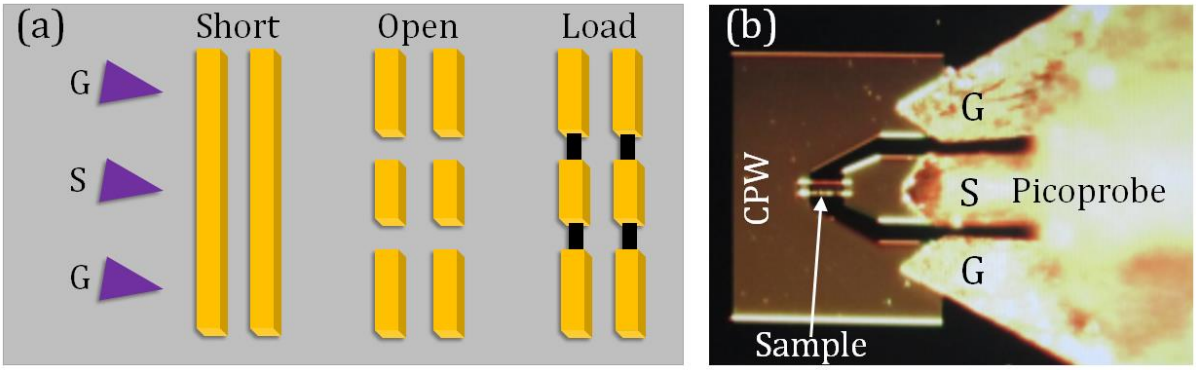

Figure 4.2: (a) Schematic diagram of the short-open-load (SOL) kit used to calibrate the vector network analyzer (VNA). (b) Optical microscope image of the CPW along with the ground-signal-ground type picoprobe.

4.2.2. Calibration Procedure

The fundamental reason behind the need of a systematic calibration of VNA is to extract best possible results from a sample. The calibration of a setup minimizes all the unwanted and erroneous signals originating from various internal and external sources [5,6]. Whenever an experimental system produces any doubtful signal from a standard sample, calibration is required to reproduce acceptable signal in accordance with the standard one. The accuracy of this calibration process is solely limited by the standard kit and expert hand of calibration. In the VNA-FMR setup, the CS-5 calibration substrate from GGB industries has been employed as a standard kit. The typical components

require to calibrate a microwave measurement system include open, short, load and through. The successive contacts are made between the probe and a set of gold pads patterned on the calibration substrate to perform short-open-load (SOL) method [7-11] of calibration in reflection measurements. The electrical 'short' is executed by making contact between the picoprobe and shorting bar or offset 'short'. The electrical characteristics in short condition include a very small inductance that depends on the pitch (tip spacing) of the probe. This inductance is thought of as an equivalent electrical path in series connection with the perfect 'short'. The 'open' circuit helps to avoid the pick-up of fringing electric fields at the tip of the probe. The 'load' pad comprises of two 100 Ω thin-film resistors in parallel to make the well-defined 50 Ω termination to execute maximum transfer of power. Particularly in high frequency regime, the 'load' can manifest as either a low shunt capacitance or a low series inductance depending upon the pitch value of the probe. Since the resistor pads and open pads are almost identical thus, load capacitance value is nearly same with the open capacitance. Similarly, the current path length in 'load' condition and 'short' condition are almost identical. As we know that, the inductance causes current to lag behind the voltage whereas current leads the voltage due to the effect of capacitance. These two opposing consequences tend to compensate each other, which makes 'load' almost purely resistive for some intermediary probe pitch.

4.2.3. Requirement of Calibration

VNA must be calibrated before performing any *S*-parameter measurement. The systematic calibration ensures that the VNA can provide the best possible accuracy during measurement. This calibration remains valid until the effects due to systematic errors are insignificant. The systematic errors in a VNA-FMR setup include directivity, load mismatching, reflection loss, crosstalk etc. Even any change of environmental parameters during the measurement time may lead to recalibration due to the significant degradation of accuracy. For instance, only 1°C change in surrounding temperature may force for recalibration. In addition, the other factors like cleanliness, calibration standards, quality of test port connectors, human errors highly influence on the measurement repeatability and accuracy. In the following, we will briefly discuss some of the important factors related to systematic error.

4.2.4. Crosstalk

In a multi-channel network system, the microwave crosstalk means coupling of high-frequency unwanted signals from one channel of the system to another. The crosstalk [12-15] can cause significant degradation of the calibration. For instance, if one probe of a VNA is calibrated employing an 'open' pad whereas another one is making contact with a nearby 'open' pad, an unwanted conducting of signals from one port to another is occurred. Consequently, this will differ the calibration of the first probe. In addition, the dissimilar probe spacing and closely spaced transmission lines increase the noise level due to the enhancement of crosstalk. Fortunately, the crosstalk effect is negligible for all the microstructures employed in the standard calibration substrate (CS-5). However, if the sample to be measured need placement in between the probes and the required area dimension is less than the pitch value (150 μm) of the probe then the crosstalk effect can limit the measurement accuracy.

4.2.5. Spurious Modes

Spurious modes are unintended modes that can originate from harmonics, intermodulation, electromagnetic interference, or frequency conversion in an electrical system. The structures (pads) used during calibration can absorb signals from the adjacent one. For example, any one of ('load' or 'open' or 'short') the calibration pads can absorb significant fraction of the signals from the adjacent pad to make an anomaly in the output spectrum [16]. The through-lines are typically patterned in the calibration substrate for the propagation of balanced coplanar mode. Where both the magnetic and electric fields are confined in a gap formed between the ground planes and the central line. If the substrate is attached with a metallic holder, the metallic holder can function as a ground plane that leads to a small fraction of signal dissipation. It can also produce anomaly in the calibration. This situation can be avoided easily by using electrically insulated holder as a replacement of metallic holder. Sometimes spurious modes are produced due to the nonlinear response of the DUT at very high frequencies.

4.2.6. Directivity

Directivity describes the ability of a coupler to separate out signals flowing in the reverse direction within the same coupler. The directivity of a coupler significantly

affects the accuracy of the measurements. Larger directivity suggests higher performance of the VNA. In essence, the directivity measures the amount of measurement error introduced by a reverse signal in a coupler. Ideally, there should not be any high frequency reverse signal at the coupled port. However, in reality, some amount of power dissipation of the reverse signal occurs at the coupled port because of finite isolation between each port. The isolation of a coupling device can be expressed as:

$$\text{Isolation (dB)} = -\log_{10}\left(\frac{\text{reverse coupled power}}{\text{reverse power}}\right)$$

Isolation is one of the important parameters of a coupling device. On the other hand, the directivity is defined as:

$$\text{Directivity (dB)} = \text{Isolation (dB)} - \text{Coupling factor (dB)} - \text{Insertion loss (dB)}$$

4.2.7. Device Measurement

The mismatch of the probing environments, i.e. between the device (sample) and standard calibration substrate during measurement is another source of errors. The base material for the device and the standard calibration substrate are typically different and more importantly the dissimilarities of line width and spacing between them lead to a difference in the output signal. A technique named “de-embedding” can be used to remove the above-mentioned difference. The de-embedding is a post-measurement procedure to extract information about the device under test after minimization of the errors. The basic idea is making exactly similar structures on top of the calibration substrate as in device to be tested (DTBT). For instance, if DTBT comprises of probe pads with connecting stripes then identical probe pads including connecting stripes but without device can be measured for testing with a probe that has been calibrated with the standard calibration substrate. These obtained test outputs can be used for the measurement of DTBT.

4.3. All-Optical Time Resolved Magneto-Optical Kerr Effect (TR-MOKE) Microscope

The development of an all-optical TR-MOKE microscopy made the TR-MOKE measurement [17] more advanced. All optical measurement process makes it a special

technique, where a femtosecond laser is used for the excitation of the spin system, while a part of the same laser is used to probe the subsequent magnetization dynamics. Additional advantages of a TR-MOKE microscope system include non-invasive nature, simple sample fabrication process and very high spatial-temporal resolution that enable to study the magnetization dynamics of a single or array of nanomagnets.

4.3.1. Primary Components of the Setup

Two photographs of the TR-MOKE microscope setup are shown in Fig. (4.3). The primary components [18-22] of the setup are labelled in the figure.

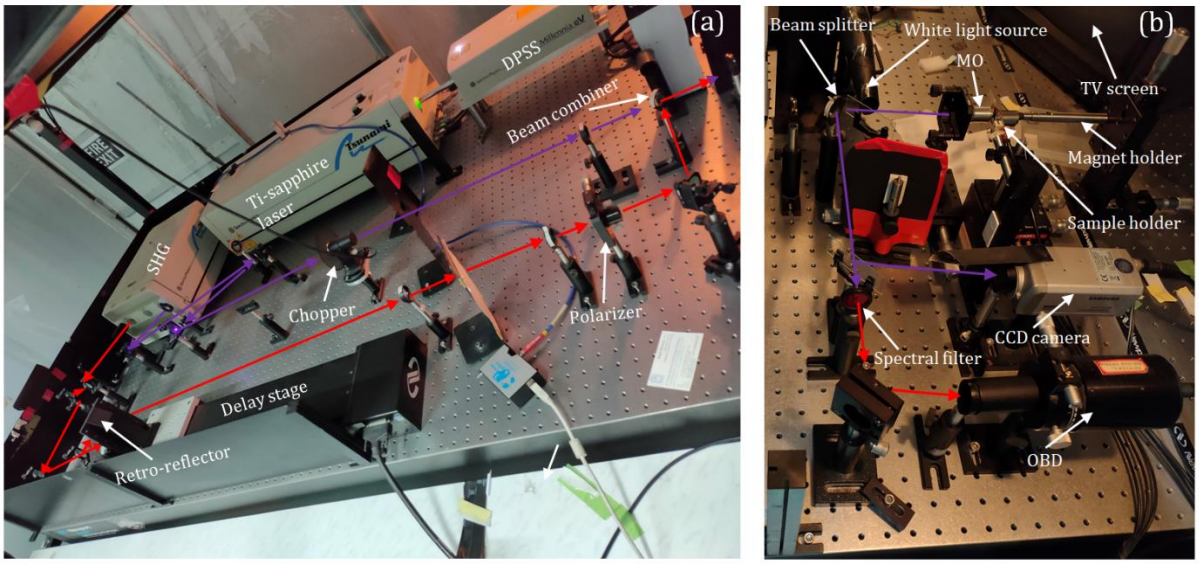

Figure 4.3: (a) Photograph of the time-resolved magneto-optical Kerr effect microscope developed in the laboratory of Prof. Anjan Barman at the S. N. Bose National Centre for Basic Sciences, Kolkata, India. (b) A magnified view of the detection procedure. The important components are labelled in the photographs.

4.3.2. Description of Laser

The TR-MOKE microscope setup has three different lasers. A diode pumped solid-state laser (DPSS) having wavelength $\lambda = 532$ nm is employed to pump the mode-locked Ti:sapphire laser or the 'Tsunami'. The wavelength of the output beam from Tsunami can be tuned in the range of 700 - 1080 nm. Tsunami generates laser output with pulse width of ~70 fs at a repetition rate of 80 MHz by applying regenerative acousto-optic mode-locking mechanism. However, the wavelength of the Tsunami is maintained at

~800 nm in our system and this fundamental beam is separated into two parts. The main beam is used as an input of a second harmonic generator to generate the second harmonic of wavelength 400 nm. This second harmonic is used as the pump beam and the time-delayed fundamental beam is used as the probe beam to investigate magnetization dynamics. In the following, we will discuss about these lasers.

Diode Lasers

A single piece of monolithic semiconductor is used to manufacture the diode laser bars, which consists of total twenty high power diode lasers. The output beams of the diode laser bars are collimated using a cylindrical microlens with high numerical aperture (N.A.) and subsequently this highly asymmetric beam is coupled into a fiber bundle applying the efficient FCbar technology. Finally, this output laser beam is used to pump the DPSS laser or Millennia.

Diode Pumped Solid State (DPSS) Laser or Millennia

- Working principle

The Neodymium Yttrium Vanadate Crystal (Nd:YVO_4) is used in the Millennia as a gain medium. The emission spectrum of the diode laser overlaps with the absorption band of Nd^{3+} ion. On the other hand, the diode laser output is focused on a specific volume in the active medium of Millennia in such a way that it can best match with radius of the desired TEM_{00} mode as shown in Fig. (4.4). Therefore, it makes very efficient pumping of the Millennia using the output of the diode laser. The Nd^{3+} ion offers a four-level laser system where a photon of wavelength 1064 nm [20] is emitted due to the most probable lasing transition from $4F_{3/2}$ state to the $4I_{1/2}$ state. However, other lasing transitions are also occurred from the same upper state to different lower states but all have relatively lower gain and higher threshold value than the previously mentioned 1064 nm transition. These factors including the wavelength-selective mechanism allow lasing at 1064 nm. Continuously a fraction of the laser output is sent as a feedback to the pump laser driver to supply a constant output. A shutter (Fig. (4.4)) is employed to mechanically block the beam for safety.

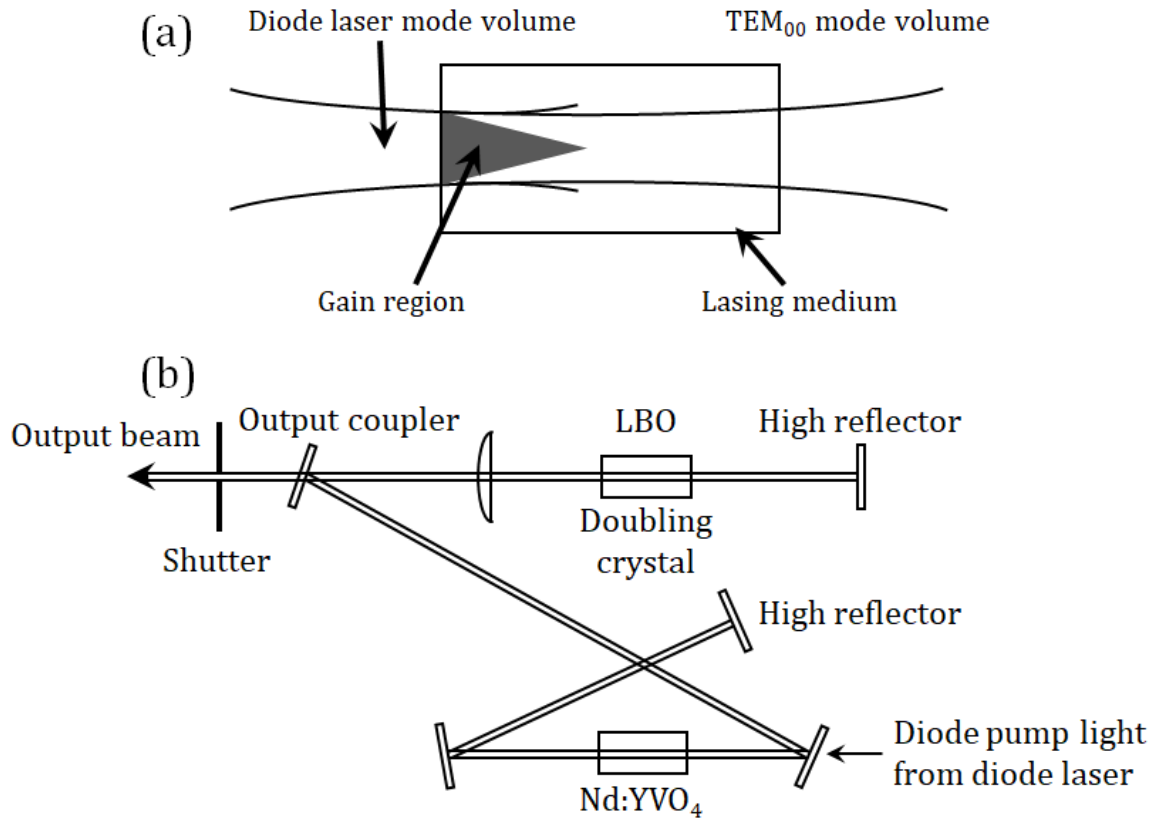

Figure 4.4: (a) Schematic illustration of mode matching between the diode laser mode volume and the TEM_{00} mode volume of Millenia. (b) Schematic description of the Millennia laser head. The figures are reproduced from Ref. [20].

- Frequency doubling

A nonlinear crystal of lithium triborate (LiB_3O_5) or LBO is used to generate the second harmonic of 1064 nm, i.e. 532 nm through frequency doubling method. Since efficiency of the LBO crystal can be tuned by its temperature, a temperature regulation oven is used to maintain the phase-matching temperature to achieve maximum conversion efficiency. The LBO crystal generates collinear fundamental and second harmonic beams, which makes alignment process simple. In addition, the LBO crystal offers relatively lower nonlinear coefficient value, and hence, it is suitable as the frequency-doubling medium.

The power of the generated second harmonic is given by [20]:

$$P_{2\omega} \propto \frac{d_{eff}^2 P_\omega^2 l^2 [\phi]}{A} \tag{4.1}$$

Here d_{eff} is the effective nonlinear coefficient, P_{ω} is the input power of the fundamental beam, l is the effective length of LBO crystal, [ϕ] is the phase-matching factor, and A is the cross-sectional area of the laser beam in the crystal.

Mode Locked Ti:sapphire Laser or Tsunami

- Working principle

Ti:sapphire is a crystalline lasing material prepared by the mixing of Ti_2O_3 with melt Al_2O_3. The Ti^{3+} (Titanium ion) makes Ti:sapphire a lasing medium. The absorption spectra of this medium includes a wide range of wavelengths from ~400 to ~600 nm. On the other hand, the fluorescence band also covers a broad transition wavelengths range from ~600 to ~1000 nm. Therefore, the overlapping of these two bands decides the possible lasing action only at wavelengths greater than 670 nm as shown in Fig. (4.5).

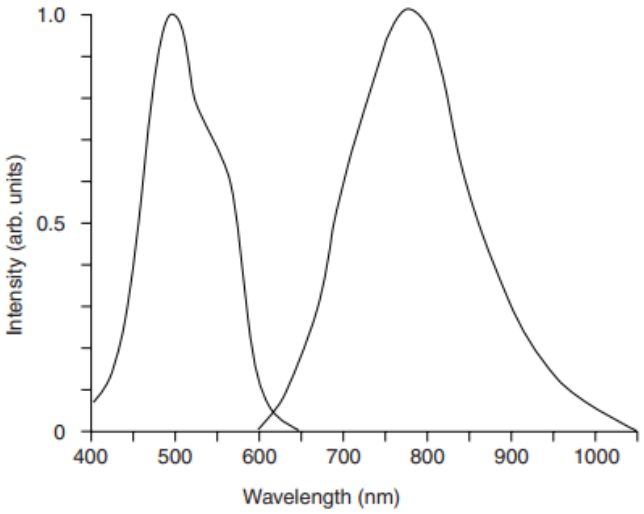

Figure 4.5: Absorption and emission spectra of Ti:sapphire crystal. The figure is reproduced from Ref. [18].

- The ten-mirror folded cavity

A relatively longer laser cavity is required to manufacture a mode-locked laser to achieve a convenient repetition frequency of ~80 MHz. To maintain the optimum performance in a minimum possible space for the fs configuration, the ten-mirror folded cavity is employed in the Tsunami as shown in Fig. (4.6).

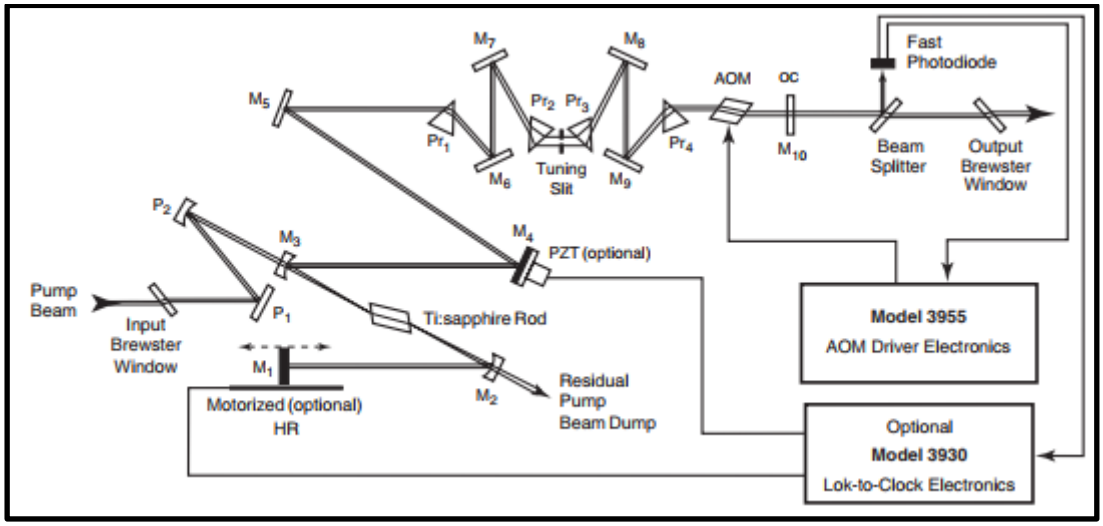

Figure 4.6: A schematic diagram showing the beam path inside the ten-mirror folded cavity of the Tsunami. The figure is reproduced from Ref. [18].

However, this complex mirror arrangement leads complicated pumping procedure. In addition, the focusing mirror introduces astigmatism in the beam when it is placed at other than the right angle with incident beam. Fortunately, this issue can be virtually solved by correct selection of the mirror angles and the length of the rod. A continuous flow of pure and dry nitrogen gas is used to the sealed laser head to purge water vapor and dust from it. In addition, a chiller is employed to maintain the fixed temperature of the Ti:sapphire rod to sustain the performance stability.

- ❖ Group Velocity Dispersion and Wavelength Selection

The product of time and bandwidth of a Gaussian pulse is limited by the Heisenberg uncertainty principal. Therefore, shorter the pulse time larger the difference between highest and lowest frequencies for a laser pulse. Since the refractive index (n) of a medium is a function of frequency, this makes a distribution of n or gradient of velocities in a laser pulse. Consequently, the transit time becomes a function of wavelength that is called group velocity dispersion (GVD). The positive GVD indicates larger wavelengths travel faster than the shorter wavelengths and the resulting pulse is called positively chirped and *vice versa*. In Tsunami laser, the four-prism and slit arrangement is used to compensate this GVD effects as shown in Fig. (4.7).

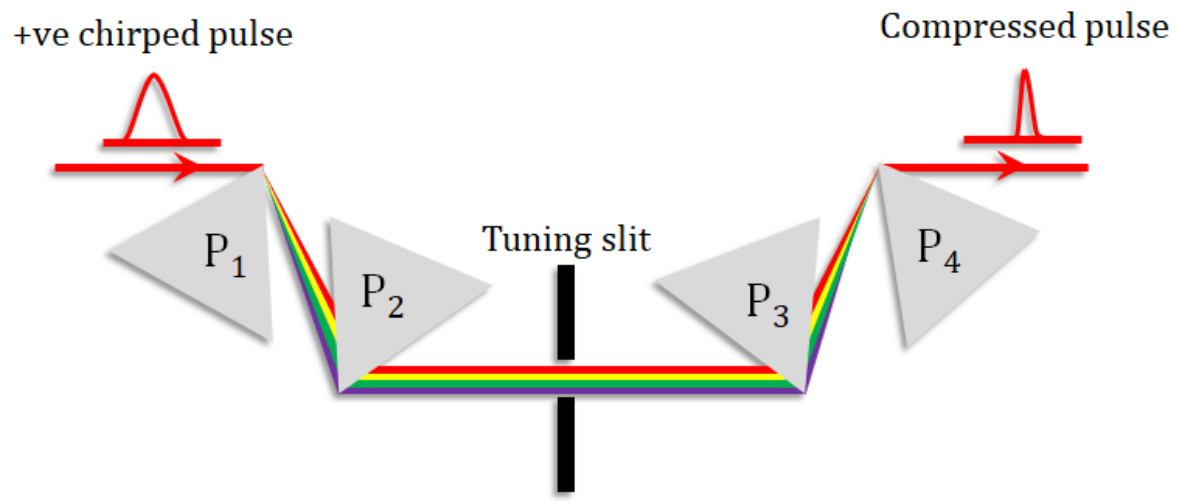

Figure 4.7: The four-prism arrangement used for the dispersion compensation in Tsunami laser.

Second Harmonic Generator

To generate the second harmonic of the fundamental beam of Tsunami laser, a highly efficient beta barium borate (BBO) nonlinear crystal is incorporated in the second harmonic generator (SHG) unit. This BBO crystal does not require any heating arrangement unlike LBO crystal. The description of a SHG unit is schematically shown in Fig. (4.8). The mirror M_1 and M_2 are employed to guide the beam, while third mirror M_3 is used to focus it to a desired position. The BBO crystal generates horizontally polarized second harmonic of the fundamental beam, while the remnant vertically polarized fundamental beam remains unaffected. The prism P_1 is used to separate the remnant fundamental and the newly generated second harmonic beams. Since the P_1 is coated with a highly reflective medium for fundamental IR beam; therefore, the fundamental beam is fully reflected and the second harmonic ray is diffracted toward the prism P_2 and subsequently toward the prism P_3. These two prisms (P_2, P_3) are coated with anti-reflection medium for the second harmonic beam. The nonlinear BBO crystal is incorporated in the SHG unit due to the following advantages:

1. It minimizes the pulse broadening issue due to group velocity dispersion.
2. Compensatory crystal is not required for the BBO crystal.
3. The BBO crystal enables phase matching over the entire wavelength tuning range (690 nm to 1090 nm).

According to Eqn. (4.1), the conversion efficiency of the SHG crystal is inversely proportional to the cross-sectional area of the beam in the crystal. The waist of the laser beam is optimized by applying telescopic arrangement of lenses L_1 and L_2 to enhance the conversion efficiency.

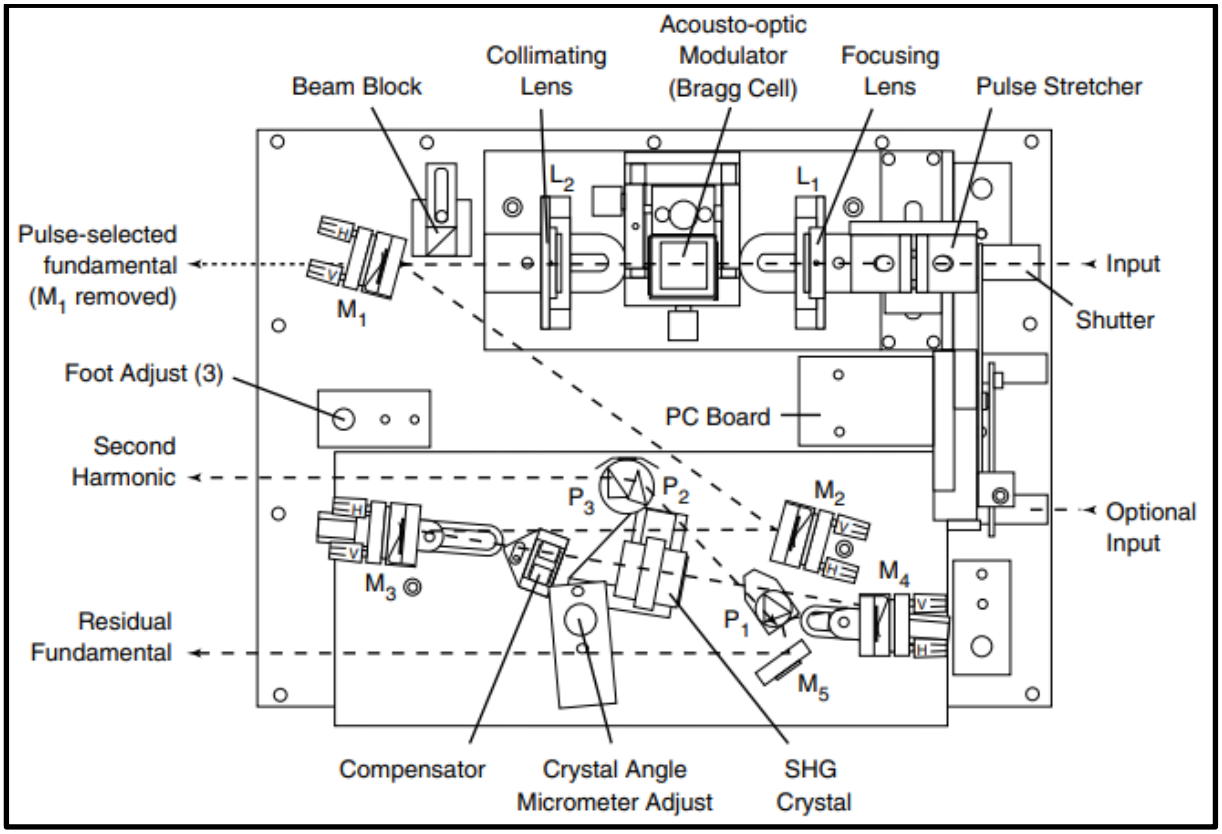

Figure 4.8: A schematic description of the SHG unit and the optical path inside the SHG are shown. The figure is reproduced from Ref. [19].

4.3.3. Description of the TR-MOKE Setup

The TR-MOKE microscope setup is installed on top of an L-shaped vibration isolation optical table as seen from the photographs in Fig. (4.3). The optical table is an essential component to execute any highly sensitive optical measurement like TR-MOKE experiment. This optical table (Newport *RS4000* series) is made of vertically bonded honeycomb core sandwiched in between the 4.8-mm-thick ferromagnetic stainless steel working surface and the 4.8-mm-thick carbon steel bottom skin. This unique design enhances the stiffness of the optical table. On the other hand, the vertically bonded honeycomb core reduces the overall weight of the table, and hence, the resonance frequency of the table is increased well above the possible external vibrational

frequencies. Therefore, it eliminates the possibility of resonance in the table due to external vibrations. In addition, the floating legs (isolators) of the optical table isolate the experimental setup from the floor vibrations. The optical table offers surface flatness of ± 0.1 mm and the array of circular holes (25 mm pitch) over the working surface enables mounting of different optical components for instance, the laser source, optics, and detectors.

A schematic illustration of the all-optical TR-MOKE microscope setup is shown in Fig. (4.9). The Millennia laser is pumped by the bunch of diode lasers and it generates output beam of wavelength 532 nm. Subsequently, the output beam of Millennia is used to pump the Tsunami laser. As mentioned earlier, the regenerative mode locking mechanism in Tsunami produces a chain of laser pulses with pulse width of ~70 fs at a stable repetition rate of 80 MHz. Though the wavelength of the Tsunami laser can be tuned in the range of 690 to 1080 nm, it is maintained at approximately 800 nm to achieve stable experimental condition and use higher spectral response from Si based detectors.

The spot size of the vertically polarized output beam (red color) from the Tsunami laser is ~2 mm. A beam splitter (B_1) is used to divide this output beam into two parts in 70:30 ratio. The intense one goes through the SHG to generate its second harmonic ($\lambda =$ 400 nm), which is employed to excite the electron and spin systems. Whereas the time-delayed (Δt) linearly polarized fundamental beam is used for probing the ensuing dynamics. A broadband mirror (M_{b1}) is placed in front of the SHG that reflects light within the wavelength range of 400 to 700 nm. Consequently, it minimizes the remnant fundamental component mixed with the second harmonic. In addition, a spectral filter (F_B) is placed on the way of the second harmonic to ensure fundamental component free second harmonic beam because even a minute amount of fundamental component mixed with the pump beam can make a noisy signal. After reflecting from two successive mirrors (M_{b2} and M_{b3}), the pump beam is travelled through a variable optical attenuator (A_2). The pump beam travels through a fixed optical path and in the way a mechanical chopper is placed to modulate the pump beam with frequency of 2 kHz. This chopper frequency (2 kHz) is saved as the reference signal in lock-in-amplifiers. On the other hand, the probe beam is initially guided through a specific optical path by using a series of mirrors (M_{r1}, M_{r2}, M_{r3}, and M_{r4}). A variable optical attenuator (A_1) is also used

here to adjust the intensity of the probe beam. The retro-reflector based delay line is employed in the path of the probe beam to tune the optical path length. Therefore, the optical path of the probe beam can be varied by moving the retro-reflector on the delay stage.

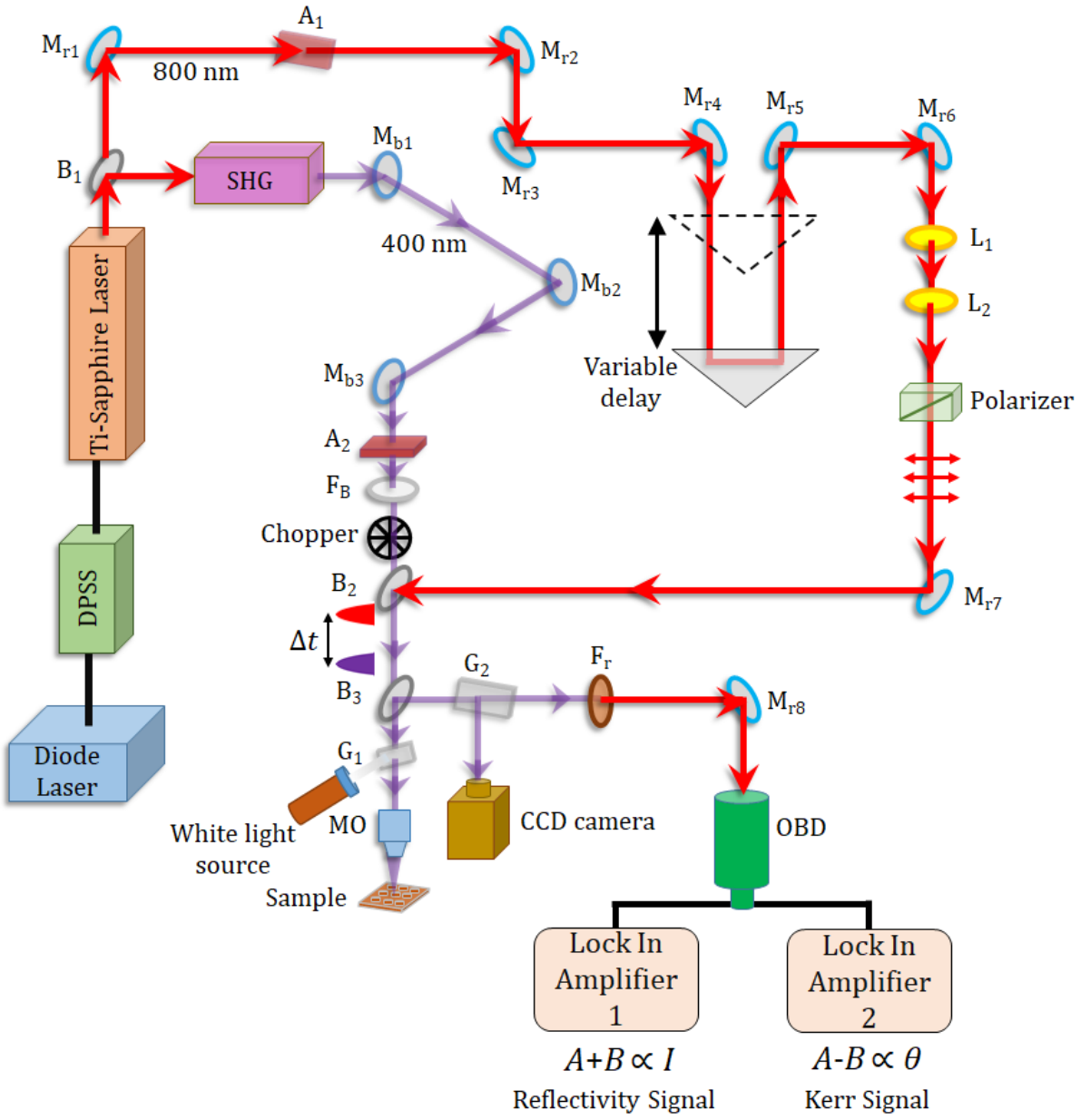

Figure 4.9: A schematic illustration of an all-optical time-resolved magneto-optical Kerr effect (TR-MOKE) microscope with collinear pump-probe geometry.

The movement of the retro-reflector on the delay stage is controlled by a motion controller with the assist of a computer interfaced with the delay stage through GPIB connection. The difference in the optical path corresponding to the pump and probe

beams leads to the time-delay (Δt) in the TR-MOKE experiment. Afterwards, the probe beam is collimated by a pair of lenses L_1 (focal length, $f_1 = 75$ mm) and L_2 (focal length, $f_2 = 200$ mm) in telescopic arrangement. This arrangement also enhances the diameter of the beam (~5 mm) so that it can cover the back-aperture of the MO (microscope objective). Subsequently, the probe beam is passed through a Glan-Thompson (extinction coefficient of 100000:1) polarizer that enables to achieve desired level of polarization state.

After that, the vertically polarized pump beam and the linearly polarized probe beam are combined with the assistance of a 50:50 non-polarized beam splitter (B_2) set at 45° about the optical path of the probe beam. The B_2 acts here as a beam combiner. The collinearity of the combined beams is optimized with the aid of steering mirrors (specifically M_{r6}, M_{r7}, M_{b1}, M_{b2}, and M_{b3}). Subsequently, the combined beams proceed through a 50:50 non-polarized beam splitter (B_3) and then through a glass slide (G_1). Both B_3 and G_1 are placed on the optical path at 45° angle. Finally, the combined beams are focused onto the sample under test by using a microscope objective (MO: M-40X and N.A. = 0.65). However, it is necessary to ensure that the sample surface is perpendicular to both the axis of MO and the direction of the combined beams. The sample holder is mounted on an *x-y-z* piezo-electric scanning stage controlled by a computer. The probe beam is focused on the sample with spot size of ~800 nm. Whereas, the pump beam is in slightly defocused state because of the chromatic aberration and falls on the sample with spot size of ~1 μm as shown in Fig. (4.10). The probe beam is placed at the centre of the pump beam with the help of MO and the *x-y-z* scanning stage to ensure uniform excitation of the desired probing volume of the sample.

The back-reflected beams (pump and probe) are passed again through the same MO. These collimated beams are reflected toward the detector by a beam splitter (B_3). A fraction of the back-reflected beams are sent to a CCD camera (after reflecting from the glass mirror (G_2)) to check the overlapping of pump and probe beams onto the sample. The residual part of the beam is passed through a spectral filter (F_r) to filter out the pump beam and finally only back-reflected probe beam is entered into an optical bridge detector (OBD).

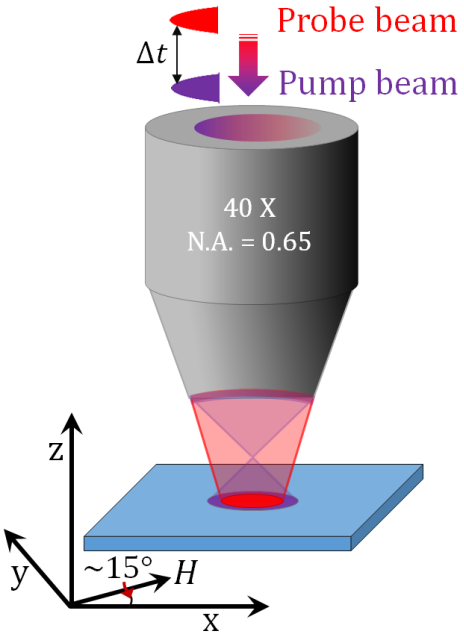

Figure 4.10: Schematic diagram of the microscope objective (MO) showing the collinear arrangement of the pump and probe beams. The bias magnetic field (*H*) orientation is shown at the bottom.

The OBD is used to measure the Kerr rotation (under balanced condition) in isolation from the total reflectivity signal. A focused white light (after reflecting from the glass slide (G_1)) is used to view the sample surface, which helps to place the pump and probe beams onto the desired location of the sample. As discussed in chapter 2, any non-zero incident angle except normal incidence leads to longitudinal Kerr effect. However, we primarily focus here to measure the polar Kerr rotation but if the incident angle of the probe beam is not perfectly normal to the sample surface, a finite amount of longitudinal Kerr rotation component can mix with this polar part. The bias magnetic field is applied at an angle of ~15° with the sample plane. The tilted bias field produces a finite amount of out-of-plane demagnetizing field. The pump beam is used to modify this demagnetizing field to induce a precessional motion of the sample magnetization and the corresponding polar Kerr rotation is measured.

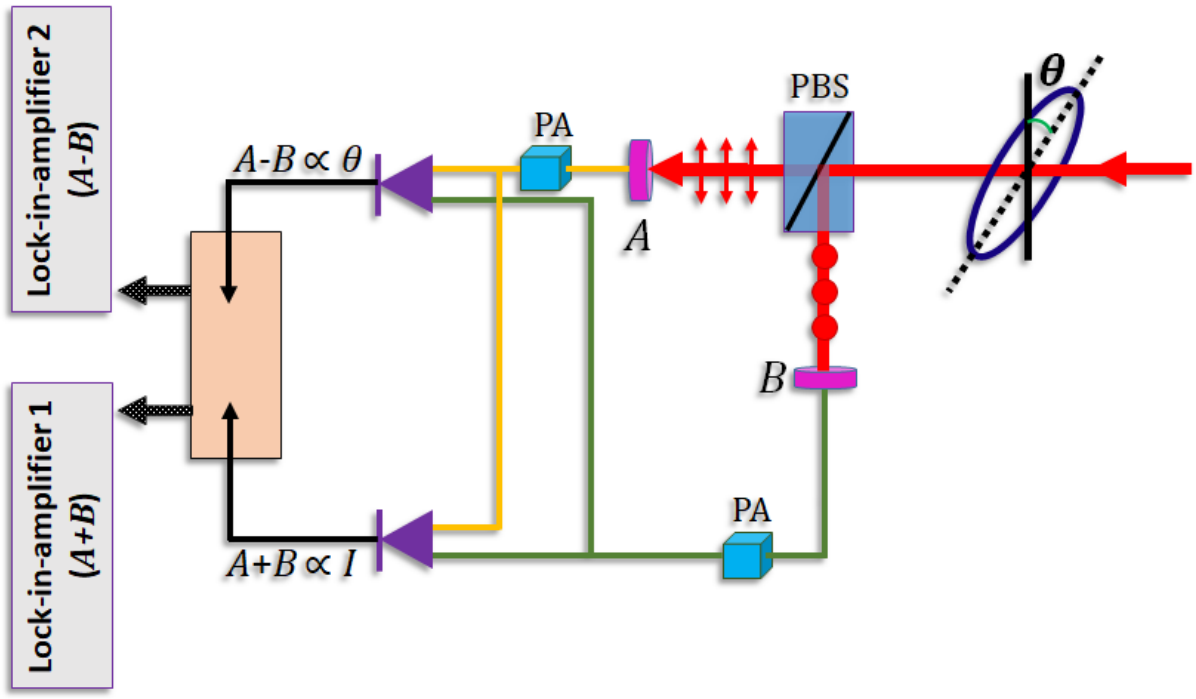

Figure 4.11: Schematic diagram of the optical bridge detector (OBD) unit.

The schematic description of the OBD used in the TR-MOKE microscope setup is shown in Fig. (4.11). The polarized beam splitter (PBS) splits the elliptically polarized probe beam into two orthogonally polarized components. Two photodiodes, namely A and B are employed to measure the intensities of I_A and I_B of the two orthogonally polarized components, respectively. Afterwards, two preamplifiers (PAs) are used to amplify the corresponding outputs from the photodiodes. Subsequently, these amplified outputs are utilized as the inputs for two independent operational amplifiers (Op-Amps). One Op-Amp calculates the sum signal $A+B$ (i.e. $I_A + I_B$) and other one calculates the difference signal $A-B$ (i.e. $I_A - I_B$). Another Op-Amp (SR830) with reference frequency same as the chopper frequency is used to measure the outputs of the previously mentioned Op-Amps in a phase sensitive manner. Initially, the PBS is set in such a way that its optical axis makes a 45° angle with the plane of polarization of the probe beam in absence of the pump beam. Therefore, this arrangement gives $I_A = I_B$ (i.e. $A-B = 0$), termed as the 'balanced' condition of the OBD. Thereupon, the magnetization of the sample is modified due to the excitation of pump beam. Consequently, the plane of polarization of the probe beam is rotated because of the magneto-optical Kerr effect. Thus, the 'balanced' condition of the OBD is disturbed, and hence, the difference signal is no longer zero i.e., $A-B \neq 0$. As we know, the linear magneto-optical Kerr rotation is directly proportional

to magnetization of the sample. Therefore, the signal $A-B$ indirectly provides the information about the magnetization of the sample. Thus by measuring $A-B$ values as a function of time, the magnetization dynamics of a sample at different time-scales are studied. We can also extract several material parameters from the obtained result for instance, saturation magnetization, Gilbert damping, gyromagnetic ratio, magnetic anisotropy of ferromagnetic thin films and nanostructures. On the other hand, the time-resolved reflectivity (related to $A+B$ signal) provides information about the charge and phonon dynamics of a sample. These sum and difference signals (i.e., $A+B$ and $A-B$) are regularly checked during alignment and optimization of the OBD. In our OBD unit, the PBS along with two photodiodes (A, B) are installed in a single stage, which is attached with a precision rotation mount. This arrangement makes alignment procedure handy and offers better signal stability. In addition, the balanced photodetector or OBD facilitates very high sensitivity (μdeg) in the measurement of Kerr signal.

In conclusion, the two-color collinear pump-probe geometry facilitates to achieve very high spatial (~800 nm) and temporal (~100 fs) resolution and non-invasive detection sensitivity to study magnetization dynamics.

4.3.4. Some Routine Alignments

The all-optical TR-MOKE microscope installed in our laboratory provides very good spatio-temporal resolution. However, it requires very thorough and high precision optical alignment of every single component of the setup. A very rigorous and thorough alignment was performed during the installation of the setup. The TR-MOKE setup comprises of highly sensitive lasers, various linear and non-linear optics, fine precision mounts and the motion controlled stages. Therefore, the TR-MOKE measurement is very sensitive to the surrounding environment, for instance, temperature, humidity etc. Hence, prior to each experiment, some systematic routine alignment procedures are performed as follows.

1. At first, the output power, central wavelength ($\lambda_0 = 800$ nm), and FWHM (~12 nm) of the fundamental laser beam are optimized by tuning the external micrometer controllers of Tsunami. The stability of the cavity is routinely checked by monitoring the number of bars (LED indicators) in the controller.

2. The alignment of the retro-reflector is examined with the help of a 'beam height'. It is placed after B_2. The nonparallel alignment of the probe beam and the axis of the retro-reflector results the unstable position of the probe beam spot on the 'beam height' with the motion of the retro-reflector. This issue can be solved by adjusting the three mirrors before the retro-reflector.

3. The collinearity of the probe and pump beams after the beam-combiner (B_2) is examined with the help of a 'beam height'. In addition, the overlap of these two beams is checked by observing their corresponding images on the TV screen connected with the CCD camera. Any further issue regarding alignment is fixed with the aid of mirrors M_{r6}, M_{r7} and M_{b1}, M_{b3}.

4. In the next step, we check whether the two beams (pump and probe) are co-axial with the microscope objective (MO). In order to do that the pump and probe beams are alternatively defocused and focused with the adjustment of MO, which is observed in the TV screen with the aid of a CCD camera. Any movement of the centre(s) of the beam spot(s) in the TV screen during the movement of the MO implies that the further alignment is required. These two beams are made collinear with the MO by adjusting the corresponding mirrors.

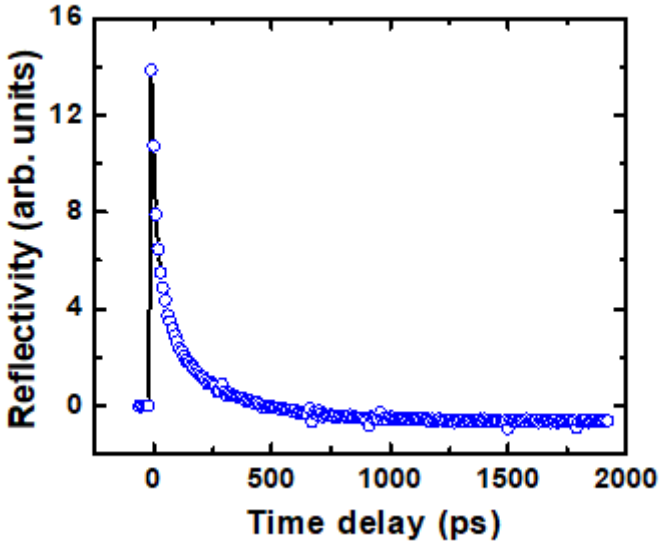

Figure 4.12: The reflectivity signal obtained from a Si (100) wafer as a function of the time delay (Δt) between the pump and probe beams.

5. Lastly, the alignment of the OBD is verified by confirming the superposition of back reflected beam from OBD with the incident probe beam.

When the desired alignment level of the setup is achieved, the time-resolved reflectivity signal from a standard Si (100) wafer is measured for the time window of about ~2000 ps. The measured reflectivity signal as a function of time-delay (Δt) between pump and probe beams is shown in Fig. (4.12). The reflectivity signal reaches its maximum value sharply after the zero delay, and subsequently, it decays exponentially with the increase of time-delay. It is observed that the reflectivity signal decays with time constant of around ~220 ps for a standard Si wafer. Before starting any experiment, the relaxation rate of the reflectivity signal for the Si wafer is compared with the standard one to ensure the alignment condition of the setup. At last, when all alignment conditions are verified this setup becomes ready for the TR-MOKE measurement.

References

[1] V. P. Denysenkov, A. M. Grishin, Rev. Sci. Instrum. **74**, 3400 (2003).

[2] M. R. Freeman, M. J. Brady, J. Smyth, Appl. Phys. Lett. **60**, 2555 (1992).

[3] M. van Kampen, C. Jozsa, J. T. Kohlhepp, P. LeClair, L. Lagae, W. J. M. de Jonge, B. Koopmans, Phys. Rev. Lett. **88**, 227201 (2002).

[4] D. F. Williams, J. C. M. Wang, U. Arz, IEEE Trans. Microw. Theory Tech. **51**, 2391 (2003).

[5] T. V. d. Broeck, J. Verspecht, in *1994 IEEE MTT-S International Microwave Symposium Digest* (Cat. No. 94CH3389-4, pp. 1069, 1994).

[6] A. Ferrero, F. Sampietro, U. Pisani, IEEE Trans. Microw. Theory Tech. **42**, 2455 (1994).

[7] R. B. Marks, J. A. Jargon, J. R. Juroshek, in *48th ARFTG Conference Digest*, pp. 38, (1996).

[8] L. A. Hayden, V. K. Tripathi, IEEE Trans. Microw. Theory Tech. **41**, 415 (1993).

[9] J. T. Barr, M. J. Pervere, in *34th ARFTG Conference Digest*, pp. 51 (1989).

[10] J. A. Jargon, R. B. Marks, D. K. Rytting, IEEE Trans. Microw. Theory Tech. **47**, 2008 (1999).

[11] L. F. Tiemeijer, R. J. Havens, A. B. M. Jansman, Y. Bouttement, IEEE Trans. Microw. Theory Tech. **53**, 723, (2005).

[12] I. Novak, B. Eged, L. Hatvani, in *IEEE Instrumentation and Measurement Technology Conference*, pp. 269 (1993).

[13] R. B. Marks, in *50th ARFTG Conference Digest*, pp. 115, (1997).

[14] D. E. Bockelman, W. R. Eisenstadt, IEEE Trans. Microw. Theory Tech. **46**, 1009 (1998).

[15] A. Ferrero, F. Sanpietro, IEEE Microw. Wirel. Compon. Lett. **5**, 119 (1995).

[16] A. Ferrero, V. Teppati, in *IEEE MTT-S International Microwave Symposium Digest*, pp. 1456 (2006).

[17] M. R. Freeman, R. R. Ruf, R. J. Gambino, IEEE Trans. Magn. **27**, 4840 (1991).

[18] User's Manual, "Tsunami: Mode-locked Ti:sapphire Laser", *Spectra-Physics*, California, USA (2002).

[19] User's Manual, "Model 3980: Frequency Doubler and Pulse Selector" *Spectra-Physics*, California, USA (2002).

[20] User's Manual, "Millennia Pro s-Series: Diode-Pumped, CW Visible Laser System" *Spectra-Physics*, California, USA (2007).

[21] W. T. Silfvast, "*Laser Fundamentals*", Cambridge University Press, (1996).

[22] O. Svelto, "*Principles of Lasers*", Springer, (2009).

Chapter 5

5. Micromagnetic Simulations

5.1. Introduction

The magnetization dynamics of a sample is theoretically studied by solving the well-known Landau-Lifshitz-Gilbert (LLG) equation. The macrospin formalism-based theories are applicable for only uniformly magnetized sample, where the nonlinear LLG equation is linearized under small angle approximation. Unfortunately, the real problems are not very straightforward. The criterion of uniform magnetization is satisfied either in infinitely long bulk samples or magnetically saturated two dimensional thin films after applying large enough external magnetic field. On the other hand, the uncompensated magnetic dipoles at finite boundaries of the confined magnetic structures usher nonuniform distribution of the demagnetizing field. This demagnetizing field plays important role in structuring of static magnetic configuration as well as in magnetization dynamics. In case of non-ellipsoidal shaped confined magnetic structures, this effect becomes more prominent. Consequently, the analytical solution becomes extremely difficult. Hence, to explore the magnetization dynamics in various magnetic samples in nanoscale regime several analytical and numerical methods have been developed. Sometimes experiments suffer critical challenges due to the various limitations in fabrication and characterization techniques. Therefore, it becomes hard to reproduce the experimental results by using simple theories. Thus, the development of micromagnetic modelling including computer-based numerical simulation have become imperative. In case of micromagnetic simulation [1], the samples are discretized into a desired number of cells. The dimensions of each cell are taken less than the exchange length of that material to consider short-range exchange interaction. The average magnetization of each cell is represented by a single spin, which takes into account all the short-range and long range interactions such exchange, dipolar etc. Finally, the dynamics of these representative spins are calculated by solving the LLG equation numerically.

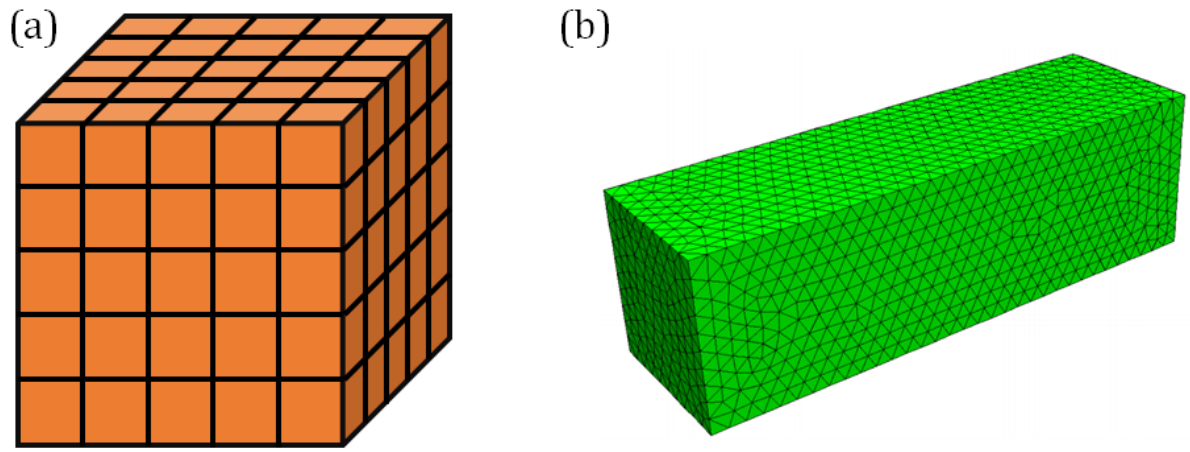

Figure 5.1: The schematic diagrams show two discretized samples. Discretization of sample into a number of (a) cuboidal cells using finite difference method and (b) tetrahedral cells using finite element method. The second figure is reproduced from Ref. [17].

5.2. Free Energies of a Ferromagnetic Material in Micromagnetics

The total free energy holds by a ferromagnetic substance in presence of an external magnetic field contains different macroscopic and microscopic free energy terms, which can be written as:

$$E_{Total} = E_Z + E_e + E_K + E_d \tag{5.1}$$

Here E_Z, E_e, E_K, and E_d represent respectively the Zeeman energy, exchange energy, anisotropy energy and demagnetization energy. On the other hand, in micromagnetism the same expression of total energy can be rewritten as:

$$E_{Total} = \int_V [-\boldsymbol{M}.\boldsymbol{H}_Z - A\left((\nabla \boldsymbol{u}_x)^2 + \left(\nabla \boldsymbol{u}_y\right)^2 + (\nabla \boldsymbol{u}_z)^2\right) + K_1(1 - (\boldsymbol{a}.\boldsymbol{u})) - \frac{1}{2}\boldsymbol{M}.\boldsymbol{H}_d] \tag{5.2}$$

Here $\boldsymbol{H}_Z$, A, K_1, and $\boldsymbol{H}_d$ are respectively Zeeman field, exchange stiffness constant, anisotropy constant and demagnetizing field. In addition, $\boldsymbol{a}$ is the unit vector parallel to the easy axis and $\boldsymbol{u}$ is the time and space dependent unit vector of magnetization. The general expression for space and time dependent magnetization is given by:

$$\boldsymbol{M}\,(x,t) = M_s(x).\boldsymbol{u}(x,t) \tag{5.3}$$

In equilibrium condition, the total free energy (E_{Total}) of a magnetic system will be minimum and the variation of E_{Total} with $\boldsymbol{u}$ must vanishes. Mathematically, this can be expressed as:

$$\frac{\delta E_{Total}}{\delta \boldsymbol{u}} = 0 \tag{5.4}$$

Therefore, we get Brown's equation using Eqn. (5.4):

$$\boldsymbol{u} \times (M_s \boldsymbol{H}_z + 2A\Delta \boldsymbol{u} + 2K_1 \boldsymbol{a}(\boldsymbol{u}.\boldsymbol{a}) + M_s \boldsymbol{H}_d) = 0 \tag{5.5}$$

The above equation suggests that in equilibrium state the magnetization ($\boldsymbol{M}$) lies parallel to the effective magnetic field ($\boldsymbol{H}_{eff}$). Where the expression of $\boldsymbol{H}_{eff}$ is given by:

$$\boldsymbol{H}_{eff} = \boldsymbol{H}_z + \frac{2A}{M_s}\Delta \boldsymbol{u} + \frac{2K_1}{M_s}\boldsymbol{a}(\boldsymbol{u}.\boldsymbol{a}) + \boldsymbol{H}_d \tag{5.6}$$

Since in equilibrium $\boldsymbol{M}$ lies parallel to $\boldsymbol{H}_{eff}$ therefore, the torque on $\boldsymbol{M}$ by $\boldsymbol{H}_{eff}$ vanishes *i.e.*,

$$\boldsymbol{M} \times \boldsymbol{H}_{eff} = 0 \tag{5.7}$$

The equilibrium magnetization distribution of a magnetic system can be obtained by the minimization of Eqn. (5.2). However, the energy distribution profile of a micromagnetic system may contain several local minima, maxima including saddle points. Therefore, equilibrium magnetization in a local minimum is achieved more conveniently by considering a dynamic description of magnetization. The magnetization dynamics is illustrated by the LLG equation, which is given by:

$$\frac{d\boldsymbol{M}}{dt} = -\gamma(\boldsymbol{M} \times \boldsymbol{H}_{eff}) + \frac{\alpha}{M_s}(\boldsymbol{M} \times \frac{d\boldsymbol{M}}{dt}) \tag{5.8}$$

In micromagnetic simulation, the total system is discretized into a desired number of cells. Therefore, total energy of the system is also divided into the same number. However, all the magnetic parameters of the system, i.e., M_s, K and A are assumed constant for all discrete cell. The spatial distribution of the magnetization in terms of discrete approximation can be expressed as:

$$\boldsymbol{M}(x) \approx M_s(x) \sum_i \boldsymbol{u}_i \xi_i M_s \approx \sum_i \boldsymbol{u}_i \xi_i \, M_{s,i} = \sum_i \boldsymbol{M}_i \tag{5.9}$$

Here ξ_i represents the basis function corresponding to the i^{th} cell. The effective magnetic field corresponding to the i^{th} cell is given by:

$$\boldsymbol{H}_{eff}^{i} = -\left(\frac{\delta E_{Total}}{\delta \boldsymbol{M}}\right)_i \approx -\frac{1}{V_i}\frac{\partial E_{Total}}{\partial \boldsymbol{M}_i} = -\frac{1}{V_i M_{s,i}}\frac{\partial E_{Total}}{\partial \boldsymbol{u}_i} \tag{5.10}$$

Therefore, the Zeeman energy can be written as:

$$E_Z = \int_V (-\boldsymbol{M}.\boldsymbol{H}_Z)\, dv = \int_V \sum_j u_j \xi_j M_{s,j} \sum_k u_{j,k} \xi_j H_{Z,k} dv \tag{5.11}$$

The exchange energy can be written as:

$$E_e = \int_V \sum_j (A(\nabla u_j \xi_j)^2)\, dv \tag{5.12}$$

The anisotropy energy can be written as:

$$E_K = \int_V \sum_j K_1(1 - (a.u_j \xi_j)^2)\, dv \tag{5.13}$$

The magnetostatic self-energy can be written as:

$$E_d = \int_V \boldsymbol{\nabla}.\boldsymbol{M}\, dv = \int_V \sum_j \sum_V^{\{x,y,z\}} \nabla_k u_{j,k} \xi_j = \int_V \sum_j \sum_k^{\{x,y,z\}} u_{j,k} \nabla_k \xi_j \tag{5.14}$$

5.3. Different LLG Solvers and Evolvers

The analytical study of magnetization dynamics in ferromagnetic nanostructures are carried out by solving nonlinear Landau-Lifshitz-Gilbert (LLG) equation. However, the analytical solving process in nanostructures encounters various technical difficulties for instance, correct acquisition of boundary and initial conditions for wide variety of geometry of the samples. Fortunately, the calculation of such solutions become easier by applying numerical approach based on discretization methods. Finite difference method (FDM) and finite element method (FEM) [2,3] are two general approaches to solve the LLG equation numerically in micromagnetics. In both cases, the sample is discretized into a large number of cells and the dimensions of each cells are kept well below the exchange length (l_{ex}) of the considered material to take into account exchange interactions. Aforementioned techniques employ continuum theory to estimate the

magnetic properties of nanomagnets by considering local arrangement of magnetic moments. In FDM, all differential equations require to be solved are approximated with corresponding difference equations. The 'finite differences' of them approximates the derivatives and eventually they are solved by using matrix algebra method. In addition, the continuous domain is replaced here by discrete set of space and time points and the corresponding domain boundaries are substituted by their discrete set of counterparts. Subsequently, each discrete cell is assigned with an averaged magnetization vector and the minimization of system's total free energy is calculated. However, the FDM approach is not very precise to replicate the exact edges and corners of the complicated geometry of nanostructures. This issue can be fixed by employing FEM approach. In FEM, the whole system is discretized into large number of finite elements. In two-dimensional systems triangles, squares, or rectangles, while in three-dimensional systems tetrahedra, cubes, or hexahedra elements are used in general to replicate the identical shape of the nanostructures as shown in Fig. (5.1). This complicated replication process demands higher computational storage and longer simulation time. Thus, the fast adaptive algorithms by using FFT or multipole expansion are used to make the simulation process faster. This technique is applicable in FDM because it deals with regular grids while, it is not applicable in FEM due to irregular mesh like structures. Several simulators or codes based on FEM or FDM are available to run the micromagnetic simulations. For instance, OOMMF [4], LLG [5], MuMax3 [6,7], Magsimus [8,9], GoParallel [10] and MicroMagus [11,12] are FDM based simulators. On the other hand, MAGPAR [13,14], NMAG [15-17], MicroMagnum [18,19], FEELLGOOD [20], FastMag [21] and TetraMag [22,23] are some popular FEM based simulators.

We have used OOMMF and LLG micromagnetics simulators to solve the numerical simulation works presented in this thesis. It is essential to have knowledge on the correct selection of 'Evolvers' before proceeding to run the simulation. The evolvers update the magnetic configuration of a system in systematic steps. We have tabulated different evolvers associated with OOMMF and LLG micromagnetics simulators as shown in Table (5.1).

Table 5.1: The evolvers for OOMMF and LLG simulators are listed.

Name of the simulation code	Calculation method	Evolver
Object Oriented Micromagnetic Framework (OOMMF)	FDM	Euler, Runge-Kutta, SpinXfer and CG Evolver
LLG Simulator	FDM	Euler, Predictor-Corrector, Rotation Matrices, Gauss-Seidel Stable Method

Both the above-mentioned simulation codes solve LLG equation according to the principle of continuum micromagnetics, and hence, the obtained results are acceptable for the time scales longer than 1 ps and dimensions of the system larger than 1 nm. Appropriate modelling strategy is essential to perform any reliable numerical simulation. In this thesis, the magnetization dynamics and magnetic hysteresis loops have been simulated by using OOMMF. The magnetostatic stray field distributions have been calculated by using LLG micromagnetics simulator. A brief overview on OOMMF and LLG micromagnetics simulator are given in the following.

5.3.1. Object Oriented Micromagnetic Framework (OOMMF)

OOMMF is a FDM based public domain micromagnetic framework developed by M. J. Donahue and D. G. Porter at the National Institute of Standards and Technology (NIST), MD. This simulation software uses C++ compiler. It can be installed effectively in wide range of platform: various version of windows and UNIX platforms. The ODE solver is employed here to relax the 3-D spins on a 2-D arranged mesh of square cells and the self-magnetostatic field is computed by performing FFT. This software enables to discrete the system in three dimensions. However, it offers less flexibility compare to FEM based software to replicate complicated curved surface. In OOMMF, all the numerical calculations are performed at $T = 0$ K. The details of the problem including all essential input parameters and initial conditions are specified in a '.mif' file, which is

written in Tcl/Tk script. Various intrinsic energies, for instance, magneto-crystalline energy and exchange energy can be specified by furnishing the corresponding numerical value of anisotropy constant, exchange constant and the direction of anisotropy field in Cartesian coordinates. In addition, all the material parameters of the sample such as gyromagnetic ratio, saturation magnetization, and damping value are supplied in the SI unit. The OOMMF has mainly two kinds of evolver: (i) time evolvers, which handle the magnetization (LLG) dynamics and (ii) energy minimization evolvers, which detect the local minimum in the surface of energy distribution by applying direct energy minimization methods. On the other hand, these evolvers are paired up with corresponding compatible 'drivers' to solve a specified problem by implementing some standard methods. The drivers command the corresponding evolvers for the advancement of magnetic configuration to the next step (called an 'iteration') after providing an intermediate magnetic configuration. The drivers detect the completion of a stage/run of a simulation after achieving specified stopping criterion provided in the input MIF file. The stopping criterion is specified in the input MIF file by setting the value of torque $\boldsymbol{m} \times \boldsymbol{H}$ (where, $\boldsymbol{m} = \boldsymbol{M}/M_S$) or simulation time. For each stage, the simulation time or $\frac{d\boldsymbol{m}}{dt}$ value is set in such a manner that the maximum torque ($\boldsymbol{m} \times \boldsymbol{H}$) value must be less than 10^{-6} A/m. The whole simulation process is composed of two primary parts: (i) static and (ii) dynamic. After completion of the static part, the final magnetization state, i.e., 'ground state' is obtained and it is specified as the initial magnetization state for the dynamic part.

Subsequently, an excitation field is launched as an external perturbation to simulate the magnetization dynamics. After completion of the dynamic part, various time dependent components such as magnetization, energies and magnetic fields can be extracted from the output file in '.omf', '.ovf' or '.ohf' formats. In addition, the OOMMF has the facility to apply periodic boundary condition (PBC) to simulate the realistic bigger systems.

5.3.2. LLG Simulator

LLG micromagnetics simulator is a FDM based commercial simulation package developed by Michael R Scheinfein. It runs only Windows operating system and provides 3-D simulation facility. It has three phases of functionality to execute a micromagnetic simulation. These phases are described briefly in the following:

- Input phase: It is the control interface, which allows the user to specify the input parameters and design the customized simulation environment. This simulator utilizes rectangular pixels on a Cartesian grid to solve the LLG equation through FDM based technique by considering all the energies, fields and boundary elements. After creation of the simulation environment, it initializes all the defined arrays to start calculating the corresponding demagnetizing field coupling tensors for possible boundary conditions. The user is prompted to save the simulation parameters in different files before starting the next phase.
- Simulation phase: The desired micromagnetic simulation is performed in this phase by solving differential equations (LLG Simulation Sheet).
- Review phase: This phase allows the user to review the results with the help of a graphical animated movie (LLG Movie Viewer). The user can view any saved domain or field file utilizing viewer control.

LLG micromagnetics simulator supports four evolvers (integrators) to obtain the results. Out of them, Euler Cartesian method is primitive one, which is least accurate but fastest. The Rotational matrices method is used to study stable magnetization configurations. The Cartesian Predictor-Corrector evolver is the most accurate and fastest when damping is low (~0.01). On the other hand, the Gauss-Seidel Stable integrator is based on semi-implicit first order integration method.

Interestingly, unlike OOMMF it can incorporate temperature effects in the simulation in terms of proving random magnetic field. This simulator can compute quasistatic magnetization reversal as well as several fundamental properties like domain-wall lengths, stray fields and switching time. It can also incorporate the effect due to spin polarized current and charge current. It can also simulate the magnetization dynamics for single layered or multi-layered systems. Furthermore, it can simulate magnetic force micrograph (MFM) of a magnetic surface.

5.4. Calculation of Power and Phase Maps of the Resonating Modes

To get deeper insight into the magnetization dynamics of ferromagnetic nanostructures, the spatial mapping of power and phase profiles corresponding to the observed resonant modes are numerically calculated [24]. These mappings provide spatial distribution of precessional amplitude of the spins and phase of the resonant modes

explicitly. To execute these numerical calculations we have employed the Dotmag software developed by our research group [24]. This Dotmag software utilizes the output files of OOMMF software, which contains time varying magnetization (M (x, y, z, t)) information. A spin system can have multiple resonant modes superposed on each other containing definite powers and phases. Therefore, the extraction of spatial information for a particular resonant mode is not straightforward. To execute the mapping one of the spatial coordinates of time-dependent magnetization is kept fix and discrete Fourier transform is performed in Dotmag software with respect to time. The power and phase maps of the resonant modes are obtained at discrete frequencies (f) by plotting the output files after discrete Fourier transform. The simulations are typically performed for systems without discretizing along the z-axis. In case of discretization along z dimension, the z coordinate is kept fix at a particular value ($z = z_c$) and the discrete Fourier transform of magnetization is performed with respect to time, which can be represented as:

$$\widetilde{M}^{z_c}(f, x, y) = FFT[M\ (x, y, z_c, t)] \tag{5.15}$$

The z_c value can be chosen anywhere between top to bottom surface of the sample. Finally, Dotmag plots spatial (x-y plane) distribution of the power ($P^{z_c, f_d}(x, y)$ and phase ($\phi^{z_c, f_d}(x, y)$ maps of the resonating modes at specified frequencies according the following equations:

$$P^{z_c, f_d}(x, y) = 20\log_{10} FFT[\widetilde{M}^{z_c}(f_d, x, y)] \tag{5.16}$$

$$\phi^{z_c, f_d}(x, y) = \tan^{-1}\left(\frac{Im\,(\widetilde{M}^{z_c}(f_d, x, y))}{Re\,(\widetilde{M}^{z_c}(f_d, x, y))}\right) \tag{5.17}$$

Here f_d represents frequency of the resonant mode. The calculated power is typically scaled in dB and phase in radian. The MATLAB platform is employed to run and control the Dotmag. The frequency resolution of the calculated power and phase map depends upon the total simulation time window and the spatial resolution depends on the discretization of the system specified during micromagnetic simulations.

References

[1] S.-K. Kim, J. Phys. D: Appl. Phys. **43**, 264004 (2010).

[2] B. Dieny, R. B. Goldfard, K.-J. Lee, *Introduction to Magnetic Random-Access Memory*, Wiley-IEEE Press, New York, 2016.

[3] T. Schrefl, J. Magn. Magn. Mater. **207**, 45 (1999).

[4] M. Donahue, D. G. Porter, *OOMMF User's Guide, Version 1.0, NIST Interagency Report No.* 6376 (1999).

[5] LLG Micromagnetics Simulator, http://llgmicro.home.mindspring.com (2018).

[6] A. Vansteenkiste, B. Van de Wiele, J. Magn. Magn. Mater. **323**, 2585 (2011).

[7] A. Vansteenkiste, J. Leliaert, M. Dvornik, M. Helsen, F. Garcia-Sanchez, B. Van Waeyenberge, AIP Adv. **4**, 107133 (2014).

[8] J. O. Oti, IEEE Trans. Magn. **46**, 2338 (2010).

[9] A. Bordianu, V. Ionita, L. Petrescu, Rev. Roum. Sci. Tech. EI. **57**, 3 (2012).

[10] L. Lopez-Diaz, D. Aurelio, L. Torres, E. Martinez, M. A. Hernandez-Lopez, J. Gomez, O. Alejos, M. Carpentieri, G. Finocchio, G. Consolo, J. Phys. D: Appl. Phys. **45**, 323001 (2012).

[11] O. Dmytriiev, M. Dvornik, R. V. Mikhaylovskiy, M. Franchin, H. Fangohr, L. Giovannini, F. Montoncello, D. V. Berkov, E. K. Semenova, N. L. Gorn, A. Prabhakar, V. V. Kruglyak, Phys. Rev. B **86**, 104405 (2012).

[12] MicroMagus, http://www.micromagus.de/home.html.

[13] W. Scholz, J. Fidler, T. Schrefl, D. Suess, R. Dittrich, H. Forster, V. Tsiantos, Comput. Mater. Sci. **28**, 366 (2003).

[14] T. Blachowicz, A. Ehrmann, Iop, in *4th International Conference on Competitive Materials and Technology Processes* (Iop Publishing Ltd, Bristol, 2017).

[15] H. Fangohr, M. Albert, M. Franchin, Ieee, *Nmag Micromagnetic simulation tool-software engineering lessons learned* (Ieee, New York, 2016), Proceedings of 2016 Ieee/Acm International Workshop on Software Engineering for Science.

[16] T. Fischbacher, M. Franchin, G. Bordignon, H. Fangohr, IEEE Trans. Magn. **43**, 2896 (2007).

[17] H. Fangohr, T. Fischbacher, M. Franchin, G. Bordignon, J. Generowicz, A. Knittel, M. Walter, M. Albert, "*NMAG User Manual Documentation, Release 0.2.1*", (2012).

[18] B. Krüger, G. Selke, A. Drews, D. Pfannkuche, IEEE Trans. Magn. **49**, 4749 (2013).

[19] C. Abert, L. Exl, G. Selke, A. Drews, T. Schrefl, J. Magn. Magn. Mater. **326**, 176 (2013).

[20] FEELLGOOD, http://feellgood.neel.cnrs.fr./.

[21] J. K. Byun, I. Volvach, V. Lomakin, IEEE Trans. Magn. **52**, 7100509 (2016).

[22] A. Kakay, E. Westphal, R. Hertel, IEEE Trans. Magn. **46**, 2303 (2010).

[23] R. Hertel, in *Handbook of Magnetism and Advanced Magnetic Materials*.

[24] D. Kumar, O. Dmytriiev, S. Ponraj, A. Barman, J. Phys. D: Appl. Phys. **45**, 015001 (2012).

Chapter 6

6. Bias Field Tunable Magnetic Configuration and Magnetization Dynamics in $Ni_{80}Fe_{20}$ Nano-cross Structures with Varying Arm Length

6.1 Introduction

Recent attention in nanomagnetism [1,2] is triggered by their fundamental properties and huge potential applications in various fields of nanotechnology such as magnetic data storage [2,3], logic devices [4], waveguides [5,6], filters [7], phase shifters [8] as well as spin torque nano-oscillators [9]. Emerging fields like magnonics [10,11] and magnon spintronics [12] promise on-chip data communication and processing, leading towards an all-magnetic computation. Future technology demands faster magnetic switching and spatial miniaturization. To design successful devices based on arrays of nanomagnets, it is crucial to understand their static and dynamic magnetic properties and to find means to control those by intrinsic and extrinsic parameters. To this end, significant efforts have been put towards understanding the dynamics of single nanomagnets [13-15] and arrays of nanomagnets [16-23]. The intrinsic magnetization dynamics of ferromagnetic nanodot arrays are primarily governed by nanodot size [18,19], shape [22], and areal density [21] and lattice symmetry [23] of the array. On the other hand, by varying the extrinsic parameters such as strength and orientation of the bias magnetic field, temperature, spin transfer torque, the magnetization dynamics can be efficiently and directly controlled. The static magnetic configurations of the nanomagnet arrays play a crucial role in their magnetization dynamics and it may vary between single domain, quasi-single domain, closure domain and multi-domain structures due to the interplay between the internal magnetic field, inter-element interaction field, and external bias field. Hence, by varying the above parameters many static magnetic configurations and spin wave (SW) properties, including SW frequency, damping, and spatial coherence, can be obtained.

Ferromagnetic cross-shaped elements showed complex spin configurations [24], while the magnetization dynamics of $Ni_{80}Fe_{20}$ sub-micron cross arrays studied by a time-resolved magneto optical Kerr effect (TR-MOKE) microscope showed a strong configurational anisotropy [25]. A Subsequent report [26] proposed application of ferromagnetic cross-shaped elements as reconfigurable spin-based logic devices using SW scattering and interference. The above results open a door for application of ferromagnetic cross structures as a building block of magnetic storage, memory, on-chip data communications, and spin-based logic devices, and hence, investigation of the static and dynamic magnetic properties of this structure with its size, inter-element interaction, and variation of the bias magnetic field has become important. Here, we report an extensive study of SW dynamics in $Ni_{80}Fe_{20}$ (Py) nanocrosses with varying arm lengths by using the broadband ferromagnetic resonance technique. We demonstrate the evolution of different types of magnetic configurations with bias magnetic field and the ensuing dynamical phenomena including a crossover between SW modes, a minimum in the frequency spectra, and a mode splitting, which varied significantly with the size of the cross structure.

6.2 Experimental Details

Arrays (200 μm × 20 μm) of Py nanocrosses with the arm length (L) varying between 600 nm and 200 nm, fixed thickness (20 nm), and edge-to-edge separation (150 nm), as well as a continuous Py film of 20 nm thickness were fabricated on a self-oxidized Si-substrate [001] by a combination of e-beam lithography and e-beam evaporation. The 20 nm thick Py film coated with a 60 nm thick Al_2O_3 protective layer was deposited in an ultra-high vacuum chamber at a base pressure of 2×10^{-8} Torr on a bi-layer (PMMA/MMA) resist pattern on the Si substrate made by using e-beam lithography. A Au made coplanar waveguide (CPW) of 150 nm thickness, 30 μm central conductor width, 300 μm length, and 50 Ω nominal characteristic impedance was deposited on top of the nanocross structures and the continuous Py film at a base pressure of 6×10^{-7} Torr. Subsequently, a 5 nm thick Ti protective layer was deposited on top of the Au layer at the same base pressure.

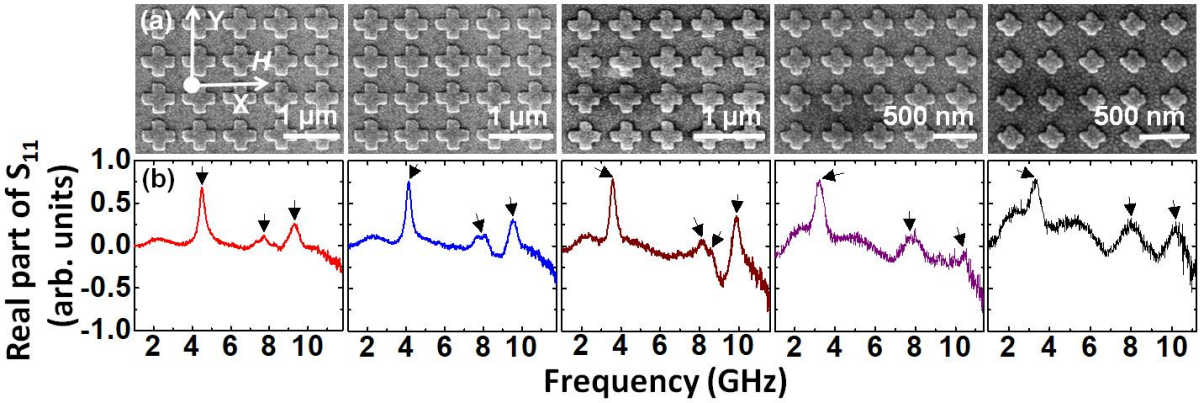

Figure 6.1: (a) Scanning electron micrographs of $Ni_{80}Fe_{20}$ nanocross arrays with varying arm lengths. The inset shows the applied magnetic field direction. (b) Real part of the S_{11} parameter as a function of frequency at $H = 497$ Oe for all samples. The SW modes are marked by arrows.

The waveguide was patterned by using mask-less photolithography. The FMR experiments were performed using a vector network analyzer (Agilent, PNA-L N5230C, 10 MHz to 50 GHz) and a homebuilt high frequency probe station with a non-magnetic G-S-G type probe (GGB Industries, Model No. 40A-GSG-150-EDP) [27]. A microwave signal with a power of -15 dBm and varying frequencies is applied to the CPW structure, and the output signal is collected from the CPW in the reflection geometry. A rotating electromagnet is used to apply an in-plane bias magnetic field up to 1.6 kOe. All the experiments are carried out at room temperature.

6.3 Results and Discussion

Figure 6.1(a) shows the scanning electron micrographs of all arrays while the bias magnetic field orientation is shown in the inset. The cross structures show rounded corners and edge deformations, which increases with the reduction of the cross size. The dimensions of the individual crosses and their separations in the arrays also vary by up to $\pm 8\%$. Figure 6.1(b) shows representative FMR spectra from the nanocross structures, with the resonant peaks marked by arrows. There are some humps in the FMR spectra, which do not show any bias field dependence, and hence, considered of non-magnetic origin. The bias-field-dependent FMR spectra of the continuous Py film are also measured and the data are fitted using Kittel formula to extract the material

parameters, which are: saturation magnetization $M_S = 850$ emu/cc, gyromagnetic ratio $\gamma = 17.85$ MHz/Oe, and the anisotropy field $H_K = 0$.

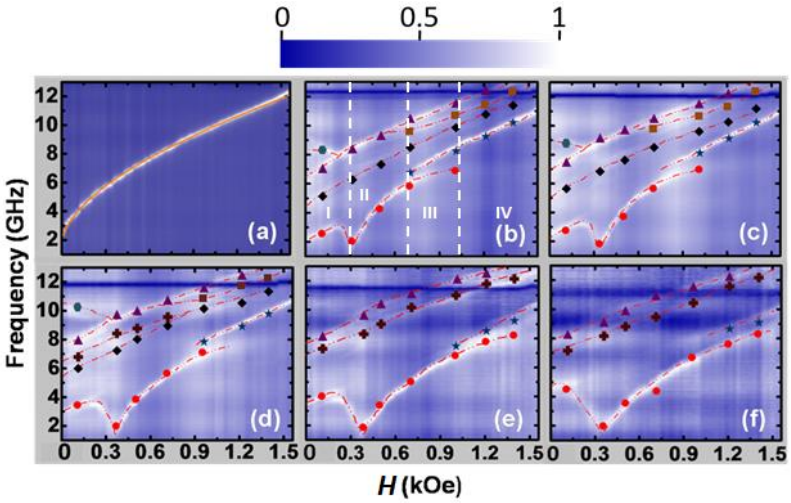

Figure 6.2: Surface plots of bias-field-dependent SW mode frequencies for (a) $Ni_{80}Fe_{20}$ thin film of 20 nm thickness and nanocross arrays with arm length (L) of (b) 600 nm, (c) 500 nm, (d) 400 nm, (e) 300 nm, and (f) 200 nm. The Kittel fit to (a) is shown by the solid line. Simulated SW frequencies are shown by filled symbols, while the dotted lines are guide to the eye. The color map is shown at the top of the figure.

The bias-field-dependent FMR spectra for the Py nanocross arrays with 200 nm $\leq L \leq$ 600 nm are shown in Figs. 6.2(b)-(f). All the nanocross arrays show several SW modes, which depend on the bias field magnitude and the dimensions of the nanocross structures. Some important features of the bias field dependence of the SW modes are as follows. (a) With the decrease in bias field, a crossover between the two lowest frequency branches is observed at an intermediate bias field value. This is followed by observation of a minimum, then one maximum, and a subsequent decrease in frequency with further reduction in the bias field of the lowest frequency branch. (b) A continuous decrease in frequency with the decrease in bias field for the intermediate frequency branch. (c) The frequency of two highest frequency branches decreases with bias field and merges to form a single mode for an intermediate range of bias field, which is again split into two modes at a lower magnetic field and the splitting amplitude increases steeply with further reduction of the bias field value. With the variation of nanocross dimensions, the features (a) and (b) remained qualitatively similar, while some quantitative variations occur. With the reduction in the arm length (L) of the nanocross,

the crossover field and the field at which the minimum occurs both increase monotonically, while the field at which the maximum occurs decreases monotonically for feature (a). For feature (b), both the frequency values and the rate of variation of frequency with bias field increase with the reduction of arm length, L. For feature (c), however, a qualitative change also occurs in addition to the quantitative variation. With the reduction in arm length (L), both the fields at which the two frequency branches merge and then split again increase monotonically, while for $L \leq 300$ nm, both these features disappear and a single branch with frequency reducing monotonically with the bias field is observed.

To understand the experimental results, we performed micromagnetic simulations using OOMMF software [28]. The simulated arrays were mimicked from the SEM images and two-dimensional periodic boundary condition was applied for considering large areas of the arrays studied experimentally.

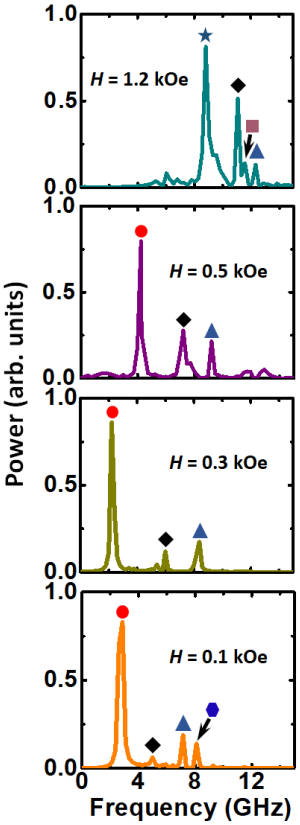

Figure 6.3: Simulated spin wave spectra of the $Ni_{80}Fe_{20}$ nanocross array with arm length (L) = 600 nm at four different bias field values. Filled colored symbols represent different SW modes.

The arrays were discretized into a number of rectangular prism-like cells with dimensions $4 \times 4 \times 20$ nm^3. The material parameters, γ, M_S, and H_K, used in the simulations were extracted from the Kittel fit of the bias-field-dependent frequency of the Py thin film as discussed earlier, while the exchange stiffness constant $A_{ex} = 1.3 \times 10^{-6}$ erg/cm is taken from literature [29]. The damping constant of 0.008 is used during dynamic simulations, while the detailed methods of simulations are described elsewhere [21]. Figures 6.2(b)-(f) show the simulated results (filled symbols), which reproduced the experimental results very well. Figure 6.3 shows some representative simulated SW spectra for the nanocross with $L = 600$ nm at different bias fields, the peak values of which are plotted as symbols in Fig. 6.2.

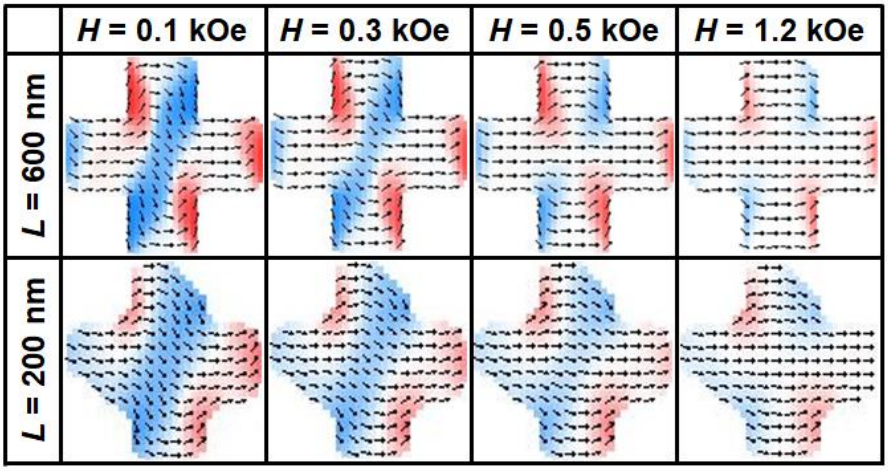

Figure 6.4: Simulated static magnetic configurations for $Ni_{80}Fe_{20}$ nanocross samples with arm length (L) of 600 nm and 200 nm at four different bias field values.

The simulated static magnetic configurations at four different bias fields and for nanocross with two different arm lengths (L) are shown in Fig. 6.4. It is clear that the onion magnetization ground state becomes more stable for the sample with $L = 200$ nm as compared to that for the sample with $L = 600$ nm. We further simulated the power and phase profiles of the SW modes using a home-built code, [30] and Fig. 6.5 shows the phase profiles of the nanocross array with $L = 600$ nm at four different bias fields.

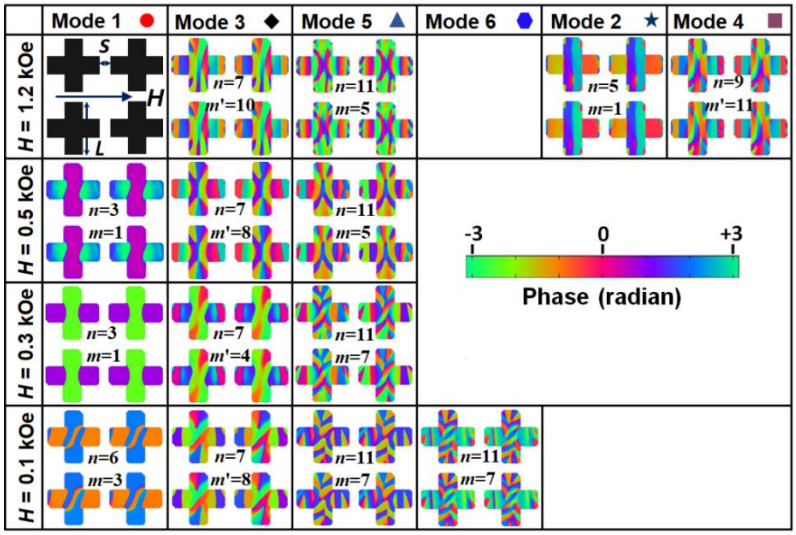

Figure 6.5: Simulated spatial distribution of phase profiles corresponding to different SW modes at four different bias field values for the $Ni_{80}Fe_{20}$ nanocross with $L = 600$ nm. The applied field direction is shown at the top left image. Symbols with different colors represent different SW modes. The color map is shown in the right side of the figure.

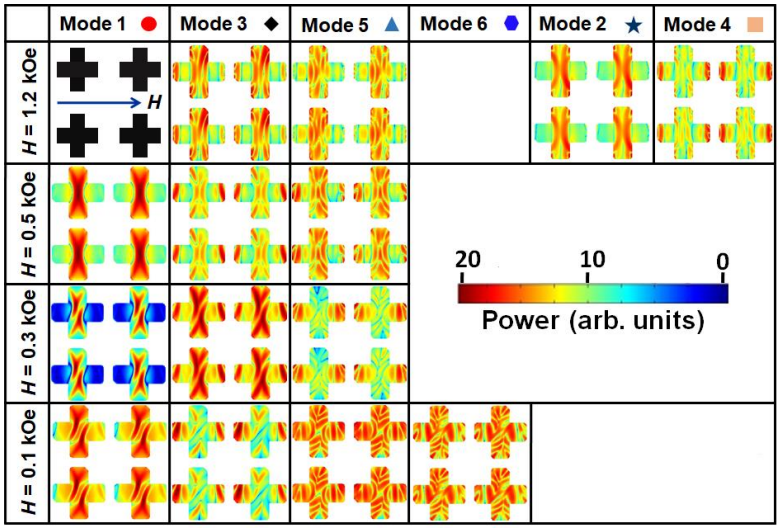

Figure 6.6: Simulated spatial distribution of power profiles corresponding to different SW modes at four different bias field values for the $Ni_{80}Fe_{20}$ nanocross with $L = 600$ nm. The applied field direction is shown at the top left image. Symbols with different colors represent different SW modes. The color map is shown in the right side of the figure.

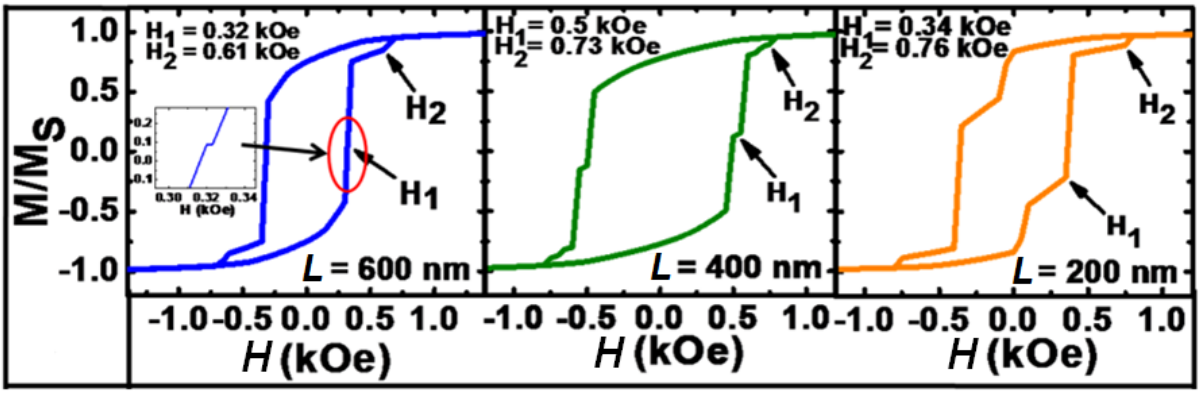

Figure 6.7: Simulated hysteresis loops corresponding to nanocrosses with $L = 600$ nm, 400 nm and 200 nm. H_1 and H_2 in these graphs correspond to two switching fields. Both H_1 and H_2 increase to with the reduction of arm length, L.

The power profiles of the same are shown in Fig. 6.6. The simulated magnetic hysteresis loops of three nanocross arrays ($L = 600$, 400 and 200 nm) are shown in Fig. 6.7.

We have divided the whole range of the bias field dependence of frequency into four significant regimes. Regime-I ranges from $H = 0$ to the minimum of the lowest frequency branch. The static magnetic configuration shows formation of an S state in this regime, which switches to an onion state at the centre of the cross in regime-II (Fig. 6.4). The static magnetic configuration shows it remains qualitatively similar for further increase in field but the spins become increasingly parallel to the bias field, which weakens the onion state. This has a strong effect on the SW modes and mode 1 is particularly affected. In regime-I, mode 1 shows a mixed backward volume (BV; n) and Damon Eshbach (DE; m) like character with mode quantization numbers $n = 6$, $m = 3$. The sudden switching of the magnetic configuration to the onion state causes a mode softening [31,32] and quantization numbers for mode 1 becomes $n = 3$, $m = 1$ and it remains like that as long as this mode exists. At $H = 0.8$ kOe, a crossover from mode 1 to mode 2 occurs (regime-III), with mode 2 showing primarily a BV-like character with $n = 5$, $m = 1$ (regime-IV). Mode 3, on the other hand, shows an azimuthal character (m') instead of the DE-like character in the vertical arm of the cross [33]. In regime-I, mode 3 is characterized by $n = 7$, $m' = 8$. However, at $H = 0.3$ kOe, where a minimum in mode 1 is observed, mode 3 becomes $n = 7$, $m' = 4$, possibly due to mode softening. In regime-II, mode 3 again shows $n = 7$, $m' = 8$. However, beyond the crossover (regime-IV), it becomes $n = 7$, $m' = 10$. The highest frequency mode shows a mode splitting for $H \leq$

0.225 kOe, with opposite slopes in the variation with bias field and the mode profiles for both modes (mode 5 and mode 6) correspond to $n = 11$, $m = 7$ but with opposite phases. The bias field variation with two opposite slopes of these two modes probably stems from a competition between the spin configurations in the two orthogonal arms of the nanocross, which increases with the reduction in the bias field.

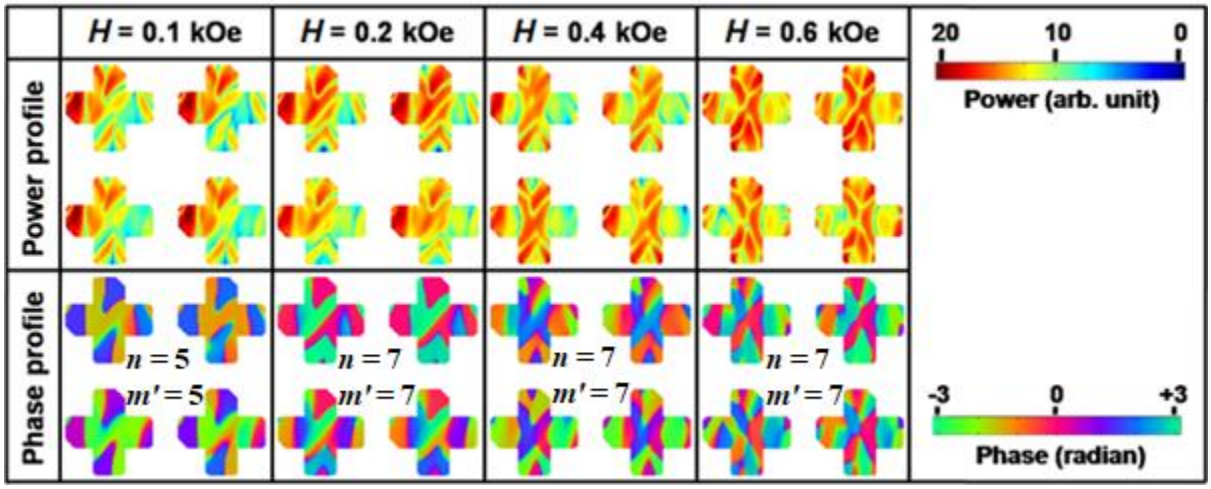

Figure 6.8: Simulated spatial distribution of power and phase profiles corresponding to the 3rd branch of SW mode at four different bias field values (H) for the nanocross with $L = 400$ nm. The color maps for the power and phase distributions are shown in the right most column of the figure.

For 0.225 kOe $\leq H \leq$ 0.62 kOe, this mode remains as a single mode but it splits again for $H \geq 0.62$ kOe, with the appearance of a new mode (mode 4) with $n = 9$, $m' = 11$. Although we characterize mode 5 and mode 6 as mixed BV-DE mode, they still have partial azimuthal character, while mode 4 is primarily azimuthal in nature. Another interesting transition occurs for $L = 400$ nm where mode 3 shows a branching for $H \leq$ 0.88 kOe, and this new mode shows a mixture of BV and azimuthal characters, which is shown in Fig. 6.8. For $L > 400$ nm, mode 3 and mode 5 show no branching with almost monotonic variation with bias field. The power profiles of the modes, as shown in Fig. 6.6, show the regions in the cross structures where the above modes are concentrated. The simulated hysteresis loops reveal the transition between different static magnetic configurations and the corresponding field values (Fig. 6.7). The variation of the transition fields with the arm length in the static magnetic configurations of the cross structures is reflected in the variation of field values at which various important features in the dynamics occurs.

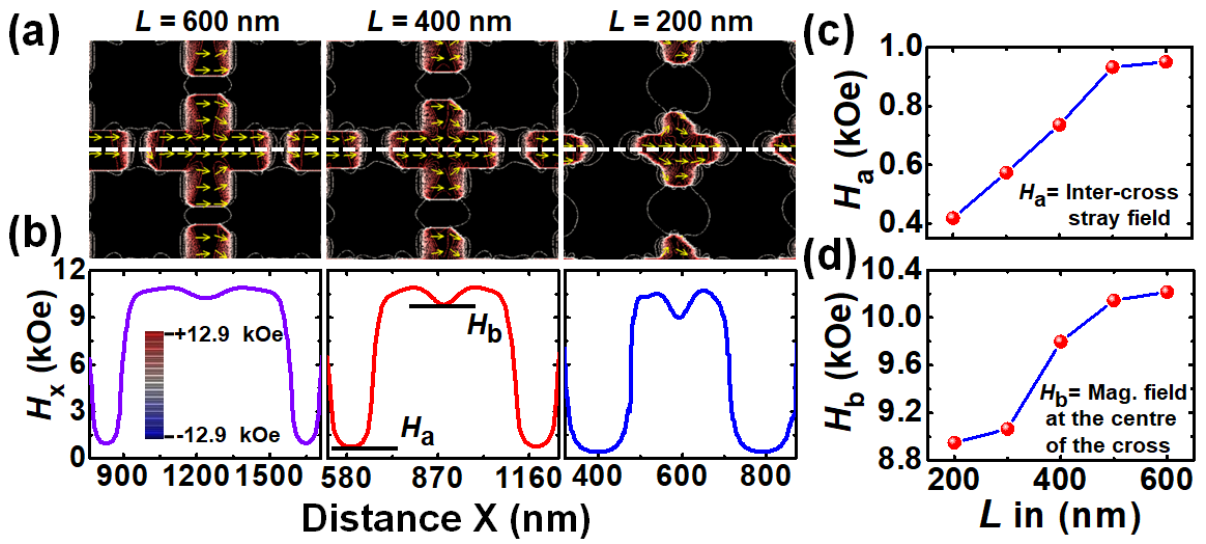

Figure 6.9: (a) Contour plots of the simulated magnetostatic field distribution in $Ni_{80}Fe_{20}$ nanocross arrays with different arm lengths (L) for $H = 0.6$ kOe. Line scans are taken along the white dotted lines. b) Line scans of the simulated magnetostatic fields. The color map is shown in the inset of bottom left of the figure. c) Inter-cross stray field and (d) effective magnetic field at the centre of the nanocross for different arm lengths.

To understand the dynamics further, we have numerically calculated the magnetostatic field distributions in the nanocross arrays, and the corresponding contour plots are shown in Fig. 6.9(a) for three different sizes of the nanocross. Since the bias field is applied along the x axis, free magnetic poles, the ensuing magnetic stray fields and demagnetizing fields are created in both horizontal and vertical arms along that direction. Line scans of the fields along the dashed lines are presented in the lower panels of Fig. 6.9(b), which reveal two important features. With the decrease in arm length (L), the inter-cross interaction fields as well the internal fields decrease monotonically as plotted in Figures 6.9(c) and 6.9(d). In particular, reduction in internal field is observed near the horizontal edges and at the centre of the cross with the reduction in L. This feature is probably responsible for shifting of the observed minima and a crossover of mode 1 to higher field values. On the other hand, having reasonably smaller values of inter-cross interaction fields, particularly for the smaller sizes of the nanocross structures, ensures observation of intrinsic modes of those nanocross structures without any significant collective effects from the arrays.

6.4 Conclusions

In summary, we investigated a bias-field-dependent evolution of static magnetic configuration and magnetization dynamics in $Ni_{80}Fe_{20}$ nanocross arrays of varying sizes using the broadband ferromagnetic resonance technique. The static magnetic configuration undergoes a transition from the S state to the onion state with the increase in the in-plane bias field and the spins further straighten towards the bias field direction with a subsequent increase in its magnitude. Consequently, the SW modes show interesting variation. The lowest SW mode shows an increase in frequency with the initial increase in bias field, followed by a maximum, a minimum, subsequent increase in frequency, and then a crossover to a higher frequency mode. The third mode shows a monotonic increase with bias field, while the higher frequency modes again show a non-monotonic behavior. Two branches of modes merge to form a single mode, which again splits into two modes with the increase in bias field. Simulated SW mode profiles show two different types of modes, a mixed BV-DE like mode and another BV like mode mixed with azimuthal modes. Mode softening occurs when the static magnetic configuration switches from S state to the onion state and the crossover is found to occur between modes with different quantization numbers. With the variation of the nanocross dimension both quantitative and qualitative variations of the dynamics occur. Calculated magnetostatic field distributions indicate the origin of the variation in the mode frequencies and mode structures and the weak inter-cross stray magnetic fields confirm nearly intrinsic nature of the dynamics of the cross without any significant collective effects from the array, particularly for the smaller nanocross structures. The large tunability of the rich SW mode structures with the external bias field and the dimension of the cross structure offer new building blocks for magnetic storage, memory, logic, and communication devices.

References

[1] R. Skomskii, J. Phys.: Condens. Matter **15**, R841 (2003).

[2] S. D. Bader, Rev. Mod. Phys. **78**, 1 (2006).

[3] N. Eibagi, J. J. Kan, F. E. Spada, E. E. Fullerton, IEEE Magn. Lett. **3**, 4500204 (2012).

[4] A. Imre, G. Csaba, L. Ji, A. Orlov, G. H. Bernstein, W. Porod, Science **311**, 205 (2006).
[5] A. Haldar, D. Kumar, A. O. Adeyeye, Nature Nanotech. **11**, 437 (2016).
[6] V. E. Demidov, S. Urazhdin, A. Zholud, A. V. Sadovnikov, S. O. Demokritov, Appl. Phys. Lett. **106**, 022403 (2015).
[7] S. K. Kim, K. S. Lee, D. S. Han, Appl. Phys. Lett. **95**, 082507 (2009).
[8] Y. Au, M. Dvornik, O. Dmytriiev, V. V. Kruglyak, Appl. Phys. Lett. **100**, 172408 (2012).
[9] S. Kaka, M. R. Pufall, W. H. Rippard, T. J. Silva, S. E. Russek, J. A. Katine, Nature **437**, 389 (2005).
[10] M. Krawczyk, D. Grundler, J. Phys. Condens. Matter **26**, 123202 (2014).
[11] B. Lenk, H. Ulrichs, F. Garbs, M. Münzenberg, Phys. Rep. **507**, 107 (2011).
[12] A. V. Chumak, V. I. Vasyuchka, A. A. Serga, B. Hillebrands, Nat. Phys. **11**, 453 (2015).
[13] A. Barman, S. Wang, J. D. Maas, A. R. Hawkins, S. Kwon, A. Liddle, J. Bokor, H. Schmidt, Nano Lett. **6**, 2939 (2006).
[14] Z. Liu, R. D. Sydora, M. R. Freeman, Phys. Rev. B **77**, 174410 (2008).
[15] P. S. Keatley, P. Gangmei, M. Dvornik, R. J. Hicken, J. Childress, J. A. Katine, Appl. Phys. Lett. **98**, 082506 (2011).
[16] S. Jung, B. Watkins, L. DeLong, J. B. Ketterson, V. Chandrasekhar, Phys. Rev. B **66**, 132401 (2002).
[17] G. Gubbiotti, G. Carlotti, T. Okuno, M. Grimsditch, L. Giovannini, F. Montoncello, F. Nizzoli, Phys. Rev. B **72**, 184419 (2005).
[18] V. V. Kruglyak, A. Barman, R. J. Hicken, J. R. Childress, J. A. Katine, J. Appl. Phys. **97**, 10A706 (2005).
[19] J. M. Shaw, T. J. Silva, M. L. Schneider, R. D. McMichael, Phys. Rev. B **79**, 184404 (2009).
[20] V. V. Kruglyak, P. S. Keatley, A. Neudert, R. J. Hicken, J. R. Childress, J. A. Katine, Phys. Rev. Lett. **104**, 027201 (2010).
[21] B. Rana, D. Kumar, S. Barman, S. Pal, Y. Fukuma, Y. Otani, A. Barman, ACS Nano **5**, 9559 (2011).
[22] B. K. Mahato, B. Rana, D. Kumar, S. Barman, S. Sugimoto, Y. Otani, A. Barman, Appl. Phys. Lett. **105**, 012406 (2014).

[23] S. Saha, R. Mandal, S. Barman, D. Kumar, B. Rana, Y. Fukuma, S. Sugimoto, Y. Otani, A. Barman, Adv. Funct. Mater. **23**, 2378 (2013).

[24] K. Machida, T. Tezuka, T. Yamamoto, T. Ishibashi, Y. Morishita, A. Koukitu, K. Sato, J. Magn. Magn. Mater. **290**, 779 (2005).

[25] B. K. Mahato, B. Rana, R. Mandal, D. Kumar, S. Barman, Y. Fukuma, Y. Otani, A. Barman, Appl. Phys. Lett. **102**, 192402 (2013).

[26] K. Nanayakkara, A. P. Jacob, A. Kozhanov, J. Appl. Phys. **118**, 163904 (2015).

[27] B. K. Mahato, S. Choudhury, R. Mandal, S. Barman, Y. Otani, A. Barman, J. Appl. Phys. **117**, 213909 (2015).

[28] M. Donahue and D. G. Porter, *OOMMF User's guide*, Version 1.0, NIST Interagency Report no. 6376, National Institute of Standard and Technology, Gaithersburg, MD, 1999.

[29] K. H. J. Buschow, *Handbook of Magnetic Materials*; North Holland: Amsterdam, The Netherlands, 2009.

[30] D. Kumar, O. Dmytriiev, S. Ponraj, A. Barman, J. Phys. D: Appl. Phys**. 45**, 015001 (2012).

[31] F. Montoncello, L. Giovannini, F. Nizzoli, P. Vavassori, M. Grimsditch, T. Ono, G. Gubbiotti, S. Tacchi, G. Carlotti, Phys. Rev. B **76**, 024426 (2007).

[32] G. F. Zhang, Z. X. Li, X. G. Wang, Y. Z. Nie, G. H. Guo, J. Magn. Magn. Mater. **385**, 402 (2015).

[33] A. A. Awad, K. Y. Guslienko, J. F. Sierra, G. N. Kakazei, V. Metlushko, F. G. Aliev, Appl.Phys. Lett. **96**, 012503 (2010).

Chapter 7

7. Tunable Angle-Dependent Magnetization Dynamics in $Ni_{80}Fe_{20}$ Nanocross Structures of Varying Size

7.1 Introduction

Arrays of nanoscale ferromagnetic dots [1] have attracted wide interest in recent years, both in terms of fundamental physics as well as for their potential applications. During the last decade, investigation of spin dynamics and spin wave (SW) [2] in such nanostructures has emerged as a very potent research area. This interest is triggered by the possibility of exploring new physics in such structures. On the other hand, due to the progress of nanolithography [3], patterned nanostructures and their arrays have emerged as systems having great potential applications such as magnetic data storage [4,5], memory [6], logic devices [7], and spin-torque nano-oscillators [8]. In nanodot arrays [9], the high surface-to-volume ratio, inhomogeneous demagnetizing field, dipole-dipole [10,11] interaction between the nanodots have significant effects on their magnetic properties and can lead to complex spin configurations within a single nanomagnet [12,13] and arrays of nanomagnets [14-20]. These complex spin configurations lead to rich variety of SW modes which have strong dependence on the strength [15] and orientation [16,17] of the applied bias magnetic field, and on the shape [18-20] and size [9,32] of nano-elements. Extensive research work has been carried out to experimentally investigate the magnetization dynamics in two-dimensional (2D) arrays of nanomagnets using time-resolved scanning Kerr microscopy (TRSKM) [21] or time-resolved magneto-optical Kerr effect (TR-MOKE) microscopy [22], ferromagnetic resonance (FMR) [23-25], and Brillouin light scattering (BLS) [26,27]; and theoretically by micromagnetic simulations [28] and other numerical and analytical methods. While the optical techniques can extract the information about local behavior of the dynamics, the ferromagnetic resonance can measure the global dynamics of a large array. In addition, due to its advantage of being a much faster measurement technique, very detailed investigations of bias field strength and angle-dependence study can be made using this technique.

Ferromagnetic cross structure has received some interest in the magnetism community due to its complex spin configuration [29]. However, the ultrafast magnetization dynamics measured by the TR-MOKE has revealed very rich dynamics with a strong configurational anisotropy [30]. Later in 2015, a report [31] proposed that ferromagnetic cross-shaped elements can be used as reconfigurable spin-based logic devices using SW scattering and interference. A more recent study [32] on cross-shaped nanodot arrays using broadband FMR measurements showed a bias field tunable magnetic configuration and magnetization dynamics, including the presence of mode softening and mode crossover. The above results have opened up the possibility of applications of ferromagnetic nanocross structures as a potential building block for magnetic storage, memory, on-chip data communication, and spin-based logic devices, and hence, thorough investigation of the magnetization dynamics of this structure with its geometric parameters and external magnetic fields has become imperative. Here, we present the experimental and numerical study of the tunability of magnetization dynamics in $Ni_{80}Fe_{20}$ (Py) nanocrosses of varying arm lengths (L) with in-plane orientation of the bias magnetic field. We use broadband FMR technique and micromagnetic simulations for this work. We show that SW mode softening can be efficiently tuned by a subtle variation of the bias magnetic field orientation. Further properties such as SW mode splitting, mode crossover, mode merging, and the number of modes can also be easily tuned by bias field orientation, which significantly depend on the size of the nanocross element. We finally discuss some possible applications of the nanocross arrays based on our observations.

7.2 Experimental Details

Arrays (200×20 μm^2) of Py nanocrosses with arm length (L) varying between 400 nm $\leq L \leq$ 600 nm, and constant edge-to-edge separation (S) of 150 nm and thickness of 20 nm, as well as a continuous Py film of 20-nm thickness were fabricated on self-oxidized Si-substrate (001) by a combination of e-beam lithography and e-beam evaporation. Py film of 20-nm thickness coated with a 60-nm-thick Al_2O_3 protective layer was deposited in an ultra-high vacuum chamber at a base pressure of 2×10^{-8} Torr on a bi-layer polymethyl methacrylate/methyl methacrylate (PMMA/MMA) resist pattern on the Si substrate made by using e-beam lithography. A coplanar waveguide (CPW) made by Au of 150-nm thickness, 30-μm central conductor width, 300-μm length, and 50-Ω nominal

characteristic impedance is deposited on top of the nanocross structures and the continuous Py film at a base pressure of 6×10^{-7} Torr. Subsequently, a Ti protective layer of 5-nm thickness is deposited on top of the Au layer at the same base pressure.

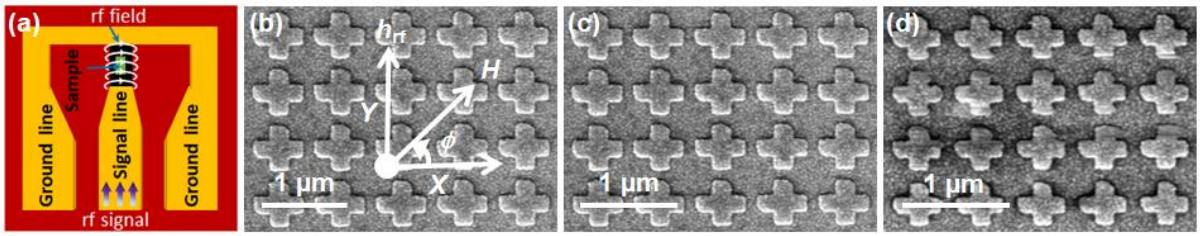

Figure 7.1: (a) Schematic of our experimental geometry. (b)-(d) Scanning electron micrographs of $Ni_{80}Fe_{20}$ nanocross arrays with varying arm lengths. The inset shows the orientation (ϕ) of the external bias magnetic field.

The waveguide is patterned by using maskless photolithography. The broadband FMR experiments are performed using a vector network analyzer (Agilent, PNA-L N5230C, 10 MHz to 50 GHz) and a homebuilt high-frequency probe station with a nonmagnetic G-S-G type probe (GGB Industries, Model No. 40A-GSG-150-EDP) [33]. A microwave output excitation is swept in a broad frequency range with power of -15 dBm and fed into the CPW structure, generating a microwave magnetic field h_{rf} along the y axis of the nanocross array. Additionally, an in-plane magnetic field, H, is applied along a varying in-plane angle ϕ with respect to the x axis and the output signal (S_{11}) is collected from the CPW in the reflection geometry. The measured reflection spectra are normalized by a reference measurement at a high static magnetic field. A rotating electromagnet is used to apply an in-plane bias magnetic field up to 1.6 kOe. All the experiments are carried out at room temperature.

7.3 Results and Discussion

Figure 7.1(a) shows a schematic of the experimental setup. Figures 7.1(b)-(d) show scanning electron micrographs (SEMs) of all three arrays with cross arm lengths (L) of 600, 500, and 400 nm. The bias magnetic field orientation (ϕ) is shown in Fig. 7.1(b). The SEM images show that the cross structures suffer from some edge deformations and rounded corners, which increase with the reduction of L. The sizes of the individual crosses and their separations in the arrays also vary by up to about $\pm$ 8%.

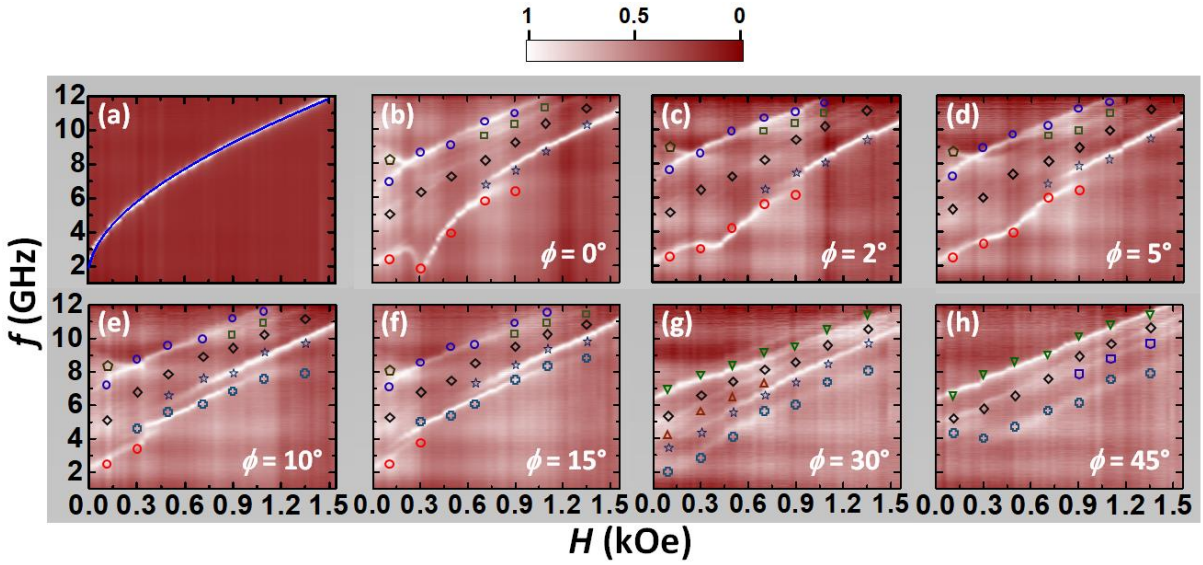

Figure 7.2: Surface plots of the bias-field-dependent SW mode frequencies for (a) thin film of 20-nm thickness and nanocross array with arm length (L) of 600 nm and for the bias field orientation (ϕ) of (b) 0°, (c) 2°, (d) 5°, (e) 10°, (f) 15°, (g) 30°, and (f) 45°. (a) The Kittel fit is shown by the solid line. Simulated SW frequencies are shown by unfilled symbols. The color map is shown at the top of the figure.

The external bias-field-(H) dependent FMR frequency (f) of the Py thin film is also measured and the data is fitted with the Kittel formula [34], which is given by:

$$f = \frac{\gamma}{2\pi}\sqrt{(H + H_K)(H + H_K + 4\pi M_s)} \tag{7.1}$$

to extract the magnetic parameters of the Py film. The magnetic parameters obtained from the fitting are saturation magnetization (M_S) = 850 emu/cc, gyromagnetic ratio (γ) = 17.85 MHz/Oe, and the anisotropy field (H_K) = 0. These will be further used for numerical micromagnetic simulations of the FMR spectra of the Py nanocross structures.

The bias-field-dependent FMR spectra (real part of S_{11} parameter) for Py nanocross arrays with 400 nm $\leq L \leq$ 600 nm at different bias field orientations are shown in Figs. 7.2-7.4. They show rich SW properties, which vary non-monotonically with the bias field magnitude. These include the observation of a crossover between the two lowest frequency branches, followed by a sharp minima and maxima of the lowest frequency branch and merging of the two highest frequency branches followed by a Y-shaped mode splitting of the highest frequency branch with the decreasing bias field.

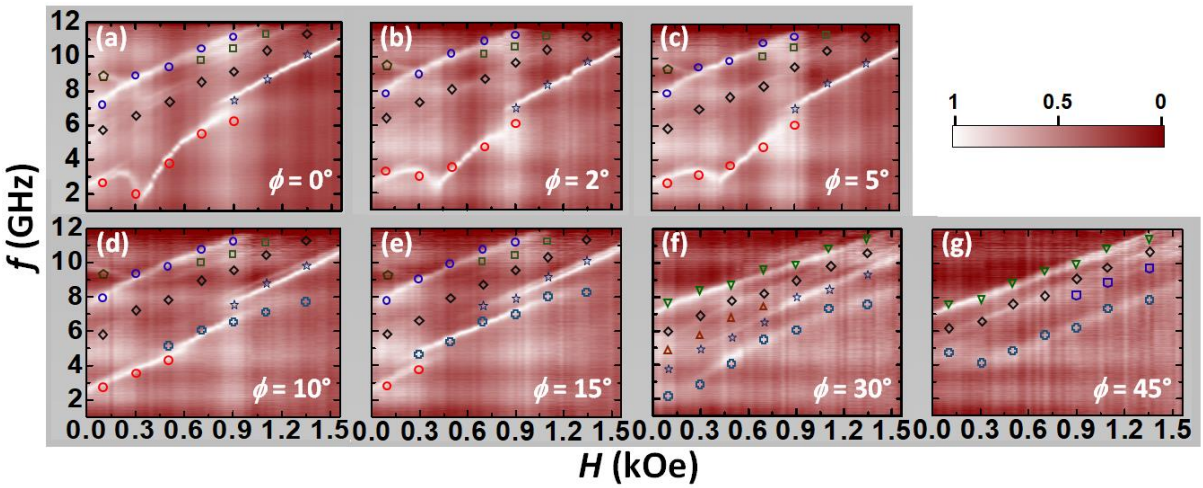

Figure 7.3: Surface plots of the bias-field-dependent SW mode frequencies for a nanocross array with arm length (L) of 500 nm and for the bias field orientation (ϕ) of (a) 0°, (b) 2°, (c) 5°, (d) 10°, (e) 15°, (f) 30°, and (g) 45°. Simulated SW frequencies are shown by unfilled symbols. The color map is shown at the right side of the figure.

These features are further modified by changing the nanocross dimensions, i.e., the magnitude of the bias field at which these features appear shifts toward higher field values with the reduction of nanocross arm length. Our purpose here is to study how these fascinating features are affected by the orientation of the bias magnetic field and whether new features can be generated.

The dip in the lowest frequency branch (Fig. 7.2(b)), which is a signature of mode softening appearing due to the variation in static magnetic configuration from an S state to the onion state, reduces significantly and shifts drastically to a higher field value as the bias field angle ϕ is rotated by only 2° (Fig. 7.2(c)). This trend continues up to 5° (Fig. 7.2(d)), beyond which the dip disappears and instead a mode crossover appears at around 300 Oe for $\phi = 10°$ for the nanocross array with $L = 600$ nm. This continues up to 15°, beyond which the crossover also disappears and at $\phi = 45°$ a dip starts to appear again. The bias field for crossover between the two lowest branches at around 700 Oe suddenly extends over a broad field range at $\phi = 10°$ with the appearance of a new SW branch and the crossover completely disappears at $\phi = 30°$.

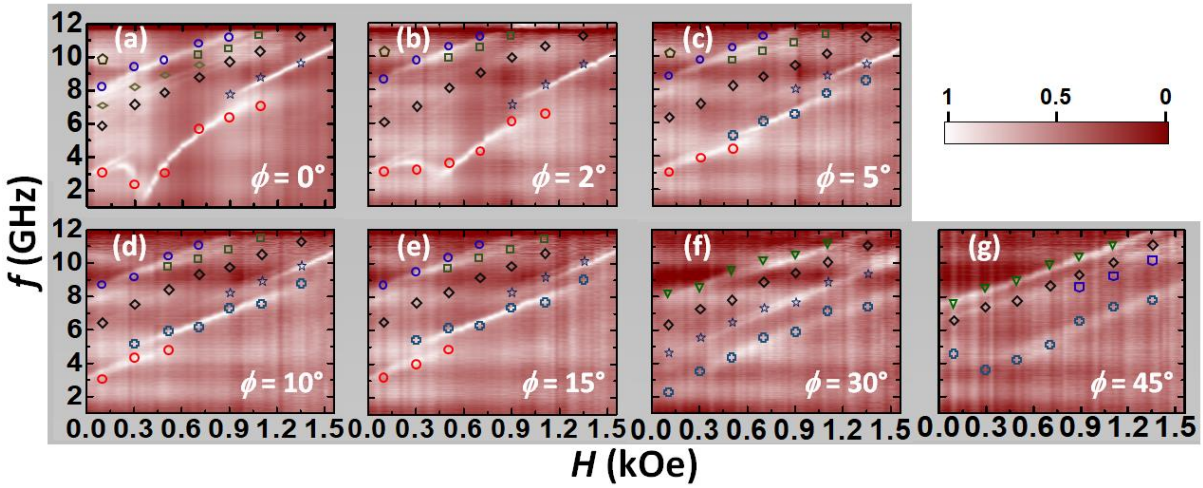

Figure 7.4: Surface plots of the bias-field-dependent SW mode frequencies for a nanocross array with arm length (L) of 400 nm and for the bias field orientation (ϕ) of (a) 0°, (b) 2°, (c) 5°, (d) 10°, (e) 15°, (f) 30°, and (g) 45°. Simulated SW frequencies are shown by unfilled symbols. The color map is shown at the right side of the figure.

The merging of the two highest frequency branches at around 500 Oe gets blurred at ϕ = 10° and disappears at ϕ = 30°. The Y-shaped mode splitting of the two highest frequency branches with positive and negative slopes appearing at around 150 Oe for ϕ = 0° shifts to higher bias field values with increasing values of ϕ, which finally disappears at ϕ = 30°.

Table 7.1: Effect of varying the dimensions of a nanocross structure on the critical angles of four prime features observed in the spin wave dynamics.

Arm length (L)	Disappearance of mode softening & creation of new mode crossover	Disappearance of Y shape (mode splitting) at lower H value	Disappearance of mode crossover at higher H value	Appearance of mode splitting at higher H value
L = 600 nm	$\phi_a \approx 10°$	$\phi_b \approx 15°$	$\phi_c \approx 10°$	$\phi_d \approx 45°$
L = 500 nm	$\phi_a \approx 10°$	$\phi_b \approx 10°$	$\phi_c \approx 15°$	$\phi_d \approx 45°$
L = 400 nm	$\phi_a \approx 5°$	$\phi_b \approx 5°$	$\phi_c \approx 30°$	$\phi_d \approx 45°$

With the variation of the nanocross dimensions, some more changes are observed. For example, (a) the disappearance of the dip and consequent onset of crossover for the sample with L = 500 nm still occurs at ϕ_a = 10°, but the effect is rather feeble, while for L = 400 nm, the same occurs at ϕ_a = 5°. (b) The disappearance of the Y-shaped mode splitting occurs at $\phi_b \approx 15°$ for L = 600 nm and gradually decreases to $\phi_b \approx 10°$ for L = 500 nm and $\phi_b \approx 5°$ for L = 400 nm. (c) The disappearance of mode crossover at higher

field value, on the other hand, increases from $\phi_c \approx 10°$ at $L = 600$ nm to 15° and 30° for $L = 500$ nm and 400 nm, respectively. (d) On the contrary, the angle for the appearance of mode splitting at a higher field value for the intermediate frequency branch remains unaltered with the arm length of the nanocross. These observations are tabulated in Table (7.1). Here, ϕ_a, ϕ_b, ϕ_c, and ϕ_d correspond to the angles where features described as (a), (b), (c) and (d) above occur, respectively.

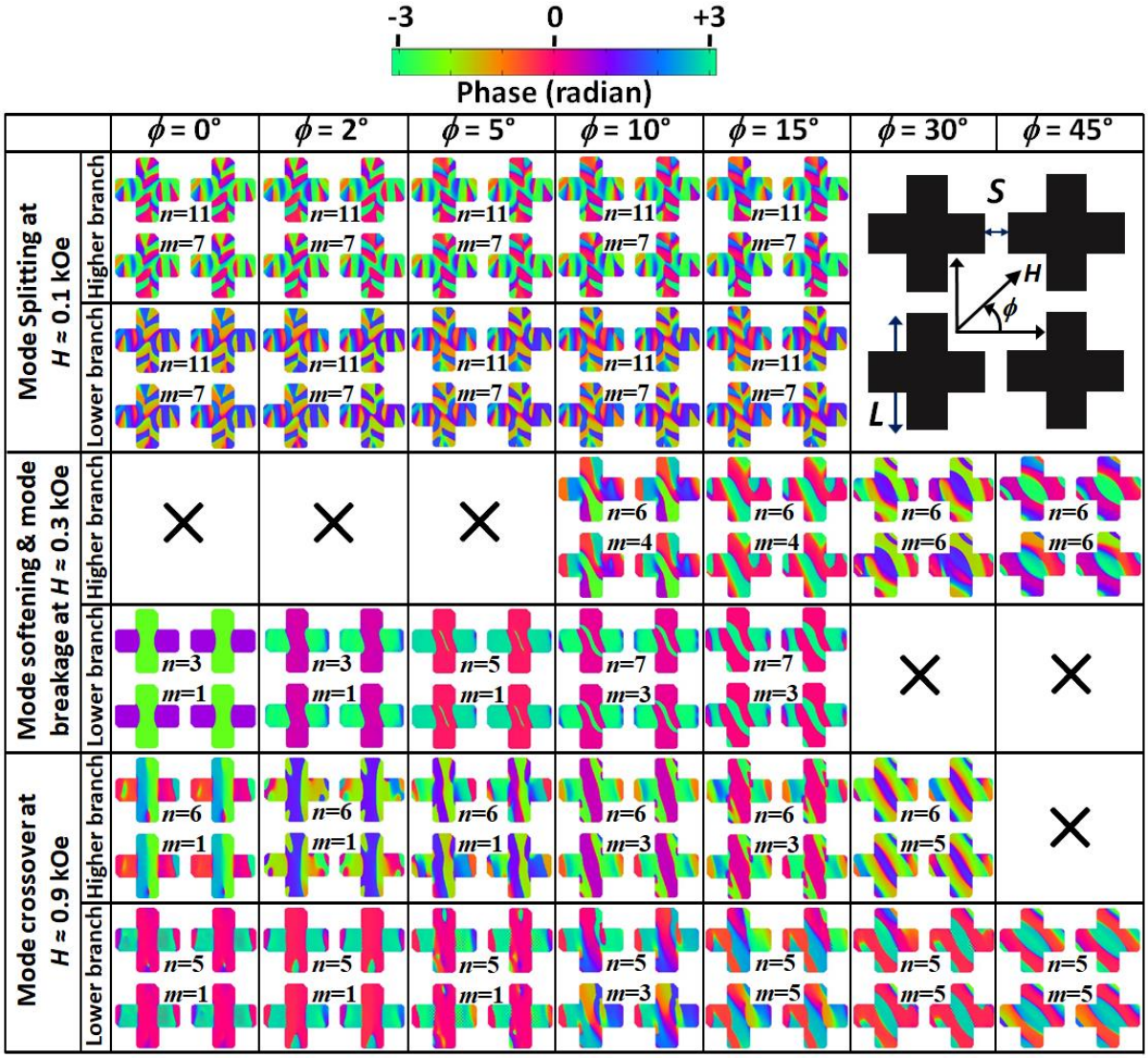

Figure 7.5: Simulated spatial distribution of phase profiles corresponding to different salient SW modes at seven ϕ values and three different bias-field values for a $Ni_{80}Fe_{20}$ nanocross array with $L = 600$ nm. The color map is shown at the top of the figure.

To interpret the experimental results, we perform micromagnetic simulations by using OOMMF [35] software. The arrays for performing the simulation are mimicked from the SEM images and a 2D periodic boundary condition (2D-PBC) was applied for

considering large areas of the arrays studied experimentally. The arrays are discretized into a number of rectangular prism-like cells of $4 \times 4 \times 20$ nm^3 dimensions. The material parameters of the sample such as γ, M_S, and H_K used in the simulations are extracted from the Kittel fit of the bias-field-dependent frequency of the Py thin film as discussed earlier, while the exchange stiffness constant $(A_{ex}) = 1.3 \times 10^{-6}$ erg/cm is taken from literature [36]. The damping constant is used as $\alpha = 0.008$ during dynamic simulations.

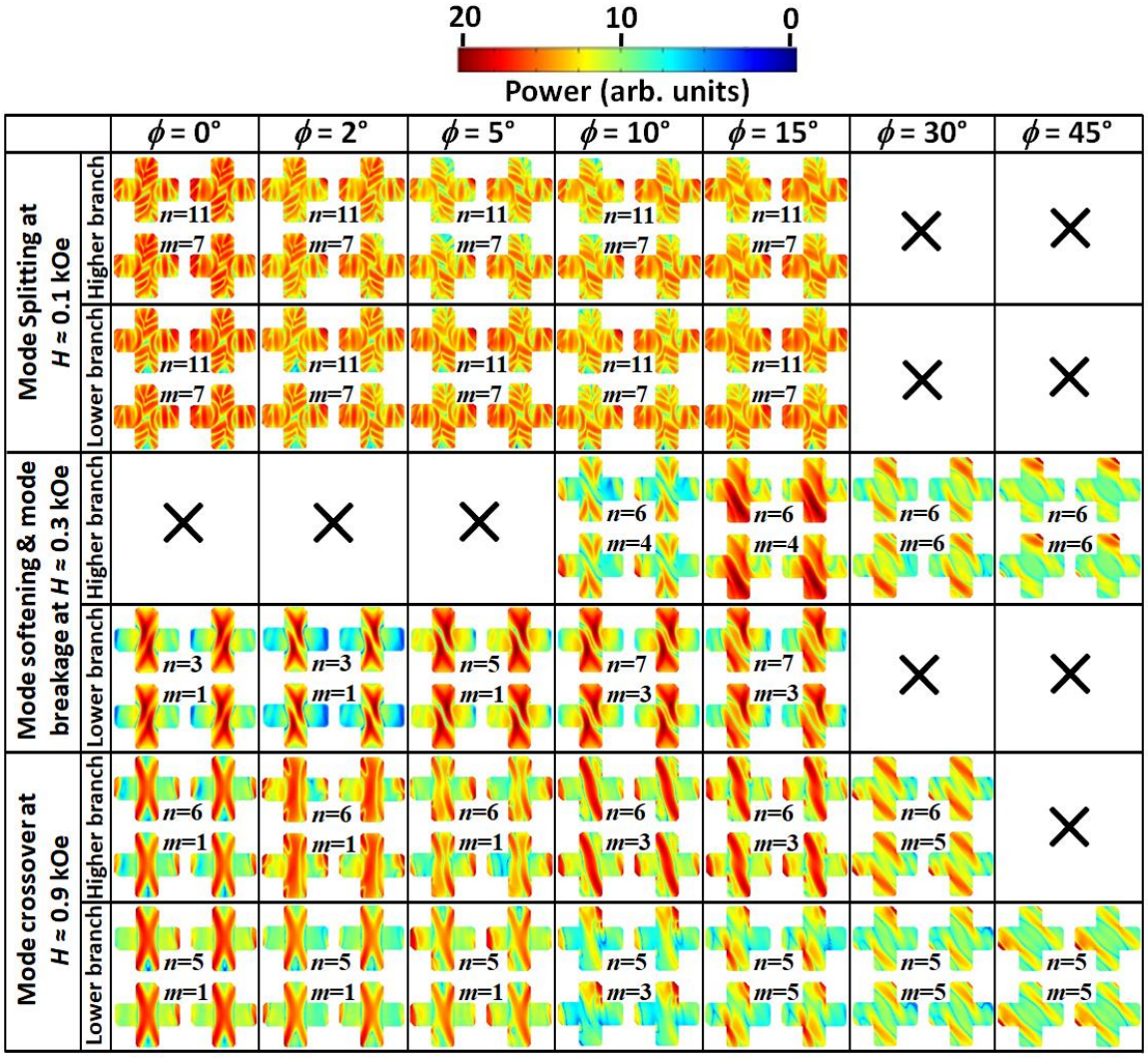

Figure 7.6: Simulated spatial distribution of power profiles corresponding to different salient SW modes at seven ϕ values and three different bias-filed values for a $Ni_{80}Fe_{20}$ nanocross array with $L = 600$ nm. The color map is shown at the top of the figure.

The detailed methods of simulations are described elsewhere. Figures 7.2-7.4 show the simulated SW frequencies as a function of the magnetic field (unfilled symbols), which

reproduce all the important features of the experimental results very well. We further simulate the power and phase profiles of the SW modes using a home-built code [37].

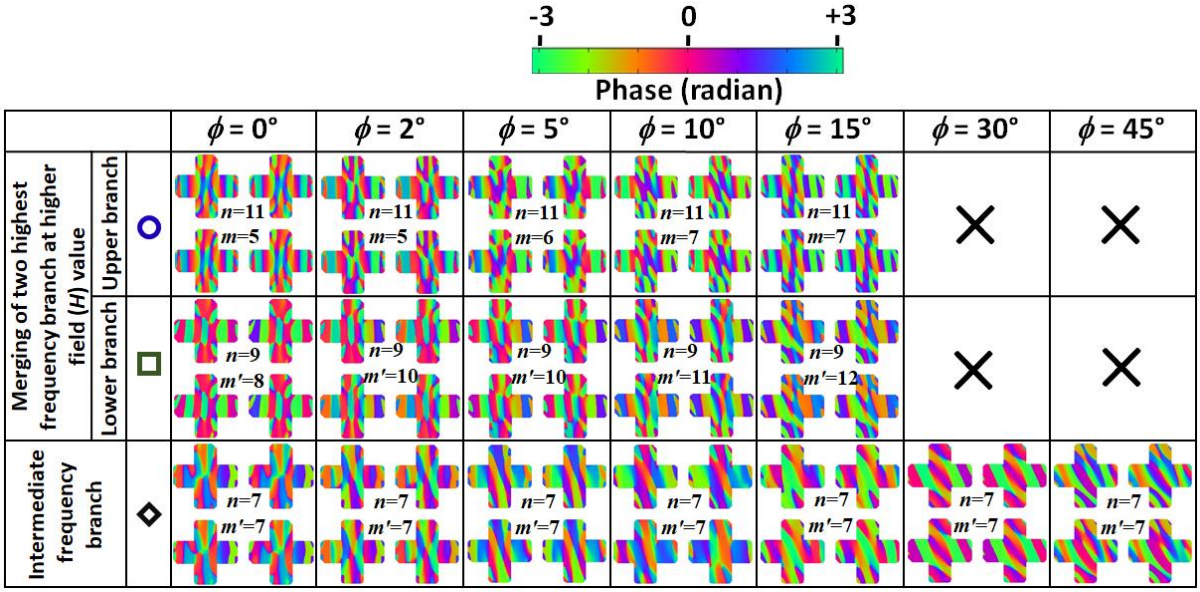

Figure 7.7: Simulated spatial distribution of phase profiles of two highest frequency branches which merge with the reduction of bias field, and the intermediate frequency branch at $H =$ 0.9 kOe for the nanocross array with $L =$ 600 nm at different values of ϕ.

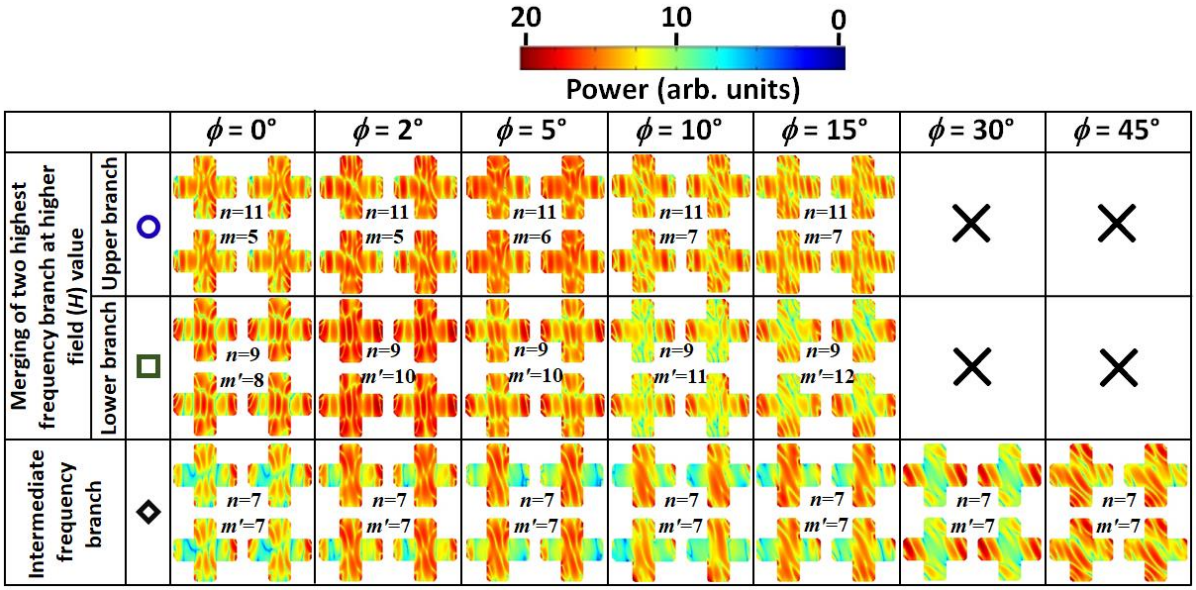

Figure 7.8: Simulated spatial distribution of power profiles of two highest frequency branches which merge with the reduction of bias field, and the intermediate frequency branch at $H =$ 0.9 kOe for the nanocross array with $L =$ 600 nm at different values of ϕ.

Figure 7.5 shows the simulated spatial distribution of phase profiles for various SW modes of the nanocross array with $L = 600$ nm at three different bias fields (H) and seven different ϕ values. The power profiles of the same are shown in Fig. 7.6. SW modes with an azimuthal character [32] do not show significant changes with ϕ due to azimuthal symmetry.

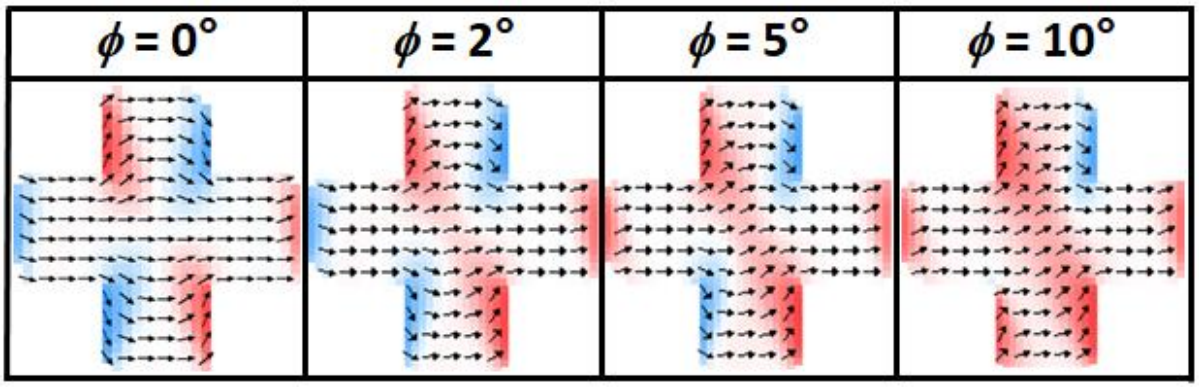

Figure 7.9: Simulated static magnetic configurations for a nanocross array with arm length (L) of 600 nm at bias field (H) = 0.5 kOe for four different ϕ values. We have shown a single cross from the center of the array to prominently represent spin configurations.

The simulated spatial distribution of phase and power profiles corresponding to the two highest frequency branches, which merge with the reduction of H and an intermediate frequency branch at $H = 0.9$ kOe for nanocross array with $L = 600$ nm are shown in Figs. 7.7 and 7.8, respectively. The new mode, which appears from the splitting of the highest frequency branch at a higher H value, and the intermediate frequency branch, which shows monotonic increase of the resonance frequency with H, both show an azimuthal character instead of a Damon-Eshbach (DE) character. We mainly focus here on radial SW modes. As ϕ changes, the phase profiles of both of the SW modes of feature (a) remain the same. These modes show a mixed backward volume (BV; n) and Damon-Eshbach (DE; m)-like character with mode quantization numbers $n = 11$ and $m = 7$ with opposite phases. The higher frequency branch of feature (a) disappears at $\phi \approx 15°$ for $L = 600$ nm. From the phase profile, the reason for the disappearance of mode softening with the increase of ϕ becomes clear. Mode softening is the result of the sudden switching of the magnetic configuration from the S state to the onion state. Figure 7.9 shows that a subtle increase in ϕ wipes away the onion state and the S state appears and

stabilizes with further increase in ϕ as the bias field helps to align the spins accordingly. Consequently, as ϕ increases, the height of the minima due to mode softening decreases and the position of the minima shifts to a higher field value. For $H \approx 0.3$ kOe at $\phi \geq 5°$, the S state of magnetic configuration starts to arise again. Beyond the critical angle (ϕ_a), a mode crossover appears at the position of the minima, which is probably due to the reformation of the S state. For feature (b) at $\phi = 0°$, the mode quantization numbers are $n = 3$ and $m = 1$, which transform to a new mode with $n = 7$ and $m = 3$ at $\phi = 15°$ for $H = 0.3$ kOe. A new SW mode appears at the position of mode softening due to mode splitting at $\phi \approx 10°$ with mode quantization numbers $n = 6$ and $m = 4$ for $\phi = 10°$, which changes to $n = 6$ and $m = 6$ for $\phi = 45°$. The higher frequency branch of feature (c) changes qualitatively with the variation of ϕ. The mode quantization numbers of this mode are modified to $n = 6$ and $m = 5$ at $\phi = 30°$ from $n = 6$ and $m = 1$ at $\phi = 0°$. The mode quantization numbers of the lower frequency branch of feature (b) are $n = 5$ and $m = 1$ at $\phi = 0°$, which transform to $n = 5$ and $m = 5$ at $\phi = 45°$. The size of the nanocross structure also has a significant effect on the above-mentioned features (Table 7.1). For feature (a), the ϕ_a value at which the disappearance of mode softening and the creation of a new mode crossover occur decreases with the reduction in L. This confirms that the bias field is more crucial for the lower dimension of nanocross in the case of mode softening. The ϕ_a value related to the disappearance of mode splitting at the lower field decreases monotonically with the decrement in L. The competition between the spin configurations in the two orthogonal arms is the reason for the appearance of this mode splitting. As L decreases, the competition gets weaker as configurational anisotropy drops, which might be a possible reason for the decrease of ϕ_b with a reduction in L. Interestingly, the ϕ_c values in feature (c) increase with the increment in L. The higher frequency branch between the two modes of this mode crossover is primarily showing a BV-like mode character and it appears at $H \approx 0.7$ kOe for $L = 600$ nm. This mode crossover shifts to a higher H value as L decreases. This is responsible for the increment of ϕ_c with the decrease of L. At $\phi = 45°$, the components of the bias field in both the orthogonal arms become equal, which may be responsible for the occurrence of the minima in the lowest frequency mode at an intermediate H value. A new mode splitting appears at a higher H value for $\phi = 45°$, which is independent of the size of the nanocross in this size regime.

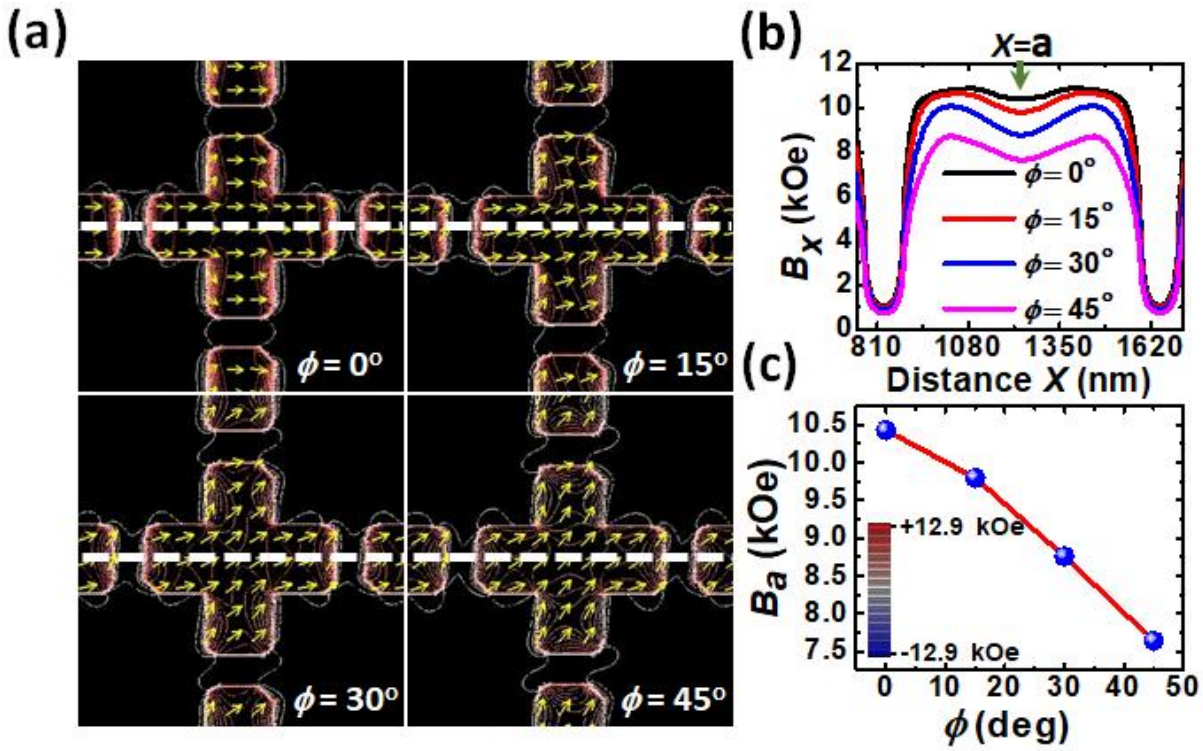

Figure 7.10: (a) Contour plots of the simulated magnetostatic field distribution in a $Ni_{80}Fe_{20}$ nanocross array with arm length $L = 600$ nm in four different orientations (ϕ) of bias field for $H = 0.6$ kOe. Line scans are taken along the white dotted lines. (b) Line scans of the simulated magnetostatic fields. The color map is shown in the inset of the bottom right of the figure. (c) Effective magnetic field at the centre of the nanocross for different ϕ values.

To further understand the dynamics, we have numerically calculated the magnetostatic field distributions in the nanocross arrays and the corresponding contour plots are shown in Fig. 7.10(a) for four different orientations (ϕ) of the bias field. The important observation here is that with the increase of the ϕ value, the magnetic stray field-line density inside the nanocross structures increases, which is probably due to increase of the uncompensated magnetic charges in the nanocross structures in the direction of the bias field along both arms. Line scans of the fields along the dashed lines are presented in Fig. 7.10(b), which reveal an important feature. With the increase of ϕ, the internal fields decrease monotonically as plotted in Fig. 7.10(c).

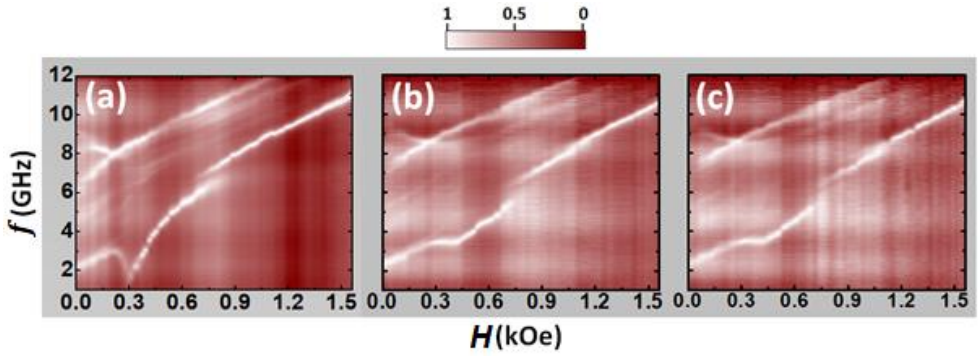

Figure 7.11: Surface plots of bias-field-dependent SW mode frequencies for nanocross arrays with arm length (L) of 600 nm and for the edge-to-edge separation (S) of (a) 150 nm, (b) 250 nm, and (c) 350 nm. The color map is shown at the top of the figure.

For $\phi = 0°$, the maximum stray field value is $B_X \approx 10.4$ kOe, which decreases to $B_X \approx 7.6$ kOe at $\phi = 45°$. In particular, a reduction of the internal field is observed near the center of the cross with an increase in ϕ. This feature is probably responsible for the increase of ϕ_c with a reduction in L. Figure 7.10(b) shows that the width of the stray field distribution along the x axis at maximum B_X value decreases with an increase in ϕ. The calculated magnetostatic field distributions indicate weak intercross stray magnetic fields. However, even such a weak interaction field has some effect on the dynamics, particularly at lower bias field value. We perform FMR measurement for nanocross arrays with an arm length (L) of 600 nm and with the edge-to-edge separations (S) of 150, 250, and 350 nm. Figure 7.11 shows that the variation of S from 150 to 250 nm affects the minimum in the frequency for the lowest frequency branch due to mode softening, while no further changes occur as S is increased to 350 nm.

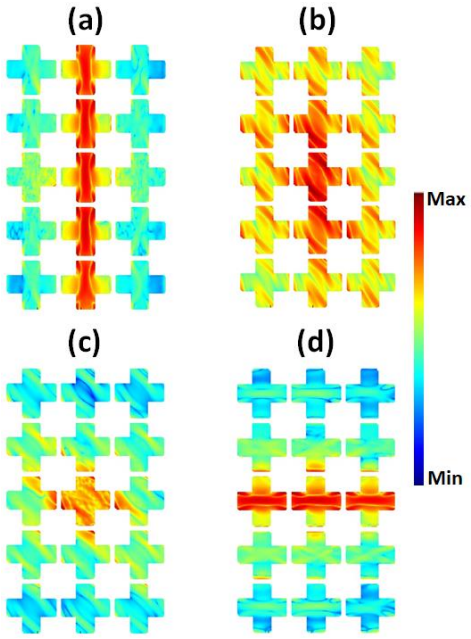

Figure 7.12: Simulated power profiles of spin wave mode of frequency (f) 8.4 GHz excited locally at the centre of the array for (a) $\phi = 0°$, (b) $\phi = 25°$, (c) $\phi = 45°$ and (d) $\phi = 90°$ geometries.

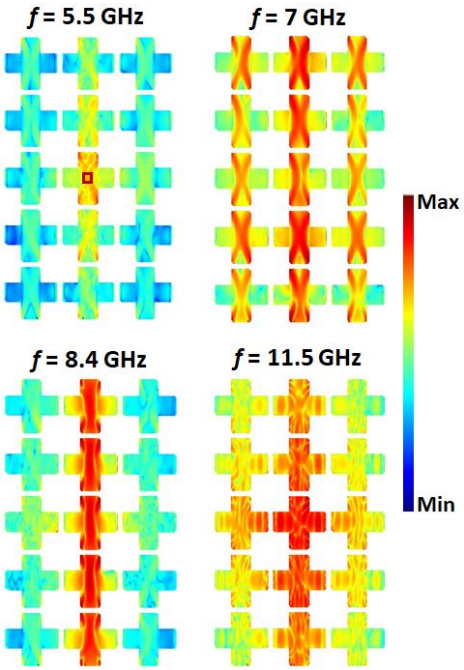

Figure 7.13: Simulated power profiles of SW modes of different frequencies.

Figure 7.12 provides an exemplary demonstration of how the SW propagation direction can be manipulated using a nanocross array. To that end, using OOMMF software, we launch a time-varying field of "sinc" profile (frequency cutoff of 30 GHz) at the center of the array over a small square region of 100 × 100 nm^2 area. We then simulate the

propagation of the SW mode at $f = 8.4$ GHz for different orientations of the bias field. For $\phi = 0°$, the beam propagates along the vertical direction, for $\phi = 90°$, the beam propagates along the horizontal direction, for $\phi = 25°$ the beam propagates nearly isotropically in all directions, while at $\phi = 45°$, the beam cease to propagate. This property may lead to possible applications of the nanocross array as a directional coupler or splitter. Figure 7.13 demonstrates a proposal of how a densely packed nanocross array may be used as a frequency-dependent coupler. The above possible applications promote ferromagnetic nanocross arrays as building blocks of a variety of spintronic and magnonic devices.

7.4 Conclusions

In summary, we investigate the magnetization dynamics in $Ni_{80}Fe_{20}$ nanocross arrays of varying sizes as a function of the orientation (ϕ) of an external bias magnetic field using a broadband FMR technique. As the bias field orientation (ϕ) deviates from 0°, the chances of formation of onion state decrease. Consequently, the height of the dip in the lowest frequency branch reduces and the dip position shifts to a higher H value. Further increase of ϕ causes a new mode crossover at lower H value in the place of the dip. Interestingly, the frequency difference between modes for mode crossover at a higher H value increases with the increment of ϕ and further increases of ϕ leads toward the disappearance of this high-field crossover resulting in two nearly parallel SW modes at $\phi = 30°$, while at $\phi = 45°$, the higher frequency branch disappears. The intermediate frequency branch shows a monotonic increase of frequency with the bias field. The orientation of the bias magnetic field (ϕ) strongly affects the Y-shaped mode splitting of the highest frequency branch at a lower H. The frequency gap between these two modes decreases with the increment of ϕ. Finally, at $\phi = \phi_b$, this mode splitting disappears. Higher field mode splitting shifts to a lower H value with the enhancement of ϕ and finally disappears. The number of SW modes decreases at $\phi = 45°$ compared to $\phi = 30°$. At $\phi = 45°$, the lowest frequency branch shows again a minimum at the intermediate H. A simulated SW mode profiles show that the modes showing strong dependence on the bias field angle are of mixed BV & DE character. Interestingly, the DE mode quantization number m increases with ϕ for most SW modes. With the variation of the nanocross dimension, both quantitative and qualitative variations of the magnetization dynamics occur. Calculated magnetostatic field distributions reveal the origin of the variation in

the SW mode frequencies and mode profiles. Such an ability to tune the spin configuration and magnetization dynamics in a nanocross structure by a subtle variation of the external bias field angle is very important for the design of magnetic storage, memory, logic, and magnonic devices as demonstrated by our further micromagnetic simulations.

References

[1] S. D. Bader, Rev. Mod. Phys. **78**, 1 (2006).

[2] S. O. Demokritov, B. Hillebrands, A. N. Slavin, Phys. Rep. **348**, 441 (2001).

[3] J. I. Martin, J. Nogues, K. Liu, J. L. Vicent, Ivan K. Schuller, J. Magn. Magn. Mater. **256**, 449 (2003).

[4] B. D. Terris, T. Thomson, J. Phys. D: Appl. Phys. **38**, R199 (2005).

[5] T. Thomson, G. Hu, B. D. Terris, Phys. Rev. Lett. **96**, 257204 (2006).

[6] Y. Wang, F. Xiu, Y. Wang, J. Zou, W. P. Beyermann, Y. Zhou, K. L. Wang, Nanoscale Res. Lett. **6**, 134 (2011).

[7] A. Imre, G. Csaba, L. Ji, A. Orlov, G. H. Bernstein, W. Porod, Science **311**, 205 (2006).

[8] S. Kaka, M. R. Pufall, W. H. Rippard, T. J. Silva, S. E. Russek, J. A. Katine, Nature **437**, 389 (2005).

[9] J. M. Shaw, T. J. Silva, Phys. Rev. B **79**, 184404 (2009).

[10] P. P. Horley, A. Sukhov, J. Berakdar, L. G. Trapaga-Martinez, Eur. Phys. J. B **88**, 165 (2015).

[11] V. Novosad, K. Yu. Guslienko, H. Shima, Y. Otani, S. G. Kim, K. Fukamichi, N. Kikuchi, O. Kitakami, Y. Shimada, Phys. Rev. B **65**, 060402 (2002).

[12] A. Barman, S. Wang, J. D. Maas, A. R. Hawkins, S. Kwon, A. Liddle, J. Bokor, H. Schmidt, Nano Lett. **6**, 2939 (2006).

[13] P. S. Keatley, P. Gangmei, M. Dvornik, R. J. Hicken, J. R. Childress, J. A. Katine, Appl. Phys. Lett. **98**, 082506 (2011).

[14] G. Gubbiotti, G. Carlotti, T. Okuno, M. Grimsditch, L. Giovannini, F. Montoncello F. Nizzoli, Phys. Rev. B **72**, 184419 (2005).

[15] G. Gubbiotti, M. Conti, G. Carlotti, P. Candeloro, E. D. Fabrizio, K. Y. Guslienko, A. Andre, C. Bayer, A. N. Slavin, J. Phys.: Condens. Matter **16**, 7709 (2004).

[16] C. Schoeppner, K. Wagner, S. Stienen, R. Meckenstock, M. Farle, R. Narkowicz, D. Suter, J. Lindner, J. Appl. Phys. **116**, 033913 (2014).

[17] X. Cui, S. Yakata, T. Kimura, Physica E **75**, 28 (2016).
[18] Y. P. Ivanov, A. I. Ilin, E. V. Pustovalov, K. V. Nefedov, L. A. Chebotkevich, The Physics of Metals and Metallography **113**, 222 (2012).
[19] B. K. Mahato, B. Rana, D. Kumar, S. Barman, S. Sugimoto, Y. Otani, A. Barman, Appl. Phys. Lett. **105**, 012406 (2014).
[20] Z. Liu, R. D. Sydora, Phys. Rev. B **77**, 174410 (2008).
[21] V. V. Kruglyak, P. S. Keatley, A. Neudert, R. J. Hicken, J. R. Childress, J. A. Katine, Phys. Rev. Lett. **104**, 027201 (2010).
[22] V. V. Kruglyak, A. Barman, R. J. Hicken, Phys. Rev. B **71**, 220409 (2005).
[23] S. Jung, B. Watkins, L. Delong, J. B. Ketterson, V. Chandrasekhar, Phys. Rev. B **66**, 132401 (2002).
[24] G. N. Kakazei, Yu. G. Pogorelov, M. D. Costa, T. Mewes, P. E. Wigen, P. C. Hammel, V. O. Golub, T. Okuno, V. Novosad, Phys. Rev. B **74**, 060406 (2006).
[25] O. N. Martyanov, V. F. Yudanov, R. N. Lee, S. A. Nepijko, H. J. Elmers, C. M. Schneider, G. Schonhense, Appl. Phys. A **18**, 679 (2005).
[26] Z. K. Wang, H. S. Lim, V. L. Zhang, J. L. Goh, S. C. Ng, H. L. Su, S. L. Tang, M. H. Kuok, Nano Lett. **6**, 1083 (2006).
[27] G. Gubbiotti, M. Madami, S. Tacchi, G. Carlotti, T. Okuno, J. Appl. Phys. **99**, 08C701 (2006).
[28] A. Barman, S. Barman, Phys. Rev. B **79**, 144415 (2009).
[29] K. Machida, T. Tezuka, T. Yamamoto, T. Ishibashi, Y. Morishita, A. Koukitu, K. Sato, J. Magn. Magn. Mater. **290**, 779 (2005).
[30] B. K. Mahato, B. Rana, R. Mandal, D. Kumar, D. Kumar, S. Barman, Y. Fukuma, Y. Otani, A. Barman, Appl. Phys. Lett. **102**, 192402 (2013).
[31] K. Nanayakkara, A. P. Jacob, A. Kozhanov, J. Appl. Phys. **118**, 163904 (2015).
[32] K. Adhikari, S. Choudhury, R. Mandal, S. Barman, Y. Otani, A Barman, J. Appl. Phys. **121**, 043909 (2017).
[33] A. Barman, J. Sinha, Springer International Publishing AG, 2018.
[34] Charles Kittel, Phys. Rev. **73**, 155 (1948).
[35] M. Donahue and D. G. Porter, OOMMF User's Guide, Version 1.0, NIST Interagency Report No. 6376, National Institute of Standard and Technology, Gaithersburg, MD, 1999.

[36] K. H. J. Buschow, *Handbook of Magnetic Materials* (North Holland, Amsterdam, The Netherlands, 2009).
[37] D. Kumar, O. Dmytriiev, S. Ponraj, A. Barman, J. Phys. D: Appl. Phys. **45**, 015001 (2012).

Chapter 8

8. Large Nonlinear Ferromagnetic Resonance Shift and Strong Magnon-Magnon Coupling in $Ni_{80}Fe_{20}$ Nanocross Array

8.1 Introduction

Hybrid systems have emerged as strong candidates in quantum information processing [1] where quantum states are coherently transferred from one medium to another using different carrier such as superconducting qubits, optical and microwave photons, spin ensembles, and phonons. To this end, coupling of magnons and microwave photons in a resonator has been extensively studied [2-5]. In this system, magnons in magnetic materials with high spin density are utilized where the 'coupling strength' is collectively enhanced by square root of number of spins (N) to overcome the weaker coupling strength (g_0) between individual spins and the microwave field, i.e., $g = g_0\sqrt{N}$ [2,6]. Recently, magnon-magnon interactions in ferromagnetic heterostructures [7] and interlayer coupled atoms in two-dimensional antiferromagnet $CrCl_3$ [8] have been demonstrated. However, for on-chip integration of hybrid systems scalability to nanoscale is important, which is nontrivial from the $\sqrt{N}$ dependence. Although recent papers have claimed magnon-magnon coupling in ferromagnetic nanowires of tens of micrometers length [9,10], strong coupling in nanoscale magnets in all three dimensions remains elusive.

The nonlinear ferromagnetic resonance (FMR) in thin films and nanostructures has attracted attention over the years because nonlinearity can lead to a wide variety of effects, e.g., premature saturation of magnetic resonance [11], spin wave (SW) instabilities [12-15], auto-oscillations [16], solitons [17], chaos [18], as well as Bose-Einstein condensation [19] of excited magnons. Early experiments in nonlinear FMR concentrated mainly on determining the magnetic-field threshold of SW instability in ferromagnetic thin films [20,21] and few nonlinear FMR measurements [22-24] in

nanostructured samples have been reported. Recent studies [25-27] of SW dynamics in $Ni_{80}Fe_{20}$ (Py) nanocross structures manifested a variety of anisotropic SW properties by tuning both applied bias field strength and orientation, including the presence of SW mode softening and mode splitting. Hence, this structure can be considered for an interesting testbed for studying nonlinear FMR effect and magnon-magnon coupling.

In this paper, we report strong magnon-magnon coupling in Py nanocrosses with the help of broadband FMR technique and micromagnetic simulations. The number of spins in the nanocross structure is several orders of magnitude smaller than the smallest value ($N \sim 10^{13}$) reported in the literature [10]. We observe two anticrossing phenomena with anticrossing gaps as large as 1.03 GHz at a bias field of about 0.8 kOe for microwave power, $P = +4$ dBm. Both the anticrossing gaps show strong dependence on microwave power. We find that the strong magnon-magnon coupling originates from dynamic dipolar interactions between neighbouring nanocross structures, driven by the microwave power. We also observe power-dependent large FMR shift depending on the bias field strength. The observation of a negative FMR frequency shift at high bias field and a positive FMR frequency shift at low bias field with increased microwave power stems from the two contrasting internal spin configurations of the nanocross structure.

8.2 Experimental Details

A continuous Py film of 20 nm thickness and Py nanocross array with arm length (L) of 600 nm, edge-to-edge separation (S) of 150 nm, and thickness of 20 nm were fabricated on self-oxidized Si-substrate (001) by a combination of e-beam lithography and e-beam evaporation at a base pressure of 2×10^{-8} Torr. A coplanar waveguide (CPW) made by Au of 150 nm thickness, having 30 μm central conductor width (w), 300 μm length, and 50 Ω nominal characteristic impedance (Z_0), was integrated on top of the nanocross array at a base pressure of 6×10^{-7} Torr. Subsequently, a Ti protective layer of 5 nm thickness was deposited on top of the Au layer at the same base pressure. We excite and detect SWs using CPWs integrated on top of the nanocross array. Excitation power of the microwave input signal is varied in the range of -15 dBm to $+4$ dBm by a vector network analyzer (VNA). Additionally, an in-plane bias magnetic field, H, is applied along the x axis and the output scattering parameter S_{11} for reflection is measured by the VNA connected with the CPW [27]. The surface topography of the sample is measured by scanning electron microscope.

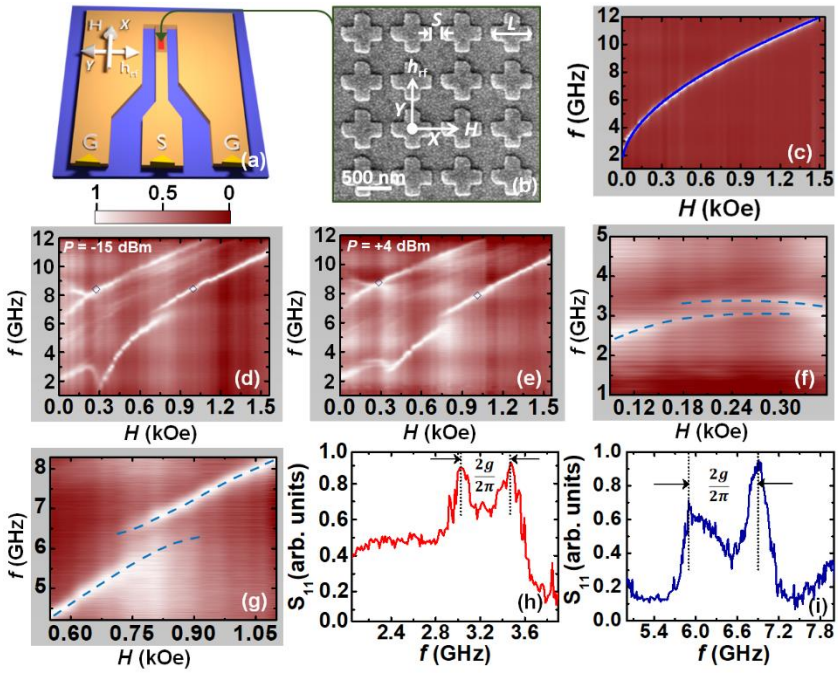

Figure 8.1: Schematic of the experimental geometry. The directions of the bias field (H) and rf field (h_{rf}) are shown in the schematic. (b) Scanning electron micrograph of Py nanocross array. The inset again shows the orientation of H with respect to h_{rf}. (c) Surface plot of bias-field-dependent SW mode frequencies for Py thin film of 20 nm thickness at excitation power of $P = -15$ dBm. The Kittel fit is shown by solid line. Surface plots of bias-field-dependent SW mode frequencies for nanocross array at (d) $P = -15$ dBm and (e) $P = +4$ dBm, respectively. (f) First and (g) second anticrossings from the nanocross array. The dotted line is to guide the eye. Real part of S_{11} parameter as a function of frequency to highlight (h) first anticrossing and (i) second anticrossing. The frequency gap in the anticrossing mode reveals the coupling strength $g/2\pi$.

8.3 Results and Discussion

Figure 8.1(a) represents a schematic of the experimental setup. Figure 8.1(b) shows a scanning electron micrograph (SEM) of a ferromagnetic nanocross array. The applied bias field orientation is shown in the inset of Fig. 8.1(b). The SEM image shows that the fabricated structures suffer from slight edge deformations and rounded corners. All these deformations have been incorporated in the micromagnetic simulations as described later. Figure 8.1(c) shows the applied bias field (H)-dependent FMR frequency, f, of the Py thin film and the data are fitted with the Kittel formula [28], which is given by:

$$f = \frac{\gamma}{2\pi}\sqrt{(H + H_K)(H + H_K + 4\pi M_s)} \tag{8.1}$$

to extract the magnetic parameters of Py. The magnetic parameters extracted from the fit are, saturation magnetization $(M_S) = 850$ emu/cc, gyromagnetic ratio $(\gamma) = 17.85$ MHz/Oe and the anisotropy field $(H_K) = 0$. These parameters will be further used to numerically simulate the FMR spectra of the Py nanocross array using micromagnetic simulations.

The bias-field-dependent FMR spectra (real part of S_{11} parameter) for Py nanocross array at $P = -15$ dBm is shown in Fig. 8.1(d), which reveals rich anisotropic SW properties and FMR mode frequencies vary nonmonotonically with the bias field magnitude.

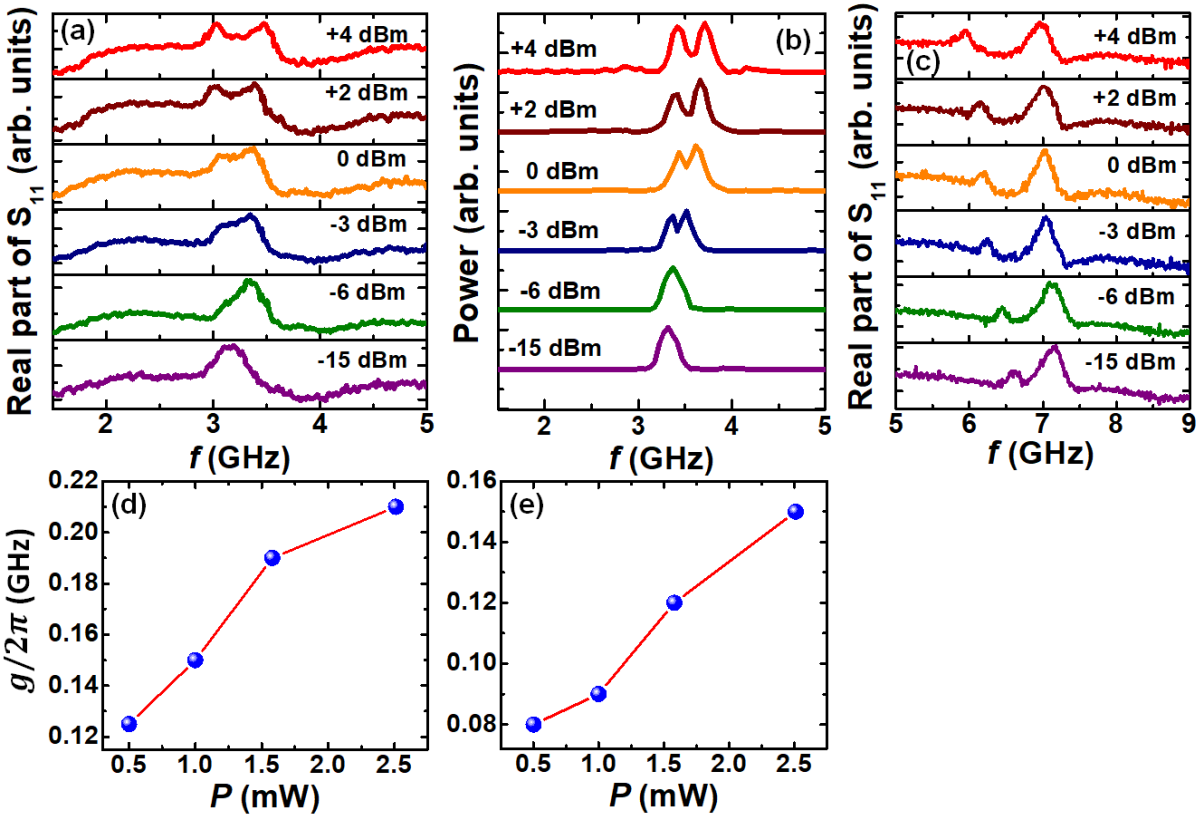

Figure 8.2: (a) Real part of S_{11} parameters of lowest frequency SW branch as a function of frequency at $H = 0.29$ kOe for different values of P showing the first anticrossing. (b) Simulated SW spectra for the same. (c) Real part of S_{11} parameters of lowest frequency SW branch as a function of frequency at $H = 0.8$ kOe for different values of P showing the second anticrossing. (d) Experimental and (e) simulated values of $g/2\pi$ as a function of P for the first anticrossing are shown by filled symbols. The solid lines are lines joining the symbols.

We observe merging of the two highest frequency branches followed by a Y-shaped mode splitting of the highest frequency branch and an anticrossing between the two lowest frequency branches, followed by sharp minima and maxima of the lowest frequency branch with the decreasing bias field value [26,27]. Our goal is to study how these fascinating features respond to the nonlinear magnetic effects arising from higher microwave excitation power.

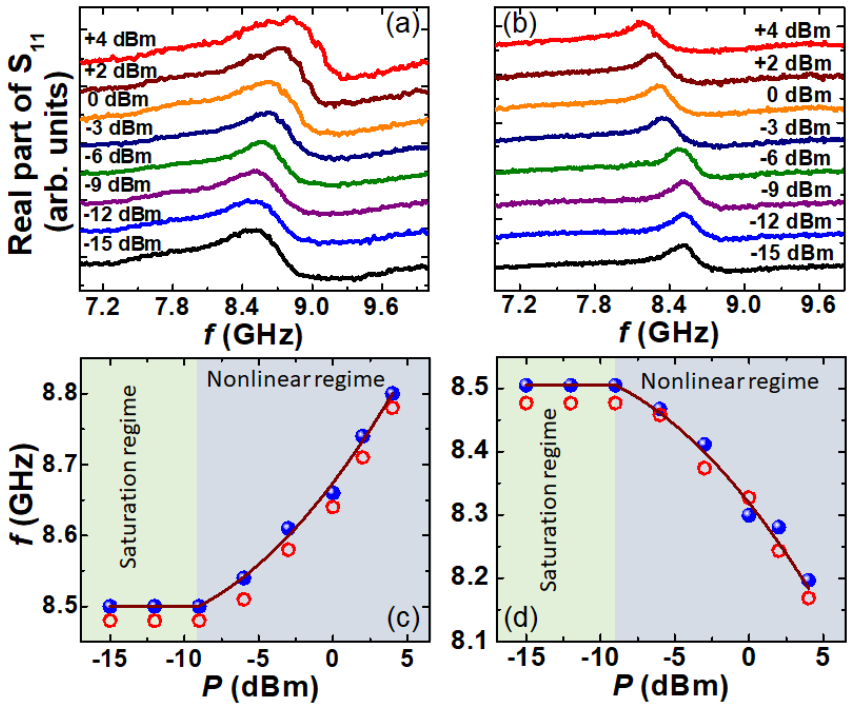

Figure 8.3: (a) Real part of S_{11} parameters as a function of frequency for highest frequency SW branch from nanocross array for different values of P at (a) $H = 0.3$ kOe and (b) $H = 1.025$ kOe, respectively. Ferromagnetic resonance peak frequencies as a function of microwave excitation power show (c) positive shift at $H = 0.3$ kOe and (d) negative shift at 1.025 kOe, respectively. Filled spherical symbols correspond to experimental and unfilled circular symbols correspond to simulated results. The saturation and nonlinear regimes of magnetization dynamics are indicated by two different color shades.

The sudden dip in the lowest frequency branch (Fig. 8.1(d)), which is a signature of mode softening appearing due to the variation in static magnetic configuration from an S state to the onion state, reduces significantly and shifts drastically to higher field value with the increment of P (Fig. 8.1(e)). Figures 8.1(f) and 8.1(g) represent two anticrossings phenomena. First and second anticrossings appear at around $H = 0.29$

kOe and 0.8 kOe, respectively. The inter-nanocross magnon-magnon coupling strength $g/2\pi$ is defined as half of the minimal peak-to-peak frequency spacing in the anticrossing, which is shown in Figs. 8.1(h) and 8.1(i) for the first and second anticrossings, respectively. First anticrossing in the spectrum starts to appear at $H \approx 0.29$ kOe for $P \geq -6$ dBm in Fig. 8.2(a). Figure 8.2(b) shows the simulated SW spectra as a function of P at $H = 0.29$ kOe. The power-dependent FMR spectra showing the second anticrossing are presented in Fig. 8.2(c). The $g/2\pi$ value is tunable by P, which is shown experimentally in Fig. 8.2(d) and by simulation in Fig. 8.2(e) for the first anticrossing. We have also calculated the magnon-magnon cooperativity [9] $C = \frac{g^2}{k^2}$, where $k/2\pi$ is average half width at half maximum of the linewidth. We have obtained a large value of $C = 0.28$ for the first anticrossing at $P = +4$ dBm [9]. For the second anticrossing, we have obtained a $g/2\pi$ value of 0.515 GHz and the corresponding C value of 0.60 at $P = +4$ dBm. The second anticrossing exhibits remarkably large $g/2\pi$ and C values.

To investigate the nonlinear FMR shift with microwave excitation power, we have chosen two different SW modes with same frequency of $f \approx 8.5$ GHz from two different branches of the FMR spectra, indicated in Figs. 8.1(d) and 8.1(e). The variations of the peak frequencies with P for these two modes are illustrated in Figs. 8.3(a) and 8.3(b). Remarkably, both positive and negative FMR frequency shifts are observed as a function of P at two different bias field strengths. At lower bias field (0.29 kOe, i.e., less than mode softening field, in S state), the sign is positive, and at higher field (1.025 kOe, in saturated state), the sign becomes negative. We have plotted the peak frequencies of the SW branches at $H = 0.3$ kOe and $H = 1.025$ kOe for different P values which are shown by filled spherical symbol in Figs. 8.3(c) and 8.3(d), respectively.

To interpret the experimental results, we have performed micromagnetic simulations by using Object Oriented Micromagnetic Framework (OOMMF) [29] software. The mimicked array from the SEM image has been discretized into rectangular prism-like cells of $4 \times 4 \times 20$ nm^3 dimensions and two-dimensional periodic boundary condition was applied. The lateral dimensions of the cells were taken below the exchange length (~5 nm), $l_{\text{ex}} = \sqrt{\frac{2A_{ex}}{\mu_0 M_S^2}}$ of Py. The material parameters of the sample such as γ, M_S, and H_K used in the simulations were extracted from the Kittel fit of the bias-field-dependent frequency of the Py thin film as discussed earlier, while the exchange stiffness constant $(A_{ex}) = 1.3 \times 10^{-6}$ erg/cm was taken from the literature [30]. The damping constant

was used as $\alpha = 0.008$ during dynamic simulations. To observe the magnetization dynamics, we first simulated the static magnetic ground state at desired bias field value and then a sinusoidal excitation field [$h_{\mathrm{rf}} = h_{\mathrm{d}}{*}\cos(wt)\hat{y}$] was applied along the y axis of the array to trigger the precessional dynamics. The amplitude of the microwave excitation field was given by $h_{\mathrm{d}} = \sqrt{\frac{P}{(4Z_0 w^2)}}$ [31], where P is the microwave power, Z_0 is the characteristic impedance of the CPW, and w is the central conductor width of the CPW. We have computed the z component of the magnetization dynamics data after turning off the sinusoidal excitation field. Consequently, we have performed first Fourier transformation on simulated time-resolved data to obtain the SW power spectra. Figure 8.2(b) shows the simulated SW spectra as a function of P at $H = 0.29$ kOe, which reproduces the first anticrossing quite well. The simulated $g/2\pi$ values as a function of P are plotted in Fig. 8.2(e). Figures 8.3(c) and 8.3(d) show the simulated SW peak frequencies as a function of excitation power by unfilled circular symbol at $H = 0.3$ kOe and $H = 1.025$ kOe, respectively. Simulation results qualitatively reproduce all the important features of the experimental results as discussed above. Experimental results reveal that there is no significant nonlinear effect up to $P = -9$ dBm. The threshold of microwave power (P_{th}) for the onset of nonlinear dynamics is found to be about -6 dBm.

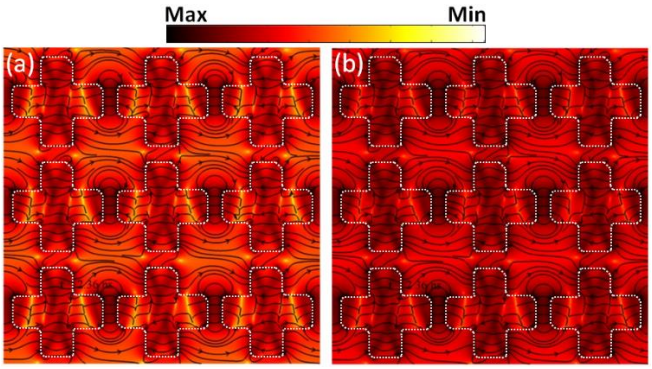

Figure 8.4: Simulated stray field distribution between the neighbouring nanocrosses at (a) $P = -15$ dBm and (b) $P = +4$ dBm, respectively, at $H = 0.3$ kOe. The color map is shown at the top of the figure.

The experimental data [Figs. 8.3(c) and 8.3(d)] fit with a function given by $f = aP + bP^2 + c$, showing the nonlinear power dependence. We have also calculated the stray-field distribution between neighboring nanocrosses. Figures 8.4(a) and 8.4(b) show stray field distribution at $P = -15$ dBm and $P = +4$ dBm, respectively. Significant decrease of

uncompensated magnetic charge is observed, when microwave power is increased from −15 dBm to +4 dBm, due to increment of dynamic dipolar interaction between the neighboring nanocrosses.

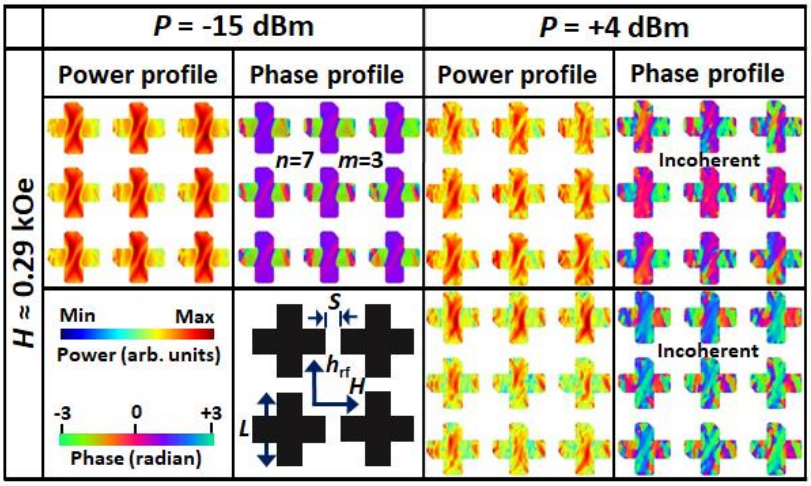

Figure 8.5: Simulated spatial distribution of power and phase profiles corresponding to lowest frequency SW branch, which shows SW anticrossing at higher excitation powers. The color maps are shown in the inset.

We have further simulated the spatial distribution of power and phase profiles of SW modes using a home-built code [32]. Figure 8.5 represents simulated spatial distribution of power and phase profiles at two extreme P values corresponding to the lowest frequency SW mode, which shows anticrossing at higher microwave powers ($P \geq -3$ dBm). Simulated power and phase profiles reveal that a mixed backward volume (n)–Damon-Esbach (m) mode (7, 3) in the low-P regime transforms into a rather incoherent mode as P enters into the nonlinear regime. The observed reduction in the dip and the increase in the bias field value corresponding to the mode softening with the increase in P is associated with the shift in the dynamic magnetization from its equilibrium direction due to the increase in the rf excitation field at large value of P. A sharp change in the magnetization state from S state to onion state is thereby halted, leading to the observed behavior.

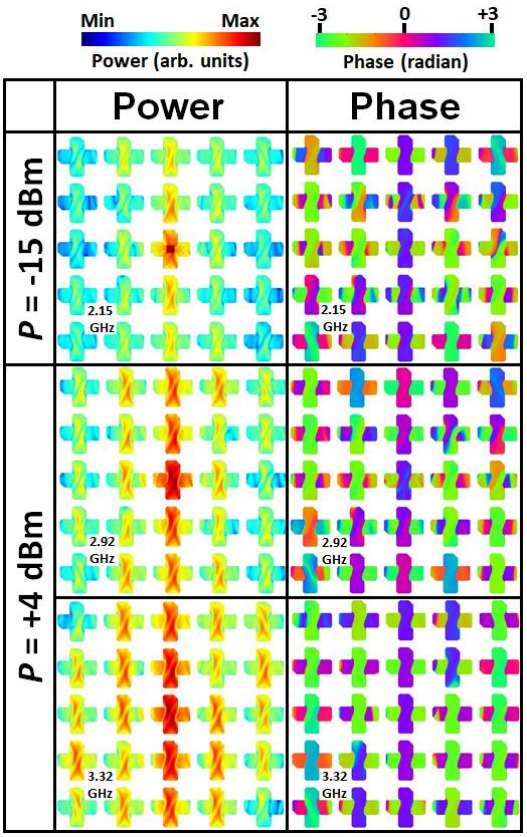

Figure 8.6: Simulated spatial distribution of power and phase profiles of lowest frequency SW mode(s). We have locally excited the center of the array with excitation power of $P = -15$ dBm and $P = +4$ dBm. At $P = -15$ dBm, only a single mode was observed at 2.15 GHz, while at $P = +4$ dBm, two modes appear at 2.92 GHz and 3.32 GHz due to the anticrossing. The color map is shown at the top of the figure.

Figure 8.6 shows that the observed anticrossing at low field (0.29 kOe) with large P values can be understood from the observed spatial power and phase maps for those two frequency modes. To this end, using OOMMF software, we have launched a time-varying field of "sinc" profile (frequency cutoff of 20 GHz) at the center of the array over a small square region of 100 nm × 100 nm area. We have then simulated the spatial distribution of power and phase profiles for the lowest frequency SW mode(s) at two extreme P values. At $P = -15$ dBm, the spatial power corresponding to this mode is weak on the array, while the phase shows sharp changes due to mode quantization. On the contrary, at $P = +4$ dBm, the spatial power distribution is stronger over the whole array for both the modes. However, while the spatial phase change is sharp and regular for the lower frequency mode, it is rather incoherent showing random-phase fluctuations for the higher frequency mode.

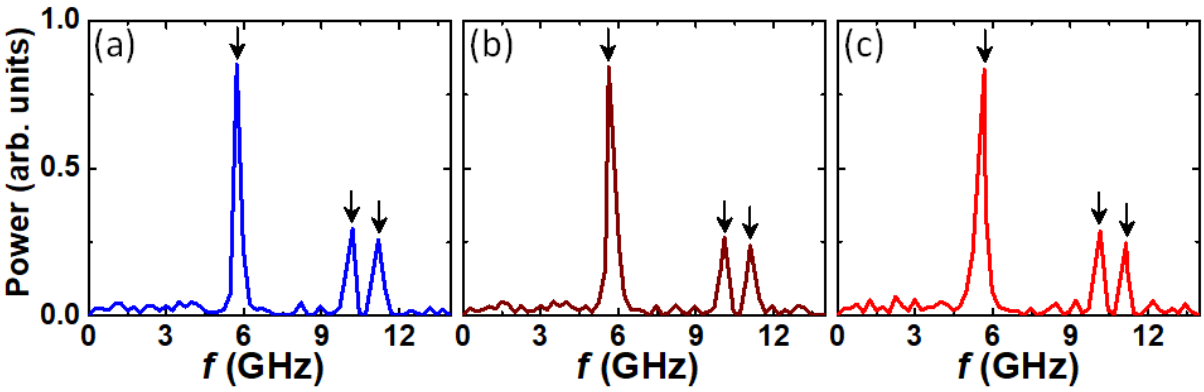

Figure 8.7: Simulated SW spectra of a single Py nanocross at bias field value of $H = 0.8$ kOe at three different values of microwave excitation power of (a) $P = -15$ dBm, (b) $P = 0$ dBm and (c) $P = +4$ dBm, respectively. The second anticrossing observed in the nanocross array is absent in all these spectra from a single Py nanocross.

The strong coupling between these two magnon modes leads to the observed anticrossing induced by the microwave excitation power. The increase in microwave power also increases the dynamic dipolar interactions between the nanocross structures (Fig. 8.4), which boasts the magnon-magnon interactions responsible for the appearance and increment of the first anticrossing gap, as well as the continuous increment of the second anticrossing gap. This is further confirmed by the numerical simulation of microwave power dependent FMR spectra of a single Py nanocross, which does not open any anticrossing gap even at the highest power of +4 dBm as shown in Fig. 8.7. In ref. 21, positive and negative shifts of FMR frequency at low and high bias field, respectively, were reported in a Py thin film. However, the positive and negative shifts were asymmetric and the negative shift was negligibly small even at a very high power. On the other hand, in Py elliptical nanodots again positive and negative frequency shifts were observed but both shifts were observed at a very large microwave power [22]. On the contrary, we have observed relatively large and symmetric positive and negative frequency shifts of up to 0.35 GHz at much smaller microwave power of +4 dBm as opposed to the above two reports. The answer to this lies in the nanocross structure and its rich and flexible spin configurations. The nanocross structure shows drastic variation in spin configurations with bias magnetic field strength as described before [26].

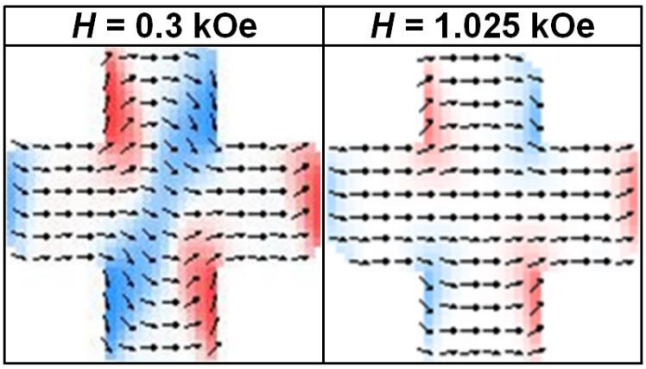

Figure 8.8: Simulated static magnetic configurations for Py nanocross array at two different bias magnetic field values. We have shown here a single nanocross from the center of the array to prominently represent the spin configurations. The nanocross structure shows a drastic variation in spin configurations with bias magnetic field strength.

At large bias field (e.g., 1.025 kOe), the spins are nearly aligned along the bias field direction (*x* axis) and increased microwave excitation power increases the magnitude of the rf field along the *y* axis. This causes a reduction of the effective field along the bias field direction leading towards a decrease in FMR frequency. On the contrary, Fig. 8.8 shows that at smaller bias field (e.g., 0.3 kOe), the magnetization inside the nanocross shows an S state with significant amount of spins making a large angle with the bias field [26]. An increase in rf field (along the *y* axis) may reorient the spins towards the bias field, increasing the effective field along that direction. This can cause a positive shift in FMR frequency of this system. Due to the magnetic instability of this structure even in the equilibrium configuration, the reorientation of spins and the corresponding precession trajectory force the dynamics to a nonlinear regime even at a very moderate rf field (microwave power).

8.4 Conclusions

In conclusion, we have reported microwave power (*P*)-dependent FMR in Py nanocross array. We have observed microwave power driven anticrossing, where the anticrossing gap increases systematically with *P*. We have also observed a power dependent nonlinear frequency shift in the FMR frequency, the sign of which depends on the strength of the applied bias magnetic field and the internal spin configuration of the nanocrosses. Beyond a threshold power, $P_{\text{th}} = -6$ dBm, the dynamics enters into a nonlinear regime and the FMR frequency varies quadratically with *P*. The SW mode

softening can also be efficiently controlled by microwave power. Remarkably, we detect two strong magnon-magnon coupling induced anticrossings, where the coupling strength is tunable over a large range by varying *P*. Micromagnetic simulations show that microwave power driven modulation of inter nanocross dynamic dipolar interactions results in the observed anticrossings. Micromagnetic simulations have also reproduced the power dependent FMR frequency shift. Additionally, simulated power and phase maps of SW modes demonstrate a transformation of the linear SW dynamics into a nonlinear dynamics for $P > P_{\mathrm{th}}$. Nonlinear FMR study in artificial spin-ice structures would also produce very interesting results due to its metastable ground state spin configuration. Finally, the observed nonlinear FMR and strong magnon-magnon coupling in ferromagnetic nanocross array are promising for applications in microwave-assisted fast magnetic storage, logic, and communication devices.

References

[1] Y. Tabuchi, S. Ishino, A. Noguchi, T. Ishikawa, R. Yamazaki, K. Usami, Y. Nakamura, Science, **349**, 405 (2015).

[2] Y. Tabuchi, S. Ishino, T. Ishikawa, R. Yamazaki, K. Usami, Y. Nakamura, Phys. Rev. Lett. **113**, 083603 (2014).

[3] D. Zhang, X.-Q. Luo, Y.-P. Wang, T.-F. Li, J. Q. You, Nat. Commun. **8**, 1368 (2017).

[4] Y. Li, T. Polakovic, Y.-L. Wang, J. Xu, S. Lendinez, Z. Zhang, J. Ding, T. Khaire, H. Saglam, R. Divan, J. Pearson, W.-K. Kwok, Z. Xiao, V. Novosad, A. Hoffmann, W. Zhang, Phys. Rev. Lett. **123**, 107701 (2019).

[5] Y.-P. Wang, J. W. Rao, Y. Yang, P.-C. Xu, Y. S. Gui, B. M. Yao, J. Q. You, C.-M. Hu, Phys. Rev. Lett. **123**, 127202 (2019).

[6] G. S. Agarwal, Phys. Rev. Lett. **53**, 1732 (1984).

[7] S. Klingler, V. Amin, S. Geprägs, K. Ganzhorn, H. Maier-Flaig, M. Althammer, H. Huebl, R. Gross, R. D. McMichael, M. D. Stiles, S. T. B. Goennenwein, M. Weiler, Phys. Rev. Lett. **120**, 127201 (2018).

[8] D. MacNeill, J. T. Hou, D. R. Klein, P. Zhang, P. J.-Herrero, L. Liu, Phys. Rev. Lett. **123**, 047204 (2019).

[9] J. Chen, C. Liu, T. Liu, Y. Xiao, K. Xia, G. E. W. Bauer, M. Wu, H. Yu, Phys. Rev. Lett. **120**, 217202 (2018).

[10] J. T. Hou, L. Liu, Phys. Rev. Lett. **123**, 107702 (2019).

[11] H. M. Olson, P. Krivosik, K. Srinivasan, C. E. Patton, J. Appl. Phys. **102**, 023904 (2007).
[12] W. Wettling, W. D. Wilber, P. Kabos, C. E. Patton, Phys. Rev. Lett. **51**, 1680 (1983).
[13] F. M. de Aguiar, S. M. Rezende, Phys. Rev. Lett. **56**, 1070 (1986).
[14] G. Bertotti, I. D. Mayergoyz, C. Serpico, Phys. Rev. Lett. **87**, 217203 (2001).
[15] P. Bryant, C. Jeffries, Phys. Rev. Lett. **60**, 1185 (1988).
[16] X. Y. Zhang, H. Suhl, Phys. Rev. B **38**, 4893 (1988).
[17] N. N. Rosanov, N. V. Vysotina, A. N. Shatsev, A. S. Desyatnikov, Y. S. Kivshar, Phys. Rev. Lett. **108**, 133902 (2012).
[18] T. Devolder, D. Rontani, S. Petit-Watelot, K. Bouzehouane, S. Andrieu, J. Létang, M.-W. Yoo, J.-P. Adam, C. Chappert, S. Girod, V. Cros, M. Sciamanna, J.-V. Kim, Phys. Rev. Lett. **123**, 147701 (2019).
[19] S. O. Demokritov, V. E. Demidov, O. Dzyapko, G. A. Melkov, A. A. Serga, B. Hillebrands, A. N. Slavin, Nature **443**, 430 (2006).
[20] Y. Khivintsev, B. Kuanr, T. J. Fal, M. Haftel, R. E. Camley, Z. Celinski, D. L. Mills, Phys. Rev. B **81**, 054436 (2010).
[21] H. G. Bauer, P. Majchrak, T. Kachel, C. H. Back, G. Woltersdorf, Nat. Commun. **6**, 8274 (2015).
[22] F. Guo, L. M. Belova, R. D. McMichaell, Phys. Rev. B **91**, 064426 (2015).
[23] M. P. Wismayer, B. W. Southern, X. L. Fan, Y. S. Gui, C.-M. Hu, R. E. Camley, Phys. Rev. B **85**, 064411 (2012).
[24] M. T. Weiss, Phys. Rev. Lett. **1**, 239 (1958).
[25] B. K. Mahato, B. Rana, R. Mandal, D. Kumar, D. Kumar, S. Barman, Y. Fukuma, Y. Otani, A. Barman, Appl. Phys. Lett. **102**, 192402 (2013).
[26] K. Adhikari, S. Choudhury, R. Mandal, S. Barman, Y. Otani, A Barman, J. Appl. Phys. **121**, 043909 (2017).
[27] K. Adhikari, S. Barman, R. Mandal, Y. Otani, A. Barman, Phys. Rev. Appl. **10**, 044010 (2018).
[28] C. Kittel, Phys. Rev. **73**, 155 (1948).
[29] M. Donahue and D. G. Porter, OOMMF User's Guide, Version 1.0, NIST Interagency Report No. 6376, National Institute of Standard and Technology, Gaithersburg, MD, 1999.

[30] K. H. J. Buschow, *Handbook of Magnetic Materials* (North Holland, Amsterdam, The Netherlands, 2009).
[31] J. Topp, D. Heitmann, Phys. Rev. B **80**, 174421 (2009).
[32] D. Kumar, O. Dmytriiev, S. Ponraj, A. Barman, J. Phys. D: Appl. Phys. **45**, 015001 (2012).

Chapter 9

9. Observation of Magnon-Magnon Coupling with High Cooperativity in $Ni_{80}Fe_{20}$ Cross-shaped Nanoring Array

9.1 Introduction

Hybrid systems [1] are promising for their fundamental importance and potential application in the field of quantum information processing and communication [2,3]. Hitherto, diverse carriers [1-5], e.g. photons, phonons, superconducting qubit, atoms etc have been employed for the coherent transfer of quantum states from one platform to another to execute quantum information processing. Recently, magnons, the quanta of spin waves (SWs), have been introduced as a new candidate in the list of quantum state carriers.

During the last decade, extensive research have been carried out especially on coupled magnon-photon [6-11] hybrid systems to explore the strong coupling phenomenon [12,13]. However, the magnon-magnon coupling in hybrid systems of ferromagnetic patterned nanostructures are not extensively explored yet. The study of magnon-magnon coupling in magnetic nanostructures can open the door to develop magnon-based energy efficient on-chip quantum information processing system where processing frequency can go up to gigahertz range. The coupling between magnons of different magnon modes in nanomagnets can be efficiently tuned by varying various external and internal parameters such as orientation of the bias magnetic field and size, shape and periodicity of the nanomagnet. Strong magnon-magnon coupling induced anticrossing of magnon modes has been observed in voltage controlled on demand magnonic nanochannels [14]. In a single nanomagnet, the magnon-magnon coupling strength was found [15] to be strongly dependent on the geometric parameters of the magnon cavity. In addition, external magnetic field controlled tuning of magnon-magnon coupling strength has been reported [16]. The 'coupling strength' ($g/2\pi$) is one of the key parameters in the study of strong coupling to quantify the strength of interaction. In a resonator the magnon-photon coupling strength is proportional to the

square root of the total number of spins (N) present in the magnetic material, i.e. $g \propto \sqrt{N}$ [6,17]. It suggests that to achieve significant amount of coupling strength a large enough spin ensemble is required, which enhances the dimensions of the magnetic material to millimeter scale.

Fortunately, the magnon modes present in confined magnetic nanostructures are analogous to cavity modes as discussed above, which have the potential to replace the millimeter-sized microwave cavity for device miniaturization. Besides, the magnon-magnon hybrid systems have become a trending topic in quantum information processing because magnons provide charge-less diffusion, longer temporal and spatial coherence, and gigahertz range working frequency [18,19]. The strong magnon-magnon coupling in a compensated ferrimagnet [20] and a single material two-dimensional (2D) antiferromagnetic $CrCl_3$ [16] have been reported. Recently, magnon-magnon coupling in coupled YIG/Co heterostructures [21], tunable magnon-magnon coupling in synthetic antiferromagnets [22] and coherent spin pumping in strongly coupled magnon-magnon hybrid system of yttrium iron garnet/permalloy (YIG/Py) bilayer [23] have been demonstrated. However, scalability in nanoscale is essential for the development of on-chip integration of hybrid systems, which is restricted by the $\sqrt{N}$ dependence. Very recently, strong magnon-magnon coupling have been observed experimentally in ferromagnetic nanowires of tens of micrometers length [24] and between edge and centre magnon modes in a single nanomagnet by micromagnetic simulation [15]. Furthermore, microwave power driven ferromagnetic resonance [25] in $Ni_{80}Fe_{20}$ nanocross array exhibited strong magnon-magnon coupling, including the presence of SW mode softening and mode splitting. However, studies of magnon-magnon coupling in nanoscale ferromagnets is still at a nascent stage. Therefore, search and optimization for this phenomenon in different geometrical shapes and environment is imperative, which may lead towards magnon-based quantum information technology.

In this work, we explore magnon-magnon coupling in $Ni_{80}Fe_{20}$ (Py) cross-shaped nanoring (CNR) array with the help of time-resolved magneto-optical Kerr effect (TR-MOKE) microscope and micromagnetic simulations. Remarkably, we observe an anticrossing feature [1] between the two lowest frequency SW modes with anticrossing gap of 0.96 GHz and the corresponding high cooperativity value of 2.25. We also detect an anisotropic dipolar interaction-induced SW mode splitting of the highest frequency SW mode. Moreover, by employing micromagnetic simulations we demonstrate that the

coupled SW modes propagate longer distance as opposed to other modes in ferromagnetic CNR array.

9.2 Sample Fabrication and Characterization

The 20 nm thick Py CNR array, as well as a continuous Py thin film were fabricated on a self-oxidized Si substrate (001) by a combination of electron beam evaporation and electron beam lithography (EBL). A bilayer of polymethyl methacrylate/methyl methacrylate (PMMA/MMA) was used to prepare resist pattern on the Si substrate by using EBL.

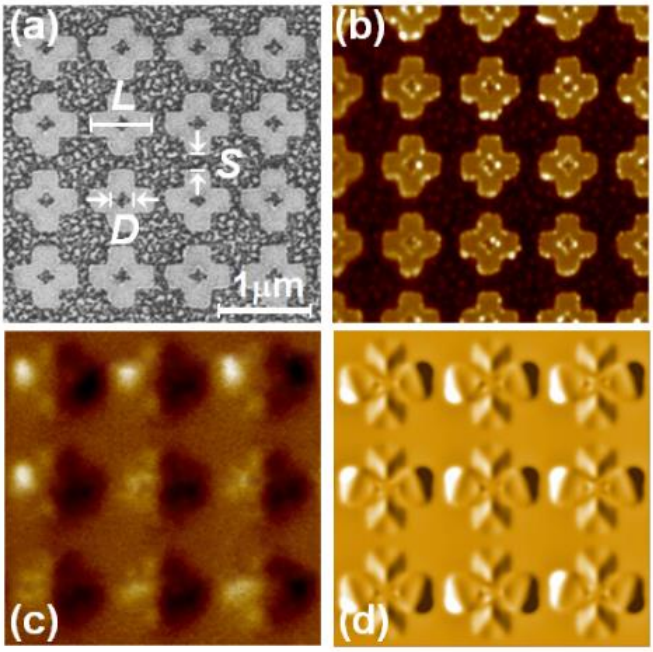

Figure 9.1: (a) Scanning electron micrograph of Py CNR array. (b) Atomic force micrograph for the same array. (c) Magnetic force micrograph of the sample at magnetic remanent state. (d) Simulated magnetic force micrograph for the same array.

The EBL was performed for a dose time of 1.0 μs and at a beam current of 500 pA. The outer (L) and inner arm (D) lengths of the CNR were chosen as 600 nm and 200 nm, respectively. The edge-to-edge separation (S) between the CNR was fixed at 150 nm. The deposition of Py film was performed in an ultra-high vacuum chamber at a base pressure of 2×10^{-8} Torr. Py is a soft ferromagnet possessing negligible magnetocrystalline anisotropy making it an ideal material for patterning into all sorts of geometrical configuration. The negligible magnetocrystalline anisotropy of Py enables

the investigation of the effects of shape anisotropy of nano-patterned elements and their inter-element interactions when placed in a 2D array. In this particular study, the complex internal and stray magnetic fields and their dynamic coupling led to the clear observation of magnon-magnon coupling without being masked or smeared by the additional energy term like magnetocrystalline anisotropy. Figure 9.1(a) shows the scanning electron micrograph (SEM) of the array. Figure 9.1(b) shows the atomic force micrograph (AFM) of the same array. Both SEM and AFM images reveal that the fabricated structures have slight edge deformations. The dimensions of the individual CNR and their edge-to-edge separations also vary by up to $\pm 6\%$. All these deformations in the structures have been incorporated in the micromagnetic simulations as described later. Figure 9.1(c) shows the magnetic force micrograph (MFM) of the sample, which was taken at magnetic remanent state. The opposite color contrast is observed inside the CNR. We have also simulated the MFM image of the CNR array by using LLG Micromagnetics simulator [26] as shown in figure 9.1(d). The color contrast in the sample, i.e. bright region on the left side and dark region on the right side show good agreement between the experimental and simulated images, despite the fact that the experimental MFM image is slightly blurred as opposed to a clean simulated image due to the limitations in the spatial resolution of the MFM measurements.

9.3 Experimental Details

The bias magnetic field dependent magnetization dynamics of the Py CNR array was studied using a custom-built TR-MOKE microscope based upon two-color optical pump-probe experiment in a collinear geometry [27]. The second harmonic (spot size ~1 μm, $\lambda = 400$ nm) of a Ti-sapphire oscillator [Tsunami, Spectra-Physics], called as the pump beam, was used to excite the spin dynamics of the sample, while the time delayed (Δt) fundamental laser (spot size ~800 nm, $\lambda = 800$ nm) was exploited to probe the dynamics. The pump and probe beams were brought to collinear alignment and made to incident upon the sample through a single microscope objective with numerical aperture (N.A.) = 0.65. The probe beam was placed at the centre of the pump beam using a piezoelectric scanning *x*-*y*-*z* stage to ensure uniform excitation of the desired probing volume of the sample.

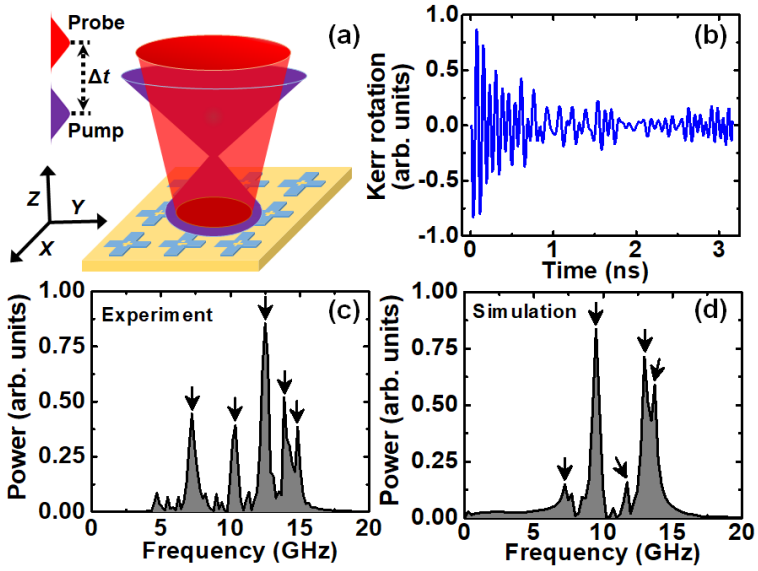

Figure 9.2: (a) Schematic of the experimental geometry used in optical pump-probe technique. (b) Background subtracted time-resolved magnetization traces for Py CNR array at $H = 1.32$kOe. Corresponding FFT power spectra of (c) experimental and (d) simulated time-domain precession at $H = 1.32$ kOe. Arrow signs represent different SW modes.

The back-reflected probe beam was analyzed by using an optical bridge detector and two lock-in-amplifiers to measure the polar Kerr rotation (out-of-plane magnetization component) and the reflectivity of the sample as a function of the time delay (Δt) between the pump and the probe beams. In our experiment, the measurement time window of 3.25 ns was used which was sufficient for resolving all the SW modes clearly. The external magnetic field was applied at a small tilt angle of ~15° from the sample plane, while the in-plane component of this magnetic field is considered as the bias magnetic field (H). The small tilt in the external magnetic field from the sample plane confirms the presence of substantial amount of out-of-plane demagnetizing field, which is modified by the pump laser to launch a precessional torque [28] to the sample magnetization after the ultrafast demagnetization.

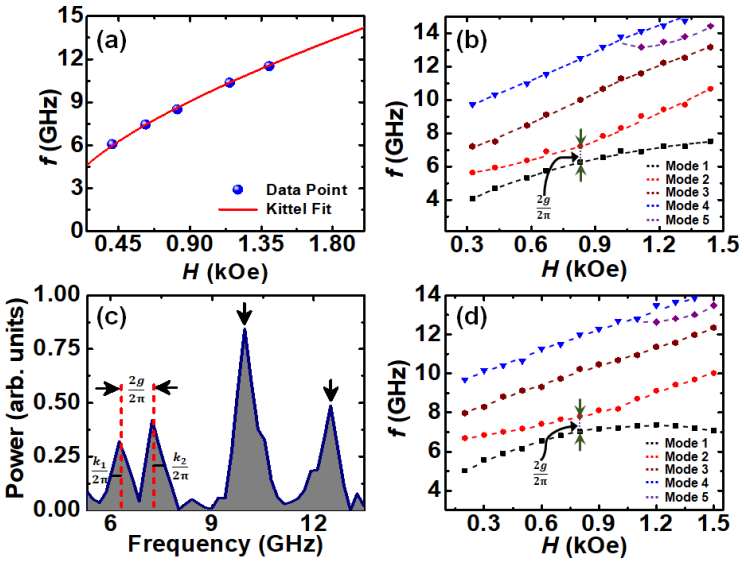

Figure 9.3: (a) Bias-field-dependent SW mode frequency for Py thin film of 20 nm thickness. The Kittel fit is shown by solid line. (b) Experimental bias-field-dependent SW mode frequencies for Py CNR array. (c) FFT power spectrum of experimental time-domain precession at $H = 0.83$ kOe. The half of the frequency gap between two lowest frequency SW modes reveals the coupling strength $g/2\pi$, and the corresponding dissipation rates $k_1/2\pi$ and $k_2/2\pi$ are defined as half width at half maximum of the peak shape of M1 and M2, respectively. (d) Simulated bias-field-dependent SW mode frequencies for Py CNR array. The dotted line is guide to eye.

9.4 Results and Discussion

A schematic of the TR-MOKE measurement geometry is presented in figure 9.2(a). The time-resolved Kerr rotation shows an ultrafast demagnetization and a two-step magnetization relaxation, superposed on which the magnetization precession appears as an oscillatory signal. We removed the initial time zone showing the ultrafast demagnetization and subtracted the bi-exponential background corresponding to the two-step relaxation from the TR-MOKE traces to show a representative time-resolved precessional data from the CNR sample for $H = 1.32$ kOe in figure 9.2(b). Subsequently, fast Fourier transformation (FFT) was performed over the time-resolved precessional oscillation to obtain the power spectrum or SW modes as shown in figure 9.2(c). The simulated SW spectrum at $H = 1.32$ kOe is shown in figure 9.2(d).

To validate the experimental results, we performed micromagnetic simulations by using Object Oriented Micromagnetic Framework (OOMMF) [29] software. The mimicked CNR array from the SEM image was discretized into rectangular prism-like cells of 4 × 4 × 20 nm^3 dimensions, while to account for the large experimental array, 2D periodic boundary condition was applied. The lateral dimensions of the cells were taken well below the exchange length (l_{ex} = 5.3 nm) of Py. The magnetic parameters of the sample such as saturation magnetization (M_S), gyromagnetic ratio (γ), and anisotropy field (H_K) used in the micromagnetic simulations were extracted from a Py thin film. Figure 9.3(a) shows the H-dependent precessional frequency (f) of a 20 nm thick Py thin film and the data was fitted by using Kittel formula [30], which is given by:

$$f = \frac{\gamma}{2\pi}\sqrt{(H + H_K)(H + H_K + 4\pi M_s)} \tag{9.1}$$

to extract the magnetic parameters of the Py film. The parameters extracted from the fit are, γ = 17.6 MHz/Oe, M_S = 860 emu/cc, and H_K = 0. The exchange stiffness constant (A_{ex}) = 1.3 × 10^{-6} erg/cm was taken from the literature [31]. The damping coefficient (α) of 0.008 [32] was used during dynamic simulations. The detailed methods of the simulations are described elsewhere [33]. Figure 9.2(d) shows the FFT power spectrum of the simulated time-domain magnetization from the CNR sample under the experimental conditions, which reproduces the experimental spectrum very well. The SW modes are marked with arrow sign, which identify the presence of five distinct modes in the sample at H = 1.32 kOe. However, all the deformations and edge roughness in CNR array could not be precisely reproduced in finite difference method based OOMMF simulation. On the other hand, the effects of temperature (T) can not be incorporated in OOMMF and the simulations are performed at T = 0 K. Consequently, we have observed a marginal quantitative disagreement between figures 9.2(c), (d).

We further studied the bias-field-dependent SW mode frequencies, and the experimental f versus H data for the SW modes from the Py CNR array is shown in figure 9.3(b). The plot reveals rich anisotropic SW properties. The SW mode frequencies vary non-monotonically with H. However, SW mode softening is not observed here unlike nanocross array due to the absence of a transition in magnetic microstates with magnetic field. The largest frequency mode (M4) shows a mode splitting (appearance of M4 and M5) for $H \gtrsim 1$ kOe. A continuous increase in frequency with the increase in H is observed for the intermediate frequency branch (M3).

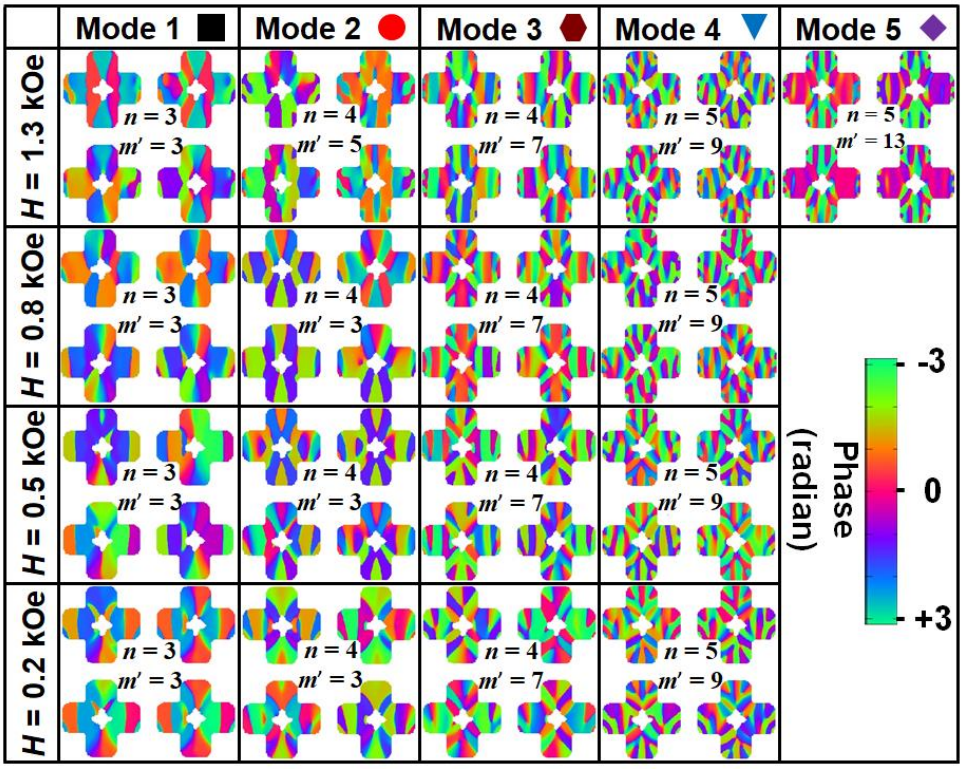

Figure 9.4: Simulated phase maps of the SW modes obtained for Py CNR array at four different bias field values. The color map for the phase distribution is shown in the inset.

On the contrary, the two lowest frequency modes (M1 and M2) show a mode repulsion and ensuing anticrossing at around $H = 0.8$ kOe due to magnon-magnon coupling. The magnon-magnon coupling strength $g/2\pi$ is defined as half of the peak-to-peak frequency spacing at anticrossing, which is shown in figure 9.3(c). In order to estimate the strength of interaction between these two modes, we have extracted the value of $g/2\pi$, and the corresponding dissipation rates $k_1/2\pi$, $k_2/2\pi$ as shown in figure 9.3(c). Here, $k_1/2\pi$ and $k_2/2\pi$ are defined as half width at half maximum of the peak shape of M1 and M2, respectively. The $g/2\pi$ value is obtained as 0.48 GHz, while $k_1/2\pi$ and $k_2/2\pi$ are found to be 0.33 GHz and 0.31 GHz, respectively. Thus, $g > k_1$ and k_2, i.e. the interaction between M1 and M2 can be considered to fall in the high coupling regime [13]. We have also calculated magnon-magnon cooperativity, which is defined as $C = g^2/k^2$, where $k = (k_1 + k_2)/2$, and obtained $C = 2.25$ for the coupling between M1 and M2. Figure 9.3(d) shows the simulated SW mode frequencies from Py CNR array as a function H. The simulation results reproduce all the important features of the experimental results, as discussed above. From the simulation, we obtained the value of $g/2\pi$, $k_1/2\pi$ and $k_2/2\pi$ as 0.39, 0.26 and 0.24 GHz, respectively. The simulated results

also show high cooperativity of 2.43, i.e. a high magnon-magnon coupling between M1 and M2.

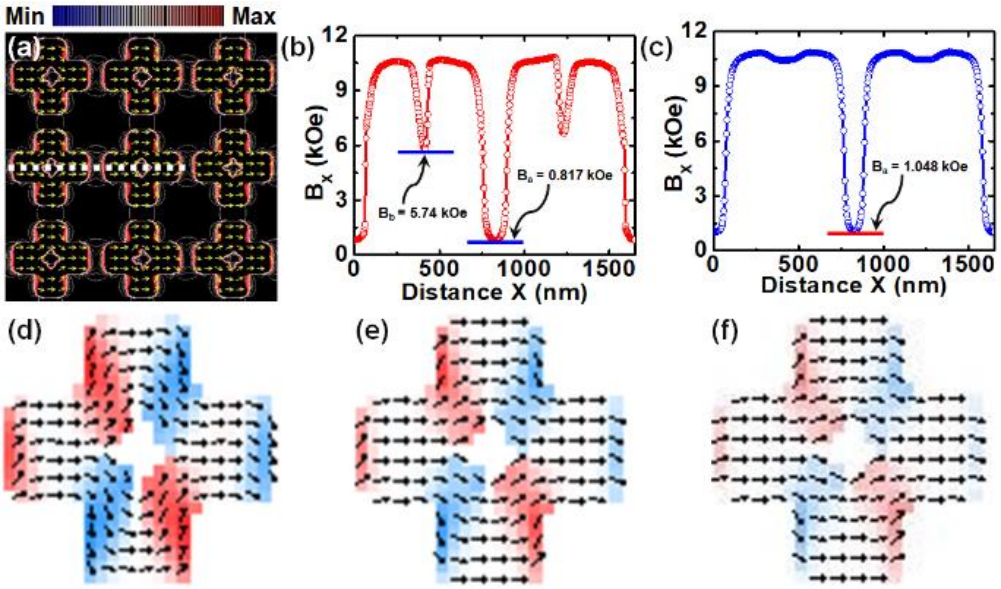

Figure 9.5: Contour plot of the simulated magnetostatic field distribution in Py CNR array at $H = 0.6$ kOe and the corresponding color map is shown at the top of the figure. Line scan is taken along the white dotted line. (b) Line scan of the simulated magnetostatic field for CNR array. (c) Line scan of the simulated magnetostatic field for nanocross array. B_a and B_b represent inter-CNR interaction field and the effective magnetic field at the centre of the CNR (air gap), respectively. Simulated static magnetic configurations for Py CNR array at (d) $H = 0.2$ kOe, (e) $H = 0.8$ kOe and (f) $H = 1.5$ kOe, respectively. We have shown here a single CNR from the centre of the array to represent the spin configuration prominently.

During the dynamics the stray magnetic fields due to the precessing magnetic moments of each CNR dynamically interact with the magnetization of the neighbouring CNRs. Consequently, neighbouring CNRs are connected by dynamic dipolar interactions. On the other hand, dynamic dipolar interaction becomes significantly high in this system due to the presence of nonuniform distribution of the local magnetic moments, which arises because of the complex geometrical structure of the CNR. The magnon-magnon coupling between the different magnon modes is mediated by this dynamic dipolar coupling.

To characterize the observed SW modes, we have further simulated the spatial distribution of phase of the modes using a home-built code [34]. OOMMF simulation

provides magnetization (M (r, t)) information of each rectangular prism-like cell at different simulation time. By performing discrete Fourier transformation with respect to time for each of these cells and subsequently extracting the phase of the dynamic magnetization for a desired frequency gives rise to spatial distribution of phase for that particular mode. Figure 9.4 represents the simulated phase maps of the SW modes at four different H values, which are above, at and below the anticrossing field. The modes are characterized by nodal planes perpendicular to the bias field direction (backward volume (BV) geometry, mode quantization number: n) in any of the horizontal arms of the CNR and azimuthal quantization number (m') in the central part of the CNR, i.e. around the cross-shaped antidot. All the modes show both BV-like and azimuthal quantization with varying n and m' as marked in figure 9.4. The values of (n, m') for modes 1, 2, 3, 4 and 5 are (3, 3), (4, 5), (4, 7), (5, 9) and (5, 13) at $H = 1.3$ kOe, i.e. above the anticrossing field. The modes at this field, however, are less phase coherent. At $H = 0.8$ kOe two remarkable events happen. The phase contrasts of all modes, particularly M1 and M2, improve drastically and (n, m') for M2 transforms to (4, 3), while quantization numbers for all other modes remain intact as for $H = 1.3$ kOe. This means the azimuthal mode number (m') for M1 and M2 becomes identical, which is likely to be a signature of high coupling between these modes. For values of H below 0.8 kOe, no further variation of (n, m') occurs for any of the modes, which is probably due to the retainment of significant coupling between M1 and M2 at lower field values.

To get deeper insight into the SW dynamics, we have numerically calculated the magnetostatic field distributions in Py CNR array, and the corresponding contour plot is shown in figure 9.5(a) at $H = 0.6$ kOe. The line scan of the field along the white dotted line is presented in figure 9.5(b). At the centre of the CNR (air gap), a significant amount of effective magnetic field ($B_b \approx 5.74$ kOe) is observed despite having no magnetic material. The inter-CNR interaction field (B_a) is found to be of 0.817 kOe. For a comparison, we have also calculated the magnetostatic field distributions in Py nanocross array (with no hole in it) and the corresponding line scan of the field is shown in figure 9.5(c). Here, B_a is found to be 1.048 kOe. Thus, the introduction of a hole at the centre of the cross does not reduce the inter-element dipolar interaction significantly. The slightly lower inter-dot interaction field suggests weaker inter-dot dipolar coupling, and hence, we observe lower value of coupling strength in CNR array as compared to nanocross array. However, CNR array exhibits larger magnon-magnon

cooperativity value compared to nanocross array ($C = 2.25$ for CNR, 0.6 for nanocross) [25]. This is most likely due to the fact that the demagnetization field around the periphery of the hole in CNR reduces the dissipation rates ($k_1/2\pi$, $k_2/2\pi$) by transforming M1 and M2 into more alike SW modes where the azimuthal mode quantization numbers merge at the anticrossing field. Consequently, the cooperativity value increases.

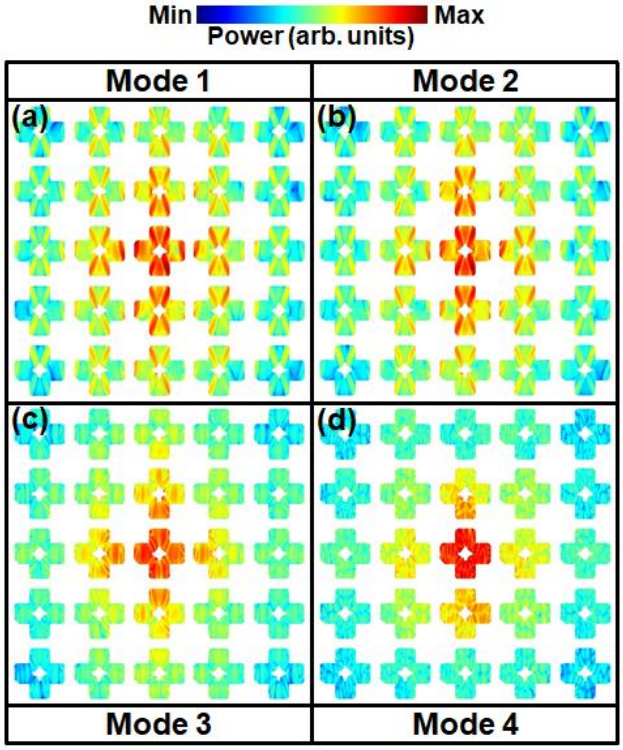

Figure 9.6: Simulated spatial distributions of the power corresponding to the different SW modes obtained for Py CNR array at $H = 0.8$ kOe. We have launched the local excitation over a small square region at the center of the array. The color map associated with the power distributions is shown at the top of the figure.

Besides, the bias-field-dependent transition in the magnetic microstate disappears in the CNR, giving rise to stable onion state at three different bias field values ($H = 0.2$ kOe, $H = 0.8$ kOe and $H = 1.5$ kOe) as shown in figures 9.5(d)-(f). In case of Py nanocross array [35,36], SW mode softening occurred at $H \approx 0.3$ kOe due to the sudden change of magnetic microstate from S state to onion state. The absence of central part in CNR inhibits the formation of S state, and thereby, eradicates the field-dependent transition in microstate and the ensuing SW mode softening in CNR array. In addition, a Y-shaped mode splitting appeared in the nanocross array [35] due to the configurational

anisotropy driven competition between the spin configurations in the two orthogonal arms of the cross structure. However, in case of CNR the weaker configurational anisotropy prompts the vanishing of Y-shaped SW mode splitting of the highest frequency mode at lower H regime. Splitting of the highest frequency SW mode (M4) occurs for $H \gtrsim 1$ kOe due to the anisotropic dipolar interactions [37] between CNRs in an array, similar to Py nanocross array [35] which also exhibited similar mode splitting. For the nanocross the splitting vanished for a shorter arm length ($L \leq 300$ nm).

Figure 9.6 provides a demonstration of different spatial propagating nature of detected SW modes through dipolar coupled CNR array. To this end, using OOMMF software, we launched a time-varying field of "sinc" profile (frequency cut-off of 20 GHz) over a small square region at the centre of the array. Subsequently, we simulated the spatial distributions of the power corresponding to the different SW modes obtained for Py CNR array at $H = 0.8$ kOe. Notably, the results reveal an exciting feature that M1 and M2, which are coupled by high magnon-magnon interaction, propagate longer distance (> 2 μm) in the array. On the contrary, the other two higher frequency SW modes show faster decay and disappear within about 1 μm length from the excitation center. The contour plot (figure 9.5(a)) of the magnetostatic field distributions exhibits nonuniform distribution of field lines around the CNR edges. It shows dense lines of force at the vicinity of the both sides of the vertical arm and two ends of the horizontal arm of CNR, where the lines of force penetrate inside the CNR due to unsaturated spins. This indicates that the SW modes are significantly coupled here by inter-CNR dipolar interactions. On the other hand, spatial distribution of power for the observed SW modes (figure 9.6) reveal that the power is localized mostly at the edges for M1 and M2, while power is uniformly distributed over the CNR for M3 and M4. This underpins the longer propagation distance for M1 and M2 as opposed to other two SW modes (M3 and M4) in Py CNR array. Finally, the number of spins in Py CNR is several orders of magnitude smaller than the existing reported values in the literature. In addition, these are planar 2D array of elements, which can be easily integrated with on-chip devices. Therefore, our study is imperative for the development of nanoscale magnonics, quantum transduction and information systems.

9.5 Conclusions

In conclusion, we have explored dynamic dipolar coupling induced magnon-magnon coupling in Py CNR array. We have observed bias-field-dependent rich anisotropic SW properties in CNR array. Remarkably, we have observed a magnon-magnon coupling induced anticrossing feature between the two lowest frequency SW modes. Furthermore, the CNR array has exhibited larger magnon-magnon cooperativity value as compared to the nanocross array. Splitting of the highest frequency SW mode (M4) has occurred for $H \gtrsim 1$ kOe due to the anisotropic dipolar interactions between the CNRs in an array. Notably, SW mode softening has not been observed here unlike nanocross array due to the absence of a transition between magnetic microstates with bias magnetic field. On the other hand, the weaker configurational anisotropy has prompted the absence of Y-shaped SW mode splitting of the highest frequency mode at lower H regime. Micromagnetic simulations have well reproduced all the observed phenomena. The calculated SW mode profiles have shown remarkable enhancement in phase contrast and merging of azimuthal mode quantization number of M1 and M2 at a bias field where the mode anticrossing occurs, hinting towards the significant coupling between those modes. Furthermore, by exciting the hybrid magnon dynamics, we have demonstrated that the coupled SW modes propagate longer distance as opposed to other modes in Py CNR array. Finally, the observed magnon-magnon coupling and the longer SW propagation length for the coupled SW modes in ferromagnetic CNR array are promising for applications in magnon-based coherent information processing.

References

[1] A. A. Clerk, K. W. Lehnert, P. Bertet, J. R. Petta, Y. Nakamura, Nat. Phys. **16**, 257 (2020).

[2] J. P. Home, D. Hanneke, J. D. Jost, J. M. Amini, D. Leibfried, D. J. Wineland, Science **325**, 1227 (2009).

[3] A. Blais, R.-S. Huang, A. Wallraff, S. M. Girvin, R. J. Schoelkopf, Phys. Rev. A **69**, 062320 (2004).

[4] C. Berk, M. Jaris, W. Yang, S. Dhuey, S. Cabrini, H. Schmidt, Nat. Commun. **10**, 2652 (2019).

[5] D. Petrosyan, M. Fleischhauer, Phys. Rev. Lett. **100**, 170501 (2008).

[6] Y. Tabuchi, S. Ishino, T. Ishikawa, R. Yamazaki, K. Usami, Y. Nakamura, Phys. Rev. Lett. **113**, 083603 (2014).

[7] D. Zhang, X.-Q. Luo, Y.-P. Wang, T.-F. Li, J. Q. You, Nat. Commun. **8**, 1368 (2017).

[8] Y. Li, T. Polakovic, Y.-L. Wang, J. Xu, S. Lendinez, Z. Zhang, J. Ding, T. Khaire, H. Saglam, R. Divan, J. Pearson, W.-K. Kwok, Z. Xiao, V. Novosad, A. Hoffmann, W. Zhang, Phys. Rev. Lett. **123**, 107701 (2019).

[9] N. Zhu, X. Han, C.-L. Zou, M. Xu, H. X. Tang, Phys. Rev. A **101**, 043842 (2020).

[10] L. V. Abdurakhimov, S. Khan, N. A. Panjwani, J. D. Breeze, M. Mochizuki, S. Seki, Y. Tokura, J. J. L. Morton, H. Kurebayashi, Phys. Rev. B **99**, 140401(R) (2019).

[11] J. Bourhill, N. Kostylev, M. Goryachev, D. L. Creedon, M. E. Tobar, Phys. Rev. B **93**, 144420 (2016).

[12] S. Gröblacher, K. Hammerer, M. R. Vanner, M. Aspelmeyer, Nature **460**, 724 (2009).

[13] X. Zhang, C.-L. Zou, L. Jiang, H. X. Tang, Phys. Rev. Lett. **113**, 156401 (2014).

[14] S. Choudhury, A. K. Chaurasiya, A. K. Mondal, B. Rana, *et al*., Sci. Adv. **6**, eaba5457 (2020).

[15] C. Dai, K. Xie, Z. Pan, F. Ma, J. Appl. Phys. **127**, 203902 (2020).

[16] D. MacNeill, J. T. Hou, D. R. Klein, P. Zhang, P. J.-Herrero, L. Liu, Phys. Rev. Lett. **123**, 047204 (2019).

[17] Y. Cao, P. Yan, H. Huebl, S. T. B. Goennenwein, G. E. W. Bauer, Phys. Rev. B **91**, 094423 (2015).

[18] L. J. Cornelissen, J. Liu, R. A. Duine, J. Ben Youssef, B. J. Van Wess, Nat. Phys. **11**, 1022 (2015).

[19] F. Heussner, M. Nabinger, T. Fischer, T. Brächer, A. A. Serga, B. Hillebrands, P. Pirro, Phys. Status Solidi Rapid Res. Lett. **12**, 1800409 (2018).

[20] L. Leinsberger, A. Kamra, H. Maier-Flaig, S. Geprägs, A. Erb, S. T. B. Goennenwein, R. Gross, W. Belzig, H. Huebl, M. Weiler, Phys. Rev. Lett. **123**, 117204 (2019).

[21] S. Klingler, V. Amin, S. Geprägs, K. Ganzhorn, H. Maier-Flaig, M. Althammer, H. Huebl, R. Gross, R. D. McMichael, M. D. Stiles, S. T. B. Goennenwein, M. Weiler, Phys. Rev. Lett. **120**, 127201 (2018).

[22] A. Sud, C. W. Zollitsch, A. Kamimaki, T. Dion, S. Khan, S. Iihama, S. Mizukami, H. Kurebayashi, Phys. Rev. B **102**, 100403(R) (2020).

[23] Y. Li, W. Cao, V. P. Amin, Z. Zhang, J. Gibbons, J. Sklenar, J. Pearson, P. M. Haney, D. M. Stiles, W. E. Bailey, V. Novosad, A. Hoffman, W. Zhang, Phys. Rev. Lett. **124**, 117202 (2020).

[24] J. Chen, C. Liu, T. Liu, Y. Xiao, K. Xia, G. E. W. Bauer, M. Wu, H. Yu, Phys. Rev. Lett. **120**, 217202 (2018).

[25] K. Adhikari, S. Sahoo, A. K. Mondal, Y. Otani, A. Barman, Phys. Rev. B **101**, 054406 (2020).

[26] M. R. Scheifein, LLG Micromagnetics Simulator, http://llgmicro.home.mindspring.com/, 2018.

[27] A. Barman, J. Sinha, *Spin Dynamics and Damping in Ferromagnetic Thin Films and Nanostructures*, Springer, Switzerland 2018.

[28] M. V. Kampen, C. Jozsa, J. T. Kohlhepp, P. LeClair, L. Lagae, W. J. M. de Jonge, B. Koopmans, Phys. Rev. Lett. **88**, 22 (2002).

[29] M. Donahue, D. G. Porter, OOMMF User's Guide, Version 1.0, NIST Interagency Report No. 6376, National Institute of Standard and Technology, Gaithersburg, MD, 1999.

[30] C. Kittel, Phys. Rev. **73**, 155 (1948).

[31] K. H. J. Buschow, *Handbook of Magnetic Materials* (North Holland, Amsterdam, The Netherlands, 2009).

[32] S. Mizukami, H. Abe, D. Watanabe, M. Oogane, Y. Ando, T. Miyazaki, Appl. Phys. Express **1**, 121301 (2008).

[33] B. Rana, D. Kumar, S. Barman, S. Pal, Y. Fukuma, Y. Otani, A. Barman, ACS Nano **5**, 9559 (2011).

[34] D. Kumar, O. Dmytriiev, S. Ponraj, A. Barman, J. Phys. D: Appl. Phys. **45**, 015001 (2012).

[35] K. Adhikari, S. Choudhury, R. Mandal, S. Barman, Y. Otani, A Barman, J. Appl. Phys. **121**, 043909 (2017).

[36] K. Adhikari, S. Barman, R. Mandal, Y. Otani, A. Barman, Phys. Rev. Appl. **10**, 044010 (2018).

[37] S. Mondal, S. Barman, S. Choudhury, Y. Otani, A. Barman, J. Magn. Magn. Mater **458**, 95 (2018).

Chapter 10

10. Summary and Future Perspectives

10.1. Summary

In summary, we have studied the quasi-static and dynamic magnetization properties in patterned ferromagnetic samples by using different experimental techniques. The principal goal of such studies was to utilize the experimental results to enrich the fundamental physics and to propose potential magnonic devices. The patterned samples were fabricated by using various techniques, including ultrahigh vacuum magnetron sputtering, electron beam evaporation and electron beam lithography. The topographical and morphological studies of the prepared samples were carried out utilizing SEM and AFM. Whereas the static magnetic properties of the samples were explored by MFM and static-MOKE magnetometer. The magnetization dynamics of the samples were measured in frequency domain by a custom-built broadband FMR spectrometer. On the other hand, the dynamics of magnetization in different time-scales were probed using a home-built TR-MOKE microscope. The experimental outcomes were analysed with the assistance of computational micromagnetic simulations (OOMMF and LLG Micromagnetics) to interpret the experimental observations.

Firstly, we have investigated the evolution of static spin configuration and dynamics of magnetization in Py nanocross arrays [1] with varying sizes as a function of bias magnetic field strength (H) employing a broadband FMR spectrometer. A drastic variation of the static spin configuration was observed with the increase of in-plane bias field strength. The initial S state spin configuration was transformed to onion state and subsequent increase in bias field strength resulted in further straightening of the spins toward the bias filed direction. The observed SW modes showed rich anisotropic properties due to this substantial variation in static spin configuration. Especially the lowest frequency SW mode showed interesting variation. The frequency of this SW mode increased with the initial increment of bias field strength, followed by a sharp maximum and minimum, subsequent rise in frequency, and finally a crossover to the

upper frequency branch. The third SW mode showed a monotonic increase in frequency with bias field strength. Interestingly, the higher frequency SW modes again manifested a non-monotonic nature. The highest frequency SW mode showed a Y-shaped mode splitting at lower bias field regime ($H \leq 0.225$ kOe), followed by a single branch in intermediate bias field regime (0.225 kOe $\leq H \leq$ 0.62 kOe). Subsequently, another SW mode splitting was observed with the increment of bias field strength. The Y-shaped mode splitting of the highest frequency branch occurred due the competition between the contrasting spin configurations hold by the two orthogonally placed arms of the nanocross. Simulated spatial distribution of phase maps revealed two different types of SW modes in this system, a mixed BV-DE-like SW mode and another BV-like SW mode mixed with azimuthal character. The sudden transition of static spin configuration from S state to onion state resulted a mode softening. The two lowest frequency branches with different mode quantization numbers showed mode crossover. Further, the variation of dimension of the nanocross affected the magnetization dynamics of the nanocross array both qualitatively and quantitatively.

Next, we studied the magnetization dynamics in Py nanocross arrays of varying dimensions as a function of the in-plane angle (ϕ) [2] of the applied bias magnetic field again by using broadband FMR. The previous study in nanocross arrays showed bias-field-dependent tunable static spin configuration and magnetization dynamics along with the presence of mode crossover and mode softening. When the bias field angle was deviated from its initial orientation, i.e., $\phi = 0°$, the chances of onion-state formation reduced. As a result, the dip height corresponding to the mode softening of lowest frequency branch reduced and the position of the dip moved to a higher bias field value. The formation of a new mode crossover occurred at the dip position with the further increase of ϕ. The frequency gap between two lowest frequency modes (i.e., for higher-field mode crossover) increased with the increment of ϕ and subsequent increase of ϕ resulted disappearance of this mode crossover at $\phi = 30°$. In addition, the higher frequency branch of this mode crossover disappeared at $\phi = 45°$. At $\phi = 45°$, the number of modes reduced as compared to $\phi = 30°$. The lower-field Y-shaped mode splitting of the highest frequency branch was highly affected with the variation of ϕ. The frequency gap of this mode splitting decreased with the increment of ϕ and finally this Y-shaped mode splitting disappeared for a certain value of ϕ. On the other hand, the higher-field mode splitting of the highest frequency branch shifted to a lower field value with the

further increment of ϕ, and subsequently, this mode splitting disappeared. Interestingly, a frequency minimum was observed again for the lowest frequency branch at $\phi = 45°$. The simulated spatial distribution of phase maps of the observed modes revealed that the SW modes, which are highly affected by the bias field orientation are characterized as mixed BV-DE-like modes. Notably, the mode quantization number corresponding to the DE mode, i.e., *m* increased with the increase of ϕ. The effect of varying the sizes of the nanocross on the prime features and their corresponding critical angles are tabulated, which shows both quantitative and qualitative variation of magnetization dynamics. The reasons behind such variation in the mode frequencies and phase profiles were explored with the help of calculated magnetostatic field distribution in nanocross arrays at different ϕ values.

Afterwards, we have studied the microwave power (*P*) dependent ferromagnetic resonance in Py nanocross array using a broadband FMR technique. A microwave power dependent [3] nonlinear frequency shift was observed in the FMR frequency, where the sign of the shift was found to depend on the strength of the bias magnetic field and internal magnetic configuration. Interestingly, above the threshold power for this system i.e., $P_{\text{th}} = -6$ dBm, the spin dynamics showed nonlinear behaviour and FMR frequency manifested a quadratic variation with *P*. The SW mode softening of the lowest frequency mode could also be efficiently modulated by microwave power. Two strong magnon-magnon coupling induced anticrossing features were also detected, where coupling strength could be tuned by varying *P*. Micromagnetic simulations revealed that the microwave power driven modulation of the inter nanocross dynamic dipolar coupling results this magnon-magnon coupling. In addition, simulated spatial distribution of power and phase maps of the SW modes demonstrated the conversion of linear SW dynamics into the nonlinear SW dynamics with the enhancement of *P*.

We also studied the bias magnetic field dependent precessional magnetization dynamics in Py cross-shaped nanoring (CNR) array [4] using TR-MOKE microscopy. Bias-field-dependent anisotropic SW properties was observed in the CNR array. Remarkably, an anticrossing feature due to magnon-magnon coupling was also detected between the two lowest frequency SW modes (M1, M2). In addition, the CNR array manifested larger cooperativity value between M1 and M2 modes as compared to the Py nanocross array. Splitting of the highest frequency branch (M4) occurred at $H \gtrsim 1$ kOe because of the anisotropic magnetic dipolar interactions between the CNRs. Some prime

features like SW mode softening and Y-shaped mode splitting was not observed in case of CNR array unlike nanocross array. The calculated phase maps also supported the significant coupling between the lowest frequency magnon branches (M1, M2). Interestingly, the coupled modes was found to propagate longer distance as opposed to other uncoupled SW modes present in Py CNR array.

Finally, all these observations were found to be promising for the applications in magnetic storage, logic and communication devices.

10.2. Future Perspectives

Mankind is gradually shifting towards a digital lifestyle. Round the clock, we are using various electronic gadgets, including mobile phone, computer, internet, navigator, e-marketing, apps etc. These devices perform logic operations, store and use data. The demand for the more efficient memory, logic and communication devices have grown rapidly with the rise of this digital lifestyle. The concern is that electronic technology is slowly reaching the limits [5,6] in terms of energy efficiency and space miniaturization. Therefore, the daunting challenge is to search for smarter alternative technologies.

On the other hand, spin-based devices have several advantages such as lower energy consumption, lower energy loss, GHz range working frequency regime etc. In addition, with the advancement of fabrication techniques, we are now able to grow samples like high quality magnetic ultrathin films, heterostructures and patterned nanostructures. The novel phenomena of these systems can be useful for the development of future potential spin-based devices.

The study of spin dynamics in ferromagnetic nanostructures (dots or antidots or rings) could play an important role for future spin-based communication devices since their outputs are efficiently tunable in terms of geometrical parameters like shape, size and periodicity. Their spin dynamics can also be easily controlled externally by tuning the bias magnetic field strength, orientation and microwave excitation power, which is useful for the construction of magnonic crystal-based networks and devices. In addition, the anisotropy (intrinsic and extrinsic) present in the system makes SWs anisotropic in nature which can be helpful for the development of SW filters, splitters, couplers and attenuators. A systematic study of magnetic band structure [7] of these samples presented in this thesis using Brillouin light scattering (BLS) spectroscopy and

simulation could be an exciting extension of works. Recently, hybrid systems [8] have become an exciting topic of research due to their rich fundamental physics and application in potential devices. Particularly, magnon-based hybrid systems [9-11] have shown recent rapid evolution. Magnons can be efficiently engineered to achieve significant coupling with other quasiparticles or platforms. In addition, magnon can be easily modulated and have high temporal coherence making it suitable for the application in information processing. Furthermore, they offer GHz frequency bandwidth and the current development in the fabrication techniques can be helpful for the manufacturing of broad frequency range device applicable in quantum information [12].

Currently, antiferromagnetic systems [13] are being preferred in data storage application. In case of antiferromagnetic systems, the adjacent magnetic moments are in reversed direction alternatively. If we look at this system macroscopically, their net magnetic moment is zero. The information stored in this system remains safe from the unwanted external magnetic field, as the nearest moments do not interact with each other. The magnetic response of an antiferromagnetic system lies in terahertz (THz) regime, which can be useful in the field of THz-spintronics. On the other hand, the study of magneto-elastic coupling in antiferromagnet-based potential systems can be an exciting topic of investigation for the evolution of spin-mechatronics [14].

We have studied bias-field-dependent complex static magnetic configurations for Py nanocross array and cross-shaped nanoring array, which have resemblance with artificial spin ice (ASI) [15,16] and anti-spin ice [17] systems. It would be exciting to study ASI systems with new possible geometries and magnetic materials. Artificial spin systems exhibit various fascinating phenomena including emergent magnetic monopoles [18], phase transitions [19] and frustration [20]. The dynamics of magnetic monopoles can be efficiently controlled in an ASI system with the assistance of various external stimuli, for instance, electric current, electric and magnetic fields, strain and temperature gradient, which is extremely important for the future device applications such as data storage, computation and encryption. In ASI, monopole defects can be identified from their frequency spectrum, which makes them suitable for the application in reprogrammable magnonic crystals [21].

In addition, the spin dynamics can be efficiently controlled in bi-component magnonic crystals (BMCs) [22] by playing with the exchange coupling between the junctions of

two different magnetic media. The dynamic dipolar coupling enhances here due to the exchange interactions at the boundary. Consequently, SWs can easily transmit through the boundary by scattering process. Interestingly, the transmission of SWs occurs across the lateral interfaces with substantial group velocity. Therefore, study of magnonic band structure and spin dynamics in new BMCs would be an interesting research for future device applications for instance microwave assisted magnetic recording (MAMR).

In brief, a comprehensive investigation of spin dynamics in patterned ferromagnetic nanostructures have been presented in this thesis. The detected fascinating phenomena and their efficient tunability are significant for the construction of new potential magnonic devices.

References

[1] K. Adhikari, S. Choudhury, R. Mandal, S. Barman, Y. Otani, A. Barman, J. Appl. Phys. **121**, 043909 (2017).

[2] K. Adhikari, S. Barman, R. Mandal, Y. Otani, A. Barman, Phys. Rev. Appl. **10**, 044010 (2018).

[3] K. Adhikari, S. Sahoo, A. K. Mondal, Y. Otani, A. Barman, Phys. Rev. B **101**, 054406 (2020).

[4] K. Adhikari, S. Choudhury, S. Barman, Y. Otani, A. Barman, Nanotechnology **32**, 395706 (2021).

[5] G. E. Moore, in *Readings in computer architecture*, (Morgan Kaufmann Publishers Inc.) edited by D. H. Mark, P. J. Norman, S. S. Gurindar, p. 56, (2000).

[6] W. M. Arden, Science **6**, 371 (2002).

[7] K. Di, V. L. Zhang, M. H. Kuok, *et al.*, Phys. Rev. B **90**, 060405 (2014).

[8] A. A. Clerk, K. W. Lehnert, P. Bertet, J. R. Petta, Y Nakamura, Nat. Phys. **16**, 257 (2020).

[9] S. Choudhury, A. K. Chaurasiya, A. K. Mondal, B. Rana, *et al.*, Sci. Adv. **6**, eaba5457 (2020).

[10] C. Dai, K. Xie, Z. Pan, F. Ma, J. Appl. Phys. **127**, 203902 (2020).

[11] D. MacNeill, J. T. Hou, D. R. Klein, *et al.*, Phys. Rev. Lett. **123**, 047204 (2019).

[12] J. P. Home, D. Hanneke, J. D. Jost, J. M. Amini, D. Leibfried, D. J. Wineland, Science **325**, 1227 (2009).

[13] V. Baltz, A. Manchon, M. Tsoi, T. Moriyama, T. Ono, Y. Tserkovnyak, Rev. Mod. Phys. **90**, 015005 (2018).

[14] M. Matsuo, E. Saitoh, S. Maekawa, J. Phys. Soc. Jpn. **86**, 011011 (2016).

[15] A. May, M. Hunt, A. Van Den Berg, A. Hejazi, S. Ladak, Commun. Phys. **2**, 13 (2019).

[16] A. A. Mistonov, N. A. Grigoryeva, A. V. Chumakova, H. Eckerlebe, *et al*., Phys. Rev. B: Condens. Matter Mater. Phys. **87**, 220408 (2013).

[17] S. Mamica, X. Zhou, A. Adeyeye, M. Krawczyk, G. Gubbiotti, **98**, 054405 (2018).

[18] C. Castelnovo, R. Moessner, S. L. Sondhi, Nature **451**, 42 (2008).

[19] O. Sendetskyi, V. Scagnoli, N. Leo, L. Anghinolfi, *et al*., Phys. Rev. B **99**, 214430 (2019).

[20] R. Wang, C. Nisoli, R. Freitas, *et al*., Nature **446**, 102 (2007).

[21] M. Krawczyk, D. Grundler, J. Phys.: Condens. Matter **26**, 123202 (2014).

[22] S. Tacchi, G. Duerr, J. W. Klos, M. Madami, *et al*., Phys. Rev. Lett. **109**, 137202 (2012).